Electrical Machines Diagnosis

Edited by

Jean-Claude Trigeassou

ISTE

WILEY

Electrical Machines Diagnosis

Edited by
Jean-Claude Trigeassou

ISTE

WILEY

First published 2011 in Great Britain and the United States by ISTE Ltd and John Wiley & Sons, Inc.

ISTE Ltd
27-37 St George's Road
London SW19 4EU
UK

www.iste.co.uk

John Wiley & Sons, Inc.
111 River Street
Hoboken, NJ 07030
USA

www.wiley.com

Library of Congress Cataloging-in-Publication Data

Electrical machines diagnosis / edited by Jean-Claude Trigeassou.
p. cm.
Includes bibliographical references and index.
ISBN 978-1-84821-263-3
1. Electric apparatus and appliances--Maintenance and repair. 2. Electric machinery--Maintenance and repair. 3. Electric fault location. I. Trigeassou, Jean-Claude.
TK452.E4155 2011
621.31'0420288--dc23

2011022945

British Library Cataloguing-in-Publication Data
A CIP record for this book is available from the British Library
ISBN 978-1-84821-263-3

Printed and bound in Great Britain by CPI Antony Rowe, Chippenham and Eastbourne.

Table of Contents

Preface

Monitoring and diagnosing faults in electrical machines is a scientific and economic issue which is motivated by objectives for reliability and serviceability in electrical drives. This concern for continuity of serviceability has been motivating electrotechnical engineers since the first industrial applications of electrical machines. To avoid failures, these engineers used experiment feedback to improve machine construction and to make the said machines more robust. Moreover, they gathered knowledge from the detected faults and developed techniques for "manual diagnosis", following examples seen in mechanics and, above all, car maintenance.

The generalization of power supplies through power electronics from the 1950s to 1960s and onward, and the decisive contribution of microcomputers at the end of the 1970s radically changed the approach to machine maintenance through the introduction of "automated" diagnosis techniques. The development of digital control and an increased power in computer systems have opened up a channel for new techniques of automatic control, integrating new functionalities, such as real-time identification and online adaptation of control algorithms. The supervision function has become a natural and necessary addition to the management of automated systems which are becoming increasingly more sophisticated and complex. Furthermore, the concept of integrating automated fault detection and diagnosis came about at the beginning of the 1980s, as a functionality of supervision systems.

This revolution in machine control has also, unfortunately, resulted in new causes for machine failures. Now, to the classic electrical, mechanical, and thermal faults, we can add failures in power electronics and information systems, as well as new faults caused by Pulse Width Modulation power supplies. Moreover, these failures may have instant destructive consequences which justify early diagnosis, whether this is followed by a somewhat instantaneous switch-off or reconfiguration of the machine's power supply.

From now on, the diagnosis of electrical machines, and more widely electrical drives, must be a fundamental aspect of the design, use, and maintenance of a variable speed system. Such a concern is perfectly justified for high powered equipment where the integrity of an expensive system must be conserved. However, we must not lose sight of the fact that the breakdown of a low powered device may also have considerable economic consequences, following the shutdown of a production line.

As for the implementation of advanced numerical control algorithms, new fault diagnosis techniques have been tested. The introduction of the Fourier analysis for detecting mechanical rolling faults or electrical squirrel-cage rotor faults using vibration and current sensors has been a natural extension of "manual" diagnosis techniques. On the other hand, a preference for artificial intelligence in the initial studies on this area can be explained by the classic approach based on expertise. A third channel that opened up used detection techniques based on mathematical models, such as state observation and identification, was initially developed by the automatic control community.

In order to harmonize their work on fault detection in electrical drives in 1995, the research groups "GDR Electrotechnique" and "GDR Automatique" (Electrical Engineering and Automatic Control) set up joint research on the subject of monitoring and diagnosing induction machines. The main French teams from these two domains, as well as a few teams in the signal processing domain, came together regularly to present their work and to discuss joint approaches. In the same way, the work group "Identification", operating on the same principle, highlighted themes regarding the identification of continuous systems and the estimation of physical parameters applied to electrical machines. Out of all these exchanges and joint efforts, two essential outcomes emerged: the need for specific modeling of machines in a fault situation, and an interest in identification for early fault detection.

More specifically, the studies by E. Schaeffer (Chapter 2) on modeling short-circuited stator windings are behind this progress in fault detection. This new approach has made it possible to develop macro-models for early fault detection as well as to define more sophisticated models for simulating electrical faults in AC machines. Also, works by J. Faucher and his students[1, 2] opened up the pathway to these simulation techniques, both in addition to or as substitutes for experiments, which are often impossible to perform due to their potential for destruction.

---

1 V. Devanneaux, Modélisation des machines asynchrones triphasées à cage d'écureuil en vue de la surveillance et du diagnostic, PhD Thesis, INP Toulouse, 2002.

2 A. Abdallah Ali, Modélisation des machines synchrones à aimants permanents pour la simulation de défauts statoriques: application à la traction ferroviaire, PhD Thesis, INP Toulouse, 2005.

With regard to identification, it has been shown that this methodology is suitable for detecting internal faults (short-circuits in stator windings, rotor broken bars), whereas approaches through state observation are better suited to detect external faults, such as sensor or actuator failures. Moreover, the combination of fault modeling/estimation of physical parameters with prior knowledge (of the characteristics of healthy operation) has enabled the development of a complete methodology for diagnosing stator and rotor faults in induction machines. These studies have already been reported in two chapters[3] of another book in the same collection, and will only be partly mentioned in Chapters 2 and 3.

The studies presented in this book come from or have been inspired by this collaboration with the aforementioned research groups. They are dedicated to electrical machine diagnosis and, in a more comprehensive approach, to electrical drives diagnosis. The faults here primarily deal with machines, but also deal with the monitoring of power electronic devices and energy storage in batteries. These faults are largely varied: electrical stator or rotor faults, mechanical faults, thermal faults, inverter faults, and estimation of state of charge. We will also note the range of techniques which are carried out to detect and diagnose these faults. These techniques are usually classified into two categories: those which are based on a model (identification, state observation, model invalidation) and those which are independent of a model (spectral analysis, artificial intelligence methods such as neural networks, fuzzy logic, etc.).

It is useful to remind the readers here that diagnosis comes under the domain of probabilities. Detecting a fault, especially early, must also correspond to a confidence index. Let us also remind the readers that normal operation may also give the same outcome as abnormal operation: thus, an increased resistance estimated by an identification algorithm may also result in rotor heating (normal) as well as bar breakage (abnormal). There is, then, no miracle solution for the problem of monitoring electrical machines, and we must not lose sight of the fact that it is a set of simultaneously acting techniques which make it possible to develop a reliable and robust diagnosis which in turn can help reduce the false alarm rate.

Chapter 1 describes failures affecting electrical machines, in order to know their occurrence and also to analyze their physical causes (either external or internal) such as induced currents in rolling or the repeated action of thermal cycles on conductor insulators. This wide range of main operational faults is followed up by a bibliographical panorama of the most commonly used diagnosis techniques.

---

3 Chapter 7, “Parameter estimation for knowledge and diagnosis of electrical machines” and Chapter 8 “Diagnosis of induction machines by parameter estimation”, in *Control Methods for Electrical Machines*, edited by René Husson, ISTE Ltd., and John Wiley, 2009.

In Chapter 2, a new modeling of a short-circuited winding is introduced, based on the induced currents in the short-circuited section which produce a disturbing magnetic field in the air gap of the machine. This physical analysis has resulted in a new Park model with short-circuited stator winding, which is then extended to the case of a squirrel-cage rotor. This approach to fault situation modeling has enabled us to define and implement a methodology for detecting and locating stator and rotor failures in the asynchronous machine by parameter estimation, validated by experiments on a laboratory benchmark.

Fault diagnosis through parametric estimation generally comes up against a practical problem: to reach convergence, identification algorithms need persistent excitation in order to disturb the machine's operation point, which indeed goes against regulation objectives. One solution is to use the charge disturbances which result in variable voltages generated by the inverter. Thus, we have a closed-loop identification problem. To this end, Chapter 3 offers an identification methodology, which takes into account the non-linear and multivariable nature of vector control algorithms, within an objective to improve electrical fault diagnosis in asynchronous machines.

Observers play a vital role in the vector control of AC machines, particularly when estimating the flux. To do so, we may use a Luenberger observer, a Kalman filter, or a high-gain observer. In addition to state variables, we can also estimate the parameters which vary with the operation point, such as the rotor resistance, for instance. We can, then, make use of an extended observer. Chapter 4 goes back to the basic theories of this methodology and applies it to a few concrete situations.

Whereas we usually imagine electrical faults in machines, the thermal causes behind these failures often go unnoticed. Thermal monitoring is therefore a vital objective within the framework of a global diagnosis system, as much for estimating the temperatures which are impossible to measure directly, as for fault detection such as the obstruction of a ventilation duct. The extended Kalman filter is perfectly suited to this use. Nonetheless, its correct usage assumes a sound prior knowledge of the different noises which affect the measurements, and a perfect control over the algorithm's parameters of adjustment. Chapter 5 offers a reference methodology applied to temperature estimates, which play an important role in thermal monitoring.

Accumulator batteries also hold a vital position in the electrical or hybrid drive chain of a car. Estimating its state of charge is a fundamental issue for continuity of serviceability and operational safety. Chapter 6 proposes an original, dual function procedure. It is original not only through the use of a technique of invalidating the model identified during an initial phase, but also through using an unconventional model of the battery by fractional calculus. This methodology can also be transposed

to machine fault diagnosis, whether it is for modeling squirrel-cage frequency effects or thermal transfers inside the machine, both governed by a diffusion partial differential equation.

Aging and the abnormal use of a rotating machine result in mechanical imbalances and sound and ultrasound vibrations. A well-trained human ear is capable of detecting and locating different types of failures, even in the early stages. Indeed, signal processing techniques are used to automate this monitoring process. The information needed to be processed may be provided by a vibration sensor. However, we prefer the already present line current sensor, which offers more general information regarding the mechanics and electrical operation. The basic tool for spectral analysis is the discrete Fourier transform and its sophistications made possible by the computing power of digital processors. Chapter 7 gives a wide view of the potentials offered by the spectral analysis when applied to mechanical and electrical fault detection of induction machines, using experimental examples.

Artificial neural networks are of high interest to the monitoring of automatic systems. They act as a reference tool for processing problems of classification. Their use for detecting and locating faults in asynchronous machines is perfectly justified, provided that a methodology which is adapted to their properties is implemented. The approach presented in Chapter 8 is based on a residual generation technique using a Park model combined with a Fourier transform algorithm, in order to make a spectral signature of the stator and rotor faults occur. The neural network is responsible for the knowledge and classification of faults using a training database, enabling their detection and location.

Since the generalization of electronic machine control, fault detection in a static converter has become a key element in a global system for monitoring an electrical drive. Conventional approaches through state estimation or identification seem unsuitable for detecting failures which affect the converter. We therefore suggest a set of techniques from the domain of artificial intelligence (neural networks, fuzzy logic) and multivariate statistical methods. Section 9.1 of Chapter 9 offers a number of examples of these applied techniques. However, following the example of electrical and mechanical faults, it is indeed necessary to analyze the failures affecting the electronic components of the converter, and more particularly, failures caused by thermal fatigue. Section 9.2 of Chapter 9 offers a panorama of these failures and outlines a few suggestions for diagnosing them.

Jean-Claude TRIGEASSOU
July 2011

Chapter 1

Faults in Electrical Machines and their Diagnosis

1.1. Introduction

This chapter gives an overview of faults found in electrical machines and their diagnosis, with a special reference to induction machines and their fault detection. These techniques may be easily extended to other types of electrical machines.

Electrical machine fault diagnosis has greatly benefited from an intense interest from research domains. Monitoring electrical machines for diagnosis and predicting breakdowns has spurred the writing of several studies, due to its significant influence on the operational continuity of many industrial processes.

A good diagnosis and early fault detection enable minimized shutdown time as well as maintenance time of the process in question. This also means that the harmful, sometimes devastating, consequences of such faults can be avoided, and there is a reduction in incurring financial losses.

A good detection procedure must use necessary minimalist measures using the process in question, as well as obtain a diagnosis which gives a clear indication of the failure modes by analyzing data in a small time frame.

Chapter written by Sadok BAZINE and Jean-Claude TRIGEASSOU.

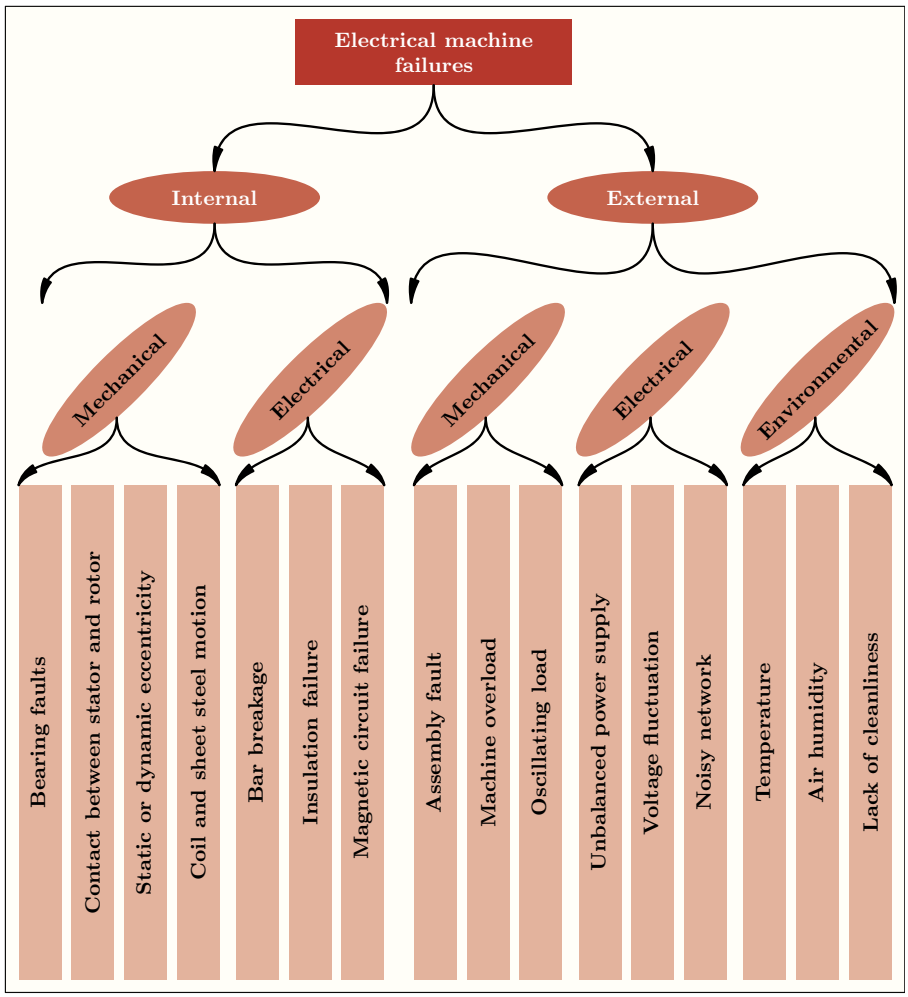

Figure 1.1. *Cause-based fault categorization*

Electrical machines and drive systems often have several types of faults. These can be categorized into two groups according to their causes (Figure 1.1): internal causes and external causes [KAZ 03, CAS 05]. External faults are caused by power supply voltage, mechanical loads, as well as by the machine's usage environment. Internal causes are generated by the machine's components (magnetic circuits, stator and rotor coils, mechanical air-gaps, rotor's cage, etc.). As an example, let us draw up a non-exhaustive list of the faults shown in Figure 1.1:

– electrical faults on the stator, manifested by a phase opening or a short-circuit within the same phase, between two phases, or between one phase and the stator frame;

– electrical faults on the rotor, which include an opening or a short-circuit on the coils for wound rotor machines, or bar and/or short-circuit ring breakages or cracks for squirrel-cage machines;

– mechanical faults on the stator bore or the rotor, such as bearing faults, eccentricity, and alignment;

– failure on the power electronic components of the drive system.

Due to the symmetry in electrical machines, any fault will induce a level of distortion in the rotating magnetic field in the machine's air-gap. It causes harmonics to appear on the measured signals which characterize these faults. Measuring relevant signals enables us to non-invasively monitor the machine's operation. These signals may be electrical or mechanical such as currents, voltages, flux, torque and speed. Fault detection and identification techniques have been widely studied because there are still some questions left unanswered:

– the definition of a single diagnostic procedure for detecting and identifying any type of fault;

– an increase in the robustness of detection techniques, making them unsusceptible to operation conditions;

– the reliable detection of breakdowns for a position, speed, and torque control;

– reliable detection of breakdowns in different working conditions.

An efficient diagnosis opens up a pathway for a tolerant fault control and must, consequently, increase the robustness of the industrial process. Over these last few decades, the advent of power electronics has made it possible to envisage new applications, as well as drawing the best performances from electrical machine operations. Nonetheless, this technological advancement has brought other failure risks with it in terms of electrical drive processes.

Currently, several research laboratories are looking into the design and development of new control strategies [BIA 07, AKI 08], making it possible to make up for performance losses which follow the appearance of failures on the machine or the control system.

This chapter has been set out in three main sections which present the composition of induction machines, the different types of faults which can occur within, and finally, the diagnosis techniques of electrical machines.

1.2. Composition of induction machines

In this section, we wish to briefly outline the composition of the induction machine. This description will enable us to better understand induction machine failures in their physical dimensions.

From a mechanical point of view, induction machines can be composed of three distinct parts:

– the stator: the fixed component where the electrical power supply is connected;

– the rotor: the rotating part which rotates the mechanical load;

– the bearings: the mechanical component which guides the shaft rotation.

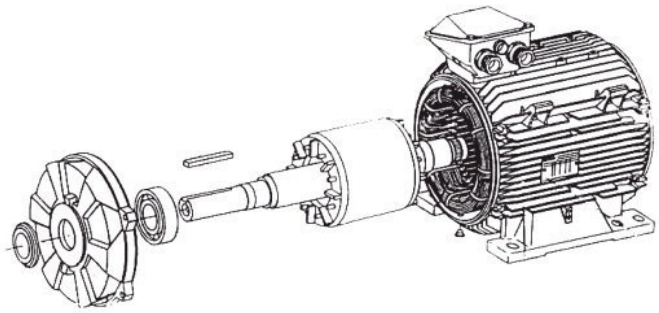

Figure 1.2. *Leroy-Somer induction squirrel-cage motor*

1.2.1. *The stator*

The induction machine stator is composed of steel sheets, where the stator coils are located. For small machines, these sheets are cut out from a single sheet, whereas for more high-powered machines, they are cut out into sections. These sheets are usually varnished to limit the Foucault current effects; they are assembled on top of each other by rivets or welding, to form the stator magnetic circuit. Stator coils are positioned in the pre-designed slots. It is into these slots that the stator coils are positioned, according to a distributed or a concentric winding [GRE 89, LOU 69].

Concentric winding is often used when the induction machine's winding mechanism is performed mechanically. The insulation between the electrical winding and the stator core is made using insulating materials, which may differ depending on the use of the machine.

The stator of the induction machine is also equipped with a terminal box where the electrical power supply is connected. Figure 1.2 shows the different components which make up the induction machine stator.

1.2.2. *The rotor*

The rotor magnetic circuit is composed of steel sheets which, generally, originate from the same place as those used to build the stator. There are two types of rotors in induction machines: wound and squirrel-cage rotors.

The wound rotors are built in the same way as the stator coil[1]. The rotor phases are therefore available with the help of a brush/slip ring assembly located in the machine's shaft.

With regard to squirrel-cage rotors, the winding is composed of copper bars for high-power motors, and aluminum bars for lower-powered motors. These bars are short-circuited at each end by two short-circuit rings, made of copper or aluminum. In Figure 1.2, we show the different elements composing a squirrel-cage rotor.

For squirrel-cage rotors (Figure 1.2), the conductors are made by molding an aluminum alloy or by large bars of precast copper hooped into the rotor's core. Generally, there is no insulation between the rotor bars and the magnetic circuit. But the resistance of the alloy used to build this cage is low enough so the currents do not flow across the magnetic sheets, except when the rotor cage shows bar breakage [MUL 94].

1.2.3. *Bearings*

Bearings are composed of ball bearings and flanges. The ball bearings are inserted when hot on the shaft, for rotation guiding of the motor shaft. The flanges, molded in cast iron alloys, are fixed onto the stator body using bolts or tightening rods as shown in Figure 1.2. All these components arranged in this way compose the induction machine.

1.3. Failures in induction machines

Although the induction machine is said to be robust, it may sometimes present different types of faults. These faults are found in the different parts of the machine, starting with the stator phase connection and finishing with the mechanical coupling between the rotating shaft and the load. These failures can be predicted or unexpected, mechanical, electrical or magnetic, and they have very different causes.

A statistical study led by [BON 08] on squirrel-cage induction machines operated in the petrochemical industry, shows that some breakdowns occur more frequently than others (see diagram in Figure 1.3 displaying the percentage of faults likely to affect these high-powered machines).

This distribution shows that faults in high-powered machines mainly stem from the bearings and the stator coil, which is due to larger mechanical constraints in the case of this machine.

1 Inserting windings in the rotor slots.

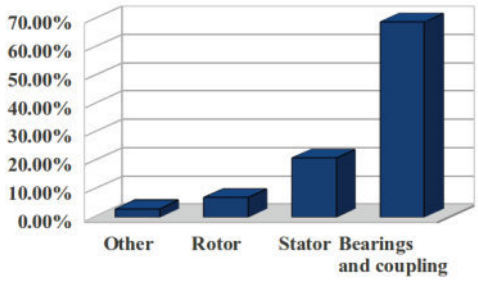

Figure 1.3. *Fault percentages (2008)*

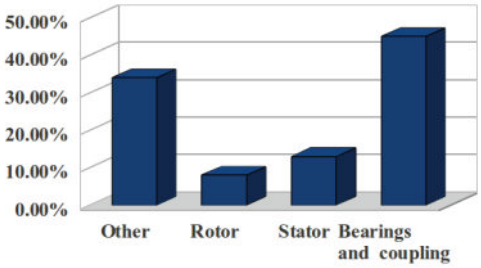

Figure 1.4. *Fault percentages (1995)*

By comparing these results to those taken from older studies carried out by [THO 95] in Figure 1.4 on same-type machines (100 kW to 1 MW), we notice that over the last few years, the distribution of the fault percentages has changed due to the manufacturing conditions in which the motors are constructed. Faults in the stator and rotor are less frequent now, with the main source of failure currently coming from the bearings. Technological advances in power electronics has also made it possible to introduce new control techniques for electrical machines. For machines controlled by power converters, the bearings are excited by voltages including high-rank harmonics. This last option has become standard for controlling electrical systems. This type of power supply accelerates ageing in the stator winding insulator. One solution is to develop a better material insulator. These statistics are not valid for all circumstances, and we must note here that these faults are highly sensitive to the machine's operating conditions, and that they may stem from very different reasons [THO 97]. For instance, let us now make a list of the different causes:

– mechanical: bad manufacturing, machine vibrations, unbalanced electromagnetic forces, centrifugal forces, load fluctuations;

– electrical: insulation damage, partial discharging, sparks;

– thermal: copper losses, lack of general or localized cooling;
– environmental: air humidity, dust.

Table 1.1 [KAZ 03] shows a summary of the causes leading to stator and rotor faults.

	Faults	Causes
Stator fault	Frame vibration	Magnetic imbalance, coil vibration, power supply imbalance, overload, bad installation, contact with the rotor.
	Fault between coils and the stator frame	Coil pressured by the frame, thermal cycle, bad insulation, angular points in the slots, shock.
	Insulation fault	Insulation damage during installation, frequent starting, extreme temperature condition.
	Inter turn short-circuit	excessive temperature, high humidity, vibration, over-voltage.
	Inter-phase short-circuit	insulation failure, high temperature, imbalanced supply, slacking of coils.
	Conductor displacement	Shock, frequent starting, winding vibration.
	Connector failure	conductor pressure, excessive vibration.
Rotor fault	Bearing fault	bad installation, magnetic imbalance, overload, loss of lubricant, high temperature, lack of cleanliness, unbalanced load.
	Bar breaks	magnetic imbalance, overload, loss of lubricant, high temperature, lack of cleanliness, unbalanced load, thermal fatigue.
	Magnetic circuit failure	manufacturing fault, thermal fatigue, overload.
	Misalignment	bad installation, bearing failure, overload, magnetic imbalance.
	Bearing lubricated badly	excessive temperature, bad quality of lubricant.
	Mechanical imbalance	short-circuit ring movement, alignment problem.

Table 1.1. *Causes of failure in the induction machine*

These faults display one or many "symptoms", which can be:

– unbalanced line currents and voltages;

– increased torque oscillations;

– decreased average torque;

– increased losses and therefore reduced energy efficiency;

– excessive heating and therefore accelerated aging.

Thus, as a brief summary, we have categorized these faults into two main groups: mechanical faults and electrical faults. These faults are briefly shown in the flow chart in Figure 1.1.

There are two reasons for studying induction machine faults:

– to understand their evolution so as to predict their gravity and development;

– to analyze their impact on the machine's behavior and to deduce from this the signatures making it possible to go back to the cause of failure, *a posteriori*.

1.3.1. *Mechanical failures*

More than 40% of induction motor faults are mechanical. These can be bearing faults and eccentricity faults.

1.3.1.1. *Bearing faults*

The main reason for machine failures concerns faults in the ball bearing [STA 05] which have several causes, such as lubricant contamination, an excessive load, or even electrical causes such as leakage current induced by multilevel inverters (MLI) [STA 05].

Bearing faults generally lead to several different mechanical effects in machines, such as an increased noise level and vibrations. It has also been shown that bearing failure leads to variations in the torque load in induction machines.

1.3.1.2. *Eccentricity faults*

The effects of mechanical faults are generally displayed at the air-gap, by static, dynamic [SAH 08] (Figure 1.5), or mixed eccentricity faults:

– static eccentricity faults are generally caused by a misalignment in the rotor's rotation pin in relation to the stator pin, where the most frequent cause is a fault in the flange centering;

– dynamic eccentricity faults can be caused by a bend in the rotor cylinder and in the stator cylinder or deterioration in the ball bearings;

– mixed eccentricity, the most common kind of fault, is a combination of static and dynamic eccentricity.

Figure 1.5. *Static and dynamic eccentricity faults*

A vibration, ultrasound, or frequential analysis of the absorbed currents, or simply a visual analysis of the machine's shaft makes it possible to detect these failure types. We can find very comprehensive studies in various works which deal with these various problems, such as those mentioned in [BIG 95, BON 99, BON 00].

1.3.2. *Electrical failures*

Electrical failures, either on the stator or on the rotor, may be of different types or have several different causes. Let us cite an example: an unbalanced power supply voltage in the machine or even frequent starting can lead to overheating in the stator coils, finally leading to a local destruction of the insulator. In the same way, the electrodynamic strains exerted on the phase conductors result in mechanical vibrations which may deteriorate the insulator. In terms of electrics, voltage fronts generated by static converters aggravate the phenomenon and consequently, the lifespan of the conductor insulators. With regard to environmental causes, we may cite air humidity, corrosive or abrasive products.

1.3.2.1. *Stator faults*

Stator faults are displayed as an inter-coil short-circuit between two phases, or a short-circuit between a phase and the stator frame [BAZ 09b]. This can be simplified by the clear connection between two points on the coil. Inter-phase short-circuits appear preferentially in the coil heads, as it is here that the different phase conductors flow together. Inter-coil short-circuits in the same phase may appear, either on the coil heads or in the notches, which leads to a reduction in the number of actual coils in the winding.

An inter-phase short-circuit would cause the machine to shutdown. However, a short-circuit between a phase and the neutral (via the yoke) or between the coils of the same phase does not have such an extreme effect. It will lead to a phase imbalance, which will have a direct effect on the torque. This type of fault also interferes with the controls developed by using the Park model (hypothesis for a balanced model).

1.3.2.2. *Rotor faults*

A wound rotor may be affected by the same faults as the stator. For a cage rotor, the faults can be summarized as bar breakages or short-circuit ring breakages (Figure 1.6).

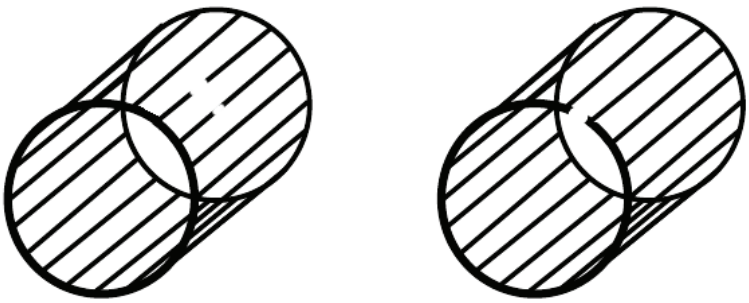

Figure 1.6. *Fault by bar and short-circuit ring breakage*

These bar or short-circuit ring breakages can be due, for example, to a mechanical overload (frequent starting up), local excessive overheating, or even a manufacturing fault (air bubbles or bad welds) [BON 92, CAS 05]. This fault will induce oscillations in the currents and the electromagnetic torque, which are more noticeable when the inertia is high (constant speed). When the drive inertia is lower, then oscillations occur in the mechanical speed and in the stator current amplitudes.

The ring section break is a fault which occurs as frequently as bar breaks. In fact, these breaks are either due to bubbles in the casting or due to different dilations between the bars and the rings, especially as the short-circuit rings conduct larger currents than the rotor bars. Due to this phenomenon, a bad ring sizing, deterioration in the operating conditions or a torque overload, and therefore a current overload, may lead to their breaking.

A bar break fault will not cause the machine to shut down because the current which runs through the broken bar is distributed over the adjacent bars. Thus, these bars are then overloaded, which can break them and a large number of broken bars causes a shutdown.

Faced with the multitude of possible faults and their consequences, monitoring techniques have rapidly been imposed on electrical machine users. They are also beginning to interest the designers.

1.4. Overview of methods for diagnosing induction machines

Electrical machines, and induction machines in particular, play a vital role today in all industrial applications. Guaranteeing availability and operating safety of these

machines is a fundamental task. It is, then, necessary to develop systems which enable monitoring and diagnosis of the health condition of these devices.

Monitoring and supervision must not be limited to the electrical machine alone. In fact, this machine is still part of an entire industrial process. Ensuring the operating safety is part of the supervision process of the whole industrial process itself. The diagram showing the supervision and accommodation of the control in Figure 1.7 shows the different stages and functionalities that a supervised system must contain.

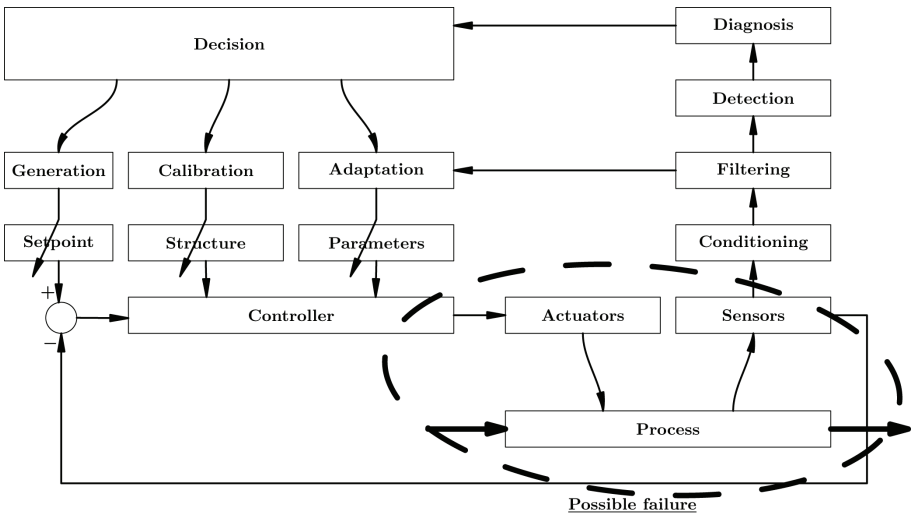

Figure 1.7. *Control supervision and accommodation*

This diagram is applicable to the induction machine and its control, or to the integrating process. The final objective for any supervision is to increase the reliability of the process, by looking to catch failures which may occur when the system is in operation. Once the levels of supervision and diagnosis have fulfilled their role by detecting and identifying the failure, then the second stage is to act on the controls to catch this operational decline. This intervention stage takes place on several different levels (Figure 1.7) according to the severity and the destructive nature of the failure.

For some highly important systems where even the smallest breakdown may be impossible (nuclear plants, aerospace industry, air transport, etc.), the designers multiply the systems so that, for a failure in one system, another system will immediately replace it. If one of the systems displays behavior which is very different from the others, then it is excluded from the set of systems. This type of maintenance (material redundancy) is clearly too expensive to implement for the most common types of industrial systems.

The aim of this section is to present an overview of diagnosis methods applied to electrical machines. These methods are classified into two large categories: those which use an analytical model of the system, and those which do not use it. The analytical approach is rather inspired by control engineers, whereas those from the electrical engineering and signal processing domains prefer to make use of more heuristic methods.

1.4.1. *Diagnosis methods using an analytical model*

These detection methods rely on a prior knowledge of the system. They assume knowledge of the models and parameters representing the system's operations. Signals generated by the models (or estimated parameters) enable detection as well as the identification of the failure which is likely to occur. These techniques assume a prior knowledge of the range of variations within these models and parameters, according to the system's operating conditions. These techniques can be categorized into three groups.

1.4.1.1. *State estimation techniques*

Analytical models involve a finite number of internal variables, called state variables. These variables are generally immeasurable for reasons concerning accessibility: they might lack physical meaning or the cost of installing sensors is too high. As the system's evolution through time is characterized by the evolution of these variables, then we often use estimation techniques (software sensor) to follow the evolution of their values. Figure 1.8 shows the diagram of the principle of state estimation using measured signals (system's input and output signals).

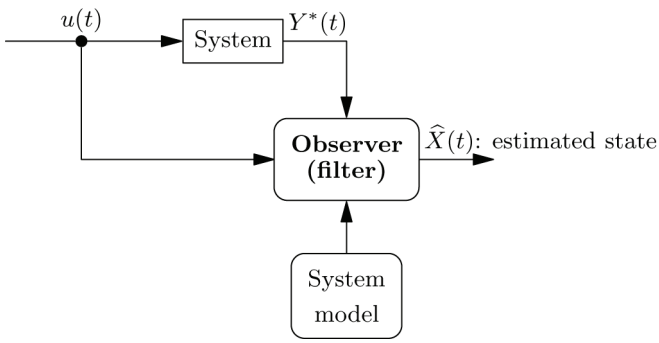

Figure 1.8. *Principle of state estimation*

Fundamental studies done by [KAL 60] and [LUE 71] offer two different approaches to reconstruct the system's state through knowing its mathematical model. The techniques which stem from these two concepts are the Kalman filter and

the Luenberger observer. Techniques based on a linear representation around the system's operating point have made it possible to adapt these techniques to non-linear models. We can cite the extended Kalman filter and the extended Luenberger observer [SAÏ 00, CHE 06, BES 07]. We can also cite other techniques which may be applied to systems which cannot be linearized by coordinate changes, such as high-gain observers [RAJ 98, GAU 92], adaptive-gain observers [RAG 94], or a combination of high-gain observers and the Kalman filter [GAU 92]... The extended Kalman filter, estimating state variables and parameters, refers us back to identification techniques. As an example, in the domain of monitoring and diagnosing the induction machine, we may use rotor currents[2] or flux, based on the Park model of the induction machine, which may inform us about the presence of certain types of faults, as these estimations are used by control algorithms.

1.4.1.2. *Residual generation technique*

Residuals are signals which reflect the deviation between a model and the system to be monitored, as shown in Figure 1.9. These residuals depend on the technique they are generated from. These techniques for extracting residuals aim to provide important and exploitable signals to detect a specific failure. When the residuals are in healthy operating mode, they must be close to zero and reflect a fault by taking important values.

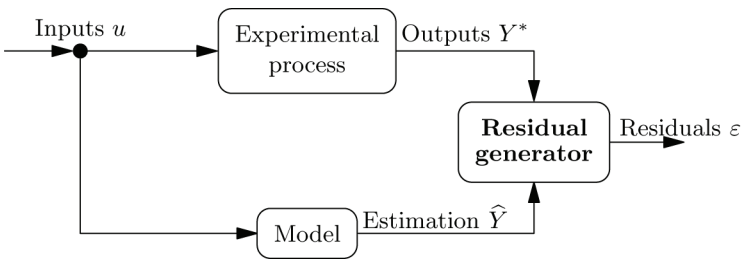

Figure 1.9. *Residual generation*

Another generation technique is based on analytical redundancy relationships (ARR) [CHR 99] in order to provide the machine's variations in stator and rotor resistance with robust residuals, which has made it possible to provide a reliable malfunction detector on the stator or rotor.

However, several studies have shown that these residual generation techniques are more suited to detect actuator, and above all sensor, faults [CHR 99]. In practice, internal faults are detected better by identification techniques.

2 For a squirrel-cage rotor.

1.4.1.3. *Identification techniques*

Identification techniques aim to determine a dynamic model of the system to be monitored using experimental input and output measures. The fundamental idea is that the parameters which characterize this identified model will be sensitive to the faults affecting the machine, and will therefore make it possible to characterize these faults through their variations; in [ISE 93], we find a formalization of this principle.

Estimating the model's parameters is ensured by an algorithm to minimize the error between the model's output and the machine's output. Figure 1.10 presents this process, which is also known as the model method [RIC 71].

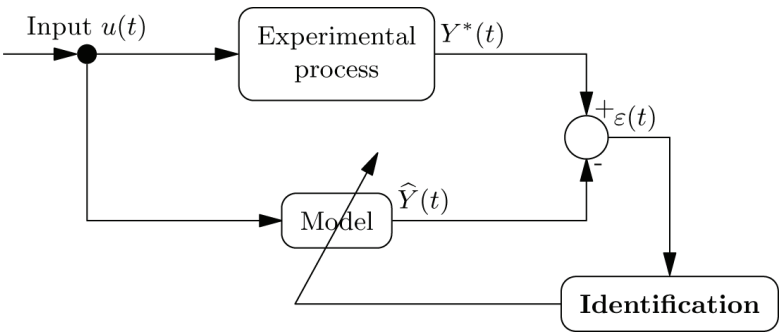

Figure 1.10. *Principle of identification techniques*

Many identification techniques based on the minimization of quadratic criteria may be used. We will categorize them according to:

– equation error techniques [LJU 87];

– output error techniques [RIC 71, TRI 96, TRI 01];

– the extended Kalman filter [LJU 87, LOR 98].

Equation error techniques are the simplest to implement. Moreover, they adapt perfectly to real time, therefore to the monitoring of parametric variations. Their main fault is providing biased estimations by noises affecting the system. Furthermore, it is important to adapt them to cases of continuous representation systems [YOU 81, MEN 99].

Output error techniques are more laborious to implement and are limited to offline operations. On the other hand, they give unbiased information which is well adapted to diagnostics via parametric monitoring, potentially with prior knowledge [MOR 99].

The extended Kalman filter [LOR 98] combines state observation and parametric estimation. Its estimations are also unbiased. Moreover, this estimator is perfectly well adapted to real-time operations. However, optimum operation requires a good level of prior knowledge regarding noises affecting the system.

The electrical parameters which characterize the induction machine can be very good fault indicators. One of the most commonly studied failures in the squirrel-cage induction machine is the rotor bar break. Although this can be identified using a spectral analysis of stator currents, monitoring the rotor resistance can also be a good failure indicator.

In fact, several studies have proven that the resistance Rr is highly sensitive to rotor faults, and that the variation in this resistance is increased when the number of broken bars is also increased. Many techniques make it possible to estimate the value of this resistance, for example, here we can cite the output error estimation [MOR 99, BAC 02], the extended Kalman filter estimation [SAÏ 00, BAZ 09a], or the non-linear high-gain observer estimation [BOU 01].

However, due to the fact that the value of this resistance is also linked to the variation in the rotor temperature, a natural cause (for instance, operation at full load) could be enough to make the resistance change. A single estimation of Rr does not allow us to detect the presence of one or many faulty bars. This ambiguity can be alleviated by taking account of the machine's internal temperature using identification algorithms and having prior knowledge [BAC 02].

These methods of diagnosis through identification are generally used for monitoring and detecting failures, most often by using precise models of [SCH 99, BAC 02]:

– broken bars or short-circuit rings;

– static and dynamic eccentricity;

– reduced coils or inter-coil short-circuit in the same stator phase.

The main limitation of identification-based techniques is the need for persistent excitation, i.e. an input $u(t)$ (Figure 1.10) which stimulates the system enough so as to generate signals which can be used by the identification algorithm. This persistent excitation [LJU 87] is clearly incompatible with controlled operation (at constant speed, for instance).

The first group of diagnostic models requires knowledge of the machine's dynamic behavior, using a knowledge model. However, these methods do not allow us to study all the faults in the machine (bearing faults, for example). In the following section, we will focus on diagnostic methods without a model, based on monitoring and analyzing magnitudes such as currents, vibrations, flux, and torques.

1.4.2. *Diagnostic methods with no analytical model*

These methods do not necessarily require a specific model of the system, but rather rely on knowledge of signatures. Fault signatures, obtained through modeling or measurements, are generally categorized in a database. The analysis is carried out by a signal-type interpretation or by an expert system.

The following faults are studied by these diagnostic methods:

– breakages in the bars or slice of the rotor ring;

– static and dynamic eccentricity;

– bearing failures;

– inter-coil short-circuit.

1.4.2.1. *Signal processing method*

For reasons of simplicity and efficiency, the signal approach is currently being widely used in diagnostics. This approach is based on knowledge of the healthy system's behavior, and it is then compared to the measured signals. The common methods of analyzing diagnostic signals in a transitory and permanent regime are spectral analysis, spectrogram, temporal analysis, and the Wigner-Ville distribution [AND 94].

Approaches based on spectral signature analysis are the most commonly found methods used for detecting an anomaly. The main fault in spectral analysis is that it is highly sensitive to the measurement quality, as well as the sampling frequency and the number of samples. The procedures for monitoring operations are generally directed toward specific failures in one of the three parts of the machine: the stator, the rotor, or the bearings.

To accurately draw out information relating to faults, research has been carried out, in particular, toward the spectrum of stator currents, for two reasons. Currents are easy to measure and they provide a lot of information on a lot of different faults. But measuring signals and then processing them in the "FFT" spectral domain can only be used, in terms of identification, if the frequential components defined for each fault are known [BEN 00, KAZ 03, SAH 08]. Besides this limitation, this method requires a sufficient number of acquisition points to guarantee a minimum frequential accuracy. This technique is generally used during the machine's permanent regime [DID 04].

The spectrogram technique means that we can carry out frequential analysis of signals in the dynamic regime of the system's operation. This technique consists of carrying out a repetitive calculation of the FFT on a temporal drop window, which makes this technique sensitive to the window length, to the window type, to the total duration of the supervision process and the step of the sliding window [FLA 93]. Although this technique means that we can analyze signals in the dynamic regime, the

speed of the dynamic regime for induction machines at 150 m/s significantly reduces the accuracy of this technique.

We must also refer to the temporal analysis, which consists of comparing temporal signals coming from the system's healthy operation to the temporal signals of the current operation [CAS 03, KRA 04, OND 06]. The phase shift introduced by the measurement instruments makes the direct comparison of these instruments insignificant. Thus, it is common practice to transform the signals before comparing them. Despite this transformation, this method does not allow us to efficiently identify the failures which could affect electrical machines.

Time-frequency methods, based on the Wigner-Ville analysis, combine the temporal analysis and the frequential analysis. [AND 94] proved that this technique will allow us to extract information from a system's dynamic regime, and that this regime is more comprehensive than the stationary process in question.

1.4.2.2. *Artificial intelligence (AI) method*

Artificial intelligence is being used widely in the supervision and diagnostics domain. It has increased the efficiency and reliability of diagnostics. In the domain of supervising electrical machines, industrialists and researchers are using this type of technique more often in order to increase the system's efficiency [ALT 99, AWA 03].

In fact, the term "artificial intelligence" involves various different techniques, such as expert systems, neural networks, and fuzzy logic, which can all be used independently or in a combination, to improve their efficiency. These methods are interesting, even if they require an initial training phase which is vital for optimal operation. The training phase requires an important set of examples, as it may be erroneous or produce results which are limited to a set of systems.

Once the training phase has been completed, these techniques are displayed as being efficient and simple, and can be successfully adopted for diagnosing failure in electrical systems. Artificial intelligence techniques may contribute to accelerating the decision-making process with a reduced amount of human intervention. But they are not a cure for solving all diagnostic problems.

Artificial intelligence-based techniques try to imitate human reasoning in different ways, which we will describe below:

Artificial neural networks imitate the neural structure of the human brain; they are formed by a complex network of simple arithmetic blocks. They can easily represent the non-linear, multi-input, multi-output systems.

This technique was widely used in the domain of diagnosing electrical machines [SAL 00, AWA 03] according to several different approaches and techniques:

– training using temporal or frequency signals drawn from simulations or experiments;

– real-time self-diagnosis;

– dynamic updating of the network structure;

– filtering transients, disturbances, and noise;

– detecting faults as soon as they occur.

Fuzzy logic translates the human perception of values. It is not limited to values such as "true or false" like traditional logic. It offers a wide variety of intermediate values. Fuzzy systems can process natural variables through fuzzy "if-then" conditions. Adaptive fuzzy systems use the training faculties of neural networks, or the robustness of genetic algorithms in the domain of optimizing the parameters of the studied system, in order to consider prior knowledge and human expertise in this domain.

In the following studies [ALT 99, BAL 07, ZID 08], we can find several articles which exploit this technique in diagnosing and monitoring electrical machines. They have varied objectives:

– detection of abnormal functioning and locating failure;

– evaluation of performance indexes;

– constructing a database taken from human expertise, and formulating a set of conditional "if-then" rules;

– design of adaptive systems for diagnostics.

The *neuro-fuzzy technique* is the combination of the two previous techniques. [ALT 99] and [BAL 07] have shown that this combination is very interesting for diagnosing and monitoring induction machines. In fact, the adaptive neuron networks may generate the corresponding fuzzy system alone. This generation of rules is performed using training examples, by minimizing expert intervention during the formulation of conditional rules.

Applying AI is of great use in automating the diagnosis procedure. It makes it possible to take advantage of human expertise in the domain at hand.

1.5. Conclusion

Electrical machine diagnosis has been, and still is, an important topic for research over the last few decades, such that it has been presented in the non-exhaustive bibliography which can be found at the end of this chapter. The advent of monitoring has revolutionized system maintenance based on electrical machines. In fact, this term refers to a monitored system, making it possible to diagnose the state of an AC motor

in order to determine the failure types and their seriousness when the motor is within its normal operating conditions.

We started this chapter by reminding readers of the composition of the induction machine. We then categorized the failures likely to affect the different components of electrical machines. Next, we drew up a non-exhaustive list of the causes which could lead to mechanical and electrical failure in these machines.

We have tried to present an outline of the methods and techniques for monitoring and diagnosing electrical machines. Two large categories of methods were reviewed: those based on an analytical model of the machine (with particular focus on the identification approach), and the methods with no model, based on the Fourier analysis and a heuristic approach.

1.6. Bibliography

[AKI 08] Akin B., Orguner U., Toliyat H.A., Rayner M., "Low order PWM inverter harmonics contributions to the inverter-fed induction machine fault diagnosis", *IEEE Transactions on Industry Electronics*, vol. 55, no. 2, p. 910-919, February 2008.

[ALT 99] Altug S., Chen M.-Y., Trussell H.J., "Fuzzy inference systems implemented on neural architectures for motor fault detection and diagnosis", *IEEE Transaction on Industry Electronics*, vol. 46, no. 6, p. 1069-1079, 1999.

[AND 94] Andria G., Savino M., Trotta A., "Application of Wigner-Ville distribution to measurement on transient signal", *IEEE Transaction on Instrumentation and measurement*, vol. 43, no. 2, April 1994.

[AWA 03] Awadallah M.A., Morcos M., "Application of AI tools in fault diagnosis of electrical machines and drives-an overview", *IEEE Transaction on Energy Conversion*, vol. 18, no. 2, p. 245-251, 2003.

[BAC 02] Bachir S., Contribution au diagnostic de la machine asynchrone par estimation paramétrique, PhD thesis, University of Poitiers, France, December 2002.

[BAL 07] Ballal M.S., Khan Z.J., Suryawanshi H.M., Sonolikar R.L., "Adaptive neural fuzzy inference system for the detection of inter turn insulation and bearing wear faults in induction motor", *IEEE Transaction on Industry Electronics*, vol. 54, no. 1, p. 250-258, 2007.

[BAZ 09a] Bazine I.B.A., Bazine S., Tnani S., Champenois G., "Online broken bars detection diagnosis by parameters estimation", *13th European Conference on Power Electronics and Applications EPE*, Spain, Barcelona, 8-10 September 2009.

[BAZ 09b] Bazine S., Conception et implémentation d'un Méta-modèle de machines asynchrones en défaut, PhD thesis, University of Poitiers, Ecole nationale d'ingénieurs de Tunis, June 2009.

[BEN 00] Benbouzid M.E.H., "Review of induction motors signature analysis as a medium for fault detection", *IEEE Transactions on Industrial Electronics*, vol. 47, p. 984-993, 2000.

[BES 07] Besançon G., *Non-linear Observers and Applications*, Springer, Berlin, 2007.

[BIA 07] Bianchi N., Bolognani S., Pré M.D., "Strategies for the fault-tolerant current control of a five-phase permanent-magnet motor", *IEEE Transactions on Industry Applications*, vol. 43, no. 4, p. 960-970, July-August 2007.

[BIG 95] Bigret R., Féron J.L., *Diagnostic - maintenance - disponibilité des machines tournantes*, Editions Masson, 1995.

[BON 92] Bonnett A.H., Soukup G.C., "Cause and analysis of stator and rotor failures in tree-phase squirrel-cage induction motor", *IEEE Transactions on Industry Applications*, vol. 28, p. 921-937, July-August 1992.

[BON 99] Bonnett A.H., "Understanding motor shaft failures", *IEEE Applications Magazine*, p. 25-41, 1999.

[BON 00] Bonnett A.H., "Root cause AC motor failure analysis with a focus on shaft failures", *IEEE Transactions on Industry Applications*, vol. 36, p. 1435-1448, 2000.

[BON 08] Bonnett A.H., Yung C., "Increased efficiency versus increased reliability", *IEEE Industry Applications Magazine*, p. 1077-2618, January-February 2008.

[BOU 01] Boumegoura T., Recherche de signature électromagnétique des défauts dans une machine asynchrone et synthèse d'observateurs en vue du diagnostic, PhD thesis, École Centrale de Lyon, March 2001.

[CAS 03] Casimir R., Diagnostic des défauts des machines asynchrones par reconnaissance des formes, PhD thesis, Ecole centrale de Lyon, 2003.

[CAS 05] Casimir R., Bouteleux E., Yahoui H., Clerc G., Henao H., Delmotte C., Capolino G., Houdouin G., Barakat G., Dakyo B., Didier G., Razik H., Foulon E., Loron L., Bachir S., Tnani S., Champenois G., Trigeassou J., Devanneaux V., Dagues B., Faucher J., Rostaing G., Rognon J., "Synthèse de plusieurs méthodes de modélisation et de diagnostic de la machine asynchrone à cage en présence de défauts", *Revue Internationale de Génie Électrique*, vol. 8, no. 2, p. 287-330, 2005.

[CHE 06] Cherrier E., Estimation de l'état et des entrées inconnues pour une classe de systèmes non linéaires, PhD thesis, Institut national polytechnique de Lorraine, France, 2006.

[CHR 99] Christophe C., Cocquempot V., Staroswiecki M., "Robust residual generation for induction motor using elimination theory", *SDEMPED-99*, 1-3 September 1999.

[DID 04] Didier G., Modélisation et diagnostic de la machine asynchrone en présence de défaillances, PhD thesis, University of Nancy 1, France, 2004.

[FLA 93] Flandrin P., *Temps - Fréquence*, Hermès, Paris, 1993.

[GAU 92] Gauthier J., Hammouri H., Othman S., "A simple observer for non-linear systems applications to bioreactors", *IEEE Transactions on Automatic Control*, vol. 37, no. 6, p. 875-880, 1992.

[GRE 89] Grellet G., "Pertes dans les machines tournantes", *Convertisseurs et machines électriques*, Techniques de l'ingénieur, dossier D3450, December 1989.

[ISE 93] ISERMAN R., "Fault diagnosis of machines via parameter estimation and knowledge processing - tutorial paper", *Automatica*, vol. 29, no. 4, p. 815-835, 1993.

[KAL 60] KALMAN R., "A new approch to linear filtering and prediction problems", *Transactions of the ASME - Journal of Basic Engineering*, vol. 82, p. 35-45, 1960.

[KAZ 03] KAZZAZ S.A.S.A., SINGH G.K., "Experimental investigations on induction machine condition monitoring and fault diagnosis using digital signal processing techniques", *Electric Power Systems Research*, vol. 65, p. 197-221, Elsevier, 2003.

[KRA 04] KRAL C., HABETLER T.G., HARLEY R.G., "Detection of mechanical unbalances of induction machines without spectral analysis of time-domain signals", *IEEE Transactions on Industrial Applications*, vol. 40, no. 4, p. 1101-1106, August 2004.

[LJU 87] LJUNG L., *System Identification: Theory for the User*, Prentice Hall, Englewood Cliffs, 1987.

[LOR 98] LORON L., Identification et commande des machines électriques, Habilitation à diriger des recherches, UTC Compiègne, 1998.

[LOU 69] LOUTZKY S., *Calcul pratique des alternateurs et des moteurs asynchrones*, Eyrolles, Paris, 1969.

[LUE 71] LUENBERGER D.G., "An introduction to observers", *IEEE Transactions on Automatic Control*, vol. 16, no. 6, p. 596-602, 1971.

[MEN 99] MENSLER M., Analyse et étude comparative de méthodes d'identification des systèmes à représentation continue. Développement d'une boîte à outil logicielle, PhD thesis, University of Nancy I, 1999.

[MOR 99] MOREAU S., Contribution à la modélisation et à l'estimation paramétrique des machines électriques à courant alternatif: Application au diagnostic, PhD thesis, University of Poitiers, 1999.

[MUL 94] MULLER G., LANDY C., "Vibration produced in squirrel-cage induction motors having broken rotor bars and interbar currents", *International Conferences on Electrical Machines*, 1994.

[OND 06] ONDEL O., Diagnostic par reconnaissance des formes : Application à un ensemble convertisseur-machine asynchrone, PhD thesis, Ecole centrale de Lyon, 2006.

[RAG 94] RAGHAVAN S., HEDRICK J., "Observer design for a class of non-linear systems", *International Journal of Control*, vol. 59, no. 2, p. 515-528, 1994.

[RAJ 98] RAJAMANI R., "Observer for lipschitz non-linear systems", *IEEE Transactions on Automatic Control*, vol. 43, no. 3, p. 397-401, 1998.

[RIC 71] RICHALET J., RAULT A., POULIQUEN R., *Identification des processus par la méthode du modèle*, Gordon and Breach, London, 1971.

[SAH 08] SAHRAOUI M., GHOGGAL A., ZOUZOU S., BENBOUZID M., "Dynamic eccentricity in squirrel-cage induction motor-Simulation and analytical study of its spectral signature on stator currents", *ELSEVIER Simulation Modeling Practice and Theory*, vol. 16, p. 1503-1513, 2008.

[SAÏ 00] Saïd M., Benbouzid M., Benchaib A., "Detection of broken bares in induction motors using an extended Kalman filter for rotor resistance sensorless estimation", *IEEE Transaction on Energy Conversion*, vol. 15, no. 1, March 2000.

[SAL 00] Salles G., Filippetti F., Tassoni C., Crellet G., Franceschini G., "Monitoring of induction motor load by neural network techniques", *IEEE Transaction on Power Electronics*, vol. 15, no. 4, p. 762-768, 2000.

[SCH 99] Schaeffer E., Diagnostic des machines asynchrones: modèles et outils paramétriques dédiés à la simulation et à la détection de défauts, PhD thesis, University of Nantes, 1999.

[STA 05] Stack J.R., Habetler T.G., Harley R.G., "Experimentally generating faults in rolling element bearings via shaft current", *IEEE Transactions on Industry Applications*, vol. 41, no. 1, p. 25-29, January-February 2005.

[THO 95] Thorsen O.V., Dalva M., "A survey of fault on induction motors in offshore oil industry, petrochemical industry, gas terminals, and oil refineries", *IEEE Industry Applications Magazine*, vol. 31, no. 5, September 1995.

[THO 97] Thorsen O.V., Dalva M., "Failure identification and analysis for high voltage motors in petrochemical industry", *Conference Publication*, *IEE 1997*, no. 444, Condition monitoring methods, 1-3 September 1997.

[TRI 96] Trigeassou J.-C., "Estimation paramétrique des systèmes continus", *Surveillance des systèmes continus*, Ecole d'été d'Automatique de Grenoble, France, 1996.

[TRI 01] Trigeassou J.-C., Poinot T., "Identification des systèmes à représentation continue - application à l'estimation de paramètres physiques", *Identification des systèmes*, p. 177-211, Landau I.D., Besançon-Voda A. (eds), Hermès, Paris, 2001.

[YOU 81] Young P., "Parameter estimation for continuous time models - a survey", *Automatica*, vol. 17, no. 1, p. 23-39, 1981.

[ZID 08] Zidani F., Diallo D., Benbouzid M.E.H., Nait-Said R., "A fuzzy-based approach for the diagnosis of fault modes in a voltage-fed PWM inverter induction motor drive", *IEEE Transaction on Industry Electronics*, vol. 55, no. 2, p. 586-593, February 2008.

Chapter 2

Modeling Induction Machine Winding Faults for Diagnosis

2.1. Introduction

2.1.1. *Simulation model versus diagnosis model*

For a *simulation model* intended to validate a control reconfiguration in the presence of a winding fault situation, the acceptable simulation time for an experimentalist may vary from a few minutes to a few hours, depending on the desired level of precision. On the other hand, if the aim of the modeling is to monitor online an electrical drive by following the parameters $\underline{\theta}$ of a *diagnosis model*, then the complexity of the model will become a prominent choice criterion.

In fact, monitoring parameters can be carried out by identification algorithms which differ depending on the model's structure and the criterion to be optimized [LJU 99, MEN 99]. In the typical case of a quadratic criterion based on the output error and the output of a non-affine model (in relation to the parameters), the classic optimization algorithms will use the criterion's limited development around the intermediate position $\underline{\hat{\theta}}_i$ to generate the orientation and depth of research in the parameter space. However, experience shows that the analytical expression of the gradient and the Hessian is often needed for algorithm convergence. Reducing the number of parameters is therefore an important objective in order to guarantee that the diagnosis model can be identified within the system's usage conditions, even if we can see that introducing *a priori* information may help us solve this problem. On the other hand, the simplex algorithm

---

Chapter written by Emmanuel SCHAEFFER and Smail BACHIR.

[DAN 98] imposes no constraint on the model's analytical structure because only the system's simulated output is required. We can therefore completely envisage using more complex models, which are more like those suggested for a more accurate simulation of the machine, but at the cost of a considerably increased convergence time.

2.1.2. *Objectives*

The problematic issue of looking for a "good" diagnosis model is actually moving toward a more global problem of searching for a better compromise, namely, the *diagnostic model* and *identification algorithm* pair. Another major aspect is the identification protocol which requires a sufficient wideband input signal. For an electric car, the frequent phases of rapid acceleration and deceleration may potentially be enough to excite all the diagnosis model poles, which is actually no longer true for a fixed-speed or slow changing application.

From an operational point of view, the final choice will depend on the criticality of the diagnosis, meaning the time elapsed between the fault interruption, its diagnosis (detection, location, characterization of fault severity), and the decision-making process. In other words, is immediate shutdown required or could a control reconfiguration limit the effects of the fault while making it possible to obtain a sufficient electromagnetic torque until the next scheduled shutdown? In fact, with the latest variable speed drives, internal current loops manage to perfectly impose the machine currents and therefore minor malfunction can be ignored, without damaging the drive performances. For example, we will see that the controls are perfectly free from imbalances induced by a stator insulation fault, whether it deals with a few short-circuited inter turns or with a resistive contact of several ohms between a high number of inter turns in the same phase. However, the fault current flowing in the involved inter turns may be much higher than the rated current, inevitably leading to rapid overheating in the conductors, and therefore, as a sort of chain reaction, to a generalized carbonization of the insulating wall.

Since the 1990s, French studies [CAS 04, LOR 93, MOR 99, SCH 99] which have focused on monitoring induction machines through parameter follow-up have shown that a short-circuit fault will not lead to any significant changes in the parameters of Park's two-phase model which is traditionally used in control. Consequently, one of the major stages in diagnosing electrical drives has been the development of diagnosis models which are fully adapted to describing winding faults, and can be identified in the machine's usage conditions. This chapter will deal with this subject.

2.1.3. *Methodology*

At a later stage, we will assume that the imbalances caused by winding faults will remain low enough so as to be able to continue to reason with the two-phase

components $\underline{i}_{s_{dq}} = \mathcal{T}_{23}\ \underline{i}_{s_{abc}}$ and $\underline{u}_{s_{dq}} = \mathcal{T}_{23}\ \underline{u}_{s_{abc}}$, where $\underline{i}_{s_{abc}}$ and $\underline{u}_{s_{abc}}$ are the stator phase currents and voltages, and $\mathcal{T}_{23}$ is the Concordia matrix. Strictly speaking, this is no longer possible: in the case of a star connection in a machine, the line currents measured for control are also the phase currents, but the phase voltages for an unbalanced machine can no longer be deduced from the line voltages imposed by the inverter! On the other hand, for a delta connection, the phase voltages are those imposed by the inverter (therefore known voltages), yet the phase currents are inaccessible[1]. This simplified assumption is highly important for the following section, because it makes it possible to use the simplified power of the Concordia and Park transforms for writing machine equations in the rotating field or rotor reference frame. This change in reference frame, in fact, makes it possible to translate the spectrum of current and voltage signals in a lower frequency domain, thus simplifying the discretization of the continuous state model for numerical integration.

From a conceptual point of view, this hypothesis enables us to propose a two-mode model: a "common" mode and a "differential" mode. The common mode relates to the model dynamics of the induction machine with no fault, as used by the control (Park model). It explains the normal evolution of the machine's characteristics when in operation: these evolutions are caused by high variations in temperature, possible variations in magnetization, or even evolutions in iron losses. With regard to the differential mode, it aims to reveal a malfunction in the machine, as its parameters ideally must only be sensitive to the faults being diagnosed.

This situation has proven to be favorable for introducing the *a priori* knowledge that we may have of the machine in order to facilitate the parameter estimation of the whole model. The Park model is typically parameterized by the stator resistance R_s, the cyclic stator inductance L_{c_s}, the rotor time constant T_r, and the dispersion coefficient $\sigma = 1 - (\frac{M_{c_{sr}}^2}{L_{c_s} L_{c_r}})$, where L_{c_r} represents the cyclic stator inductance and $M_{c_{sr}}$ represents the stator/rotor mutual inductance. In the presence of a control regulating the magnetizing flux amplitude, the inductive parameters L_{c_s} and σ can be considered as constant. However, variations in temperature of the stator, and particularly on the rotor, may lead to a large variation in the stator and rotor resistances, and therefore in $T_r = \frac{L_{c_r}}{R_r}$, where R_r is the rotor resistance. This kind of consideration means that we can significantly reduce the number of the model's parameters to be estimated for online diagnosis, and therefore also impact the excitation protocol which is necessary for the identification process.

2.1.4. *Chapter structure*

The first part of the chapter presents the assumptions for study and the underlying principles of modeling the machine in order to diagnose it. The concepts of rotating and

1 The matrix expressing the line current in relation to the phase currents is not invertible.

stationary fields (in the electrotechnical sense of the term), as well as the equivalence between winding systems, will be dealt with in this first section. These are elementary yet fundamental conceptions for understanding winding fault modeling, while allowing us to introduce the notations which will appear in the chapter. The following section will go into detail on equation formulation and obtaining models in their basic form, suitable for detecting short-circuiting in inter turns. In the third section, the approach is extended to modeling an imbalance in squirrel-cage rotor. The last section will present the method and tools used to validate this diagnostic model. This relies on the results obtained from IREENA [SCH 99] and LAII [BAC 06, BAZ 08, MOR 99] who used similar power range induction machines (induction motors of 1.1 and 1.5 kW) but used different excitation protocols and optimization algorithms.

2.2. Study framework and general methodology

2.2.1. *Working hypotheses*

Studying electrical rotating machines can be achieved either by using rotating fields and introducing concepts of permeance and electromotive force (EMF), or by means of inductances and matrix representation [DOE 10, TOL 04]. In the second case, the linearity hypothesis between the magnetic field strength $\overrightarrow{H}$ and the magnetic flux density $\overrightarrow{B}$ is essential because it allows for an extremely simplified notation of electrical equations which govern the machine's dynamic operation. This simplified hypothesis is nonetheless especially justified in our study when we focus on a machine controlled at variable speeds, generally with a regulated magnetizing flux.

In addition, the manufacturers of induction machines ideally look to obtain a sinusoidal distribution in the current (and therefore in the magnetic fields $\overrightarrow{B}$ and $\overrightarrow{H}$) on the air-gap surface to limit oscillations in the electromagnetic torque. The second working assumption is not important because we can take into account the space harmonics, but at the price of a level of complexity which is too high in relation to the issues regarding the model. In the following section, we will also model the squirrel-cage induction machine by only considering the first harmonic (meaning, fundamental harmonics), for the main rotating field as well as for the stationary field due to a winding fault.

We will ignore skin effects or capacitance effects, which are not relevant to the frequencies considered here in any way [MAK 97].

The final simplified hypothesis concerns modeling inter-coil short-circuits in the same phase through the "appearance" of a new short-circuited winding B_{cc} which is evenly distributed in all the phase slots while ignoring the reduced number of coils in the fault phase. A methodological justification of this is given in section 2.2.4. This hypothesis is probably the most debatable of all, but it is widely validated by

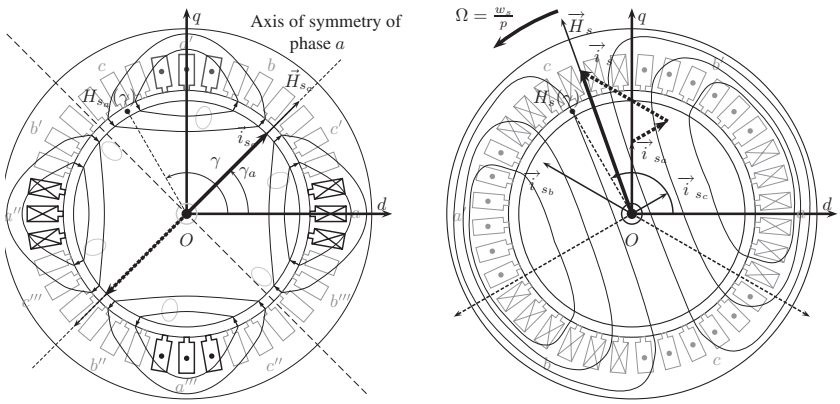

a) Machine with 2 pole pairs

b) Machine with 1 pole pair

Figure 2.1. *Creation of a stationary field (a) and a rotating field (b)*

experimental results. It will allow us, above all, to continue to exploit the concepts of rotating vectors when there is a stator or rotor winding fault, and thus to obtain an extremely simplified notation of electrical equations.

2.2.2. *Equivalence between winding systems*

2.2.2.1. *Stationary field and rotating field*

Using the hypotheses for study, the application of Ampere's theory along the magnetic lines (Figure 2.1a) shows that a current $i_{s_a}(t) = I_m \cos(w_s t)$ flowing in a stator winding a of p pole pairs creates a magnetic field strength in the air-gap at point $M(\gamma)$, whose expression can be approached by:

$$H_{s_a}(\gamma, t) = n_s k_{b_s} \cos(p(\gamma - \gamma_a))\ i_{s_a}(t) \qquad [2.1]$$

where the physical angle γ_a marks the field's point of symmetry, n_s is the number of coils in series per phase, and the coefficient k_{b_s} characterizes the winding.

This is the expression for a stationary wave[2]. This field is usually represented by vector $\overrightarrow{H_s}$, with a norm which is proportional to the magnetic field strength in the air-gap, in the direction of $p\gamma_a$:

$$\overrightarrow{H_{s_a}}(t) = n_s k_{b_s} i_{s_a}(t) \begin{bmatrix} \cos(p\gamma_a) \\ \sin(p\gamma_a) \end{bmatrix} = H_{m_a} \cos(w_s t) \begin{bmatrix} \cos(p\gamma_a) \\ \sin(p\gamma_a) \end{bmatrix} \qquad [2.2]$$

2 The description of the stationary field must not be confused with the statistical concept of stationarity.

with $H_{m_a} = n_s k_{b_s} I_m$. This vector is written in the reference frame $R_{(0,d,q)}$ that we will call a *physical frame of reference* because it also corresponds to a physical section of the machine.

By taking note of the similarity between the expressions for current $i_{s_a}(t)$ and $H_{s_a}(\gamma_a, t)$, it is interesting to represent this current in vector form in the same reference frame. If this seems natural, we must not forget that we are representing different magnitudes symbolically in the same place (meaning, in a section of the machine), because the magnetic field strength is intrinsically a spatial magnitude, whereas i_{s_a} is here a purely temporal magnitude.

If a three-phase balanced stator winding (i.e. composed of three identical coils, distanced spatially from $\frac{2\pi}{3}$) with p pole pairs which have a direct balanced sinusoidal system running through them with a current of $\underline{i}_{s_{abc}}(t)$, defined by:

$$\underline{i}_{s_{abc}}(t) = \begin{bmatrix} i_{s_a}(t) \\ i_{s_b}(t) \\ i_{s_c}(t) \end{bmatrix} = I_m \begin{bmatrix} \cos(w_s t) \\ \cos[w_s t - \frac{2\pi}{3}] \\ \cos(w_s t - \frac{4\pi}{3}) \end{bmatrix} \quad [2.3]$$

then the expression for magnetic field strength in the air-gap becomes:

$$\begin{aligned} H_s(\gamma, t) &= H_{s_a}(\gamma, t) + H_{s_b}(\gamma, t) + H_{s_c}(\gamma, t) \\ &= \frac{3}{2} n_s k_{b_s} I_m \cos(w_s t - p\gamma) \end{aligned} \quad [2.4]$$

This is a progressive sinusoidal wave p, which is periodic over one complete turn, rotating at an angular speed $\Omega_s = (\frac{w_s}{p})$ in relation to the stator *physical frame of reference* (Figure 2.1b). We can combine this with the rotating vector $\overrightarrow{H_s}$:

$$\overrightarrow{H_s}(t) = \frac{3}{2} n_s k_{b_s} I_m \cdot \begin{bmatrix} \cos(\frac{w_s}{p} t) \\ \sin(\frac{w_s}{p} t) \end{bmatrix} = H_m \begin{bmatrix} \cos(\frac{w_s}{p} t) \\ \sin(\frac{w_s}{p} t) \end{bmatrix} \quad [2.5]$$

and so everything, then, happens as though the rotating magnetic field $\overrightarrow{H_s}$ was created by a rotating current $\overrightarrow{i_s}(t)$:

$$\overrightarrow{i_s}(t) = \frac{3}{2} I_m \begin{bmatrix} \cos(\frac{w_s}{p} t) \\ \sin(\frac{w_s}{p} t) \end{bmatrix} \quad [2.6]$$

2.2.2.2. *Physical interpretation of Concordia's reference frame*

The previous result can be formalized using the Concordia orthonormal transform $\mathcal{T}_{33} = [\mathcal{T}_{31}\ \mathcal{T}_{32}]$ where:

$$\mathcal{T}_{31} = \sqrt{\frac{1}{3}}\begin{bmatrix}1\\1\\1\end{bmatrix} \quad \mathcal{T}_{32} = \sqrt{\frac{2}{3}}\begin{bmatrix}\cos(0) & \sin(0)\\ \cos(-\frac{2\pi}{3}) & \sin(-\frac{2\pi}{3})\\ \cos(-\frac{4\pi}{3}) & \sin(-\frac{4\pi}{3})\end{bmatrix} \quad \mathcal{T}_{33}^{-1} = \mathcal{T}_{33}^{\mathrm{T}} \qquad [2.7]$$

Let us consider any direct three-phase system $\underline{x}_{abc} = X_m[\cos(\varphi)\ \cos(\varphi - \frac{2\pi}{3})\ \cos(\varphi - \frac{4\pi}{3})]^{\mathrm{T}}$ corresponding to a current, voltage, or flux system. This system can be interpreted as the projection of a vector on the axes of its *natural* frame of reference $R(O, x, y, z)$ which has no particular physical meaning. The Concordia transform makes it possible to diagonalize the inductance matrix of a three-phase balanced winding. This corresponds to a transfer matrix from the *natural* reference frame toward *Concordia*'s reference frame $R(0, h, d, q)$, where the system is written as:

$$\underline{x}_{hdq} = \mathcal{T}_{33}^{-1} \cdot \underline{x}_{abc} = \begin{bmatrix} x_h \\ \underline{x}_{dq} \end{bmatrix} \qquad [2.8]$$

When the system $\underline{x}_{abc}$ is balanced, the homopolar component x_h is zero, and the vector $\underline{x}_{dq}$ is a vector from the plane $P_{(O,d,q)}$, making an angle φ with the axis $(0, d)$:

$$\begin{cases} x_h = \sqrt{\frac{1}{3}}\,(x_a + x_b + x_c) = 0 \\ \underline{x}_{dq} = \mathcal{T}_{32}^{\mathrm{T}}\,\underline{x}_{abc} = X_m\sqrt{\frac{3}{2}}\begin{bmatrix}\cos(\varphi)\\ \sin(\varphi)\end{bmatrix} \end{cases} \qquad [2.9]$$

In the case of three-phase electrical machines, this transform has a very specific meaning, making the plane $P_{(O,d,q)}$ coincide with a section of the machine. In fact, if the vector $\underline{i}_{s_{abc}} = [i_{s_a}\ i_{s_b}\ i_{s_c}]^{\mathrm{T}}$ of the stator phase currents has no physical meaning in its *natural* reference frame, then the vector $\underline{i}_{s_{dq}}$ can, however, be interpreted as the vector representation of the dummy rotating current $\overrightarrow{i_s}$, previously defined by [2.6], at the origin of the rotating magnetic field[3].

Relations [2.9] and [2.5] prompt us to write the expression of peak amplitude of the magnetic field given by equation [2.5] in the following way:

$$H_m = \frac{3}{2}n_s k_{b_s} I_m = \underbrace{\left(\sqrt{\frac{3}{2}}n_s\right)}_{n_{s_{dq}}} k_{b_s} \underbrace{\left(\sqrt{\frac{3}{2}}I_m\right)}_{|\underline{i}_{s_{dq}}|} \qquad [2.10]$$

3 Note: A homopolar stator component i_h in the reference frame $\mathcal{R}_{(O,h,d,q)}$ has no physical existence in any way in an axial component H of the machine.

meaning that everything will take place as though the magnetic field strength in the air-gap was created by a two-phase winding with $n_{s_{dq}} = \sqrt{\frac{3}{2}} n_s$ coils, with the two-phase balanced direct system with a current of $\underline{i}_{s_{dq}}$ flowing through it:

$$\underline{i}_{s_{dq}} = \sqrt{\frac{3}{2}} I_m \begin{bmatrix} \cos(\frac{w_s}{p} t) \\ \sin(\frac{w_s}{p} t) \end{bmatrix} \qquad [2.11]$$

2.2.2.3. *Voltage equations of real windings*

In fact, a three-phase system is only a special case of the q-phase system. We can show that any q-phase balanced winding system with p pole pairs and a q-phase balanced system with an angular frequency current w running through it, creates a progressive sinusoidal magnetic field in the air-gap, rotating at $\Omega = (\frac{w}{p})$. Induction machine squirrel-cages composed of n_b bars may thus be considered as a system of n_b elementary coils distanced at $(\frac{2\pi}{n_b})$, where the k-th coil corresponds to two consecutive bars linked together by two sections of the end-ring, such as was defined in Figure 2.2.

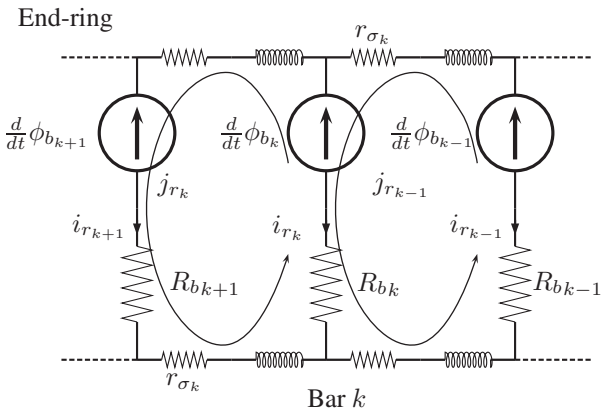

Figure 2.2. *Equivalent electrical diagram of a squirrel cage rotor*

Studying this type of rotor is, however, a special case, because rotor currents are likely to physically flow from one bar to any other bar, on the short-circuit rings.

Moreover, the number of bars is not necessarily a whole multiple of the number of pole pairs in the stator winding. A simple solution would consist of pointing out that the currents induced in the rotor tend to cancel out the effect of stator current which originally generated them (Lenz's law): the rotor currents try to flow within the bars so as to create a rotor field $\overrightarrow{B}_r$ going against the stator field $\overrightarrow{B}_s$. Furthermore, the

periodicity of the rotor field is imposed by the stator field, which is also p-periodical on one rotation. In permanent regime, with the hypothesis of a sinusoidal distribution of the field in the air-gap, the currents flowing in two consecutive rotor coils are dephased from $p(\frac{2\pi}{n_b})$ and make up a n_b-phase balanced direct current system. The generalized Concordia transform $\mathcal{T}_{2n_b}$:

$$\mathcal{T}_{2n_b} = \sqrt{\frac{2}{n_b}} \begin{bmatrix} \cos(0) & \dots & \cos(pk\frac{2\pi}{n_b}) & \dots & \cos(p(n_b-1)\frac{2\pi}{n_b}) \\ \sin(0) & \dots & \sin(pk\frac{2\pi}{n_b}) & \dots & \sin(p(n_b-1)\frac{2\pi}{n_b}) \end{bmatrix} \quad [2.12]$$

thus enables us to express the rotor mesh currents j_{r_k} defined by Figure 2.2 according to the two-phase direct system $\underline{i}_{r_{dq}}$ as follows:

$$\underline{j}_{r_{1:n_b}} = \begin{bmatrix} j_{r_1} & \dots & j_{r_k} & \dots & j_{r_{n_b}} \end{bmatrix}^T = \mathcal{T}_{2n_b}^T \, \underline{i}_{r_{dq}} \quad [2.13]$$

The voltage equations for the balanced induction machine then become:

$$\begin{cases} \underline{u}_{s_{abc}} &= \mathcal{R}_{s_{abc}} \underline{i}_{s_{abc}} + \frac{d}{dt}\underline{\phi}_{s_{abc}} \\ \underline{0} &= \mathcal{R}_{r_{1:n_b}} \underline{j}_{r_{1:n_b}} + \frac{d}{dt}\underline{\phi}_{r_{1:n_b}} \\ \underline{\phi}_{s_{abc}} &= \mathcal{L}_{s_{abc}} \underline{i}_{s_{abc}} + \mathcal{M}_{sr}(\Theta)\underline{j}_{r_{1:n_b}} \\ \underline{\phi}_{r_{1:n_b}} &= \mathcal{L}_{r_{1:n_b}} \underline{j}_{r_{1:n_b}} + \mathcal{M}_{rs}(\Theta)\underline{i}_{s_{abc}} \end{cases} \quad [2.14]$$

with:

$$\mathcal{R}_{s_{abc}} = \begin{bmatrix} R_s & 0 & 0 \\ 0 & R_s & 0 \\ 0 & 0 & R_s \end{bmatrix} \quad \mathcal{L}_{s_{abc}} = \begin{bmatrix} L_s & M_s & M_s \\ M_s & L_s & M_s \\ M_s & M_s & L_s \end{bmatrix} \quad [2.15]$$

$$\mathcal{R}_{r_{1:n_b}} = \begin{bmatrix} 2(R_b+r_\sigma) & -R_b & 0 & \dots & 0 & -R_b \\ -R_b & 2(R_b+r_\sigma) & -R_b & 0 & \dots & 0 \\ 0 & \ddots & \ddots & \ddots & \ddots & \vdots \\ \vdots & \ddots & \ddots & \ddots & \ddots & 0 \\ 0 & \dots & 0 & -R_b & 2(R_b+r_\sigma) & -R_b \\ -R_b & 0 & \dots & 0 & -R_b & 2(R_b+r_\sigma) \end{bmatrix}$$

$$\mathcal{L}_{r_{1:n_b}} = \begin{bmatrix} M_{r_{1,1}} & M_{r_{1,2}} & \dots & M_{r_{1,n_b}} \\ M_{r_{2,1}} & M_{r_{2,2}} & & M_{r_{2,n_b}} \\ \vdots & \ddots & \ddots & \vdots \\ M_{r_{n_{b,1}}} & M_{r_{n_{b,2}}} & \dots & M_{r_{n_{b,n_b}}} \end{bmatrix} \quad [2.16]$$

$$\mathcal{M}_{sr}(\Theta) = \sqrt{\frac{3}{2}}\sqrt{\frac{n_b}{2}} M_{sr} \mathcal{T}_{32} \mathcal{P}(p\Theta) \mathcal{T}_{2n_b} = \mathcal{M}_{sr}^{\mathrm{T}}(p\Theta) \quad [2.17]$$

where Θ is the rotor angular position, L_s is the self-inductance of a stator phase, M_s is the mutual between two stator phases, R_b is the bar electrical resistance, r_σ is the resistance of an end-ring portion linking two consecutive bars, and M_{sr} is the maximum mutual between a stator phase and a rotor coil.

Let us call $\mathcal{R}_p$ the reluctance of the magnetic path followed by the main field lines, and $\mathcal{R}_{fs}$ the reluctance of the circuit taken by the leakage lines. We can therefore express the stator winding inductances according to:

$$L_s = L_{p_s} + L_{f_s} = \frac{n_s^2}{\mathcal{R}_p} + \frac{n_s^2}{\mathcal{R}_{fs}} \quad [2.18]$$

$$M_s = M_{s_{(a,b)}} = M_{s_{(a,c)}} = M_{s_{(c,b)}} = \cos\left(\frac{2\pi}{3}\right)\frac{n_s^2}{\mathcal{R}_p} \quad [2.19]$$

where the coefficient $\cos\left(\frac{2\pi}{3}\right)$ of mutual inductance originates from the scalar product between the magnetic field $\overrightarrow{B}$ and the surface vector $\overrightarrow{dS}$ when calculating the winding flux. We will see further on in this study the reason for expressing inductances through reluctances in order to determine short-circuiting winding parameters.

2.2.2.4. *Electrical parameters of equivalent two-phase windings*

By applying the Concordia transform T_{23} to the three-phase stator magnitudes, and T_{2n_b} to the n_b-phase rotor magnitudes, this will lead us to equations for the two-phase dummy electrical machine on the stator and rotor:

$$\begin{cases} \underline{u}_{s_{dq}} = \mathcal{R}_{s_{dq}}\underline{i}_{s_{dq}} + \frac{d}{dt}\underline{\phi}_{s_{dq}} \\ \underline{0} = \mathcal{R}_{r_{dq}}\underline{i}_{r_{dq}} + \frac{d}{dt}\underline{\phi}_{r_{dq}} \\ \underline{\phi}_{s_{dq}} = \mathcal{L}_{s_{dq}}\underline{i}_{s_{dq}} + \mathcal{M}_{sr_{dq}}(\Theta)\underline{i}_{r_{dq}} \\ \underline{\phi}_{r_{dq}} = \mathcal{L}_{r_{dq}}\underline{i}_{r_{dq}} + \mathcal{M}_{sr_{dq}}(-\Theta)\underline{i}_{s_{dq}} \end{cases} \quad [2.20]$$

with:

$$\mathcal{R}_{s_{dq}} = \mathcal{T}_{23}\mathcal{R}_{s_{abc}}\mathcal{T}_{32} = \begin{bmatrix} R_s & 0 \\ 0 & R_s \end{bmatrix} \quad [2.21]$$

$$\mathcal{R}_{r_{dq}} = \mathcal{T}_{2n_b}\mathcal{R}_{r_{1:n_b}}\mathcal{T}_{n_b 2} = \begin{bmatrix} R_r & 0 \\ 0 & R_r \end{bmatrix} \quad [2.22]$$

$$\mathcal{L}_{s_{dq}} = \mathcal{T}_{23}\mathcal{L}_{s_{abc}}\mathcal{T}_{32} = \begin{bmatrix} L_{c_s} & 0 \\ 0 & L_{c_s} \end{bmatrix} \quad [2.23]$$

$$\mathcal{L}_{r_{dq}} = \mathcal{T}_{2n_b}\mathcal{R}_{r_{1:n_b}}\mathcal{T}_{n_b 2} = \begin{bmatrix} L_{c_r} & 0 \\ 0 & L_{c_r} \end{bmatrix} \quad [2.24]$$

$$\mathcal{M}_{sr_{dq}} = \underbrace{\sqrt{\frac{3}{2}}\sqrt{\frac{n_b}{2}}M_{sr}}_{M_{c_{sr}}}\mathcal{P}(p\Theta) \qquad [2.25]$$

$$L_{c_s} = (L_s - M_s) = \frac{3}{2}L_{p_s} + L_{f_s} \qquad [2.26]$$

The Concordia transform thus enables us to go from a *descriptive* modeling of stator and rotor windings to an equivalent, two-phase *dummy* modeling, as presented in Figure 2.3.

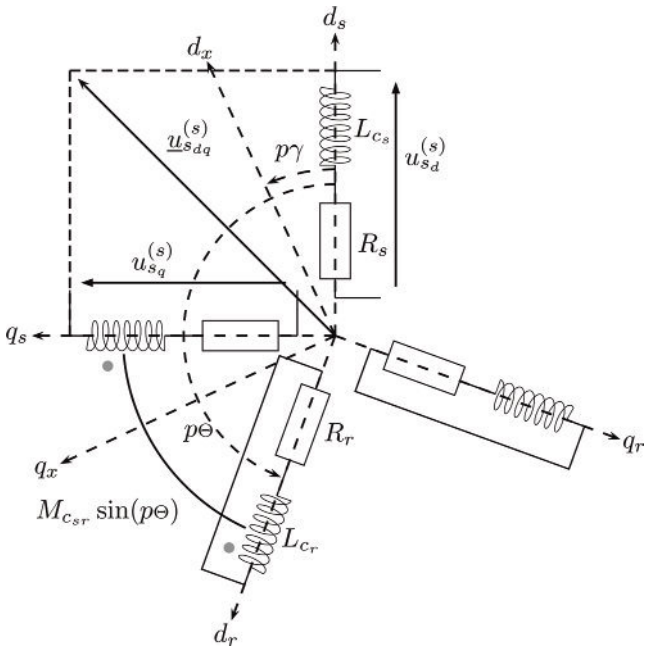

Figure 2.3. *Representation of a pole pair in the equivalent two-phase dummy machine on the stator and rotor*

As the equivalent stator windings are in phase quadrature, their mutual inductance is zero and the cyclic inductance L_{c_s} corresponds to their self-inductance, with:

$$L_{c_s} = \frac{3}{2}L_{p_s} + L_{f_s} = \frac{n^2_{s_{dq}}}{\mathcal{R}_p} + \frac{2}{3}\frac{n^2_{s_{dq}}}{\mathcal{R}_{fs}} \qquad [2.27]$$

However, with a hypothesis of sinusoidal distribution on the air-gap surface, we notice that the magnetic circuit taken by the principal field lines of a real coil, and

the circuit taken by the principal field lines of an equivalent dummy coil are identical (Figure 2.4). We can deduce from this that the inductance $\left(\frac{3}{2}L_{p_s}\right)$ also corresponds to the principal inductance of the dummy two-phase stator winding with $n_{s_{dq}} = \sqrt{\frac{3}{2}}n_s$ coils and a resistance of R_s.

In the same way, L_{c_r} corresponds to the self-inductance of the equivalent two-phase rotor winding, and $M_{csr} = \sqrt{\frac{3}{2}}\sqrt{\frac{n_b}{2}}M_{sr}$ is the maximum mutual inductance between the dummy stator and rotor two-phase windings.

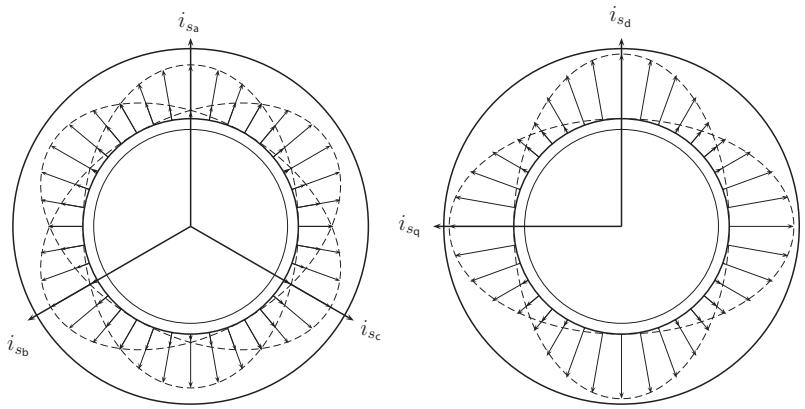

Figure 2.4. *Magnetic circuit of a real three-phase or equivalent two-phase winding*

2.2.3. *Equivalent two-phase machine with no fault*

2.2.3.1. *Equations in a non-specific reference frame*

The symbolic representation in Figure 2.3 involves *electrical* angles (for example, the electrical angle $p\Theta$ referencing the rotor), and *electrical pulsations*; it can therefore be applied to all machines, independent of the number of pole pairs. This is highly useful for understanding their operation, because it can manipulate rotating vectors in a plane which corresponds to a physical section of the machine, with the possibility of projecting them for control requirements (or identification) in any physical frame of reference $R_{(O,d_x,q_x)}$: the stator-fixed reference frame $R_{(O,d_s,q_s)}$, the rotating reference frame linked to the rotor $R_{(O,d_r,q_r)}$, or even the magnetic field reference frame $R_{(O,d_c,q_c)}$.

In the relations system [2.20], all the stator magnitudes have an angular frequency of w_s, i.e. combined with vectors rotating at $(\frac{w_s}{p})$ in relation to the stator reference

frame. All the rotor magnitudes at an angular frequency of w_r are combined with vectors rotating at $(\frac{w_r}{p})$ in relation to the rotor. To eradicate any ambiguity, we will henceforth specify the notation reference frame using an exponent. In any reference frame $R(O, d_x, q_x)$, referenced by the electrical angle $p\Theta$ (Figure 2.3), we obtain:

$$\begin{cases} \underline{v}_s^{(x)} = \mathcal{P}(\gamma)\,\underline{v}^{(s)} & \text{for stator magnitudes} \\ \underline{v}_r^{(x)} = \mathcal{P}(p\gamma - p\Theta)\,\underline{v}^{(r)} & \text{for rotor magnitudes} \end{cases} \quad [2.28]$$

hence the equations for the machine connecting the vectors to same angular frequency. In other words, they all rotate at the same speed in relation to any notation reference frame $R_{(0,d_x,q_x)}$:

$$\underline{u}_{s_{dq}}^{(x)} = R_s \underline{i}_{s_{dq}}^{(x)} + p\dot{\gamma}\mathcal{P}(\frac{\pi}{2})\underline{\phi}_{s_{dq}}^{(x)} + \frac{d}{dt}\underline{\phi}_{s_{dq}}^{(x)} \quad [2.29]$$

$$\underline{0} = R_r \underline{i}_{r_{dq}}^{(x)} + p(\dot{\gamma} - \dot{\Theta})\mathcal{P}(\frac{\pi}{2})\underline{\phi}_{r_{dq}}^{(x)} + \frac{d}{dt}\underline{\phi}_{r_{dq}}^{(x)} \quad [2.30]$$

$$\underline{\phi}_{s_{dq}}^{(x)} = L_{c_r}\underline{i}_{s_{dq}}^{(x)} + M_{c_{sr}}\underline{i}_{r_{dq}}^{(x)} \quad [2.31]$$

$$\underline{\phi}_{r_{dq}}^{(x)} = L_{c_r}\underline{i}_{r_{dq}}^{(x)} + M_{c_{sr}}\underline{i}_{s_{dq}}^{(x)} \quad [2.32]$$

2.2.3.2. *State space representation*

For most industrial applications, the inertia of rotating components is high, and the rotor speed is a slow varying magnitude compared to the other electrical magnitudes of the machine. Electrical equations [2.29] to [2.32] enable us to obtain a representation of the following linear state which depends on four electrical parameters $\{R_s,\ L_{c_s},\ T_r,\ \sigma\}$ and the ratio $\delta = \left(\frac{M_{c_{sr}}}{L_{c_r}}\right)$:

$$\sum(\underline{\theta}) \begin{cases} \underline{\theta} = [R_s \quad L_{c_s} \quad T_r \quad \sigma]^T \\ \underline{x} = \begin{bmatrix} \underline{i}_{s_{dq}}^{(x)} \\ \underline{\phi}_{r_{dq}}^{(x)} \end{bmatrix} \quad \underline{y} = \underline{i}_{s_{dq}}^{(x)} \quad \underline{u} = \underline{u}_{s_{dq}}^{(x)} \\ \dot{\underline{x}} = \mathcal{A}(\underline{\theta})\,\underline{x} + \mathcal{B}(\underline{\theta})\underline{u} \\ \underline{y} = \mathcal{C}\underline{x} \end{cases} \quad [2.33]$$

with:

$$\mathcal{A} = \begin{bmatrix} -\left(\frac{R_s}{\sigma L_{c_s}} + \frac{1-\sigma}{\sigma T_r}\right) & p\dot{\gamma} & \delta\frac{1}{\sigma L_{c_s} T_r} & \delta\frac{p\dot{\Theta}}{\sigma L_{c_s}} \\ -p\dot{\gamma} & -\left(\frac{R_s}{\sigma L_{c_s}} + \frac{1-\sigma}{\sigma T_r}\right) & -\delta\frac{p\dot{\Theta}}{\sigma L_{c_s}} & \delta\frac{1}{\sigma L_{c_s} T_r} \\ \frac{1}{\delta}\frac{L_{c_s}(1-\sigma)}{T_r} & 0 & -\frac{1}{T_r} & p(\dot{\gamma} - \dot{\Theta}) \\ 0 & \frac{1}{\delta}\frac{L_{c_s}(1-\sigma)}{T_r} & p(\dot{\Theta} - \dot{\gamma}) & -\frac{1}{T_r} \end{bmatrix} \quad [2.34]$$

$$\mathcal{B} = \begin{bmatrix} \frac{1}{\sigma L_{c_s}} & 0 \\ 0 & \frac{1}{\sigma L_{c_s}} \\ 0 & 0 \\ 0 & 0 \end{bmatrix} \quad \mathcal{C} = \begin{bmatrix} 1 & 0 & 0 & 0 \\ 0 & 1 & 0 & 0 \end{bmatrix} \qquad [2.35]$$

In fact, the system $\sum(\underline{\theta})$ is independent of δ. It is enough to bring about the change in state variable:

$$\underline{\tilde{x}} = \mathcal{K}\underline{x} \quad \text{with} \quad \mathcal{K} = \begin{bmatrix} 1 & 0 & 0 & 0 \\ 0 & 1 & 0 & 0 \\ 0 & 0 & \delta & 0 \\ 0 & 0 & 0 & \delta \end{bmatrix} \qquad [2.36]$$

in order to see that the system's transmittance has vector $\underline{u}_{s_{dq}}^{(x)}$ as an input, and the current vector $\underline{i}_{s_{dq}}^{(x)}$ for the output is actually independent of the ratio δ. This explains, from a theoretical point of view, the indetermination of the rotor's physical "realization". In fact, let us note $\mathcal{R}_p$ as the reluctance of the principal magnetic circuit, $\mathcal{R}_{fs_{dq}} = \frac{2}{3}\mathcal{R}_{fs}$ and $\mathcal{R}_{fr_{dq}}$ the reluctances combined with the stator and rotor leakage inductances of the equivalent two-phase windings. We can therefore express the different inductances depending on the characteristics (dimensions, permeability) or the machine's magnetic circuit [SCH 99]:

$$\begin{cases} L_{c_s} &= \frac{n_{s_{dq}}^2(\mathcal{R}_p+\mathcal{R}_{fs_{dq}})}{\mathcal{R}_p\,\mathcal{R}_{fs_{dq}}} \\ L_{c_r} &= \frac{n_{r_{dq}}^2(\mathcal{R}_p+\mathcal{R}_{fr_{dq}})}{\mathcal{R}_p\,\mathcal{R}_{fr_{dq}}} \\ M_{c_{sr}} &= \frac{n_{s_{dq}}n_{r_{dq}}}{\mathcal{R}_p} \end{cases} \qquad [2.37]$$

By noting ρ_r as the resistance of a rotor coil, we will finally obtain expressions for σ and T_r which only depend on the ratio $\frac{n_{r_{dq}}}{\rho_r}$ and the characteristics of the magnetic circuit:

$$\begin{cases} \sigma &= 1 - \left(\frac{\mathcal{R}_{fs_{dq}}\mathcal{R}_{fr_{dq}}}{(\mathcal{R}_p+\mathcal{R}_{fs_{dq}})(\mathcal{R}_p+\mathcal{R}_{fr_{dq}})}\right) \\ T_r &= \left(\frac{n_{r_{dq}}}{\rho_r}\right)\frac{(\mathcal{R}_p+\mathcal{R}_{fr})}{\mathcal{R}_p\mathcal{R}_{fr_{dq}}} \end{cases} \qquad [2.38]$$

The parameters R_s and L_{c_s} are clearly independent of the number of rotor coils. As the characteristics of the magnetic circuit and stator windings do not vary, the machine's input/output behavior is therefore independent of the number of rotor coils, provided that the ratio $(\frac{n_{r_{dq}}}{\rho_r})$ remains constant. To improve the rotor's solidity, machine designers have reduced the number of coils to the maximum limit by increasing their section: this is the squirrel-cage rotor. For modeling problems, choosing a value for this ratio $(\frac{M_{c_{sr}}}{L_{c_r}})$ amounts to arbitrarily fixing a number of dummy coils (as well as

their resistance) for both rotor phases in the equivalent two-phase machine. The most natural is to choose the ratio as being equal to the unit, such that:

$$\frac{M_{c_{sr}}}{L_{c_r}} = \frac{n_{s_{dq}}}{n_{r_{dq}}} \cdot \frac{\mathcal{R}_p + \mathcal{R}_{fr_{dq}}}{\mathcal{R}_{fr_{dq}}} = 1 \qquad [2.39]$$

2.2.4. *Consideration of a stator winding fault*

2.2.4.1. *Direct short-circuit or resistive contact*

The topology of the different short-circuits which may occur is varied, with chain reaction consequences which may be more or less destructive. As this was already dealt with in the introduction to this chapter, here we will focus more on the inter-coil contact in the same slot. This is a fault that can be compensated for by closed-loop control, whereas the current flowing in the respective coils may be very high.

In cases of direct contact between conductors, the short-circuit current amplitude is somewhat independent of the number of coils involved in the fault. A simple reasoning will allow us to show this: let us imagine a permanent sinusoidal regime, with a sufficiently low number of short-circuiting coils in a stator phase, so as not to modify the total rotating field $\overrightarrow{B}_t = \overrightarrow{B}_s + \overrightarrow{B}_r$ too much. By calling $\rho_s = \frac{R_s}{n_s}$ the resistance of a stator coil, n_{cc} the number of short-circuited coils, and ϕ_m the peak amplitude of the flux cut by a stator coil when there is a rotating field $\overrightarrow{B}_t$, the expression of the short-circuit current i_{cc} is given by:

$$0 = (\rho_s n_{cc}) i_{cc}(t) + \frac{d}{dt}\phi_{cc}(t) \qquad [2.40]$$

with $\phi_{cc}(t) \simeq (n_{cc}\phi_m)\cos(w_s t)$, and therefore:

$$i_{cc}(t) \simeq \left(\frac{\phi_m}{\rho_s}\right) w_s \sin(w_s t) = \left(\frac{n_s \phi_m w_s}{R_s}\right) \sin(w_s t) \qquad [2.41]$$

Equation [2.41] shows that when there is a control maintaining a constant level of magnetization ϕ_m, the current flowing through a few of the short-circuited stator coils is directly proportional to the stator angular frequency, and remains virtually independent of the number of short-circuiting coils. In addition, if we neglect the resistance voltage drop, then the product $(n_s \Phi_m w_s)$ corresponds to the amplitude of the stator phase voltage. For the experimental induction machine LS90 at 1.5 kW, the numerical application gives a short-circuit current amplitude of around 77 amperes at the nominal angular frequency, meaning,10 times more than the nominal current! Experiments can confirm this result: Figure 2.5 shows an experimental trial performed with a control on 120 in an open loop. The stator angular frequency is limited to 120 rad/s so as not to destroy the machine. We verify the proportionality between $|i_{cc}|$ and w_s.

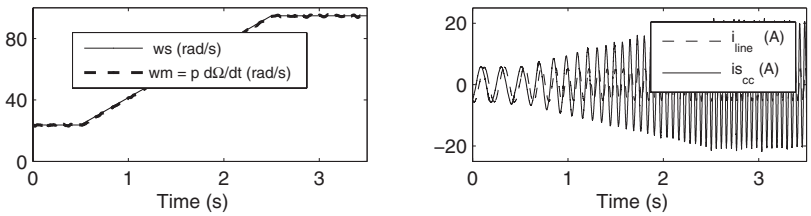

Figure 2.5. *Evolution of current i_{cc} in relation to speed*

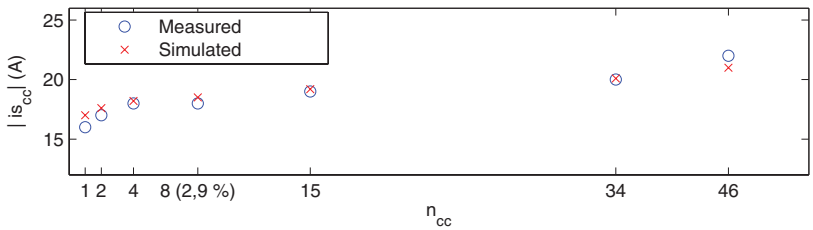

Figure 2.6. *Amplitude evolution in current i_{cc} in relation to the number of short-circuiting coils*

Figure 2.6 shows the evolution of the fault current amplitude i_{cc} in relation to n_{cc} for the angular frequency $w_s = 120$ rad/s. For low values of n_{cc}, we observe a slight difference between the experiment current and the synthetic current obtained using a multi-coil simulation model of a machine with a fault [SCH 99]. This is due to the resistance in the experimental connection performing a stator short-circuit.

However, when there is an inter-coil resistive contact, the expression for the fault current flowing in the n_{cc} coils becomes:

$$i_{cc}(t) \simeq \left(\frac{\phi_m n_s w_s}{R_s + (\frac{R_c}{n_{cc}}) n_s} \right) \sin(w_s t) \qquad [2.42]$$

where R_c is the resistance of the inter-coil contact. The amplitude of the current flowing in the short-circuiting coils now depends on the ratio $(\frac{R_c}{n_{cc}})$. This current is the source of a stationary field $\overrightarrow{H}_{cc}$ whose amplitude is given by equations [2.1] and [2.42]:

$$|\overrightarrow{H}_{cc}| \simeq k_{b_s} \phi_m w_s n_s \; \frac{n_{cc}}{R_s + \frac{R_c}{n_{cc}} n_s} \qquad [2.43]$$

We notice that there are a multitude of combinations (R_c, n_{cc}) which correspond to the same amplitude for the induced stationary field, and therefore also to the same changes in the machine's input/output behavior. To fix such ideas, the numerical

application shows that with the LS90 machine used for experimental trials, a direct short-circuit of 4 coils produces the same stationary magnetic field as 19 "short-circuited" coils through a contact resistance of $1\,\Omega$, or even 55 coils for $R_c = 10\,\Omega$.

2.2.4.2. *Fault symmetrization*

The previous argument assumes an even distribution of the short-circuiting coils in all the phase slots, which is clearly not realistic. In reality, the coils brought into contact with each other are often physically located in two slots, coming back and forth between a single pole pair in any phase. Figure 2.7a shows an example of a short-circuit in two returning slots in the phase b of a machine with 2 pole pairs.

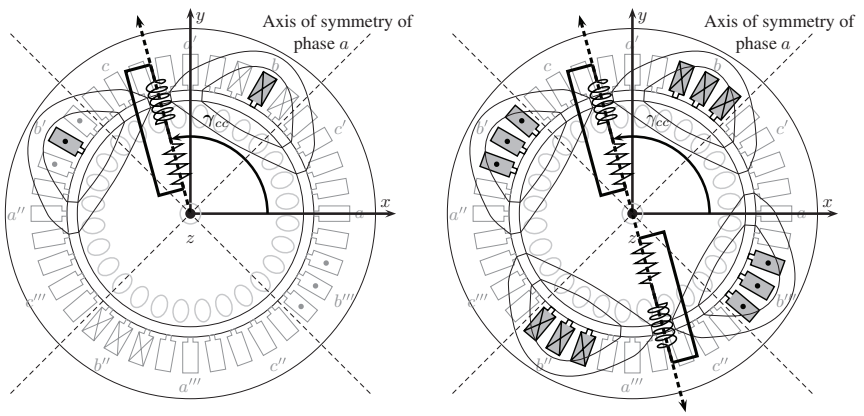

a) Back and forth slots of a short circuit

b) Set of slots of phase a

Figure 2.7. *Symmetrization of real fault (a) through dummy coils distributed in all slots of the faulty phase (b)*

These coils are the cause of a stationary field which is not p-periodic over one turn of the air-gap. Nonetheless, we can show [SCH 99] that n_{cc} short-circuiting coils located in a single pole pair will induce nearly the same electromotive forces in the different stator phases as $(\frac{n_{cc}}{m\,p})$ short-circuiting coils uniformly distributed in the m coils of p pole pairs in the machine, as is shown in Figure 2.7b.

The advantage of this fault symmetrization is to be able to continue exploiting the vector representation of different magnitudes (current, voltage, and flux), as well as the symbolic representation of the machine which is equivalent to a pole pair, such as

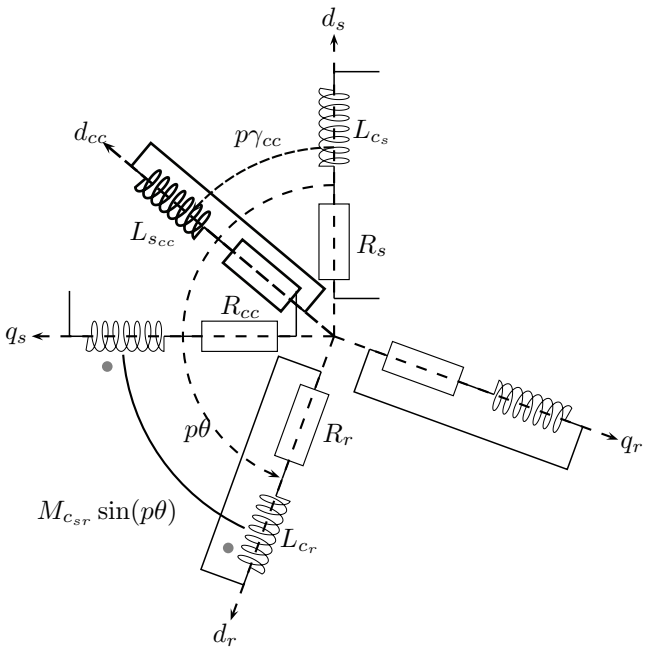

Figure 2.8. *Symbolic representation of the machine with stator short-circuit*

is shown in Figure 2.8. The electrical angle $p\gamma_{cc}$ references the axis of symmetry for the symmetrized coil B_{cc}.

This working hypothesis may seem debatable, but it also enables us to remain within the framework for studying the machine in terms of first harmonics. It is nonetheless justified more when the fault is related to a low number of coils, in agreement with the realistic and industrially relevant objectives for diagnosing a drive with variable speeds.

2.3. Model of the machine with a stator insulation fault

2.3.1. *Electrical equations of the machine with a stator short-circuit*

2.3.1.1. *Electrical parameters of short-circuit winding*

In the following section, we will consider the uniform distribution of short-circuiting coils in the phase slots concerned, and we will ignore the reduced number of coils for the faulty phase. The expressions of inductance for the equivalent faulty dummy machine are those given by the equations in relation [2.37]:

$$L_{c_s} = L_s - M_s = \frac{3}{2}L_{p_s} + L_{f_s} = \frac{n_{s_{dq}}^2}{\mathcal{R}_p} + \frac{2}{3}\frac{n_{s_{dq}}^2}{\mathcal{R}_{fs}} \quad [2.44]$$

$$M_{c_{sr}} = \frac{n_{s_{dq}} n_{r_{dq}}}{\mathcal{R}_p} \quad [2.45]$$

where $n_{s_{dq}}$ and $n_{r_{dq}}$ correspond to the number of coils in the equivalent dummy two-phase windings.

Using the same reasoning which allowed us to obtain equations [2.18], [2.19], and [2.27], we can obtain the expression of the inductances for the new short-circuiting winding:

$$L_{cc} = \eta_{cc}^2 L_s = \eta_{cc}^2 \frac{2}{3}\left(\frac{3}{2}L_{p_s} + \frac{3}{2}L_{f_s}\right) \quad [2.46]$$

$$M_{s_{(d,cc)}} = \frac{(\eta_{cc} n_s) n_{s_{dq}}}{R_p}\cos(p\gamma_{cc}) = \eta_{cc}\sqrt{\frac{2}{3}}L_{c_s}\cos(p\gamma_{cc}) \quad [2.47]$$

$$M_{s_{(q,cc)}} = \eta_{cc}\sqrt{\frac{2}{3}}L_{c_s}\sin(p\gamma_{cc}) \quad [2.48]$$

$$M_{sr_{(d,cc)}} = \eta_{cc}\sqrt{\frac{2}{3}}M_{c_{sr}}\cos(p\gamma_{cc} - p\Theta) \quad [2.49]$$

$$M_{sr_{(q,cc)}} = \eta_{cc}\sqrt{\frac{2}{3}}M_{c_{sr}}\sin(p\gamma_{cc} - p\Theta) \quad [2.50]$$

where $\eta_{cc} = \frac{n_{cc}}{n_s}$.

2.3.1.2. *Vector relations in the stator reference frame*

By observing that $L_{cc} \simeq \eta_{cc}^2 \frac{2}{3} L_{c_s}$, relations [2.46] to [2.50] allow us to write the scalar relations for voltage and flux for the short-circuiting winding:

$$0 = \eta_{cc} R_s i_{cc} + \frac{d}{dt}\phi_{cc} \quad [2.51]$$

$$\phi_{cc} = \eta_{cc}^2 \frac{2}{3} L_{c_s} i_{cc} + \eta_{cc}\sqrt{\frac{2}{3}}L_{c_s}[\cos(p\gamma_{cc}) \quad \sin(p\gamma_{cc})]\underline{i}_{s_{dq}}^{(s)} + \eta_{cc}\sqrt{\frac{2}{3}}M_{c_{sr}}[\cos(p\gamma_{cc}) \quad \sin(p\gamma_{cc})]\mathcal{P}(p\Theta)\underline{i}_{r_{dq}}^{(r)} \quad [2.52]$$

As a current flowing in a winding is the source of a stationary field, it is indeed interesting to combine the scalar quantities i_{cc} and ϕ_{cc} with the stationary vectors $\underline{i}_{cc_{dq}}^{(s)}$ and $\underline{\phi}_{cc_{dq}}^{(s)}$ whose expressions in the stator reference frame $\mathcal{R}_{(O,d_s,q_s)}$ are given by:

$$\underline{i}^{(s)}_{cc_{dq}} = \begin{bmatrix}\cos(p\gamma_{cc})\\ \sin(p\gamma_{cc})\end{bmatrix} i_{cc} \quad \text{and} \quad \underline{\phi}^{(s)}_{cc_{dq}} = \begin{bmatrix}\cos(p\gamma_{cc})\\ \sin(p\gamma_{cc})\end{bmatrix} \phi_{cc} \qquad [2.53]$$

Relations [2.51] and [2.52] then become vector relations between stationary vectors in relation to the stator reference frame:

$$\underline{0} = \eta_{cc} R_s \underline{i}^{(s)}_{cc_{dq}} + \frac{d}{dt}\underline{\phi}^{(s)}_{cc_{dq}} \qquad [2.54]$$

$$\underline{\phi}^{(s)}_{cc_{dq}} = \sqrt{\frac{2}{3}}\eta_{cc}\mathcal{Q}(p\gamma_{cc})\left[L_{c_s}\underline{i}^{(s)}_{s_{dq}} + M_{c_{sr}}\mathcal{P}(p\Theta)\underline{i}^{(r)}_{r_{dq}} + \eta_{cc}L_{c_s}\sqrt{\frac{2}{3}}\underline{i}^{(s)}_{cc_{dq}}\right] \qquad [2.55]$$

where the matrix $\mathcal{Q}$ is defined by:

$$\mathcal{Q}(p\gamma_{cc}) = \begin{bmatrix}\cos(p\gamma_{cc})\\ \sin(p\gamma_{cc})\end{bmatrix}\left[\cos(p\gamma_{cc})\,\sin(p\gamma_{cc})\right] \qquad [2.56]$$

and the electrical vector equations for the two-phase dummy machine with a short-circuit finally become:

$$\underline{u}^{(s)}_{s_{dq}} = R_s \underline{i}^{(s)}_{s_{dq}} + \frac{d}{dt}\underline{\phi}^{(s)}_{s_{dq}} \qquad [2.57]$$

$$\underline{0} = R_r \underline{i}^{(s)}_{r_{dq}} - p\dot{\Theta}\mathcal{P}(\frac{\pi}{2})\underline{\phi}^{(s)}_{r_{dq}} + \frac{d}{dt}\underline{\phi}^{(s)}_{r_{dq}} \qquad [2.58]$$

$$\underline{0} = \eta_{cc} R_s \underline{i}^{(s)}_{cc_{dq}} + \frac{d}{dt}\underline{\phi}^{(s)}_{cc_{dq}} \qquad [2.59]$$

$$\underline{\phi}^{(s)}_{s_{dq}} = L_{c_s}\underline{i}^{(s)}_{s_{dq}} + M_{c_{sr}}\underline{i}^{(s)}_{r_{dq}} + \eta_{cc}\sqrt{\frac{2}{3}}L_{c_s}\underline{i}^{(s)}_{cc_{dq}} \qquad [2.60]$$

$$\underline{\phi}^{(s)}_{r_{dq}} = M_{c_{sr}}\underline{i}^{(s)}_{s_{dq}} + L_{c_r}\underline{i}^{(s)}_{r_{dq}} + \eta_{cc}\sqrt{\frac{2}{3}}M_{c_{sr}}\underline{i}^{(s)}_{cc_{dq}} \qquad [2.61]$$

$$\underline{\phi}^{(s)}_{cc_{dq}} = \sqrt{\frac{2}{3}}\eta_{cc}L_{c_s}\mathcal{Q}(p\gamma_{cc})\left[\underline{i}^{(s)}_{s_{dq}} + \frac{M_{c_{sr}}}{L_{c_s}}\underbrace{\mathcal{P}(p\Theta)\underline{i}^{(r)}_{r_{dq}}}_{\underline{i}^{(s)}_{r_{dq}}} + \eta_{cc}\sqrt{\frac{2}{3}}\underline{i}^{(s)}_{cc_{dq}}\right] \qquad [2.62]$$

2.3.1.3. *Interpretation of the fault matrix* $\mathcal{Q}(p\gamma_{cc})$

Through observing that the matrix $\mathcal{Q}$ can also be written as:

$$\mathcal{Q}(p\gamma_{cc}) = \mathcal{P}(-p\gamma_{cc})\begin{bmatrix}1 & 0\\ 0 & 0\end{bmatrix}\mathcal{P}(p\gamma_{cc}) \qquad [2.63]$$

we note that the stationary vector $\underline{v}_{cc_{dq}}^{(s)} = \mathcal{Q}(p\gamma_{cc})\underline{v}_{dq}^{(s)}$ simply corresponds to the projection of the rotating vector $\underline{v}_{dq}^{(s)}$ on the axis of symmetry $(0, d_{cc})$ of the short-circuiting coil B_{cc}. Equations [2.59] and [2.62] finally correspond to the classic equations for the secondary winding of a transformer. Only the matrix $\mathcal{Q}(p\gamma_{cc})$ reminds us that the coupling between the primary and secondary winding is achieved here through the use of a rotating field.

2.3.2. *State model in any reference frame*

2.3.2.1. *Simplification of electrical equations*

If we choose $n_{r_{dq}}$ such as $(\frac{M_{c_{sr}}}{L_{c_r}}) = 1$ as proposed in relation [2.39], then $\sigma = (1 - \frac{M_{c_{sr}}}{L_{c_s}})$ and equation [2.62] become:

$$\underline{\phi}_{s_{dq}}^{(s)} = \sigma L_{c_s}\left(\underline{i}_{s_{dq}}^{(s)} + \underline{i}_{cc_{dq}}^{(s)}\right) + (1-\sigma)L_{c_s}\left[\underline{i}_{s_{dq}}^{(s)} + \underline{i}_{r_{dq}}^{(s)} + \eta_{cc}\sqrt{\frac{2}{3}}\underline{i}_{cc_{dq}}^{(s)}\right] \quad [2.64]$$

As this is traditionally carried out for studying transformers or induction machines, we will realize variable changes:

$$\underline{\tilde{\phi}}_{cc_{dq}}^{(s)} = \sqrt{\frac{3}{2}}\underline{\phi}_{cc_{dq}}^{(s)} \quad [2.65]$$

$$\underline{\tilde{i}}_{cc_{dq}}^{(s)} = -\eta_{cc}\sqrt{\frac{2}{3}}\underline{i}_{cc_{dq}}^{(s)} \quad [2.66]$$

meaning that we can introduce the flux and magnetizing current $\underline{i}_{m_{dq}}^{(s)}$:

$$\underline{\phi}_{s_{dq}}^{(s)} = \underbrace{\sigma L_{c_s}\left(\underline{i}_{s_{dq}}^{(s)} - \underline{i}_{cc_{dq}}^{(s)}\right)}_{\simeq \text{ leakage flux}} + \underbrace{(1-\sigma)L_{c_s}\underbrace{\left(\underline{i}_{s_{dq}}^{(s)} - \underline{\tilde{i}}_{cc_{dq}}^{(s)} + \underline{i}_{r_{dq}}^{(s)}\right)}_{\underline{i}_{m_{dq}}^{(s)}}}_{\simeq \text{ magnetizing flux}} \quad [2.67]$$

In order to simplify the equations, we realize classic variable changes:

$$L_f = \sigma L_{c_s} \quad [2.68]$$

$$L_m = (1-\sigma)L_{c_s} \quad [2.69]$$

The voltage equations *brought back* to the *primary* are written in the stator reference frame $\mathcal{R}_{(O,d_s,q_s)}$:

$$\underline{u}_{s_{dq}}^{(s)} = R_s \underline{i}_{s_{dq}}^{(s)} + L_f \frac{d}{dt}\underline{i}_{s_{dq}}^{(s)} + \frac{d}{dt}\underline{\phi}_{r_{dq}}^{(s)} \quad [2.70]$$

$$\underset{\sim}{\underline{i}}_{cc_{dq}}^{(s)} = \frac{2}{3}\frac{\eta_{cc}}{R_s}\mathcal{Q}(p\gamma_{cc})\frac{d}{dt}\underline{\phi}_{s_{dq}}^{(s)} \quad [2.71]$$

$$\frac{d}{dt}\underline{\phi}_{r_{dq}}^{(s)} = R_r \underline{i}_{r_{dq}}^{(s)} - p\dot{\Theta}\mathcal{P}(\frac{\pi}{2})\underline{\phi}_{r_{dq}}^{(s)} \quad [2.72]$$

These equations correspond to the electrical diagram in Figure 2.9 which only differs from the electrical diagram of the equivalent two-phase machine (Park model) by the introduction of an extra dipole which dissipates the energy via the Joule effect in the short-circuiting coils with a stationary current flowing through it.

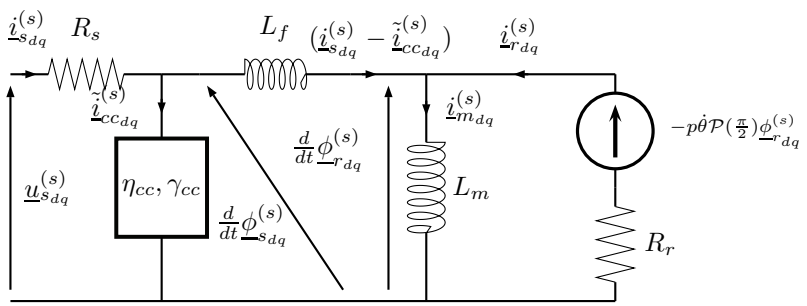

Figure 2.9. *Electrical diagram of the dummy fault machine*

2.3.2.2. *Final state space representation*

The previous vector equations can only be written simply in the stator reference frame $\mathcal{R}_{(O,d_s,q_s)}$ due to the matrix $\mathcal{Q}(p\gamma_{cc})$. But the model notation in the reference frame of the rotating field or rotor greatly improves the estimation of the model parameters. Noting that the drop of resistive voltage $|R_s \underline{i}_{s_{dq}}^{(s)}|$ remains low before $|\underline{u}_{s_{dq}}^{(s)}|$ for a wide operating range, we can obtain the new electrical diagram in Figure 2.10, where the expression of short-circuit current becomes:

$$\underset{\sim}{\underline{i}}_{cc_{dq}}^{(x)} = \frac{2\eta_{cc}}{3R_s}\mathcal{P}(-p\gamma)\mathcal{Q}(p\gamma_{cc})\mathcal{P}(p\gamma)\underline{u}_{s_{dq}}^{(x)} \quad [2.73]$$

where γ is the angle marking any reference notation $\mathcal{R}_{(O,d_x,q_x)}$.

We finally obtain a state space representation parameterized by the six classic parameters $\{R_s,\ L_f,\ L_m,\ R_r\}$ or $\{R_s,\ L_{c_s},\ T_r,\ \sigma\}$, for the ratio $\eta_{cc} = \frac{n_{cc}}{n_s}$ and the angle marking the symmetrical axis of the faulty coil γ_{cc}:

$$\sum(\underline{\theta}) \begin{cases} \underline{\theta} = [R_s \quad L_m \quad L_f \quad T_r \quad \eta_{cc} \quad \gamma_{cc}]^T \\ \underline{x} = \begin{bmatrix} \underline{i}_{s_{dq}}^{(x)} \\ \underline{\phi}_{r_{dq}}^{(x)} \end{bmatrix} \quad \underline{y} = \underline{i}_{s_{dq}}^{(x)} \quad \underline{u} = \underline{u}_{s_{dq}}^{(x)} \\ \dot{\underline{x}} = \mathcal{A}\underline{x} + \mathcal{B}\underline{u} \\ \underline{y} = \mathcal{C}\underline{x} + \frac{2\eta_{cc}}{3R_s}\mathcal{P}(-p\gamma)\mathcal{Q}(p\gamma_{cc})\mathcal{P}(p\gamma)\underline{u}_{s_{dq}}^{(x)} \end{cases} \quad [2.74]$$

We notice that the fault is similar to a simple error on the current measurement in Park's classic model. From a physical point of view, this current corresponds to the short-circuit current *brought back* to the primary. Its amplitude is different from the amplitude of current i_{cc} in equations [2.41] and [2.42] by the transform ratio $\sqrt{\frac{3}{2}}\frac{n_{cc}}{n_s} = \frac{n_{cc}}{n_{s_{dq}}}$ of an equivalent dummy transformer with $n_{s_{dq}}$ coils in the primary and n_{cc} coils in the secondary.

The point of this representation is to be able to express ourselves in an extremely simple manner in any reference frame, particularly in the rotor reference frame.

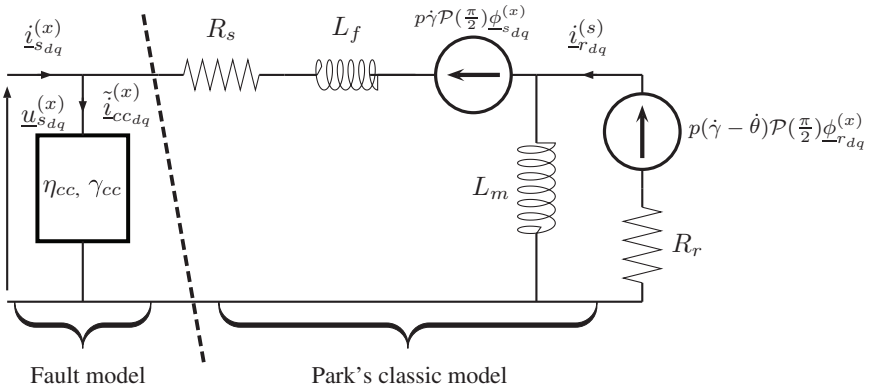

Figure 2.10. *Electrical diagram of the dummy faulty machine*

2.3.2.3. *Considering iron losses*

The consideration of iron losses in the equivalent electrical diagram for a transformer or an induction machine is traditionally achieved by introducing a dipole in a parallel circuit with the magnetizing inductance, whose expression of dissipated power can be approached by $k_{hyst.}|w_s| + k_{Fouc.}w_s^2$ [ROB 99]. We can therefore easily understand that during the parameter estimation phase, the optimization algorithm tends to attribute the fault dipole $Q(\eta_{cc}, \gamma_{cc})$ (Figure 2.10) to the iron losses. Integrating the iron losses in the diagnostic model thus greatly improves the quality of the diagnosis, particularly for a very low number of short-circuiting coils [SCH 99].

2.3.2.4. *Regarding the location of short-circuiting coils in the stator slots*

The angular position γ_{cc} of the back and forth slots in the fault can only be a finite known number with the values $k(\frac{2\pi}{n_e})$, where n_e is the number of stator slots. To reduce the number of parameters further, we can perform a spatial sweep by only estimating the five parameters $R_s(\gamma_{cc}), L_f(\gamma_{cc}), L_m(\gamma_{cc}), R_r(\gamma_{cc}), \eta_{cc}(\gamma_{cc})$. Table 2.1 and Figure 2.11 show this process by representing the estimation evolutions for different values of $p\gamma_{cc} \in [0, 2\pi]$. The results are obtained using experiment recordings with an [SCH 99] machine powered at $1,5$ kW and controlled by a generic vector control and an excitation protocol, ensuring good convergence of optimization algorithms [SCH 99]. In Figure 2.11, each curve corresponds to a fault with n_{cc} coils carried out in the phase (c) for $n_{cc} \in [8(\eta_{cc} = 2,9\%), 16(\eta_{cc} = 5,6\%), 22(\eta_{cc} = 8\%), 46(\eta_{cc} = 16,7\%)]$ and in the phase a for $n_{cc} = 4(\eta_{cc} = 1,45\%)$.

On the one hand, we can verify that the estimated values of the four Park model parameters are actually independent of $p\gamma$ (Table 2.1), and on the other hand, that the estimation of $\eta_{cc}(p\gamma_{cc})$ shows a maximum value in the angular direction corresponding to the axis of symmetry of the short-circuiting coils.

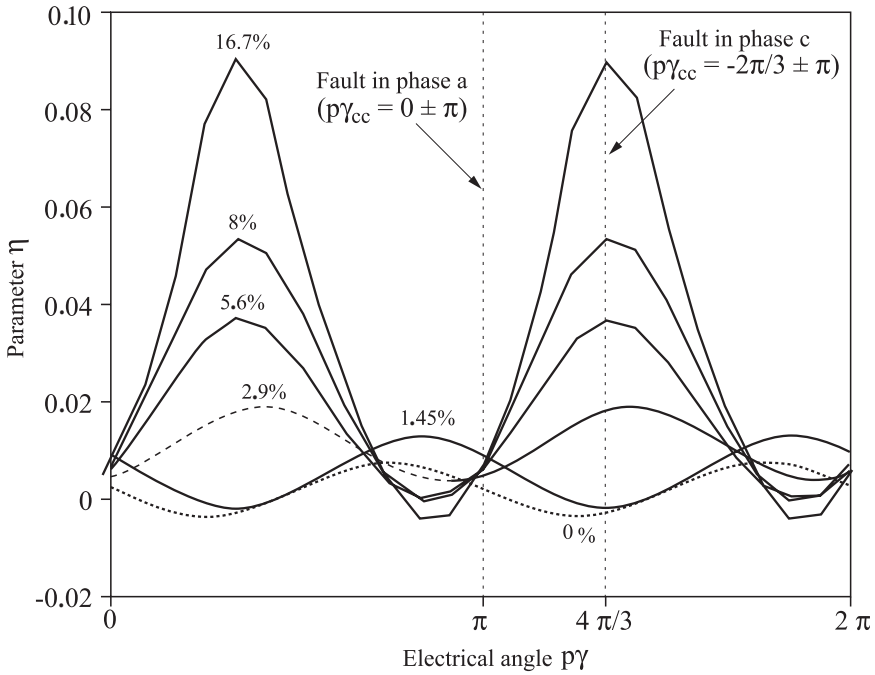

Figure 2.11. *Evolution in the estimation of η_{cc} according to the angle for research $p\gamma$ on the stationary field*

$p\gamma_{cc}$	R_s	L_{e_s}	T_r	σ	η_{cc}
0	4.20 ± 0.29	0.329 ± 0.013	0.178 ± 0.022	0.205 ± 0.037	0.010 ± 0.020
$\frac{\pi}{12}$	4.20 ± 0.28	0.330 ± 0.011	0.169 ± 0.022	0.199 ± 0.041	0.034 ± 0.023
$2\frac{\pi}{12}$	4.28 ± 0.30	0.329 ± 0.008	0.149 ± 0.019	0.166 ± 0.044	0.070 ± 0.022
$3\frac{\pi}{12}$	4.33 ± 0.25	0.328 ± 0.006	0.125 ± 0.009	0.108 ± 0.014	0.118 ± 0.008
$4\frac{\pi}{12}$	4.23 ± 0.13	0.330 ± 0.007	0.122 ± 0.006	0.097 ± 0.006	0.138 ± 0.004
$5\frac{\pi}{12}$	4.22 ± 0.17	0.330 ± 0.007	0.126 ± 0.007	0.111 ± 0.007	0.126 ± 0.012
$6\frac{\pi}{12}$	4.18 ± 0.22	0.331 ± 0.009	0.143 ± 0.015	0.154 ± 0.021	0.088 ± 0.023
$7\frac{\pi}{12}$	4.14 ± 0.22	0.332 ± 0.010	0.162 ± 0.019	0.190 ± 0.025	0.052 ± 0.024
$8\frac{\pi}{12}$	4.15 ± 0.24	0.331 ± 0.011	0.173 ± 0.020	0.206 ± 0.034	0.025 ± 0.020
$9\frac{\pi}{12}$	4.20 ± 0.26	0.330 ± 0.013	0.179 ± 0.022	0.207 ± 0.041	0.005 ± 0.014
$10\frac{\pi}{12}$	4.24 ± 0.28	0.327 ± 0.014	0.181 ± 0.024	0.203 ± 0.042	-0.007 ± 0.010
$11\frac{\pi}{12}$	4.23 ± 0.30	0.327 ± 0.014	0.180 ± 0.023	0.203 ± 0.037	-0.005 ± 0.015

Table 2.1. *Evolution of the means and standard deviations (10 tries) according to $p\gamma$ for a fault of $n_{cc} = 46$ coils*

But above all, this figure highlights that if the winding in each pole pair is distributed in a very low number of slots, or more generally, if the winding is concentric, then it is not useful to sweep $p\gamma_{cc}$ because we can be satisfied with the three values of $\left\{0, \frac{2\pi}{3}, \frac{4\pi}{3}\right\}$ which correspond to the angular directions of the axes of symmetry for the three stator windings.

We also note that the curve obtained for a healthy machine is not flat. This phenomenon, observed for several machines, can probably be explained by a fault caused by axial symmetry (the rotor axis of symmetry is shifted in relation to the stator axis of symmetry in the angular direction corresponding to the curve's maximum value). It shows the advantage in each case of performing an initial sweep in order to be able to carry out a diagnosis based on the analysis of the corrected ratio $\eta_{cc}(\gamma_{cc}) - \eta^o_{cc}(\gamma_{cc})$, where $\eta^o_{cc}(\gamma_{cc})$ corresponds to the estimated valued of $\eta_{cc}(\gamma_{cc})$ for the healthy machine. In fact, the curves clearly show that for a very low number of short-circuiting coils, not considering $\eta^o_{cc}(\gamma_{cc})$ can be extremely detrimental!

2.3.3. *Extension of the three-phase stator model*

We have just seen that a spatial sweep will allow us to dispense with estimating $p\gamma_{cc}$ and therefore to *a priori* simplify the cost of calculating the optimization phase. But this is, however, at the cost of repeating the sequence of operations for the 3 (or

more) possible values of $p\gamma_{cc}$. For some industrial applications[4], it may be interesting to use a diagnostic model which could simultaneously consider one fault in the three stator phases [BAC 06].

To do so, it is simply enough to define three short-circuit windings B_{cc_1}, B_{cc_2} and B_{cc_3} respectively, with a ratio of η_{cc_1}, η_{cc_2} and η_{cc_3}, in the angular directions 0, $\frac{2\pi}{3}$ and $\frac{4\pi}{3}$. This is a matter of putting three 4-port networks, or quadripoles, in parallel Q_{cc_k}, which explains the potential stationary field in each of the three angular directions (Figure 2.12). Each quadripole has a current $\underline{\tilde{i}}^{(r)}_{dq_{cc_k}}$ passing through it, given by:

$$\underline{\tilde{i}}^{(r)}_{cc_{dq_k}} = \frac{2}{3}\,\frac{\eta_{cc_k}}{R_s}\,P(-p\Theta)\,Q(p\gamma_{cc_k})\,P(p\Theta)\,\underline{u}^{(r)}_{s_{dq}} \qquad [2.75]$$

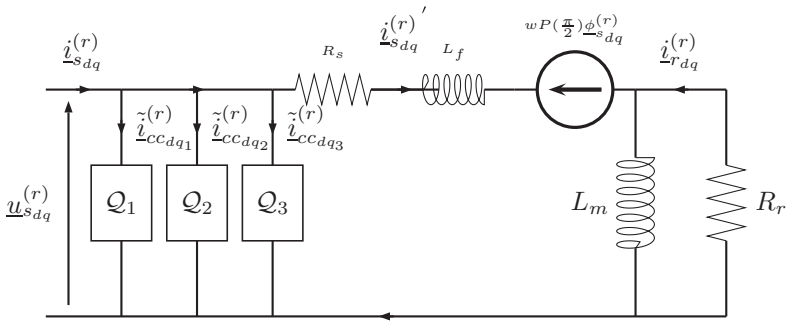

Figure 2.12. *Electrical model of the machine with faults in the three stator phases (in the rotor reference frame)*

2.3.4. *Model validation*

There are many methods of validating a diagnostic model. The first criterion to be verified is its ability to correctly simulate (i.e. explain) the fault which is to be monitored. For example, we can compare experimental currents with the currents simulated by the model for the same input (section 2.5.2), or at least in the same operating conditions. Thus, we propose to compare the spectrum of experimental and synthetic line currents for a machine powered by the network. The second criterion concerns the model's capacity to show a fault through the evolution of the parameters in its differential mode.

4 In particular, those requiring the earliest possible fault detection.

2.3.4.1. *Spectral analysis*

The simulation of a drive requires that we take into account the electrical-mechanical equation of the machine:

$$J\frac{d\Omega}{dt} = C_{em} - f_v\,\Omega - C_r \qquad [2.76]$$

where $\Omega = \dot{\Theta} = \frac{\omega}{p}$ is the speed of the driving shaft, J is the moment of inertia, C_{em} is the electromagnetic torque, C_r is the set of resistive torques, and f_v is the coefficient of viscous friction. The electromagnetic torque can be written in the two-phase reference frame connected to the rotor [GRE 97]:

$$C_{em} = p\,(i_{s_q}\,\phi_{r_d} - i_{s_d}\,\phi_{r_q}) \qquad [2.77]$$

By putting [2.77] into [2.76], we obtain the electromagnetic differential equation for the angular frequency ω:

$$\frac{d\omega}{dt} = \frac{p^2}{J}\,(i_{s_q}\,\phi_{r_d} - i_{s_d}\,\phi_{r_q}) - \frac{f_v}{J}\,\omega - \frac{p}{J}\,C_r \qquad [2.78]$$

Then, by adding the dynamics of the rotor fluxes $\underline{\phi}_{r_{dq}}$ and the stator currents $\underline{i}_{s_{dq}}$ to the electromagnetic dynamics (ω, Θ), the drive may also be described by the nonlinear state system:

$$\sum(\underline{\theta})\begin{cases}\dot{\underline{x}} = f(\underline{x}) + \mathcal{G}\cdot\underline{u}\\ \underline{y} = h(\underline{x}) + \mathcal{H}(\underline{x})\cdot\underline{u}\end{cases} \qquad [2.79]$$

with:

$$\underline{x} = [\,i'_{s_d}\;i'_{s_q}\;\phi_{r_d}\;\phi_{r_q}\;\omega\;\Theta\,]^{\mathrm{T}},\quad \underline{u} = [\,u_{s_d}\;u_{s_q}\;C_r\,]^{\mathrm{T}}\ \text{ et }\ \underline{y} = [\,i_{s_d}\;i_{s_q}\;\omega\,]^{\mathrm{T}}$$

$$f(\underline{x}) = \begin{bmatrix} -\frac{R_s+R_r}{L_f}\,i'_{s_d} + \omega\,i'_{s_q} + \frac{R_r}{L_m\,L_f}\,\phi_{r_d} + \frac{\omega}{L_f}\,\phi_{r_q}\\ -\omega\,i'_{s_d} - \frac{R_s+R_r}{L_f}\,i'_{s_q} - \frac{\omega}{L_f}\,\phi_{r_d} + \frac{R_r}{L_m\,L_f}\,\phi_{r_q}\\ R_r\,i'_{s_d} - \frac{R_r}{L_m}\,\phi_{d_r}\\ R_r\,i'_{s_q} - \frac{R_r}{L_m}\,\phi_{q_r}\\ \frac{p^2}{J}\,(i'_{s_q}\,\phi_{r_d} - i'_{s_d}\,\phi_{r_q}) - \frac{f_v}{J}\,\omega\\ \omega \end{bmatrix},\quad \mathcal{G} = \begin{bmatrix} \frac{1}{L_f} & 0 & 0\\ 0 & \frac{1}{L_f} & 0\\ 0 & 0 & 0\\ 0 & 0 & 0\\ 0 & 0 & -\frac{p}{J}\\ 0 & 0 & 0 \end{bmatrix}$$

$$h(\underline{x}) = \begin{bmatrix} i'_{s_d}\\ i'_{s_q}\\ \omega \end{bmatrix},\quad \mathcal{H}(\underline{x}) = \begin{bmatrix} \frac{2}{3\,R_s}\sum_{k=1}^{3}\eta_{cc_k}P(-p\Theta)\,Q(p\gamma_{cc_k})\,P(p\Theta) & \underline{0}\\ \underline{0} & \underline{0} \end{bmatrix}$$

In simulations, the previous state system for a three-phase sinusoidal input current $\underline{u}_s$ must be solved. The solution is obtained by using the Runge-Kutta fourth order

method with a sampling period of $0.5\,ms$. In experimentation, we can draw the power spectral density of the line currents for an induction machine of 1.1 kW, 4 poles (464 coils per phase), powered by the network, and with a short-circuit of 58 coils in phases a and b.

Figure 2.13 compares the power spectral densities obtained for the same fault in the same power supply conditions. The spectral analysis of the currents in Figure 2.13 reveals new components with frequencies of $k\,f_s$, which conform to our expectations [FIL 94, SCH 99].

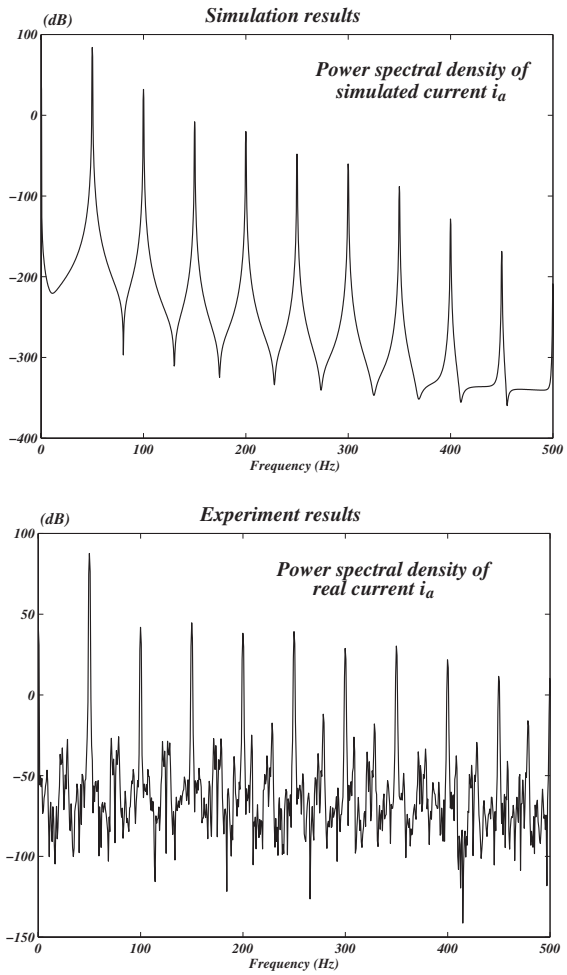

Figure 2.13. *Power spectral density of line currents during a short-circuit on phases a and b*

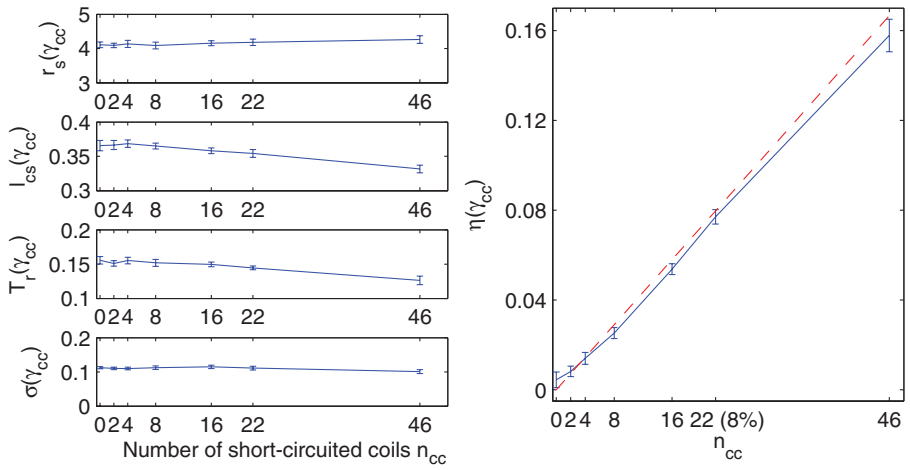

Figure 2.14. *Evolution of the model's parameters according to the number of short-circuiting coils (mean and standard deviation)*

2.3.4.2. *Evolution of fault parameter* η_{cc}

We can also verify the model's ability of finding the true value of the number of short-circuiting coils. Figure 2.14 shows the evolution (mean and standard deviation) of the parameter estimations of the diagnostic model (R_s, L_{c_s}, T_r, σ and η) in relation to the number of short-circuiting coils for $\gamma = \gamma_{cc}$. On the one hand, we can verify the relative independence of the 4 classic parameters of Park's model, and the high level of correspondence between the estimated value of η and its theoretical value $\frac{n_{cc}}{n_s}$, even for a high number of short-circuiting coils[5].

2.4. Generalization of the approach to the coupled modeling of stator and rotor faults

In the previous section, we modeled a short-circuit stator fault through a new short-circuited winding with n_{cc} inter turns at the origin of a stationary magnetic field in according to the stator, with an angular frequency w_s. The main simplified hypothesis consisted of ignoring the reduced number of corresponding inter turns in the faulty phase, as well as the effect of the homopolar component stator in the line current calculations. The idea is to extend this approach to a rotor fault study. This may be a bar break, or more generally, a rotor imbalance related to the progressively increased size of a crack during frequent temperature changes.

5 These results were obtained with a variation of model [2.74] which integrates the iron losses [SCH 99], for a series of 10 recordings.

The increased strength of a bar k limits the flow of the induced current i_{r_k} defined by Figure 2.2, and it locally deforms the magnetic rotor field $\overrightarrow{B}_r$. However, we can consider the unbalanced system $\underline{j}_{1:n_b}$ of n_b the rotor winding currents as the superposition of a balanced system with currents $\underline{j'}_{1:n_b}$ and a system of currents $\underline{j}_0$ flowing in the opposite direction in the faulty meshes. This means that everything takes place as though the rotor field was the result of the superposition of field $\overrightarrow{H}_r$ produced by a healthy rotor, and of the field $\overrightarrow{H}_0$, which is stationary in relation to the rotor, produced by a dummy short-circuiting winding B_0 whose axis of symmetry coincides with the axis of symmetry of field $\overrightarrow{H}_0$ (Figure 2.15).

Of course, this is pure abstraction which nevertheless stems from a rather classic approach based on electromagnetism. In addition, with the angular frequency of the rotor currents being $w_r = (w_s - p\dot{\Theta})$, then the stationary field $\overrightarrow{H}_0$ oscillates at a frequency of w_r according to the rotor. Moreover, if we want the dynamic of the fault currents $\underline{j}_0$ to be identical to the dynamic of the currents $\underline{j'}_{1:n_b}$, then a simple solution would consist of considering (by analogy with the previous approach) that the inter turns in the dummy winding B_0 have the same electrical characteristics (resistance and inductance) as those characteristics in the two equivalent dummy rotor phases.

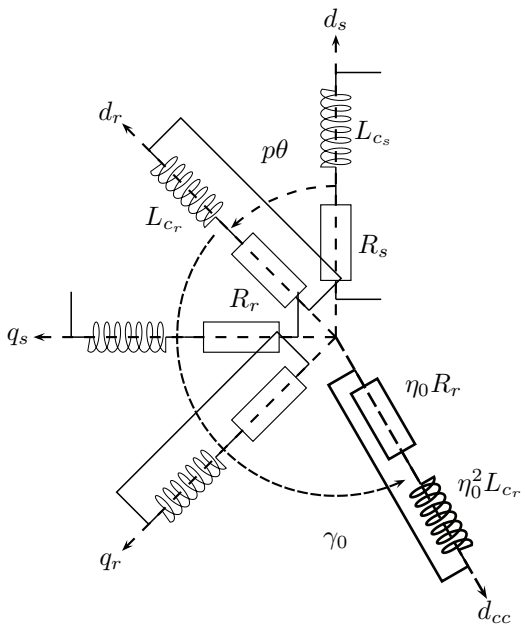

Figure 2.15. *Symbolic diagram of the machine with rotor imbalance*

2.4.1. *Electrical equations in the presence of rotor imbalance*

Let us now consider our rotor as the superposition of a balanced two-phase system and an additional short-circuiting winding with $n_0 = \eta_0 n_{r_{dq}}$ inter turns, where η_0 characterizes the importance of the fault, and where $n_{r_{dq}}$ is the number of inter turns in the equivalent dummy rotor phases. The equations of voltage and flux can be written in the rotor reference frame:

$$0 = \eta_0 R_r i_0 + \frac{d\phi_0}{dt} \quad [2.80]$$

$$\phi_0 = {\eta_0}^2 L_{c_r} i_0 + \eta_0 M_{c_{sr}} [\cos(\gamma_0) \ \sin(\gamma_0)] \underline{i}_{s_{dq}}^{(r)} + L_{c_r} [\cos(\gamma_0) \ \sin(\gamma_0)] \underline{i}_{r_{dq}}^{(r)} \quad [2.81]$$

where the angle γ_0 denotes the axis of symmetry of the stationary field $\overrightarrow{H}_0$ in relation to axis (O, d_r) (Figure 2.15).

In addition, we recall here that it is indeed possible to choose the dummy number of inter turns $n_{r_{dq}}$ from the equivalent rotor winding such as $M_{c_{sr}} = L_{c_r} = (1-\sigma)L_{c_s} = L_m$. By combining the scalar quantities i_0 and ϕ_0 to the stationary vectors:

$$\underline{i}_{0_{dq}}^{(r)} = \begin{bmatrix} \cos(\gamma_0) \\ \sin(\gamma_0) \end{bmatrix} i_0 \qquad \underline{\phi}_{0_{dq}}^{(r)} = \begin{bmatrix} \cos(\gamma_0) \\ \sin(\gamma_0) \end{bmatrix} \phi_0$$

and combining relations [2.80] and [2.81] to the classic rotor equations in the induction machine, we can finally obtain the system of equations for the machine in the presence of rotor imbalance:

$$\underline{u}_{s_{dq}}^{(r)} = R_s \underline{i}_{s_{dq}}^{(r)} + \frac{d}{dt}\underline{\phi}_{s_{dq}}^{(r)} + \omega P(\frac{\pi}{2}) \underline{\phi}_{s_{dq}}^{(r)} \quad [2.82]$$

$$\underline{\phi}_{s_{dq}}^{(s)} = L_f \underline{i}_{s_{dq}}^{(r)} + L_m (\underline{i}_{s_{dq}}^{(r)} + \underline{i}_{r_{dq}}^{(r)} + \eta_0 \underline{i}_{0_{dq}}^{(r)}) \quad [2.83]$$

$$\underline{0} = R_r \underline{i}_{r_{dq}}^{(r)} + \frac{d}{dt}\underline{\phi}_{r_{dq}}^{(r)} \quad [2.84]$$

$$\underline{\phi}_{r_{dq}}^{(r)} = L_m (\underline{i}_{s_{dq}}^{(r)} + \underline{i}_{r_{dq}}^{(r)} + \eta_0 \underline{i}_{0_{dq}}^{(r)}) \quad [2.85]$$

$$0 = \eta_0 R_r \underline{i}_{0_{dq}}^{(r)} + \frac{d}{dt}\underline{\phi}_{0_{dq}}^{(r)} \quad [2.86]$$

$$\underline{\phi}_{0_{dq}}^{(r)} = \eta_0 L_m \mathcal{Q}(\gamma_0) (\underline{i}_{s_{dq}}^{(r)} + \underline{i}_{r_{dq}}^{(r)} + \eta_0 \underline{i}_{0_{dq}}^{(r)}) \quad [2.87]$$

with:

$$Q(\gamma_0) = \begin{bmatrix} \cos(\gamma_0)^2 & \cos(\gamma_0)\sin(\gamma_0) \\ \cos(\gamma_0)\sin(\gamma_0) & \sin(\gamma_0)^2 \end{bmatrix} \quad [2.88]$$

2.4.1.1. *Equivalent electrical diagram*

In the rest of the chapter, all the vectors will be written in the rotor reference frame. The change in the variable $\underline{\tilde{i}}_{0_{dq}}^{(r)} = -\eta_0 \underline{i}_{0_{dq}}^{(r)}$ allows us to rewrite [2.83] and [2.86] in the following way:

$$\underline{\phi}_{r_{dq}}^{(r)} = L_m \left(\underline{i}_{s_{dq}}^{(r)} + \underline{i}_{r_{dq}}^{(r)} - \underline{\tilde{i}}_{0_{dq}}^{(r)}\right) \quad [2.89]$$

$$\underline{\tilde{i}}_{0_{dq}}^{(r)} = \frac{\eta_0}{R_r} \mathcal{Q}(\gamma_0) \frac{d}{dt} \underline{\phi}_{r_{dq}}^{(r)} = \mathcal{Z}_0^{-1} \frac{d}{dt} \underline{\phi}_{r_{dq}}^{(r)} \quad [2.90]$$

These correspond to the electrical diagram in Figure 2.16. We notice that the coil B_0 which represents the fault is brought back to a simple resistive dipole $\mathcal{Z}_0$ which is put in a parallel circuit with the magnetizing inductance and the rotor resistance.

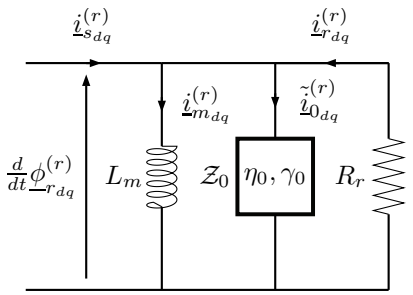

Figure 2.16. *Modeling rotor imbalance*

To simplify the formulation of state system equations further, it would be well-advised to total the impedances of the rotor $\mathcal{R}_r$ and the fault $\mathcal{Z}_0$ in the equivalent impedance matrix $\mathcal{Z}_{eq}$ by putting them in a parallel circuit [BAC 06]:

$$\mathcal{Z}_{eq}^{-1} = \mathcal{R}_r^{-1} + \mathcal{Z}_0^{-1} = \frac{1}{R_r}(\mathcal{I}_{d_2} + \eta_0 \mathcal{Z}_0^{-1}) \quad [2.91]$$

where the matrix $\mathcal{I}_{d_2}$ is the identity matrix of dimension 2.

By remembering that $\mathcal{Q}(\gamma_0) = \mathcal{P}(-\gamma_0) \begin{bmatrix} 1 & 0 \\ 0 & 0 \end{bmatrix} \mathcal{P}(\gamma_0)$, we can easily obtain the expression for the impedance matrix $\mathcal{Z}_{eq}$:

$$\mathcal{Z}_{eq} = R_r \mathcal{I}_{d_2} + \underbrace{\frac{\eta_0}{1+\eta_0} R_r \, \mathcal{Q}(\gamma_0)}_{\mathcal{Z}_{def}} \quad [2.92]$$

Figure 2.17 shows the dynamic equivalent diagram, illustrated in the rotor's reference frame, of the induction machine with a rotor fault. When the machine is healthy (therefore $\eta_0 = 0$), we find again Park's classic model. For a non-zero value of η_0, the fault matrix $\mathcal{Z}_{def}$ introduces an imbalance as well as coupling terms on the rotor's two axes d and q.

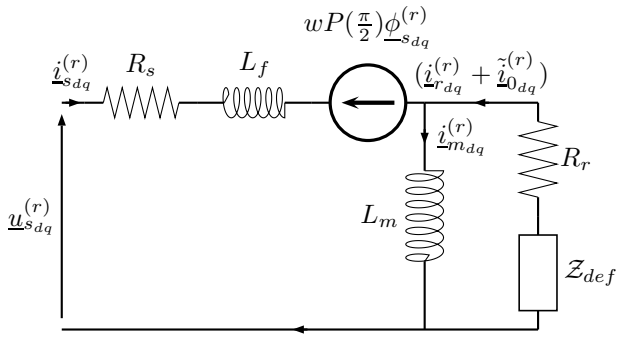

Figure 2.17. *Model of machine with rotor fault*

2.4.1.2. *Validation in stationary regime*

The numerical integration of the model is performed in the same conditions as those described in section 2.3.4.1. The rotor used is a squirrel-cage rotor with two broken bars [BAC 06]. Figures 2.18 and 2.19 show that in experiments, as well as in simulations, we find harmonic components with $(1 \pm 2\,k\,g)\,f_s$ signatures of a rotor fault [INN 94].

2.4.2. *Generalized model of the machine with stator and rotor faults*

We previously saw how a winding fault results in the appearance of a stationary field (in relation to the winding involved), with the main consequences being abnormal over-heating in the concerned zone through the Joule effect, and the appearance of new spectral components in the machine's signals (currents, voltages, torque, etc.). Whether it is a design problem on the rotor (impurity or static eccentricity), or a failing weld joint between a bar and its short-circuit end-ring, or even advanced degradation in the stator insulation, any imbalance leads to accelerated aging in the machine's components through a chain effect. It might be interesting to perform a simultaneous diagnosis of imbalances on the stator and rotor.

As these have different signatures, we can combine the two models obtained previously. In the following, we will propose to study the global model of stator/rotor faults (Figure 2.20) which involves modeling the healthy machine (Park's model), and

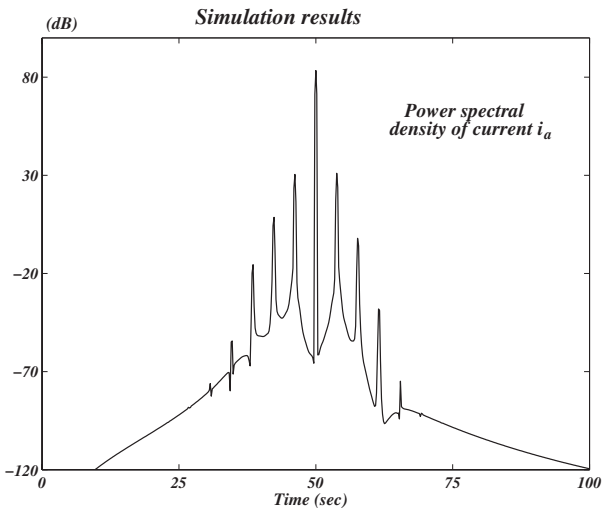

Figure 2.18. *Spectral analysis of line currents for bar breakage: simulation*

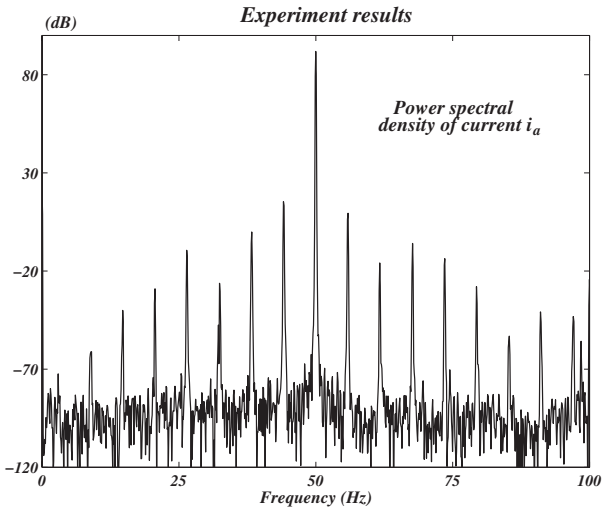

Figure 2.19. *Spectral analysis of line currents for bar breakage: experiment*

modeling the contact between stator inter turns in the same phase and an imbalance in the rotor resistances through the fault matrices $\mathcal{Q}_k$ and $\mathcal{Z}_{def}$.

To simplify the notation, we will no longer indicate the reference frame (specified by the exponent).

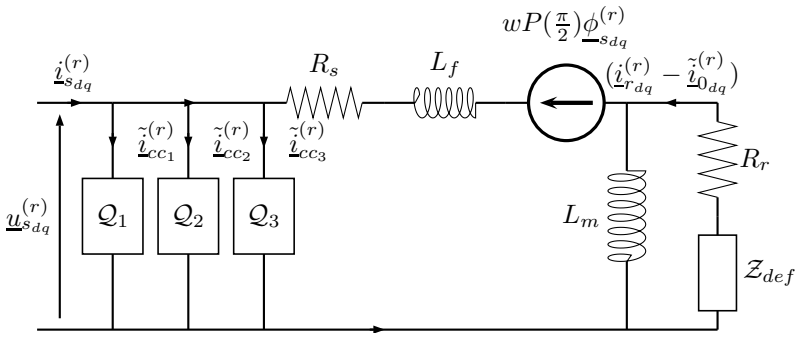

Figure 2.20. *Model of stator and rotor faults*

The fourth-order state space representation of the induction machine with a winding fault (where the measured speed w is a pseudo-input) relating to the electrical diagram 2.20 is in the following form:

$$\sum(\underline{\theta}) \begin{cases} \underline{\theta} = [R_s \quad L_m \quad L_f \quad R_r \quad \eta_{cc_1} \quad \eta_{cc_2} \quad \eta_{cc_3} \quad \eta_0 \quad \gamma_0]^T \\ \underline{x} = \begin{bmatrix} \underline{i}_{s_{dq}} \\ \underline{\phi}_{r_{dq}} \end{bmatrix} \quad \underline{y} = \underline{i}_{s_{dq}} \quad \underline{u} = \underline{u}_{s_{dq}} \\ \dot{\underline{x}} = \mathcal{A}\,\underline{x} + \mathcal{B}\underline{u} \\ \underline{y} = \mathcal{C}\underline{x} + \mathcal{D}\underline{u} \end{cases} \qquad [2.93]$$

with:

$$\mathcal{A} = \begin{bmatrix} (\mathcal{R}_s + \mathcal{Z}_{eq})\,\mathcal{L}_f - w\,\mathcal{P}(\frac{\pi}{2}) & \left(\mathcal{Z}_{eq}\,\mathcal{L}_m^{-1} - w\,\mathcal{P}(\frac{\pi}{2})\right)\,\mathcal{L}_f^{-1} \\ \mathcal{Z}_{eq} & -\mathcal{Z}_{eq}\,\mathcal{L}_m^{-1} \end{bmatrix}$$

$$\mathcal{B} = \begin{bmatrix} \frac{1}{L_f} & 0 & 0 & 0 \\ 0 & \frac{1}{L_f} & 0 & 0 \end{bmatrix}^{\mathrm{T}}, \quad C = \begin{bmatrix} 1 & 0 & 0 & 0 \\ 0 & 1 & 0 & 0 \end{bmatrix}$$

$$\mathcal{D} = \sum_{k=1}^{3} \frac{2}{3}\,\frac{\eta_{cc_k}}{R_s}\,\mathcal{P}(-p\Theta)\,\mathcal{Q}(p\gamma_{cc_k})\,\mathcal{P}(p\Theta)$$

$$\mathcal{Z}_{eq} = R_r \cdot \left(\mathcal{I}_{d_2} - \frac{\eta_0}{1+\eta_0}\,\mathcal{Q}(\gamma_0)\right)$$

2.5. Methodology for monitoring the induction machine

The diagnosis strategy consists of monitoring the parameters of the differential mode (fault parameters). Of course, monitoring parameters must also take into account normal and predictable variations in the parameters of the common mode which are

exclusively due to the operating conditions (temperature, the machine's magnetic state, etc.).

2.5.1. *Parameter estimation for induction machine diagnosis*

The theoretical concepts of identification using output error are widely discussed in literature [LJU 99, RIC 98, TRI 01]. Also in this section, we will endeavor to present its application in the special case of diagnosing induction machines.

2.5.1.1. *Parameter identification using output error method*

The generally implemented method, commonly known as the model method, applied to estimating the parameters of the induction machine can be symbolized by Figure 2.21. In this case, the approach used is a "direct approach" which processes data gathered in a closed loop in the same way as for an open loop. With the presence of feedback on a speed of w, and currents[6], $\underline{i}_{s_{dq}}$ is therefore not taken into account and is not supposed to alter the parameter identification. In fact, with this feedback, we used a voltage input $\underline{u}_{s_{dq}}$ in an identification mechanism which is correlated with the output disturbance $\underline{b}$ (and also that for the speed measurement): the estimation is, therefore, asymptotically biased [BAZ 08, LJU 99]. In our case, we circumvent this difference by paying particular attention to the measurement in order to make the signal-to-noise ratio the highest possible. However, there are algorithms for identification through output error intended for the closed loop, and they will be demonstrated in the following chapter. They allow a perfect rejection of the bias, but at the cost of a more complex implementation.

Let us consider the monitoring model which describes the superposition of the common mode $M_n(\underline{\theta}_n)$ characterized by the vector parameters $\underline{\theta}_n$, of the differential stator $\Delta M_{cc}(\underline{\theta}_{cc})$ and rotor $\Delta M_{bc}(\underline{\theta}_{bc})$ mode. In this model, $M_n(\underline{\theta}_n)$ summarizes the expertise of the machine user, in other words, his/her knowledge on the electrical parameters $\underline{\theta}_n = [\ R_s \quad R_r \quad L_m \quad L_f\ ]^T$ and their variance $Var\{\underline{\theta}_n\}$, as well as noise affecting the output, i.e. their variance σ_b^2. This nominal model is only sensitive to predictable parametric variations. This is the contrary to the error models $\Delta M_{cc}(\underline{\theta}_{cc})$ and $\Delta M_{bc}(\underline{\theta}_{bc})$ which constitute a true fault signature, both in terms of their structure as well as their parameters $\underline{\theta}_{cc} = [\ \eta_{cc_1} \quad \eta_{cc_2} \quad \eta_{cc_3}\ ]^T$ and $\underline{\theta}_{bc} = [\ \eta_0 \quad \gamma_0\ ]^T$. Within the framework of diagnosing simultaneous stator/rotor faults in the machine, we therefore define the vector of the extended parameters $\underline{\theta} = [\ \underline{\theta}_n^T \quad \underline{\theta}_{cc}^T \quad \underline{\theta}_{bc}^T\ ]^T$ to be estimated as:

$$\underline{\theta} = \begin{bmatrix} R_s & R_r & L_m & L_f & \eta_{cc_1} & \eta_{cc_2} & \eta_{cc_3} & \eta_0 & \gamma_0 \end{bmatrix}^T \qquad [2.94]$$

6 On the speed varying devices, current looping operates by internal regulation loops.

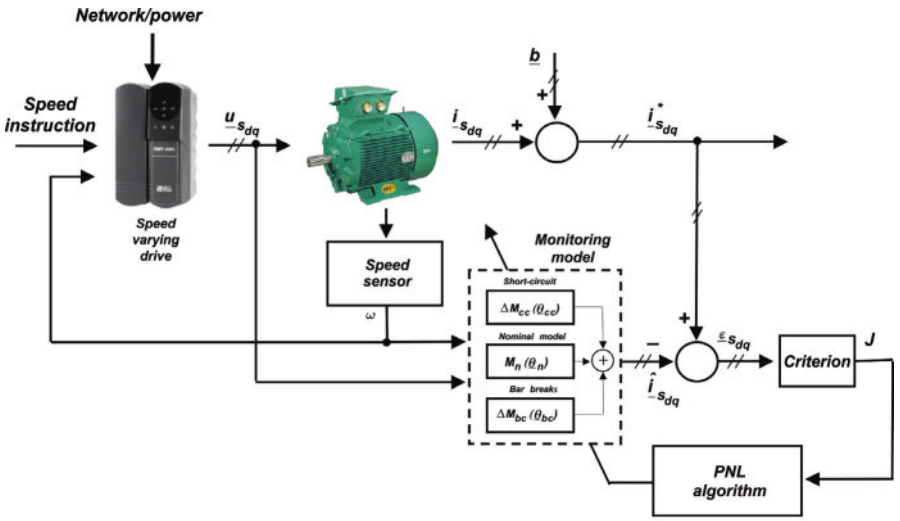

Figure 2.21. *Principle of the output error method applied to the induction machine*

The strategy of induction machine diagnosis consists of carrying out many estimations of vector $\underline{\theta}$. The mean of the parametric estimations $\hat{\eta}_{cc_k}$ indicates the number of inter turns short-circuiting on each of the three phases. The parameter $\hat{\eta}_0$ enables us to evaluate the magnitude of a potential rotor fault.

We define the estimation error vector (identification residual written $\underline{\varepsilon}_{s_{dq}}$ between the measured $\underline{i}^*_{s_{dq}}$ and simulated $\underline{\hat{i}}_{s_{dq}}$ currents) by:

$$\begin{cases} \varepsilon_{s_{d_k}} = i^*_{s_{d_k}} - \hat{i}_{s_{d_k}} \\ \varepsilon_{s_{q_k}} = i^*_{s_{q_k}} - \hat{i}_{s_{q_k}} \end{cases} \quad [2.95]$$

The optimum value of $\underline{\theta}$ is obtained by minimizing the multivariable quadratic criterion according to:

$$J = \sum_{k=1}^{K} \varepsilon^2_{s_{d_k}} + \sum_{k=1}^{K} \varepsilon^2_{s_{q_k}} \quad [2.96]$$

where $i^*_{s_{d_k}}$ and $i^*_{s_{q_k}}$ are sampled measurements at period T_e (with $t = k\,T_e$, k varying from 1 to K points). The estimated currents $\hat{i}_{s_{d_k}}$ and $\hat{i}_{s_{q_k}}$ represent the model simulation based on an estimation of the parameter vector $\underline{\hat{\theta}}$.

As the output $\underline{i}_{s_{dq}}$ is not linear in parameters $\underline{\hat{\theta}}$, minimizing this criterion can be achieved by a nonlinear programming method [RIC 98]. The optimum

value of the parameter vector written $\underline{\theta}_{opt}$ is obtained by an iterative optimization algorithm. Marquardt's algorithm [MAR 63] offers a good compromise between robustness and convergence speed. The parameters to be estimated are updated in the following way:

$$\underline{\hat{\theta}}_{i+1} = \underline{\hat{\theta}}_i - \left\{ [J''_{\underline{\theta}\underline{\theta}} + \lambda\, I]^{-1} \cdot J'_{\underline{\theta}} \right\}_{\underline{\hat{\theta}}=\underline{\hat{\theta}}_i} \qquad [2.97]$$

Optimization management is achieved by calculating the gradient and the Hessian by using an output sensitivity function:

– $J'_{\underline{\theta}} = -2 \sum_{k=1}^{K} \varepsilon_{s_{d_k}}\ \underline{\sigma}_{d_k,\underline{\theta}_i} - 2 \sum_{k=1}^{K} \varepsilon_{s_{q_k}}\ \underline{\sigma}_{q_k,\underline{\theta}_i}$: gradient;

– $J''_{\underline{\theta}\underline{\theta}} \approx 2 \sum_{k=1}^{K} \underline{\sigma}_{d_k,\underline{\theta}_i} . \underline{\sigma}^T_{d_k,\underline{\theta}_i} + 2 \sum_{k=1}^{K} \underline{\sigma}_{q_k,\underline{\theta}_i} . \underline{\sigma}^T_{q_k,\underline{\theta}_i}$: Hessian approximation;

– $\lambda > 0$: monitoring parameters;

– $\underline{\sigma}_{d_k,\underline{\theta}_i} = \frac{\partial \hat{y}_k}{\partial \underline{\theta}_i}$: output sensitivity functions i_{s_d};

– $\underline{\sigma}_{q_k,\underline{\theta}_i} = \frac{\partial \hat{y}_k}{\partial \underline{\theta}_i}$: output sensitivity functions i_{q_s}.

This algorithm, thanks to the control over parameter λ during the research, enables us to evolve between a gradient technique which is far from being the optimum (thus $\lambda >> 1$)) and a Newton technique (when $\lambda \longrightarrow 0$) which makes it possible to accelerate the convergence around the optimum.

The differential system enabling the simulation of sensitivity functions can be directly deduced from a state space representation of the induction machine (equation [2.93]):

$$\begin{cases} \dot{\underline{\sigma}}_{\underline{x},\theta_i} = \mathcal{A}(\underline{\theta})\, \underline{\sigma}_{\underline{x},\theta_i} + \left[\frac{\partial \mathcal{A}(\underline{\theta})}{\partial \theta_i} \right] \underline{x} + \left[\frac{\partial \mathcal{B}(\underline{\theta})}{\partial \theta_i} \right] \underline{u} \\ \sigma_{\underline{y},\theta_i} = \mathcal{C}^T(\underline{\theta})\, \underline{\sigma}_{\underline{x},\theta_i} + \left[\frac{\partial \mathcal{D}(\underline{\theta})}{\partial \theta_i} \right] \underline{u} \end{cases} \qquad [2.98]$$

where $\sigma_{\underline{y},\underline{\theta}} = \frac{\partial \underline{y}}{\partial \underline{\theta}}$ represents the output sensitivity matrix according to the parameters, and $\sigma_{\underline{x},\underline{\theta}} = \frac{\partial \underline{x}}{\partial \underline{\theta}}$ represents the sensitivity matrix according to the state.

2.5.1.2. *A priori information and diagnosis*

Introducing *a priori* information into a parameter estimation process was originally intended for problems of sensitization. In fact, the identifier using the aforementioned algorithm is often faced with anomalies, such as obtaining parameters which are far removed from physical reality, or even completely absurd parameters such as negative resistances or inductances. This is partly due to problems of sensitization or identifiability which can be solved by a more persistent excitation when the process

allows it. Another method consists of imposing realistic constraints on the parametric space by introducing the user's expertise. In fact, when we have available knowledge on the parameters which are to be estimated, then to the experimental criterion J which is weighted by the noise variance σ_b^2, we may combine a quadratic term which represents this information (parameter values written $\underline{\theta}_0$ weighted by their variance $M_0 = Var(\underline{\theta}_0)$) according to the following formula [MOR 99]:

$$J_C = (\underline{\hat{\theta}} - \underline{\theta}_0)^T M_0^{-1} (\underline{\hat{\theta}} - \underline{\theta}_0) + \frac{J}{\sigma_b^2} \qquad [2.99]$$

When the *a priori* information is certain and accurate, this methodology may prove to be very useful and ensures good convergence, particularly for processes which are sensitive to the choice of excitation, as for electrical drives [TRI 09].

In the diagnostic framework, only the nominal model $M_n(\underline{\theta}_n)$ must include the *a priori* information, summarized by $\left\{\underline{\theta}_{n_0},\ Var\{\underline{\theta}_{n_0}\}\right\}$. As there is no available knowledge on these faults, the *a priori* values of the parameters for the differential modes $\Delta M_{cc}(\underline{\theta}_{cc})$ and $\Delta M_{bc}(\underline{\theta}_{bc})$ are zero, whereas their variances are infinite (or extremely high), such that:

$$\underline{\theta}_0 = \begin{bmatrix} \underline{\theta}_{n_0} = [R_{s_0} \ \ R_{s_0} \ \ L_{m_0} \ \ L_{f_0}]^T \\ \underline{\theta}_{cc} = \underline{0} \\ \underline{\theta}_{bc} = \underline{0} \end{bmatrix}$$

$$M_0 = Var\{\underline{\theta}_0\} = \begin{bmatrix} \sigma_{R_s}^2 & & & & & & \\ & \sigma_{R_s}^2 & & & 0 & & \\ & & \sigma_{L_m}^2 & & & & \\ & & & \sigma_{L_f}^2 & & & \\ & 0 & & & \infty & & \\ & & & & & \ddots & \\ & & & & & & \infty \end{bmatrix}$$

In practice, variances in the electrical parameters $\underline{\theta}_{n_0}$ are obtained either through physical knowledge (manufacturer's data and/or elementary experiment), or by preliminary estimates. In each case, these variances must tolerate predictable parametric estimations (for instance, a change in the operating conditions). In addition, no constraint is imposed on the fault parameters because their estimates can only provide experimental data via criterion J.

2.5.2. *Experimental validation of the monitoring strategy*

2.5.2.1. *Experimental system*

In practice, the academic testing stand which makes it possible to test all monitoring methods is shown in Figure 2.22. The machine is speed controlled by a vector control

speed-varying device. A dynamic load producing a resistive torque is positioned on the machine's shaft, followed by a position/speed sensor (incremental encoder). The three-phase currents and voltages are measured and conditioned by anti-folding filters before acquisition.

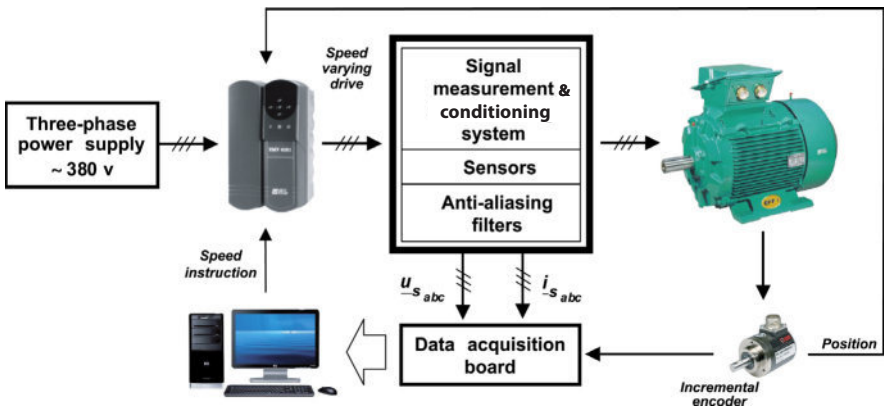

Figure 2.22. *Experiment setup for identification and control of the induction machine*

Parameter identification algorithms require, in order to converge, persistent excitation which sufficiently sensitizes all the modes in the system. As the induction machine is speed controlled, the simplest and most natural excitation consists of interfering with the reference speed by adding a pseudo-random binary sequence (PRBS) to it. However, this excitation remains problematic for applications with constant speed. So as not to restrict ourselves to a particular application, we may define another excitation protocol under constant speed obtained by adding sinusoidal signals to the inverter's reference voltage [BAC 05]. The results will be presented for both methods in the following section.

In order to realize the faults experimentally, stator windings were modified in order to access the intermediate tap points. These tap points are distributed over phases a and b with the aim being able to short-circuit a number of inter turns in a quasi-geometric progression. Thus, the terminals which are accessible from the exterior correspond to 18 inter turns (3.88%), 29 inter turns (6.25%), 58 inter turns (12.5%), and 116 inter turns (25%). There are different interchangeable rotors available on the testing stand, including a healthy rotor with 28 bars and two faulty rotors (one and two broken bars). As the technique shown previously enables us to pinpoint predictable parametric fault variations (due to over-heating, for instance), we may imagine a test at a high operating temperature (50 instead of 35). To do so, a temperature sensor is inserted between the motor and the stator windings.

2.5.2.2. *Implementation*

A priori information is gathered using an average of 10 preliminary recordings for different temperatures in order to envisage all the situations likely to vary the parameters (normal change in the machine's state). For all the identification tests, we used:

$$\underline{\theta}_{ref} = \left[\begin{array}{cccccccccc} 9.81 & 3.83 & 0.436 & 7.62.10^{-2} & 0 & 0 & 0 & 0 & \gamma_0 \end{array} \right]^T$$

$$M_0^{-1} = diag(5.10^2, \quad 65.10^2, \quad 17.10^5, \quad 10^7, \quad 0, \quad 0, \quad 0, \quad 0, \quad 0)$$

The noise variance is equal to: $\sigma_b^2 = \begin{cases} \hat{\sigma}_{b_v}^2 = 0,046 & \textit{Speed excitation} \\ \hat{\sigma}_{b_t}^2 = 0.064 & \textit{Voltage excitation} \end{cases}$

It is important to note here that the initial angle γ_0 results from the first sweep in order to detect a peak in the parameter η_0.

It may be interesting to analyze the behavior of the model during the simultaneous stator and rotor faults. Thus, we proceed with a series of tests using short-circuits on several stator phases and bar breaks. The following tests were carried out:

1) healthy machine,

2) short-circuit of 18 inter turns on phase a and one broken bar,

3) short-circuit of 18 inter turns on phase a and 58 coils on phase b, and two broken bars,

4) high heat test (50): short-circuit of 58 coils on phase a and 29 coils on phase b, two broken bars.

Table 2.2 summarizes the results from the parameter estimation for the set of tests.

For the inter turn short-circuits on the stator, the results achieved show the similarity between the estimated parameters and the real parameters of the fault (a maximum error of five inter turns for speed excitation, and two inter turns for voltage excitation). The indicator η_0 denotes the rotor's fault rate: the higher the number of broken bars, the higher this parameter will be, and vice versa. Thus, the parameter identification algorithm using *a priori* information is robust when faced with simultaneous stator/rotor faults. This indicates that the fault quadripoles are not competing for an explanation of the imbalance in the machine.

In addition, we may notice that on the last test, only the resistances R_s and R_r were affected by the change in temperature. Figures 2.23 and 2.24 show precisely how the rise in temperature does not affect the differential mode.

Still for the same test, Figures 2.25 and 2.26 compare the measured current and the estimated current on Park's axis d. We notice that the error of estimation ε_{s_d} is insignificant for both modes of excitation, which allows us to draw a conclusion with regard to the model's ability to interpret simultaneous stator/rotor faults.

$\hat{\underline{\theta}}$	**Speed excitation** 750 ± 90 **tr/min**				**Voltage excitation** 750 **tr/min**			
	Test 1	**Test 2**	**Test 3**	**Test 4**	**Test 1**	**Test 2**	**Test 3**	**Test 4**
$\hat{R}_s$ (Ω)	9.83	9.84	9.97	12.45	10.14	9.97	10.54	12.45
$\hat{R}_r$ (Ω)	3.99	4.00	3.00	4.41	4.06	3.99	4.07	4.50
$\hat{L}_{m_s}$ (H)	0.432	0.440	0.440	0.442	0.440	0.440	0.432	0.440
$\hat{L}_f$ (mH)	77.025	74.012	76.99	74.50	69.19	67.87	69.22	71.49
$\hat{n}_{cc_1}$	3.540	17.864	16.052	53.69	0.75	19.05	19.12	60.02
$\hat{n}_{cc_2}$	2.51	- 1.11	53.31	26.87	- 0.84	- 0.25	59.57	30.01
$\hat{n}_{cc_3}$	- 0.04	2.51	- 2.54	- 2.46	0.08	0.58	- 0.41	0.03
$\hat{\eta}_0$	0.008	0.10	0.20	0.19	0.007	0.09	0.21	0.20

Table 2.2. *Results from parametric estimation*

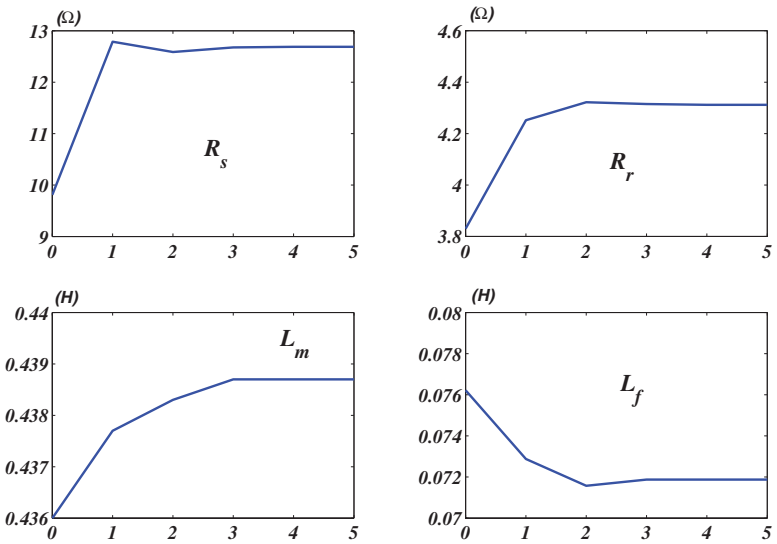

Figure 2.23. *Parameter evolution for a high heat test with faults (test 4) – resistance and inductance*

2.6. Conclusion

An advanced degradation in the stator insulator will result, electrically, in a resistive contact between the winding inter turns, depending on different topologies, which can be very varied. In some cases, through a chain effect, the contact may lead to a somewhat immediate destruction of the winding. In other cases, the drive controls

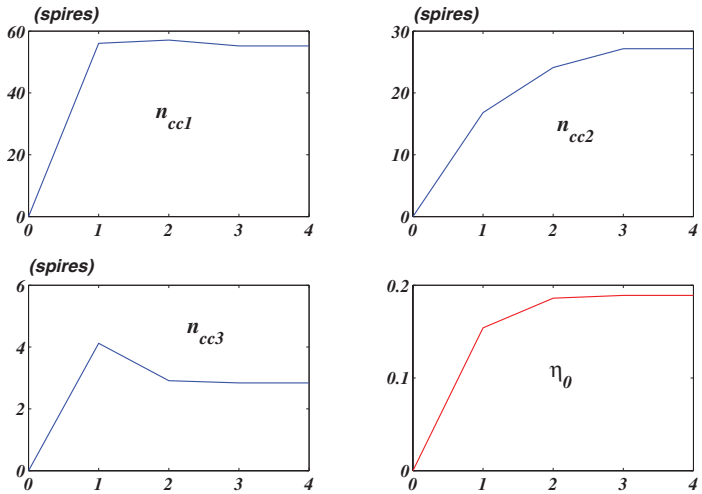

Figure 2.24. *Parameter evolution for a high heat test (test 4) – number of short-circuiting inter turns*

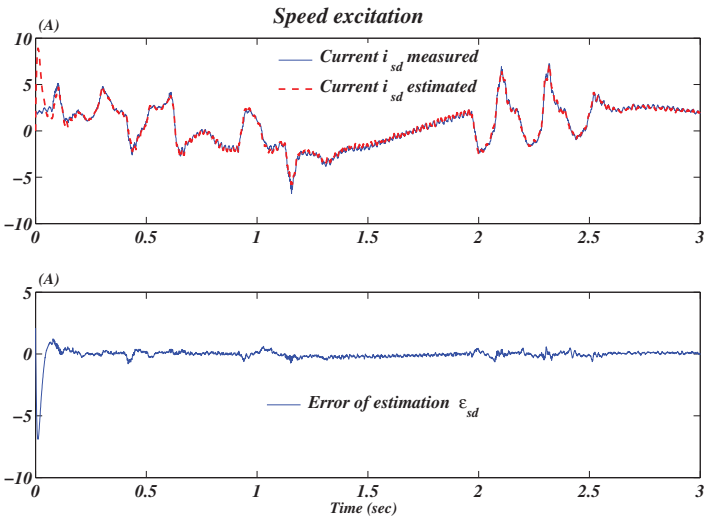

Figure 2.25. *Comparison between measured i_{s_d} and $\hat{i}_{s_d}$ – estimated currents for speed excitation*

at variable speeds using current loops may partly compensate for its effects, by immediately maintaining the drive's dynamic performances. This is a typical example of the direct or resistive short-circuit between a few consecutive inter turns in the same phase. Implementing a monitoring strategy or reconfiguring the control in damaged

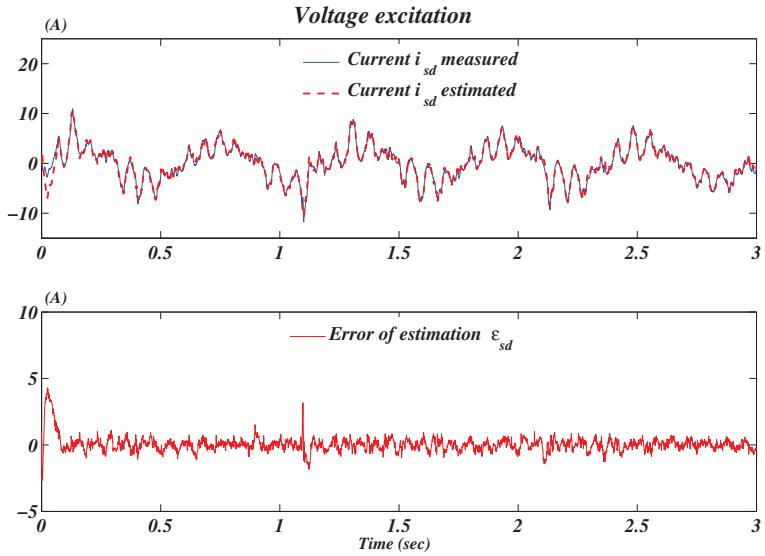

Figure 2.26. *Comparison between measured i_{s_d} and $\hat{i}_{s_d}$ – estimated currents for voltage excitation*

mode requires a diagnosis of the short-circuit current amplitude, as it is this (via the Joule effect) which will accelerate the degradation process. This is the entire problem with diagnostic-oriented modeling of induction machines, as presented in this chapter.

The approach used for modeling is based on a fundamental hypothesis of superimposing two operating modes: a common mode combined with the rotating field, created by the machine's windings with no fault, and a differential mode combined with a stationary field in relation to the rotor, induced in the short-circuit of the inter turns. An important characteristic of the diagnostic model is that it remains extremely close to the model which is classically used to control at variable speeds, with, notably, the possibility of notation within the different reference frames (stator, rotor, or rotating field).

This characteristic is essential for converging estimation algorithms well. In this chapter, we have proposed and validated the diagnosis of the machine through parameter identification in a more global, comprehensive approach. We have shown that parameter monitoring of the diagnosis model not only makes it possible to locate a fault in the stator or rotor winding, but also to determine its severity.

Identifying the parameters of the induction machine has been performed for a long time in a quasi-open-loop approach, even in the presence of a speed regulator

which ensures its drive. However, by working on the machine's control voltages and on the line current measurements, we forget that the drive is ensured by output feedback. Fundamentally, this type of identification causes theoretical problems due to the stochastic disturbances that we find on the control variable via the regulation loop, which makes the estimation asymptotically biased. This specific problem will be the main object for study in the next chapter, through a general and realistic methodology of closed-loop identification applied to induction machines.

2.7. Bibliography

[BAC 05] Bachir S., Tnani S., Chanpenois G., Gaubert J.P., "Stator faults diagnosis in induction machines under fixed speed", *European Conference on Power Electronics and Applications, EPE*, Dresden, Germany, September 2005.

[BAC 06] Bachir S., Tnani S., Trigeassou J.C., Chanpenois G., "Diagnosis by parameter estimation of stator and rotor faults occurring in induction machines", *IEEE Transactions on Industrial Electronics*, vol. 53, no. 3, p. 963-973, 2006.

[BAZ 08] Ben Ameur Bazine I., Identification en boucle fermée de la machine asynchrone: application à la détection de défaut, PhD Thesis, University of Poitiers, Ecole Supérieure d'Ingénieurs de Poitiers/Ecole Nationale d'Ingénieurs de Tunis, 2008.

[CAS 04] Casimir R. *et al.*, "Comparison of modeling methods and of diagnostic of asynchronous motor in case of defects", *9th IEEE International Power Electronics Congress*, *CIEP*, Celaya, GTO, October 2004.

[DAN 98] Dantzig G.B., *Linear Programming and Extensions*, Princeton University Press, 1998.

[DOE 10] Le Doeuff R. Zaïm E.H., *Rotating Electrical Machines*, ISTE, London, John Wiley & Sons, New York, 2010.

[FIL 94] Fillippitti F., Franceshini G., Tassoni C., Vas P., "Broken bar detection in induction machine: comparaison between current spectrum approach and parameter estimation approach", *IAS'94*, New York, p. 94-102, 1994.

[GRE 97] Grellet G., Clerc G., *Actionneurs Électriques. Principes*, *Modèles et Commande*, Eyrolles, Paris, 1997.

[INN 94] Innes A.G., Langman R.A., "The detection of broken bars in variable speed induction motors drives", *ICEM'94*, December 1994.

[LJU 99] Ljung L., *System Identification: Theory for the User*, Prentice Hall, Upper Saddle River, 1999.

[LOR 93] Loron L., "Application of the extended kalman filter to parameter estimation of induction motors", *EPE'93*, vol. 05, p. 85-90, Brighton, September 1993.

[MAK 97] Makki A., Ah-jaco A., Yahoui H., Grellet G., "Modeling of capacitor single-phase asynchronous motor under stator and rotor winding faults", *IEEE International SDEMPED'97*, Carry-le-Rouet, p. 191-197, September 1997.

[MAR 63] MARQUARDT D.W., "An algorithm for least-squares estimation of nonlinear parameters", *Society of Industrial and Applied Mathematics*, vol. 11, no. 2, p. 431-441, 1963.

[MEN 99] MENSLER M., Analyse et étude comparative de méthodes d'identification des systèmes à représentation continue. Développement d'une boîte à outil logicielle, PhD Thesis, University of Nancy I, 1999.

[MOR 99] MOREAU S., Contribution à la modélisation et à l'estimation paramétrique des machines électriques à courant alternatif: Application au diagnostic, PhD Thesis, University of Poitiers, Ecole Supérieure d'Ingénieurs de Poitiers, 1999.

[RIC 98] RICHALET J., *Pratique de l'identification*, 2nd edition, Hermès, Paris, 1998.

[ROB 99] ROBERT P., *Traité de l'électricité vol. 2: Matériaux de l'électrotechnique*, Presses polytechniques et universitaires romandes, 1999.

[SCH 99] SCHAEFFER E., Diagnostic des machines asynchrones: modèles et outils paramétriques dédiés à la simulation et à la détection de défauts, PhD Thesis, University of Nantes, Ecole Centrale de Nantes, 1999.

[TOL 04] TOLIYAT H.A., KLIMAN G.B., *Handbook of Electrical Motors*, Marcel Dekker, New York, 2004.

[TRI 01] TRIGEASSOU J.C., POINOT T., "Identification des systèmes à représentation continue – Application à l'estimation de paramètres physiques", in LANDAU L.D., BESENÇON-VODA A., (eds), *Identification Des Systèmes*, Hermès, Paris, 2001

[TRI 09] TRIGEASSOU J.C., POINOT T., BACHIR S., "Parametric estimation for knowledge and diagnosis of electrical machines", in HUSSON R. (ed.), *Control Methods for Electrical Machines*, ISTE Ltd., London and John Wiley & Sons, New York, 2009.

Chapter 3

Closed-Loop Diagnosis of the Induction Machine

3.1. Introduction

Fault detection, early if possible, in electrical drives is both a scientific matter due to the complexity and variety of problems raised, as well as an industrial one due to the economic advantage of a useful predictive maintenance strategy. For around 20 years, many research organizations have become involved in electrical machine diagnosis, and especially, induction machine diagnosis. Several approaches can be implemented to detect electrical machine faults, such as vibration analysis, observers, parameter estimation, etc.

Recent studies have succeeded in showing the relevance of identification using parameter estimation for fault detection. In [MOR 99], the contribution of *a priori* information has proven to be a decisive element in order to strengthen output error algorithm convergence, and to integrate user expertise. In [BAC 02], a genuine diagnosis method using parameter estimation was developed by integrating fault signatures using specific models and user expertise in relation to healthy machine operation. It has also been shown that it is indeed possible to detect stator coil short-circuits and rotor bar breaks in an induction machine which is integrated into a speed regulating device through vector control.

Chapter written by Imène BEN AMEUR BAZINE, Jean-Claude TRIGEASSOU, Khaled JELASSI and Thierry POINOT.

Although the results obtained from a laboratory pilot test have been very encouraging, several fundamental questions have been raised. Parameter estimation requires full excitation in order to excite the relevant modes within the machine. Unfortunately, this excitation richness most often contradicts operating constraints, especially when the user needs a highly efficient speed regulator. Moreover, although electrical faults are well detected, there is still a relatively high level of uncertainty which cannot be reduced by improving excitation. This last point raises two fundamental questions:

– is a high portion of this uncertainty due to a modeling error?

– in addition, even though the induction machine will operate in a closed loop, is it true that the user of an identification algorithm planned to work in an open loop is the cause, at least partly, for this uncertainty which might also be a bias?

The research that will be conveyed in this chapter proposes to provide a few answers to this set of questions, as the problem of modeling errors is too vast to be dealt with at the same time. In addition, we have particularly emphasized identification problems by trying to set them out in a fundamental way, independent of diagnosis through parameter estimation.

It was highly important to us to study closed-loop identification of the induction machine. In fact, this will only fulfil industrial requirements for speed variation if it is included in a looped device, composed of a torque and speed control. It is a well-known fact that identifying a closed-loop system, without explicit consideration of this closed loop, results in an asymptotic bias due to the correlation of output noises with the looped control applied to the system.

However, identification algorithms using closed-loop output errors have provided a solution to this fundamental problem [SÖD 87, HOF 95, LAN 97, DON 00, GRO 00a], where the controller is explicitly taken into account. This consideration may be realized either by having *a priori* knowledge of the controller, or (which is the more realistic solution) by estimating it.

The second answer that we have tried to offer for the diagnosis problem concerns the mode of excitation. In speed variation, it is natural to disturb the speed reference by a pseudo-random binary sequence (PRBS) in order to fulfil the requirements of excitation richness, which is essential for the identification algorithm. Unfortunately, this mode of excitation will go completely against manufacturing objectives when the control is specifically designed to maintain constant speed. But this speed is disturbed by the variations in the load torque (caused by manufacturing requirements) that the control precisely wants to minimize. These changes in the load torque vary the machine's operating point: are these changes enough to fulfil objectives for excitation richness, and do they not induce an asymptotic bias due to the looped nature of the operation?

The studies in this chapter try to offer an answer to these questions as a general methodology for identifying the closed-loop induction machine, which can be applied to its diagnosis by parameter estimation.

This chapter is divided into 3 sections. In section 3.2, we will present the problems regarding closed-loop identification. Section 3.3 will introduce the principle of the methodology for closed-loop induction machine identification. In section 3.4, we will apply this methodology to closed-loop diagnosis of simultaneous stator/rotor faults.

3.2. Closed-loop identification

3.2.1. *Problems in closed-loop identification*

The typical problem of closed-loop identification lies within the correlation between output noise and the control signal due to the closed-loop. Another problem caused by data collected in closed-loop systems is that it generally contains less information than data collected in an open loop. In fact, an important objective of the control is to minimize the looped system's sensitivity to disturbances, which makes the problem of identification much more difficult to deal with [FOR 99].

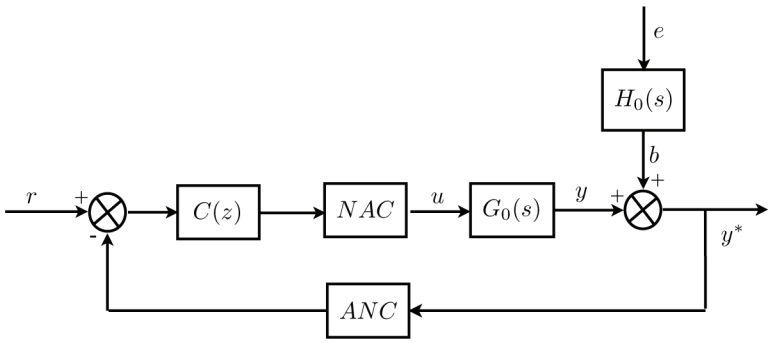

Figure 3.1. *Looped system*

Here we are working within the framework of a numerically controlled looped process shown in Figure 3.1. The input/output data of the process are described by the following relations:

$$y(s)^* = G_0(s)u(s) + H_0(s)e(s) \quad [3.1]$$

$$u(q^{-1}) = C(q^{-1})\left[r(q^{-1}) - y(q^{-1})\right] \quad [3.2]$$

where G_0 represents the real process to be identified, and $C(z)$ is the controller. The output vector is written as y^*, and the input vector is u.

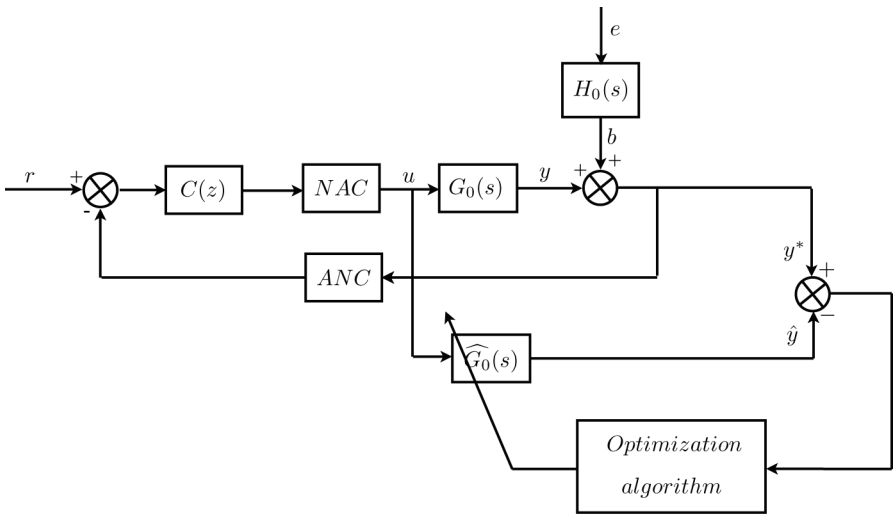

Figure 3.2. *Principle of direct identification of induction machine*

The expression $b(s) = H_0(s)e(s)$ models the disturbances: e is a sequence of independent random variables, distributed identically with a zero mean (white noise), $H_0(s)$ is a stable and standardized invariant linear filter (process generator). The term $b(s)$ groups together electronic noises and disturbances acting on the system, as well as modeling errors. Moreover, contrary to the open-loop system, input $u(s)$ and disturbances $e(s)$ are correlated, due to the closed loop. The signal r_k may represent an excitation signal or an external signal.

The study carried out in this chapter was developed using the fundamental hypothesis that: r is a quasi-stationary signal which is independent of disturbances e [LJU 87]. The excitation applied to the system is persistent and of a sufficient order. The identification procedure aims to determine an estimate of the process $G_0(s)$. In some cases, it is indeed interesting to also determine an estimate of controller $C(z)$. For direct identification, the data u_k and y_k collected in the closed loop are processed in the same way as in the open loop (Figure 3.2).

Thus, the closed loop is not taken into account. *A priori*, this method raises no real practical usage problems, and is therefore frequently used. However, as we are ignoring the presence of the controller, we find ourselves with an input $u(s)$ which is correlated with the disturbance of output $b(s)$: the estimate is therefore asymptotically biased [BAZ 08b, BAZ 08a]. This is the main disadvantage of the direct approach which has also prompted the development of algorithms that explicitly take the closed loop into account.

When the system is operating in closed loop (which is the case for AC vector controlled machines), the disturbance b_k is correlated with the control u_k by the controller (or the control algorithm). Therefore, the sensitivity functions σ_k (necessary for the optimization algorithm to operate), which are calculated using excitation u_k, are correlated with disturbance b_k. This means that the estimation $\underline{\theta}_{opt}$ is asymptotically biased. This bias is not really important when the signal-to-noise ratio is very low. We can, then, ignore this in an initial approximation.

However, identification algorithms using closed-loop output errors have been proposed in [SÖD 87, HOF 95, LAN 97, DON 00, GRO 00a, BAZ 07]; they reject this asymptotic bias perfectly but at the cost of a much more complex identification procedure.

One analysis [GRO 00b] shows that if b_k is white noise, due to an delay which is inherent to the numerical closed loop, then the sensitivity functions are not correlated with the white noise, meaning that $E\{\sigma_{k,\theta_i}, b_k\} = 0$. On the other hand, if b_k is correlated noise, then a bias will appear whose value depends on the process generating this noise.

3.2.2. *Identification problems for diagnosing electrical machines*

For two decades, many studies in electrical engineering and identification have enabled the development of new offline and online diagnosis strategies of electrical drives; the induction machine, in particular [LOR 93, FIL 94, BAC 03b, BAZ 05].

Techniques of parameter estimation have been intensively studied and tested, especially in laboratory test pilots. Equation error type algorithms are generally not considered because they are asymptotically biased and sensitive to stochastic disturbances and modeling errors. On the contrary, the Kalman filter and output error techniques enable us to obtain realistic and reliable estimations in real situations [BAC 01, BAC 06].

Thus, the development of algorithms designed to estimate physical parameters, by considering *a priori* knowledge of the induction machine has enabled a promising advance in parameter estimation diagnostics.

When the induction machine is powered directly on the sector, it therefore operates in an open loop, but at a quasi-constant speed. Speed variation is most often due to a vector control, in which case the machine operates in closed loop with a cascade control structure. In these conditions, we are justified in asking ourselves the question of the controller's impact on the bias in direct identification (without taking the looped structure into account) [GRO 99, GRO 00a].

Moreover, we propose to identify the electrical model of the induction machine with no explicit excitation. In fact, excitation of the speed reference which disturbs the machine's operating point cannot fulfil industrial objectives: it is for this reason that indirect excitation by varying the load torque was maintained.

We pay special attention to induction machine identification through an output error method [TRI 03, BAC 08] (see Chapter 2 for further details on algorithms) based on a closed-loop decomposition. However, the main constraint imposed by this identification technique is the highly important controller knowledge.

The induction machine is currently the basis for many industrial applications which cover a huge domain. Depending on the application involved, the industrialist can access all the control's details, just as he/she can ignore certain parts of the control structure's interior. In this case, we have proposed a preliminary identification of the "equivalent" controller, using an over-parameterization technique in order to avoid *a priori* knowledge of the structure and the controller's parameters [BAZ 08c, BAZ 08b].

3.3. General methodology of closed-loop identification of induction machine

3.3.1. *Taking control into account*

The looped control of an induction machine requires a torque control (current control) and generally, a speed control (hence successive controllers), as well as a flux control. Moreover, as torque and flux controls are not naturally decoupled, it is vital to predict a decoupling phenomenon (generally nonlinear) which complicates the controller's structure (multi-variable and nonlinear imbricated controllers).

Figure 3.3 shows the operational organization of the control taken from the previously discussed principles. This is a vector control moving toward the rotor flux. This is the most commonly used because it eliminates the influence of rotor and stator leakage reactance and gives better results than methods based on the stator flux or air-gap direction [FAI 95, JEL 91].

The converter and its control do not figure explicitly on this diagram as we are studying the control process. Thus, we are focusing directly on the controller output u_{ds} and u_{qs}, and on currents i_{ds} and i_{qs}. These voluntary choices prevent an unnecessary cluttering of the presentation, whose main aim is to show the mechanisms which are specific to this control.

Thus, the induction machine control is considered as a multi-dimensional system (multi-input, double-output). We can break this relationship down into two specific relations, both corresponding to two multi-input, single-output subsystems. In other terms, this means that one subsystem corresponds to output u_{ds}, and the other corresponds to output u_{qs} (see Figure 3.4).

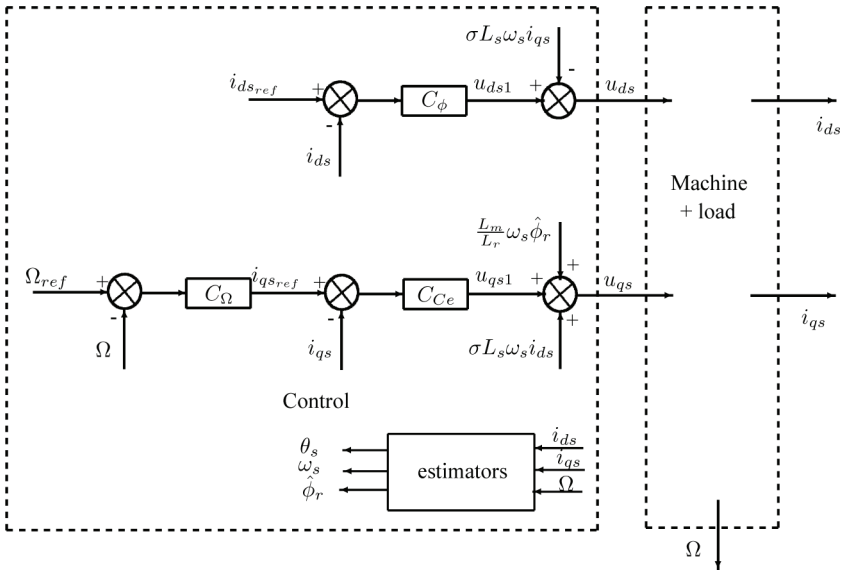

Figure 3.3. *Decoupling by adding compensation terms*

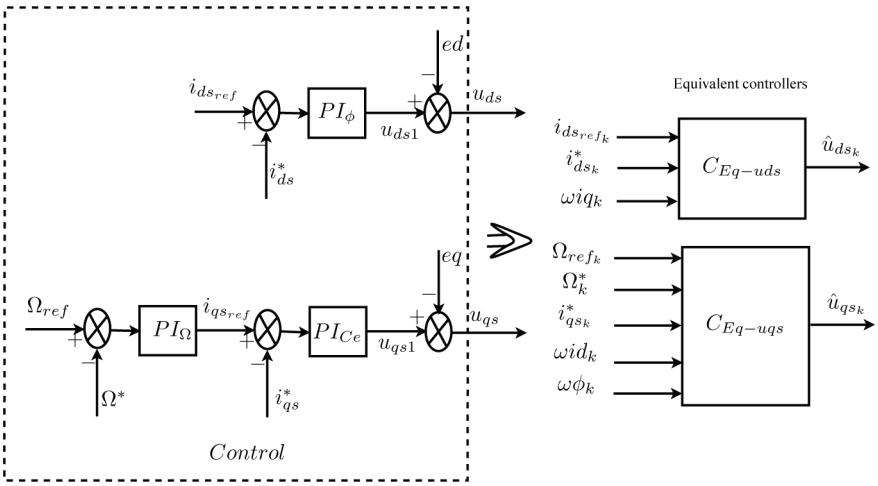

Figure 3.4. *Breakdown of the machine control into multi-input, single-output subsystems*

We propose to describe the behavior of this system by determining those relations which link the control outputs (u_{ds}, u_{qs}) expressed within the rotating field reference frame to the inputs (Ω_{ref}, Ω^*, $i_{ds_{ref}}$) and (i^*_{ds} et i^*_{qs}), which are also expressed in the rotating field reference frame.

The variables used in Figure 3.4 correspond to:

$$ed = C_d \cdot \omega_s \cdot i_{qs}^*$$

$$eq = -C_{1q} \cdot \omega_s \cdot i_{ds}^* - C_{2q} \cdot \omega_s \cdot \widehat{\phi}_r$$

and:

$$C_\phi(q^{-1}) = \frac{r_{0\phi} + r_{1\phi} q^{-1}}{1 - q^{-1}}$$

$$C_\Omega(q^{-1}) = \frac{r_{0\Omega} + r_{1\Omega} q^{-1}}{1 - q^{-1}}$$

$$C_{Ce}(q^{-1}) = \frac{r_{0Ce} + r_{1Ce} q^{-1}}{1 - q^{-1}}$$

Within the context of an indirect approach, we proposed to extend the field of application of this method by identifying an "equivalent" controller beforehand, using an over-parameterization technique in order to avoid *a priori* knowledge of the structure and the controller's parameters. The equivalent structure is more often than not complex and misunderstood in the case of the induction machine and is, moreover, nonlinear. This "equivalent" corrector is estimated by an over-parameterized least squares technique. A minimum structure is obtained with the help of a moment test. For more details on the "equivalent" controller identification principle, see [BAZ 08b].

In the following sections, we will only present the result of the closed-loop identification of the induction machine by assuming that the control algorithm is *a priori* known (either because the user knows the control algorithms, or because they were identified beforehand).

3.3.2. *Machine identification by closed-loop decomposition*

3.3.2.1. *Principle*

When the control algorithm for the induction machine is known (through *a priori* knowledge or over-parameterized identification [BAZ 08b]), then we may consider identifying the continuous model of the machine.

Let us now refer to the diagram in Figure 3.5: in this case, the excitation $\underline{\hat{u}} = \{\hat{u}_{ds}\ ,\ \hat{u}_{qs}\}$ of the continuous model is obtained by simulating the controller C_{Eq} using external signals (Ω_{ref}, $i_{ds_{ref}}$), the measurement Ω^*, the angular frequency ω_s, the flux ϕ_r and predicted outputs $\hat{i}_{ds}$ and $\hat{i}_{qs}$.

The induction machine's operation is usually analyzed in three reference frames: reference linked to the stator, rotor, and rotating field:

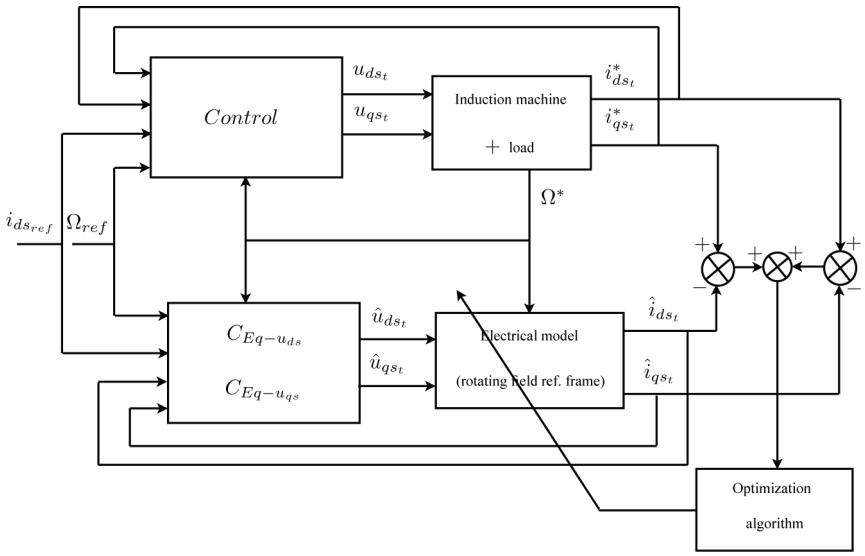

Figure 3.5. *Principle of indirect identification of induction machine*

– if the reference frame is fixed in relation to the stator $\omega_a = 0$, then we obtain an electrical system where the stator outputs are purely alternating and the system runs at the power supply frequency. Simulating the induction machine (which is necessary for output error identification) in this reference frame therefore does not require knowledge of the rotor's position, which is indeed an advantage for control with no position sensor. The major disadvantage is the manipulation of high frequency signals;

– if the reference frame rotates at a synchronized speed $\omega_a = \omega_s = 2\pi f_s$, then we obtain a purely continuous electrical system which is highly suited to identification techniques. However, the position of the rotating field must be restored with each sample taken;

– if the reference frame is fixed in relation to the rotor $\omega_a = \omega$, then the electrical signals are therefore quasi-continuous. The angular frequency of the electrical magnitudes is thus equal to $g\omega$ (where $g = \frac{\omega_s - \omega}{\omega_s}$ is the machine's shifting), which is ω_s low in real operating conditions. When we can access the mechanical position, this reference frame is favored due to the quasi-continuity of the electrical magnitudes.

The direct identification of the induction machine is performed in the rotor reference frame because it requires a lesser amount of transformations/estimates.

If we wish to proceed with an indirect identification which takes the controllers into account, then they must be positioned in the reference frame of the rotating field. In fact, the control and the controllers were designed in the rotating field reference frame,

in order to control the flux and torque. This means that these controllers have constant parameters in this frame, but that they are speed dependent in any other reference frame. It is therefore imperative for us to refer to the rotating field. Additionally, indirect identification must be carried out in the rotating field frame by using knowledge of its calculated position in the control frame.

The continuous model of the induction machine which is obtained after applying the Park transform connected to the rotating field is presented in the following form:

$$\begin{cases} \dot{\underline{\hat{x}}}(t) = A(\hat{\underline{\theta}})\underline{\hat{x}}(t) + B(\hat{\underline{\theta}})\underline{\hat{u}}(t) \\ \underline{\hat{y}}(t) = C(\hat{\underline{\theta}})\underline{\hat{x}}(t) \end{cases} \quad [3.3]$$

with:

$$\underline{X} = \begin{bmatrix} i_{ds} & i_{qs} & \varphi_{dr} & \varphi_{qr} \end{bmatrix}^T : \text{state vector} \quad [3.4]$$

$$\underline{u} = \begin{bmatrix} u_{ds} \\ u_{qs} \end{bmatrix}, \quad \underline{Y} = \begin{bmatrix} i_{ds} \\ i_{qs} \end{bmatrix} : \text{electrical model inputs and outputs} \quad [3.5]$$

The following matrices are used in this case:

$$A = \begin{bmatrix} -\frac{R_s+R_r}{L_f} & \omega_s & \frac{R_r}{L_f.L_m} & \frac{\omega}{L_f} \\ -\omega_s & -\frac{R_s+R_r}{L_f} & -\frac{\omega}{L_f} & \frac{R_r}{L_f.L_m} \\ R_r & 0 & -\frac{R_r}{L_m} & (\omega_s - \omega) \\ 0 & R_r & -(\omega_s - \omega) & -\frac{R_r}{L_m} \end{bmatrix} \quad [3.6]$$

$$B = \begin{bmatrix} \frac{1}{L_f} & 0 & 0 & 0 \\ 0 & \frac{1}{L_f} & 0 & 0 \end{bmatrix}^T, \qquad C = \begin{bmatrix} 1 & 0 & 0 & 0 \\ 0 & 1 & 0 & 0 \end{bmatrix}$$

The electrical model of the machine is characterized by four physical parameters R_s, R_r, L_m, and L_f. We will aim to estimate these parameters for a healthy machine.

3.3.2.2. *Calculating sensitivity functions*

We will now refer to the diagram in Figure 3.5. It is important to note that the outputs ($\hat{i}_{ds}$, $\hat{i}_{qs}$) and inputs ($\hat{u}_{ds}$, $\hat{u}_{qs}$) are actually simulated using excitations ($i_{ds_{ref}}$, Ω_{ref}), the measurement Ω^*, two equivalent (or exact) controllers C_{Eq-uds}, C_{Eq-uqs}, and the continuous model of the induction machine. Thus, $\{\hat{u}_{ds}\ ,\ \hat{u}_{qs}\}$ and $\left\{\hat{i}_{ds}\ ,\ \hat{i}_{qs}\right\}$ are completely uncorrelated with the current noise. This is illustrated by the numerical simulations which are carried out in the following section.

The principle of generating the predictive control $\underline{\hat{u}} = [\hat{u}_{ds}\hat{u}_{qs}]^T$ is explained in [BAZ 08b].

The sensitivity functions in relation to $\underline{\sigma}_{\hat{y}} = \left[\underline{\sigma}_{\hat{i}_{ds}}\ \underline{\sigma}_{\hat{i}_{qs}}\right]^T$ must be calculated by considering the sensitivity of $\underline{\hat{u}} = [\hat{u}_{ds}\ \hat{u}_{qs}]^T$ à $\underline{\hat{\theta}}$, meaning that $\underline{\sigma}_{\hat{u}} = \left[\underline{\sigma}_{\hat{u}_{ds}}\ \underline{\sigma}_{\hat{u}_{qs}}\right]^T$.

Let us now define $\underline{\sigma}_{\hat{i}_{ds},\theta_i} = \frac{\partial \hat{i}_{ds}}{\partial \theta_i}$ and $\underline{\sigma}_{\hat{i}_{ds},\theta_i} = \frac{\partial \hat{i}_{ds}}{\partial \theta_i}$. Thus, we obtain the sensitivity functions from the differential system:

$$\begin{cases} \dot{\underline{\sigma}}_{\hat{x},\theta_i} = A(\hat{\theta})\underline{\sigma}_{\hat{x},\theta_i} + \frac{\partial A(\hat{\theta})}{\partial \theta_i}\underline{\hat{x}} + \frac{\partial B(\hat{\theta})}{\partial \theta_i}\underline{\hat{u}}(t) + B(\hat{\theta})\underline{\sigma}_{\hat{u},\theta_i} \\ \underline{\sigma}_{\hat{y},\theta_i} = C\underline{\sigma}_{\hat{x},\theta_i} \end{cases} \quad [3.7]$$

Let us remember here that reconstructing controls $\hat{u}_{ds}$ and $\hat{u}_{qs}$ can be achieved either by using the real control (where we assume that the control is known perfectly), or by using the equivalent structure (where the structure and the control parameters are not known, therefore by using a preliminary identification of the control).

By using the exact structure of the control to calculate the sensitivity of $\underline{\hat{u}}$ in relation to the machine's parameters, we find that:

$$\underline{\sigma}_{\hat{u}_{ds_k},\theta_i} = \frac{\partial \hat{u}_{ds}(k)}{\partial \theta_i} \quad \text{and} \quad \underline{\sigma}_{\hat{u}_{qs_k},\theta_i} = \frac{\partial \hat{u}_{qs}(k)}{\partial \theta_i}$$

which are obtained from the difference equation:

$$\frac{\partial \hat{u}_{ds}(k)}{\partial \theta_i} = \frac{\partial \hat{u}_{ds1}(k)}{\partial \theta_i} - \frac{\partial \hat{ed}(k)}{\partial \theta_i} \quad [3.8]$$

$$\frac{\partial \hat{u}_{qs}(k)}{\partial \theta_i} = \frac{\partial \hat{u}_{qs1}(k)}{\partial \theta_i} - \frac{\partial \hat{eq}(k)}{\partial \theta_i} \quad [3.9]$$

The sensitivity of the linear operators $\hat{u}_{ds1}$ and $\hat{u}_{qs1}$ in relation to the parameters is equal to:

$$\frac{\partial \hat{u}_{ds1}(k)}{\partial \theta_i} = -\frac{\partial \hat{u}_{ds1}(k-1)}{\partial \theta_i} - r_{0\phi} \cdot \frac{\partial \hat{i}_{ds}(k)}{\partial \theta_i} - r_{1\phi} \cdot \frac{\partial \hat{i}_{ds}(k-1)}{\partial \theta_i} \quad [3.10]$$

$$\frac{\partial \hat{u}_{qs1}(k)}{\partial \theta_i} = -\frac{\partial \hat{u}_{qs1}(k-1)}{\partial \theta_i} - r_{0Ce} \cdot \frac{\partial \hat{i}_{qs}(k)}{\partial \theta_i} - r_{1Ce} \cdot \frac{\partial \hat{i}_{qs}(k-1)}{\partial \theta_i} \quad [3.11]$$

We will assume that the terms $\omega_s i_{qs}$, $\omega_s i_{ds}$, and $\omega_s \phi_r$ which figure in the decoupling are measurements. In this case:

$$\frac{\partial \hat{ed}(k)}{\partial \theta_i} = 0 \quad \text{and} \quad \frac{\partial \hat{eq}(k)}{\partial \theta_i} = 0$$

If we assume that the decoupling terms are a function of the estimated outputs $\hat{i}_{ds}$ and $\hat{i}_{qs}$, then the decoupling sensitivity in relation to the parameters therefore becomes:

$$\frac{\partial \hat{ed}(k)}{\partial \theta_i} = C_d \cdot \omega_s \cdot \frac{\partial \hat{i}_{qs}(k)}{\partial \theta_i} \quad [3.12]$$

$$\frac{\partial \hat{eq}(k)}{\partial \theta_i} = -C_{1q} \cdot \omega_s \cdot \frac{\partial \hat{i}_{ds}(k)}{\partial \theta_i} \quad [3.13]$$

3.3.3. *Identification results*

We have tested identification techniques on an induction machine whose parameters are given in Table 3.1.

R_s	$9.8\,\Omega$
R_r	$5.3\,\Omega$
L_m	0.5 H
L_f	0.04 H
f	$1.9\,10^{-03}\ N.m.s/rad$
J	$29.3\,10^{-03}\ N.m.s^2/rad$
Number of pole pairs	2
Number of rotor bars	28
Number of coils per phase	464

Table 3.1. *Characteristics of the induction machine*

We used two noise-generating processes for the speed and currents in order to test our methodology in different stochastic situations.

We used noise conditions such as the ratio $S/B = 15$ for the currents $\{i_{ds}, i_{qs}\}$ expressed in the rotating field and $S/B = 20$ for the speed.

The output noise is generated by the model $A.R$: $b_k + c_1 b_{k-1} = e_k$, where e_k is white noise and $-1 < c_1 < 0$. We studied two situations:

– $c_1 = 0$, thus b_k corresponds to white noise;

– $c_1 = -0.95$, thus b_k corresponds to a highly correlated noise.

We used an implicit excitation by varying the load torque as a $PRBS$ of $\pm 1.5\ N.m$ around the load $C_r = 4N.m$.

The Monte Carlo simulations were carried out on 10 realizations, each containing $6,000$ data couples. Thus, we will present the mean value of each identified parameter, with a margin of error equal to ± 3 times the standard deviation (from Monte Carlo distribution).

NOTE.–

– DI: Direct Identification

– IIRC: Indirect Identification, Real Control

– IIOC3: Indirect Identification, with Over-parameterized Controllers, order 3.

3.3.3.1. *Case of a white noise in currents*

Figure 3.6 shows the range of variations in each parameter of the induction machine. Using this simulation, we verify that there is no important bias when the electronic noise from the currents is white noise (and that the speed is measured with no error). We notice that the parameter estimation result obtained for both types of identification (DI and $IIRC$) are very close.

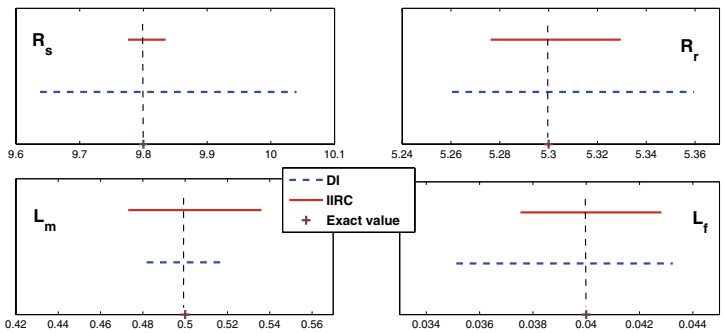

Figure 3.6. *Identification in the presence of white noise in the currents*

3.3.3.2. *Case of a highly correlated noise in the currents, and white noise in the speed*

In this simulation (Figure 3.7), we notice (in the presence of highly correlated noise on the currents and white noise on the speed) that the indirect identification gives estimations which are centered perfectly on the exact parameter values, whereas the estimations of R_r, L_m, and L_f introduce a bias in direct identification.

The simulation results show that indirect identification gives better estimations than direct identification, and in particular, that it makes it possible to reject the asymptotic bias due to looping.

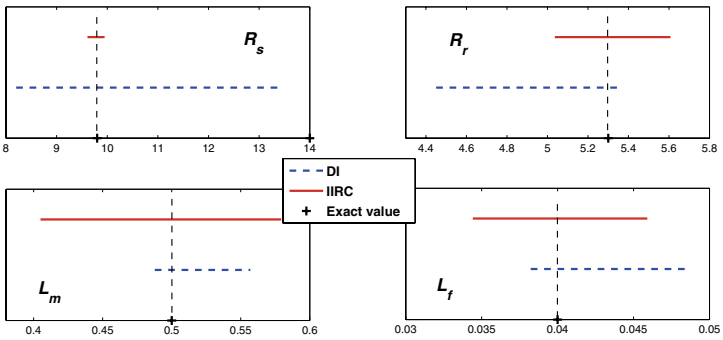

Figure 3.7. *Identification in the presence of highly correlated noise in the currents and white noise in the speed*

This closed-loop induction machine identification methodology may therefore be applied to the machine diagnosis in the following section, in the case of simultaneous stator/rotor faults.

3.4. Closed-loop diagnosis of simultaneous stator/rotor faults

3.4.1. *General model of induction machine faults*

Chapter 2 gives a detailed description of the stator/rotor fault model. By using this fault model, we obtain a fourth-order state space representation of the induction machine (where the speed is a measured pseudo-input) which corresponds to indirect identification. The state vector as well as the system's input and output are expressed in the rotating field (reference frame chosen for diagnosis through indirect approach):

$$\begin{cases} \dot{\underline{\hat{X}}}(t) = A(\omega).\underline{\hat{X}}(t) + B.\underline{\hat{u}}(t) \\ \underline{\hat{Y}} = C.\underline{\hat{X}}(t) + D.\underline{\hat{u}}(t) \end{cases} \quad [3.14]$$

with:

$$\underline{X} = \begin{bmatrix} i'_{ds} & i'_{qs} & \varphi_{dr} & \varphi_{qr} \end{bmatrix}^T : \text{state vector} \quad [3.15]$$

$$\underline{\hat{u}} = \begin{bmatrix} \hat{u}_{ds} \\ \hat{u}_{qs} \end{bmatrix}, \underline{\hat{Y}} = \begin{bmatrix} \hat{i}_{ds} \\ \hat{i}_{qs} \end{bmatrix} : \text{electrical model inputs and outputs} \quad [3.16]$$

$$A = \begin{bmatrix} -\left(L_f^{-1}(R_s.I_2 + R_{eq}) + \omega_s P(\frac{\pi}{2})\right) & L_f^{-1}\left(R_{eq}L_m^{-1} - \omega P(\frac{\pi}{2})\right) \\ R_{eq} & -\left(R_{eq}L_m^{-1} + (\omega_s - \omega)P(\frac{\pi}{2})\right) \end{bmatrix}$$

$$B = \begin{bmatrix} \frac{1}{L_f} & 0 & 0 & 0 \\ 0 & \frac{1}{L_f} & 0 & 0 \end{bmatrix}^T, \quad C = \begin{bmatrix} 1 & 0 & 0 & 0 \\ 0 & 1 & 0 & 0 \end{bmatrix}$$

$$D = \sum_{k=1}^{3} \frac{2\eta_{sc_k}}{3R_s} P(-\theta_s) Q(\theta_{sc_k}) P(\theta_s)$$

$$[R_{eq}] = R_r \cdot \left(I_2 + \frac{\alpha}{1-\alpha} Q(\theta_0)\right)$$

$$I_2 = \begin{bmatrix} 1 & 0 \\ 0 & 1 \end{bmatrix}$$

Thus, we write the vector expression of the parameters to be estimated as:

$$\underline{\theta} = [R_s\ R_r\ L_m\ L_f\ \eta_{sc_1}\ \eta_{sc_2}\ \eta_{sc_3}\ \eta_0\ \theta_0]^T \qquad [3.17]$$

3.4.2. *Parameter estimation with* a priori *information*

Studies by [MOR 99, BAC 02] have shown that adding *a priori* information to an output error using a composite criterion makes it possible to introduce an initial knowledge relating to the healthy machine, and thus to accelerate and strengthen the convergence of the nonlinear programming algorithm.

Knowledge of healthy functioning is the result of one (or many) preliminary estimation(s) allowing us to obtain nominal values of vector $\underline{\theta}$, or the output noise variance σ_b, as well the covariance matrix of estimation $Var\{\theta_{opt}\}$. These values are actually essential for constructing the different weighting factors of the composite criterion $(\theta_0, \sigma_b, M_0)$. To do so, an estimation of the electrical parameters belonging to the healthy induction mean value, with no *a priori* information, enables us to obtain this vital information.

For this, we propose generating *a priori* information by using the mean of 10 indirect identification estimations (all corresponding to the machine's healthy operation), in order to determine the different weighting factors of the composite criterion:

$$J_C = (\underline{\hat{\theta}} - \underline{\theta_0})^T M_0^{-1} (\underline{\hat{\theta}} - \underline{\theta_0}) + \frac{1}{\sigma_b^2} \sum_{k=1}^{K} (\varepsilon_{d_{s_k}}^2 + \varepsilon_{q_{s_k}}^2) \qquad [3.18]$$

with:

$$\underline{\theta}_0 = \begin{bmatrix} R_{s_0} \\ R_{r_0} \\ L_{m_0} \\ L_{f_0} \end{bmatrix} = \begin{bmatrix} 9.7921 \\ 5.3079 \\ 5.0456\,10^{-01} \\ 4.0625\,10^{-02} \end{bmatrix} \quad [3.19]$$

$$M_0 = \begin{bmatrix} \sigma^2_{R_s} & 0 & 0 & 0 \\ 0 & \sigma^2_{R_r} & 0 & 0 \\ 0 & 0 & \sigma^2_{L_m} & 0 \\ 0 & 0 & 0 & \sigma^2_{L_f} \end{bmatrix} \quad [3.20]$$

$$= \begin{bmatrix} 4.587\,10^{-03} & 0 & 0 & 0 \\ 0 & 5.241\,10^{-04} & 0 & 0 \\ 0 & 0 & 1.451\,10^{-04} & 0 \\ 0 & 0 & 0 & 4.588\,10^{-07} \end{bmatrix}$$

$$\widehat{\sigma_b}^2 = \frac{J_{opt}}{K - N} \quad [3.21]$$

K, N, and J_{opt} respectively represent the number of points, parameters, and the value of the criterion at its optimum.

To generate the covariance matrix of parameters M_0, in practice we only retain the diagonal terms.

Relation [3.21] is obtained by hypothesizing that the electronic noise is identical on both Park axes. In the case when the electronic noise is different on both axes, we must calculate the respective variances on both Park axes d and q and weigh both quadratic terms of the composite criterion differently.

3.4.3. *Detection and localization*

The simulations are carried out within the framework of a load torque excitation, only with implicit excitation. Here we are working within noise conditions, such that the noise of currents $\{i_{ds}, i_{qs}\}$ are highly correlated with the ratio $S/B = 20$ in the rotating field. The speed noise is white noise with a ratio of $S/B = 30$.

NOTE.– For more clarity, we will directly replace:

– the short-circuit ratios η_{sc_k} per number of corresponding short-circuiting coils n_{sc_k}. As each phase has 464 coils, the number of coils short-circuiting on the k-th phase is obtained in agreement with the relation:

$$n_{sc_k} = \eta_{sc_k} \cdot n_s = \eta_{sc_k} \cdot 464$$

– the parameter η_0 per number of corresponding broken bars n_{bb}. The total number of rotor bars is equal to 28, and the number of broken bars is obtained in agreement with the relation:

$$n_{bb} = \eta_0 \cdot \frac{n_b}{3} = \eta_0 \cdot \frac{28}{3}$$

In concrete terms, we will firstly proceed with a test on a healthy machine. Figure 3.8 shows the evolution of fault parameters estimated during the indirect identification procedure in the case of a healthy machine.

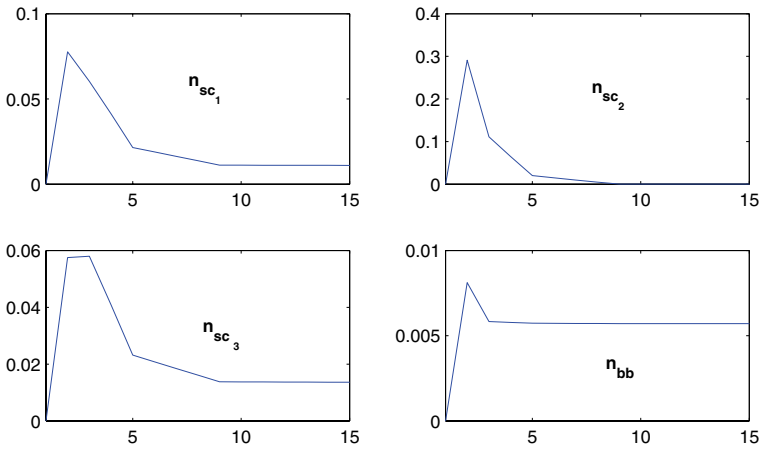

Figure 3.8. *Evolution of fault parameters in a healthy machine through indirect identification*

We verify, according to Figure 3.8, that in the presence of a fault in the induction machine and by using the global fault model as an identification model, the fault parameters present negligible fault rates, therefore demonstrating that there are no faults.

To analyze the model's behavior during the simultaneous stator/rotor faults, we will perform a test on a short-circuit with 29 coils on phase a, 18 coils on phase c, and 2 consecutive broken bars with $\Delta\theta = \frac{2\pi}{28}$.

As an example, it is interesting to present the evolution of the parameters which are estimated during the indirect identification procedure and the direct identification procedure. In fact, the objective is to compare the convergence speed as well as the accuracy of the parameter estimation for both identification types.

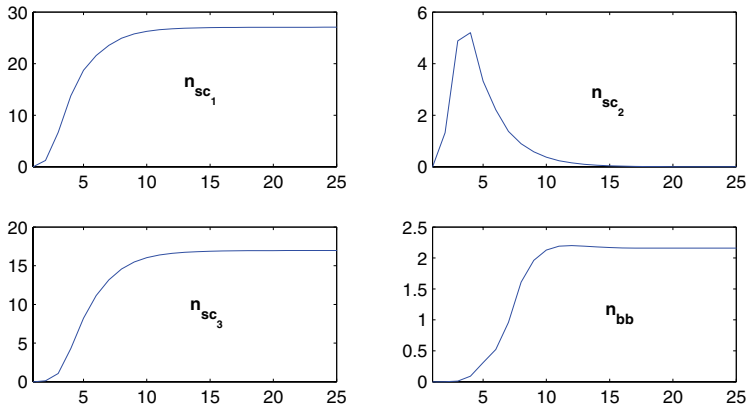

Figure 3.9. *Evolution of parameters for a short-circuit with* 29 *coils on phase a,* 18 *coils on phase c, and* 2 *broken bars through indirect identification*

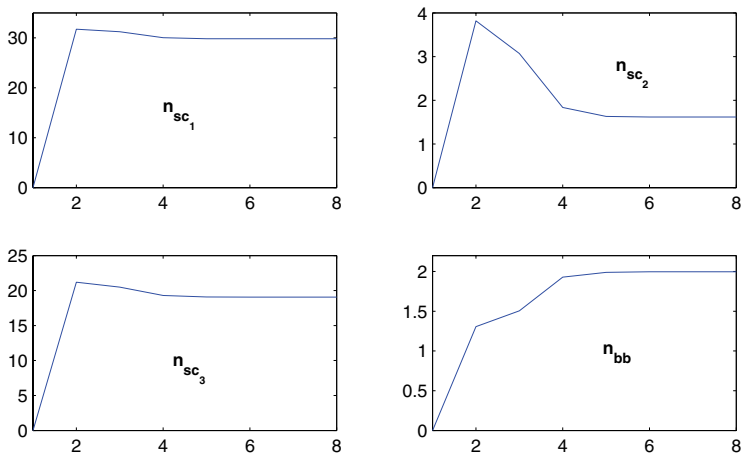

Figure 3.10. *Evolution of parameters for a short-circuit with* 29 *coils on phase a,* 18 *coils on phase c, and* 2 *broken bars through direct identification*

As shown in Figures 3.9 and 3.10, the number of estimated short-circuiting coils and the number of broken bars can explain the fault. In fact, during the identification process, the electrical parameters of the induction machine remain virtually fixed on the optimum value (due to the *a priori* information $\underline{\theta}_0$, weighted by M_0), whereas the

ratios between the short-circuit and the broken bars evolve freely in order to come close to the real fault.

We also notice that direct identification requires fewer iterations for convergence than the indirect approach. However, the estimation of fault parameters through the indirect approach seems much more accurate than via the direct approach.

Figure 3.11 shows the comparison between the simulated and estimated currents (and voltages) in the rotating field reference frame, in the case of a short-circuit of 29 coils on phase a, 18 coils on phase c, and 2 broken bars (corresponding to indirect identification).

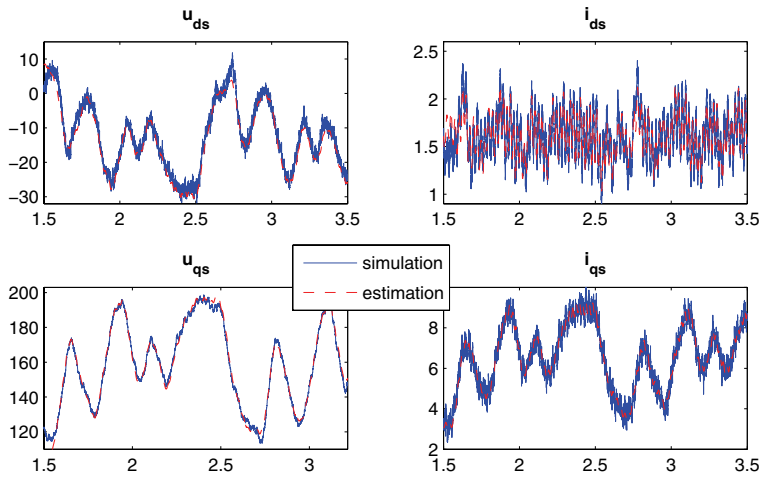

Figure 3.11. *Comparison of simulated and estimated currents (and voltages) for a short-circuit of* 29 *coils on phase a,* 18 *coils on phase c, and* 2 *broken bars*

3.4.4. *Comparison of identification results through direct and indirect approaches*

As seen previously, the strategy for diagnosing the induction machine consists of many parameter estimations of the global fault model. The mean value of the estimations of parameters η_{sc_k} indicates the number of short-circuiting coils on each of the three phases, and parameter η_0 allows us to obtain the number of broken rotor bars, in agreement with:

– the number of faulty coils on the k-th phase: $\hat{n}_{sc_k} = \eta_{sc_k} \cdot n_s$;

– the number of broken rotor bars: $\hat{n}_{bb} = \frac{\hat{\eta}_0 n_b}{3}$.

The diagnosis procedures using the direct and indirect approaches have been applied to the case of a short-circuit with 29 coils on phase a, 18 coils on phase c, and two consecutive broken bars with $\Delta\theta = \frac{2\pi}{28}$.

Table 3.2 summarizes the results of the parameter estimations for the set of simulations. The obtained results show the match between the fault's estimated parameters and the real parameters (a maximum error of 3 coils for indirect identification on faulty phases and more than 5 coils for direct identification).

$\hat{\theta}$	DI	$IIRC$	$IIOC3$
$\hat{R}_s$	$9.8895\,10^{+00}$ $\pm 6.4223\,10^{-02}$	$9.7927\,10^{+00}$ $\pm 1.8141\,10^{-03}$	$9.7930\,10^{+00}$ $\pm 2.5298\,10^{-03}$
$\hat{R}_r$	$5.3102\,10^{+00}$ $\pm 1.9567\,10^{-03}$	$5.3079\,10^{+00}$ $\pm 9.9975\,10^{-05}$	$5.3080\,10^{+00}$ $\pm 1.6172\,10^{-04}$
$\hat{L}_m$	$4.9116\,10^{-01}$ $\pm 1.2460\,10^{-03}$	$4.8377\,10^{-01}$ $\pm 6.0462\,10^{-05}$	$4.8377\,10^{-01}$ $\pm 9.3287\,10^{-05}$
$\hat{L}_f$	$3.8601\,10^{-02}$ $\pm 1.7313\,10^{-04}$	$4.0629\,10^{-02}$ $\pm 2.3874\,10^{-05}$	$4.0634\,10^{-02}$ $\pm 1.5670\,10^{-05}$
$\hat{n}_{sc_1}$	$2.9854\,10^{+01}$ $\pm 2.9300\,10^{+00}$	$2.8626\,10^{+01}$ $\pm 2.1003\,10^{+00}$	$2.8248\,10^{+01}$ $\pm 2.2901\,10^{+00}$
$\hat{n}_{sc_2}$	$4.9395\,10^{-01}$ $\pm 8.5083\,10^{-01}$	$1.2838\,10^{-01}$ $\pm 2.3694\,10^{-01}$	$1.2619\,10^{-01}$ $\pm 1.6647\,10^{-01}$
$\hat{n}_{sc_3}$	$1.9054\,10^{+01}$ $\pm 1.9662\,10^{+00}$	$1.8267\,10^{+01}$ $\pm 5.7173\,10^{-01}$	$1.8001\,10^{+01}$ $\pm 9.5223\,10^{-01}$
$\hat{n}_{bb}$	$2.1043\,10^{+00}$ $\pm 1.9851\,10^{-01}$	$2.0459\,10^{+00}$ $\pm 3.3049\,10^{-01}$	$2.0504\,10^{+00}$ $\pm 2.3863\,10^{-01}$

Table 3.2. *Results from parameter estimation (simultaneous faults)*

We may also notice that the machine's electrical parameters are not affected by the different faults introduced in the machine. Only the fault parameters vary according to the cause of the imbalance.

In conclusion, the parametric identification algorithm with *a priori* information is strong when confronted with simultaneous rotor/stator faults. We may also note here that the parameter estimation using the indirect approach gives good results in the simulation, offering a very realistic image of the imbalance found in the machine.

A projection of the estimation of the number of short-circuiting coils and the number of broken bars shown in Figure 3.12 allows us to visualize a good relationship between

the estimated values and the real values. Moreover, we note better estimations and lower scattering in the results for indirect identification.

We may note that with this approach, estimating faults is better centered than with the direct approach. Furthermore, the estimation variance is lower. The advantage of this lower variance is clear when there is no fault, whereas the direct approach leaves doubts for n_{sc_2} (Figure 3.12).

As the indirect approach estimations give a negligible dispersion around zero, we may deduce that this approach makes it possible to reduce the rate of false alarms.

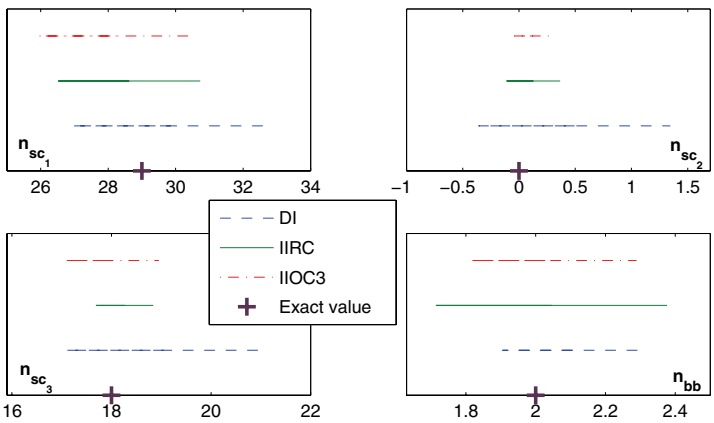

Figure 3.12. *Results from parameter estimation (simultaneous results)*

3.5. Conclusion

We have given the fundamental objective of improving induction machine diagnosis through parameter estimation. To do so, we defined two areas of research: one concerning an acceptable mode of excitation by the user, making use of disturbances induced by load torque variations, and the other which is dedicated to induction machine identification by a methodology explicitly taking into account the closed-loop control algorithm. Thus, we proposed a closed-loop identification methodology for the induction machine based on the indirect approach.

We usually choose the reference frame related to the induction machine rotor for direct identification, because this requires fewer transforms/estimations. As we wish to proceed on to an indirect identification which takes the controllers into account, we must work within the rotating field reference frame. In fact, the control and controllers

were designed in the rotating field frame in order to control the flux and torque. It is therefore fundamentally important to refer to the rotating field. Unfortunately, we do not know the position of this rotating field, and it must therefore be estimated. The comparative study in a numerical situation has shown that the asymptotic bias on the electrical parameter estimation is practically non-existent for the indirect approach, whereas for the direct approach it clearly depends on the nature and the variance of the noises in the currents. In addition, we verified that the excitation via load torque has proven to be satisfactory and sufficient, guaranteeing a better level of accuracy with the indirect approach.

However, the main constraint caused by indirect identification is the essential knowledge of the controller. The problem for industrial control is that there is no real installed regulator which perfectly corresponds to its theoretical expression. Also, we propose to extend the scope of this methodology by performing a preliminary identification of an "equivalent" controller, using an over-parameterization technique to avoid *a priori* knowledge of the structure and parameters of the said controller [BAZ 08b].

The application of our methodology to the induction machine diagnosis using parameter estimation is the essential answer to our initial question. This fault detection methodology is based on the definition of fault models [BAC 03a] We therefore used a global model in simultaneous stator/rotor fault situation, allowing us to explain a short-circuit on several stator phases. It also takes the bar break-type rotor imbalance into account, for generalized monitoring of the squirrel-cage induction machine. Moreover, comparative studies carried out via numerical simulation have shown that the indirect approach enables improved fault detection by making it possible to reject the assumption of fault occurrence in healthy operation. This is due to the single excitation created by variations in the load torque. It must, however, be noted that there is a clear increase in algorithm convergence time in the indirect approach. A solution to this practical problem would be to use the direct approach to initialize an indirect approach.

3.6. Bibliography

[BAC 01] Bachir S., Tnani S., Trigeassou J.-C., Champenois G., "Diagnosis by parameter estimation of stator and rotor faults occuring in induction machines", *EPE'01*, Graz, August 2001.

[BAC 02] Bachir S., Contribution au diagnostic de la machine asynchrone par estimation paramétrique, PhD Thesis, University of Poitiers, 2002.

[BAC 03a] Bachir S., Tnani S., Champenois G., Trigeassou J.-C., "Diagnostic de la machine asynchrone", in Husson R. (ed.), *Méthodes de commande des machines électriques*, p. 253-276, Hermès, Paris, 2003.

[BAC 03b] Bachir S., Tnani S., Trigeassou J.-C., "online stator faults diagnosis by parameter estimation", *EPE'03*, *European Conference on Power Electronics and Applications*, p. 209-219, Toulouse, 2003.

[BAC 06] Bachir S., Tnani S., Trigeassou J.-C., Champenois G., "Diagnosis by parameter estimation of stator and rotor faults occurring in induction machines", *IEEE Transactions on Industrial Electronics*, vol. 53, June 2006.

[BAC 08] Bachir S., Bazine I.B.A., Poinot T., Jelassi K., Trigeassou J.-C., "Estimation paramétrique pour le diagnostic des processus : application à la bobine à noyau de fer", *Journal Européen des Systèmes Automatisés (JESA)*, vol. 42, 2008.

[BAZ 05] Bazine I.B.A., Bazine S., Jelassi K., Trigeassou J.-C., Poinot T., "Identification of stator fault parameters in induction machine using the output-error technique", *The Second International Conference on Artificial and Computational Intelligence for Decision*, *Control and Automation (ACIDCA)*, Tunisia, 2005.

[BAZ 07] Bazine I.B.A., Trigeassou J.-C., Jelassi K., Poinot T., "Closed-loop identification of DC motor using the output-error technique", *Fourth International Multi-Conference on Systems*, *Signals and Devices SSD-07*, Tunisia, March 2007.

[BAZ 08a] Bazine I.B.A., Trigeassou J.-C., Jelassi K., Poinot T., "Identification de la machine asynchrone en boucle fermée par approche indirecte", *Conférence Internationale Francophone d'Automatique (CIFA)*, Bucharest, September 2008.

[BAZ 08b] Bazine I.B.A., Identification en boucle fermée de la machine asynchrone: application à la détection de défaut, PhD Thesis, University of Poitiers and University of Tunis El Manar, 2008.

[BAZ 08c] Bazine I.B.A., Trigeassou J.-C., Jelassi K., Poinot T., "Identification de la machine asynchrone par une méthode OE basée sur une décomposition de la boucle fermée", *International Conference JTEA*, Tunisia, May 2008.

[DON 00] Donkelaar E.V., Hof P.V.D., "Analysis of closed-loop identification with a tailor-made parametrization", *European Journal of Control*, no. 6, p. 54-62, 2000.

[FAI 95] Faidallah A., Contribution à l'identification et à la commande vectorielle des machines asynchrones, PhD Thesis, University of Lorraine, 1995.

[FIL 94] Fillippitti F., Franceshini G., Tassoni C., Vas P., "Broken bar detection in induction machine: comparison between current spectrum approach and parameter estimation approach", *IEEE-IAS Annual Meeting*, p. 94-102, New York, 1994.

[FOR 99] Forssel U., Ljung L., "Closed loop identification revisited", *Automatica*, vol. 10, p. 149-155, 1999.

[GRO 99] Grospeaud O., Poinot T., Trigeassou J.-C., "Unbiased identification in closed-loop by an output error technique", *European Control Conference*, Germany, 1999.

[GRO 00a] Grospeaud O., Contribution à l'identification en boucle fermée par erreur de sortie, PhD Thesis, University of Poitiers, 2000.

[GRO 00b] Grospeaud O., Trigeassou J.-C., Maamri N., "Unbiased identification of a nonlinear continuous system in closed-loop", *International Conference on Methods and Models in Automation and Robotics*, 2000.

[HOF 95] HOF P.V.D., SCHRAMA R., "Identification and control-closed loop issues", *Automatica*, vol. 31, p. 1751-1770, 1995.

[JEL 91] JELASSI K., Positionnement d'une machine asynchrone par la méthode de flux orienté, PhD Thesis, University of Toulouse, 1991.

[LAN 97] LANDAU I.-D., KARIMI A., "Recursive algorithms for identification in closed loop: a unified approach and evaluation", *Automatica*, vol. 33, p. 1499-1523, 1997.

[LJU 87] LJUNG L., *System Identification: Theory for the User*, Prentice Hall, USA, 1987.

[LOR 93] LORON L., "Application of the extended Kalman filter to parameter estimation of induction motors", *EPE'93*, vol. 5, p. 85-90, Brighton, 1993.

[MOR 99] MOREAU S., Contribution à la modélisation et à l'estimation paramétrique des machines électriques à courant alternatif: application au diagnostic, PhD Thesis, University of Poitiers, 1999.

[SÖD 87] SÖDERSTRÖM T., STOICA P., TRULSSON E., "Instrumental variable methods for closed-loop systems", *10th IFAC World Congress*, Germany, p. 363-368, 1987.

[TRI 03] TRIGEASSOU J.-C., POINOT T., BACHIR S., "Estimation paramétrique pour la connaissance et le diagnostic des machines électriques", in HUSSON R. (ed.), *Méthodes de commande des machines électriques*, p. 215-251, Hermès, Paris, 2003.

Chapter 4

Induction Machine Diagnosis Using Observers

4.1. Introduction

Electrical machine diagnosis may either use methods with no *a priori* information, based on frequency or statistical analysis for instance, or on system modeling-based methods (internal method). In each case, the aim is to determine a signature (a pattern vector), enabling us to discriminate one or several faults according to the other operating modes.

In this last example of model-based methods, the diagnosis is carried out either using a residual analysis, obtained between the real process and the device model (Figure 4.1a), or from the evolution of the model's parameters, which are identified online (Figure 4.1b).

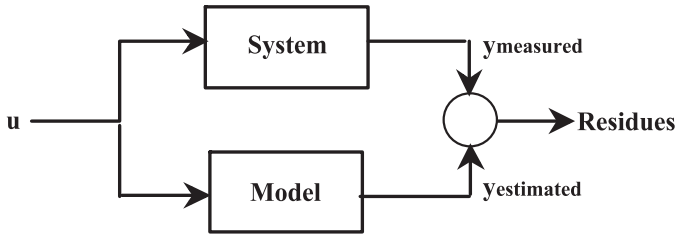

Figure 4.1a. *Residual generation-based diagnosis*

Chapter written by Guy CLERC and Jean-Claude MARQUES.

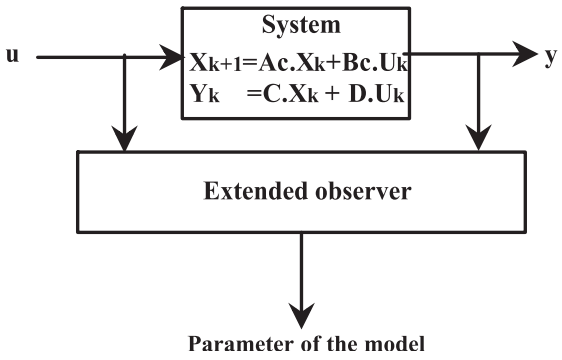

Figure 4.1b. *Extended observer-based diagnosis*

In the hypothesis where the diagnosis relies on monitoring the parameters of an induction machine model, there are two possible cases:

– case 1: the diagnosis is developed using the parameters of a healthy model of the machine. A parameter drift results in the occurrence of a fault. However, the model no longer represents the machine's real behavior. It is used as a signature;

– case 2: the machine model may represent the machine's behavior in its fault regimes. It allows for a physical representation of the system in its different operating regimes. It also allows for a better localization of the fault, and possibly of its description. However, it is more complex.

Parametric monitoring can be carried out in online mode, either by an identification algorithm (recursive least squares), or by using an extended observer.

In the case of a linear model, the machine is modeled by state space equation in the following form:

$$\frac{dX}{dt} = AX + BU$$
$$Y = CX \qquad [4.1]$$

where X denotes a state vector representing the components related to the energies stored in the machine (current, flux), A represents the state matrix, and B the input matrix.

In the latter case, the system (augmented by the observed parameters) must remain observable.

A new augmented system is created by introducing the parameters θ into the state vector, whose evolution enables us to characterize the faults:

$$X_{extended} = \begin{pmatrix} X \\ \theta \end{pmatrix}$$

The observer allows us to reconstruct this state space vector using the data from the system's inputs and outputs. This observer is called the *extended observer*.

Compared to classic signal processing methods, this method has the advantage of being usable in transient regime and with variable power feeds (inverters). The table below summarizes the advantages and disadvantages of this method.

	Advantages	**Disadvantages**
Parameter identification	- consideration of more complex methods able to show faulty behavior, - can be used in variable speed drives with a converter, - many suitable algorithms for this application.	- used in offline mode.
Parameter observation	- can be used in online mode, - can be integrated in controls where the state must be reconstructed (return to state), - can be used in variable speed drives with a converter.	- requires simple models, - requires slow varying parameters.

Table 4.1. *Comparison between observer and identification-based methods*

As we can see in the table above, an identification algorithm uses models which may be complex and which represent the real phenomena involved. Their main objective is to monitor the parameters. An extended observer estimates the state vector and a limited number of parameters. The model below remains limited.

This chapter will present diagnosis methods based on observers which are built on models of electrical machines with or without a fault.

In section 4.2, we will succinctly present the models on which the observer-based diagnosis techniques are centered.

The third section will explore the different types of observers used, namely the Luenberger, Kalman, and high-gain observers.

We will then proceed to demonstrate how these observers are used to monitor parameters by describing the modeling linearization technique and the construction of extended models. Finally, section 4.4 will illustrate application examples.

All these techniques will be applied to induction machines but can be transferred to synchronous [KEY 86] or Direct Current machines.

4.2. Model presentation

Observer-based induction machine diagnosis is based on modeling the machine either with or without a fault. We will develop models of three-phase or two-phase induction machine models and the signatures allowing us to discriminate faults in each case.

4.2.1. *Three-phase model of induction machine without fault*

4.2.1.1. *Model description*

The machine is modeled according to the following hypotheses:

– the saturation is ignored. As a result, we see that the self-inductance and mutual inductances are independent of the currents flowing in the different windings;

– the MMFs (magnetomotive forces) are distributed sinusoidally in the machine's air-gap. We can see symmetry in relation to the magnetic axes in the windings;

– the slots are presumed to be non-existent;

– we do not consider the hysteresis and Foucault currents in the magnetic components.

The generalized Ohm's law gives the following electrical equations:

– on the stator:

$$\begin{bmatrix} v_{as} \\ v_{bs} \\ v_{cs} \end{bmatrix} = R_s \begin{bmatrix} i_{as} \\ i_{bs} \\ i_{cs} \end{bmatrix} + \frac{d}{dt} \begin{bmatrix} \psi_{as} \\ \psi_{bs} \\ \psi_{cs} \end{bmatrix} \qquad [4.2]$$

– on the rotor:

$$\begin{bmatrix} v_{ar} \\ v_{br} \\ v_{cr} \end{bmatrix} = R_r \begin{bmatrix} i_{ar} \\ i_{br} \\ i_{cr} \end{bmatrix} + \frac{d}{dt} \begin{bmatrix} \psi_{ar} \\ \psi_{br} \\ \psi_{cr} \end{bmatrix} \quad [4.3]$$

The magnetic equations give:

$$\begin{bmatrix} \Psi_{as} \\ \Psi_{bs} \\ \Psi_{cs} \end{bmatrix} = L_{ss} \begin{bmatrix} i_{as} \\ i_{bs} \\ i_{cs} \end{bmatrix} + L_{sr} \begin{bmatrix} i_{ar} \\ i_{br} \\ i_{cr} \end{bmatrix} \quad [4.4]$$

$$\begin{bmatrix} \Psi_{ar} \\ \Psi_{br} \\ \Psi_{cr} \end{bmatrix} = L_{rr} \begin{bmatrix} i_{ar} \\ i_{br} \\ i_{cr} \end{bmatrix} + L_{rs} \begin{bmatrix} i_{as} \\ i_{bs} \\ i_{cs} \end{bmatrix} \quad [4.5]$$

with:

$$L_{ss} = \begin{bmatrix} L_{as} & M_{as} & M_{as} \\ M_{as} & L_{as} & M_{as} \\ M_{as} & M_{as} & L_{as} \end{bmatrix}$$

$$L_{rr} = \begin{bmatrix} L_{ar} & M_{ar} & M_{ar} \\ M_{ar} & L_{ar} & M_{ar} \\ M_{ar} & M_{ar} & L_{ar} \end{bmatrix}$$

$$L_{sr} = \begin{bmatrix} M_{rs}\cos(\theta_r) & M_{rs}\cos\left(\theta_r + \frac{2\pi}{3}\right) & M_{rs}\cos\left(\theta_r - \frac{2\pi}{3}\right) \\ M_{rs}\cos\left(\theta_r - \frac{2\pi}{3}\right) & M_{rs}\cos(\theta_r) & M_{rs}\cos\left(\theta_r + \frac{2\pi}{3}\right) \\ \cos\left(\theta_r + \frac{2\pi}{3}\right) & M_{rs}\cos\left(\theta_r - \frac{2\pi}{3}\right) & M_{rs}\cos(\theta_r) \end{bmatrix}$$

These equations can then be re-written in the following form:

$$[V] = ([R] + [G]\omega_r)[I] + [L]\frac{d[I]}{dt} \quad [4.6]$$

with:

$$[V]^t = [v_{as} \quad v_{bs} \quad v_{cs} \quad 0 \quad 0 \quad 0] \text{ the input vector}$$

$$[I]^t = [i_{as} \quad i_{bs} \quad i_{cs} \quad i_{ar} \quad i_{br} \quad i_{cr}] \text{ the state vector}$$

$$[R] = \begin{bmatrix} R_{s_a} & 0 & 0 & 0 & 0 & 0 \\ 0 & R_{s_b} & 0 & 0 & 0 & 0 \\ 0 & 0 & R_{s_c} & 0 & 0 & 0 \\ 0 & 0 & 0 & R_{r_a} & 0 & 0 \\ 0 & 0 & 0 & 0 & R_{r_b} & 0 \\ 0 & 0 & 0 & 0 & 0 & R_{r_c} \end{bmatrix}$$

$$[L] = \begin{bmatrix} L_{as} + L_{fas} & M'_{asbs} & M''_{ascs} & M_{asar} & M'_{as\,br} & M''_{ascr} \\ M''_{bsas} & L_{bs} + L_{fbs} & M'_{bscs} & M''_{bsar} & M_{bsbr} & M'_{bscr} \\ M'_{ascs} & M''_{csbs} & L_{cs} + L_{fcs} & M'_{csar} & M''_{csbr} & M_{csc\,r} \\ M_{aras} & M'_{arbs} & M''_{arcs} & L_{ar} + L_{far} & M'_{arbr} & M''_{arbr} \\ M''_{bras} & M_{brbs} & M'_{brcs} & M''_{brar} & L_{br} + L_{fbr} & M'_{brcr} \\ M'_{cras} & M''_{crbs} & M_{crcs} & M'_{brar} & M''_{crbr} & L_{rcr} + L_{fcr} \end{bmatrix}$$

$$[G] = -L_m \cdot p. \begin{bmatrix} 0 & 0 & 0 & \sin(p.\theta) & \sin\left(p.\theta + \frac{2\pi}{3}\right) & \sin\left(p.\theta + \frac{4\pi}{3}\right) \\ 0 & 0 & 0 & \sin\left(p.\theta + \frac{4\pi}{3}\right) & \sin(p.\theta) & \sin\left(p.\theta + \frac{2\pi}{3}\right) \\ 0 & 0 & 0 & \sin\left(p.\theta + \frac{2\pi}{3}\right) & \sin\left(p.\theta + \frac{4\pi}{3}\right) & \sin(p.\theta) \\ \sin(p.\theta) & \sin\left(p.\theta + \frac{4\pi}{3}\right) & \sin\left(p.\theta + \frac{2\pi}{3}\right) & 0 & 0 & 0 \\ \sin\left(p.\theta + \frac{2\pi}{3}\right) & \sin(p.\theta) & \sin\left(p.\theta + \frac{4\pi}{3}\right) & 0 & 0 & 0 \\ \sin\left(p.\theta + \frac{4\pi}{3}\right) & \sin\left(p.\theta + \frac{2\pi}{3}\right) & \sin(p.\theta) & 0 & 0 & 0 \end{bmatrix}$$

In a balanced motor: $R_s = R_{s_a} = R_{s_b} = R_{s_c}$ and $R_r = R_{r_a} = R_{r_b} = R_{r_c}$, and the inductance matrix [L] become:

$$[L]=\begin{bmatrix} L_s+L_{fs} & -\frac{L_s}{2} & -\frac{L_s}{2} & L_m.\cos(p.\theta) & L_m.\cos\left(p.\theta+\frac{2\pi}{3}\right) & L_m.\cos\left(p.\theta+\frac{4\pi}{3}\right) \\ -\frac{L_s}{2} & L_s+L_{fs} & -\frac{L_s}{2} & L_m.\cos\left(p.\theta+\frac{4\pi}{3}\right) & L_m.\cos(p.\theta) & L_m.\cos\left(p.\theta+\frac{2\pi}{3}\right) \\ -\frac{L_s}{2} & -\frac{L_s}{2} & L_s+L_{fs} & L_m.\cos\left(p.\theta+\frac{2\pi}{3}\right) & L_m.\cos\left(p.\theta+\frac{4\pi}{3}\right) & L_m.\cos(p.\theta) \\ L_m.\cos(p.\theta) & L_m.\cos\left(p.\theta+\frac{4\pi}{3}\right) & L_m.\cos\left(p.\theta+\frac{2\pi}{3}\right) & L_r+L_{fr} & -\frac{L_r}{2} & -\frac{L_r}{2} \\ L_m.\cos\left(p.\theta+\frac{2\pi}{3}\right) & L_m.\cos(p.\theta) & L_m.\cos\left(p.\theta+\frac{4\pi}{3}\right) & -\frac{L_r}{2} & L_r+L_{fr} & -\frac{L_r}{2} \\ L_m.\cos\left(p.\theta+\frac{4\pi}{3}\right) & L_m.\cos\left(p.\theta+\frac{2\pi}{3}\right) & L_m.\cos(p.\theta) & -\frac{L_r}{2} & -\frac{L_r}{2} & L_r+L_{fr} \end{bmatrix}$$

θ is the mechanical angle between the stator and rotor, and p is the number of pole pairs. These equations can be simplified into a single non-linear state equation [BOU 01]:

$$\dot{[I]}=[L]^{-1}\left([V]-\left([R]+[G]\omega\right)[I]\right) \qquad [4.7]$$

Matrix L is non-singular and its determinant is independent of θ.

4.2.1.2. *Fault discrimination*

Monitoring three stator or rotor resistances will enable us to distinguish the healthy operation of a short-circuit or bar break. In fact, a natural evolution due to over-heating, for instance, results in a simultaneous growth in the three stator or rotor resistances.

Thus, a rotor fault caused by broken bars will lead to a trajectory where the three phase resistances are not identical [BOU 01] (Figure 4.2).

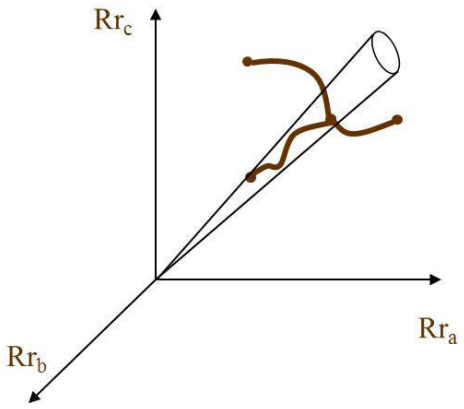

Figure 4.2. *Discrimination of rotor faults*

For a stator fault, [MOR 99] proposes the given in Table 4.2 strategy

Fault phase A		**Fault phase B**		**Fault phase C**	
R_{sa}, L_{fsa}	↘	R_{sb}, L_{fsb}	↘	R_{sc}, L_{fsc}	↘
R_{sb}, R_{sc}	↗	R_{sa}, R_{sc}	↗	R_{sb}, R_{sa}	↗
L_{fsb}, L_{fsc}	↗	L_{fsa}, L_{fsc}	↗	L_{fsb}, L_{fsa}	↗

Table 4.2. *Discriminating stator faults*

4.2.2. *Park's model of an induction machine without fault*

4.2.2.1. *Model description*

The previous equations can be projected into an orthonormal reference frame dq0 (0 denotes the machine's axis of rotation) [VAS 92, GRE 00].

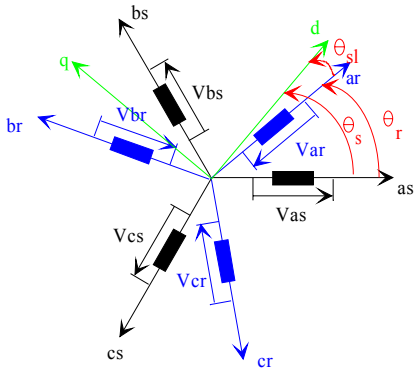

Figure 4.3. *Representation of reference frame dq*

The reference frame dq0 may be:

– connected to the stator $\frac{d\theta_s}{dt} = 0$ *and* $\frac{d\theta_{sl}}{dt} = -\omega_m$;

– the rotor $\frac{d\theta_s}{dt} = \omega_m$ *and* $\frac{d\theta_{sl}}{dt} = 0$;

– or the rotating field $\frac{d\theta_s}{dt} = \omega_e$ *and* $\frac{d\theta_{sl}}{dt} = \omega_e - \omega_m$; .

The first case is preferably reserved for synthesizing observers because the reference frame dq is naturally connected to the reference frame where the measurable components are projected. The last case is usually reserved for field-oriented induction machine controls.

The following transform will enable us to change the reference frame:

$$T_{dq0/abc} = \sqrt{\frac{2}{3}} \begin{bmatrix} \cos\theta_x & \cos(\theta_x - \frac{2\pi}{3}) & \cos(\theta_x + \frac{2\pi}{3}) \\ -\sin\theta_x & -\sin(\theta_x - \frac{2\pi}{3}) & -\sin(\theta_x + \frac{2\pi}{3}) \\ \frac{1}{\sqrt{2}} & \frac{1}{\sqrt{2}} & \frac{1}{\sqrt{2}} \end{bmatrix} \quad [4.8]$$

with θ_x as the angle between the reference frame dq and the stator (x = s) or the rotor (x = sl) depending on the case in question.

We therefore obtain the magnetic equations which no longer involve the angle of rotation:

$$\begin{bmatrix} \Psi_{ds} \\ \Psi_{dr} \end{bmatrix} = \begin{bmatrix} L_s & L_m \\ L_m & L_r \end{bmatrix} \begin{bmatrix} i_{ds} \\ i_{dr} \end{bmatrix} \quad [4.9]$$

$$\begin{bmatrix} \Psi_{qs} \\ \Psi_{qr} \end{bmatrix} = \begin{bmatrix} L_s & L_m \\ L_m & L_r \end{bmatrix} \begin{bmatrix} i_{qs} \\ i_{qr} \end{bmatrix} \quad [4.10]$$

$$\begin{bmatrix} \Psi_{0s} \\ \Psi_{0r} \end{bmatrix} = \begin{bmatrix} L_{0s} & 0 \\ 0 & L_{0r} \end{bmatrix} \begin{bmatrix} i_{0s} \\ i_{0r} \end{bmatrix} \quad [4.11]$$

and the following electrical equations:

$$\begin{bmatrix} v_{ds} \\ v_{qs} \end{bmatrix} = \begin{bmatrix} R_s & 0 \\ 0 & R_s \end{bmatrix} \begin{bmatrix} i_{ds} \\ i_{qs} \end{bmatrix} + \frac{d}{dt} \begin{bmatrix} \Psi_{ds} \\ \Psi_{qs} \end{bmatrix} + \begin{bmatrix} 0 & -\omega_s \\ \omega_s & 0 \end{bmatrix} \begin{bmatrix} \Psi_{ds} \\ \Psi_{qs} \end{bmatrix} \quad [4.12]$$

$$\begin{bmatrix} v_{dr} \\ v_{qr} \end{bmatrix} = \begin{bmatrix} R_r & 0 \\ 0 & R_r \end{bmatrix} \begin{bmatrix} i_{dr} \\ i_{qr} \end{bmatrix} + \frac{d}{dt} \begin{bmatrix} \Psi_{dr} \\ \Psi_{qr} \end{bmatrix} + \begin{bmatrix} 0 & -\omega_{sl} \\ \omega_{sl} & 0 \end{bmatrix} \begin{bmatrix} \Psi_{dr} \\ \Psi_{qr} \end{bmatrix} \quad [4.13]$$

$$\begin{bmatrix} v_{0s} \\ v_{0r} \end{bmatrix} = \begin{bmatrix} R_s & 0 \\ 0 & R_r \end{bmatrix} \begin{bmatrix} i_{0s} \\ i_{0r} \end{bmatrix} + \frac{d}{dt} \begin{bmatrix} \Psi_{0s} \\ \Psi_{0r} \end{bmatrix} \quad [4.14]$$

The electromagnetic torque then becomes:

$$C_e = \Psi_{ds} i_{qs} - \Psi_{qs} i_{ds} \quad [4.15]$$

The previous equations can be re-written in order to show the system in the state space model form. For example, in a reference frame linked to the rotating field:

$$X = \begin{bmatrix} i_{ds} \\ i_{qs} \\ \Psi_{dr} \\ \Psi_{qr} \end{bmatrix}, \; U = \begin{bmatrix} v_{ds} \\ v_{qs} \end{bmatrix}, \; \frac{dX}{dt} = AX + BU \quad [4.16]$$

with:

$$A = \begin{bmatrix} -\left(\frac{1}{T_s\sigma} + \frac{1}{T_r}\frac{1-\sigma}{\sigma}\right) & \omega_e & \frac{1-\sigma}{\sigma}\frac{1}{L_m T_r} & \frac{1-\sigma}{\sigma}\frac{1}{L_m}\omega_m \\ -\omega_e & -\left(\frac{1}{T_s\sigma} + \frac{1}{T_r}\frac{1-\sigma}{\sigma}\right) & -\frac{1-\sigma}{\sigma}\frac{1}{L_m}\omega_m & \frac{1-\sigma}{\sigma}\frac{1}{L_m T_r} \\ \frac{L_m}{T_r} & 0 & -\frac{1}{T_r} & \omega_{sl} \\ 0 & \frac{L_m}{T_r} & -\omega_{sl} & -\frac{1}{T_r} \end{bmatrix}$$

$$B = \begin{bmatrix} \frac{1}{\sigma L_s} & 0 \\ 0 & \frac{1}{\sigma L_s} \\ 0 & 0 \\ 0 & 0 \end{bmatrix}$$

$$C_e = \frac{pL_m}{L_r}\left(\Psi_{dr} i_{qs} - \Psi_{qr} i_{ds}\right)$$

The state space model can also be written according to the stator resistances R_s and rotor resistances R_r, the stator inductance L_s, and the leakage inductance N, in other words: a 4-parameter model:

$$\frac{dX}{dt} = AX + BU$$

$$A = \begin{bmatrix} -\frac{1}{L_f}\left(\frac{L_f + L_s}{L_s}.R_s + \frac{L_s}{L_f + L_s}R\right) & \omega_s & +\frac{1}{L_f}\frac{R}{L_s + L_f} & \frac{1}{L_f}(\omega_s - \omega_{sl}) \\ -\omega_s & -\frac{1}{L_f}\left(\frac{L_f + L_s}{L_s}.R_s + \frac{L_s}{L_f + L_s}R\right) & -\frac{1}{L_f}(\omega_s - \omega_{sl}) & +\frac{1}{L_f}\frac{R}{L_s + L_f} \\ R.\frac{L_s}{L_s + L_f} & 0 & -\frac{R}{L_s + L_f} & \omega_{sl} \\ 0 & R.\frac{L_s}{L_s + L_f} & -\omega_{sl} & -\frac{R}{L_s + L_f} \end{bmatrix}$$

$$B = \begin{bmatrix} \frac{L_f + L_s}{L_f.L_s} & 0 \\ 0 & \frac{L_f + L_s}{L_f.L_s} \\ 0 & 0 \\ 0 & 0 \end{bmatrix} \qquad [4.17]$$

With the input vector $U = \begin{bmatrix} u_{ds} \\ u_{qs} \end{bmatrix}$ and the state space vector $X = \begin{bmatrix} i_{ds} \\ i_{qs} \\ \psi_{dr} \\ \psi_{qr} \end{bmatrix}$

These state space equations will be used as a basis for synthesizing the observers in the reference frame dq0.

4.2.2.2. *Fault discrimination*

The evolution of the parameters in the induction machine generalized model will enable us to discriminate stator and rotor faults [MOR 99, BOU 01]:

– when rotor bars break, the estimated values for the rotor resistance increase, but the values for the stator resistance and the stator and rotor leakage inductances in fact decrease;

– during a short-circuit between the stator winder coils, the estimated value for the stator resistance increases and the value for the other parameters decreases.

	R_s	R_r	L_r	L_f
Break in rotor bars	↘	↗	↘	↘
Stator short-circuit	↗	↘	↘	↘

Table 4.3. *Parameter evolution according to faults*

However, let us note that by minimizing the error criterion, the observation algorithm corrects the estimated values without showing a physical evolution in the system. But, observing these parameters will enable to us to discriminate the faults.

Discriminating the healthy state in relation to a faulty state on the one hand, and different faults on the other hand, therefore requires that we monitor at least one pair of parameters.

In fact, over-heating may cause the resistances to increase, without actually being characterized as a fault.

4.2.3. *Induction machine models with fault*

These models allow us to represent machines with a fault, and to therefore quantify this fault. However, they are specific to a given fault and more complex than the previously presented models. Many models have been explored in literature on this subject, and we can cite Schaeffer [SCH 99a, SCH 99b] or Bachir [BAC 02, BAC 05, BAC 06], for example. These models, already described in Chapter 2 of this book, make it possible to represent inter-coil short-circuits. They have primarily been used with an identification algorithm, but could be used with an observer.

4.3. Observers

4.3.1. *Principle*

An observer is a mathematical tool which can restore the internal states of a system using inputs and measured outputs [BOR 90]. It acts as a sort of “virtual sensor” or “software sensor”. Within this diagnosis framework, it is used to restore the electromagnetic components which are sensitive to known faults (electromagnetic torque, for instance, [THO 93, CAS 03], or model parameters which can change in the presence of a fault).

A system's ability to be observed is known as its *observability*. By definition, a discrete-time linear time invariant (LTI) system is observable if and only if we can reconfigure the initial state of the state space vector $X(k_0T_e)$ using the observation of its input and output over a finite number of sampling periods.

In the continuous case, the state space representation of the time-invariant linear model of the system is given by equation [4.1]. Observability is a concept linked to the notion of output sensitivity to the system's state space. In fact, being able to observe a system over a time interval T_{Obs} amounts to being able to reconstruct the whole model state space of this system by only using the information provided, firstly by the sensors which constitutes the model's output, and secondly, by the knowledge of the input. The output is sensitive to the state space, and the system is observable if, with one given input $u(t)$ and two non-specific unequal conditions $x(0) \neq \bar{x}(0)$, the outputs, in relation to these initial conditions, are not identically equal on the time interval T_{Obs}.

More precisely, the solutions to differential equation [4.1] on the interval $T_{Obs} = [0,t]$ are in the following form:

$$x(t) = e^{tA}x(0) + \int_0^t e^{(t-s)A}Bu(s)ds \qquad [4.18]$$

and the output is given by:

$$y(t) = Ce^{tA}x(0) + C\int_0^t e^{(t-s)A}Bu(s)ds \qquad [4.19]$$

Observability is thus equivalent to: for all initial conditions $x(0) \neq \bar{x}(0)$, $t > 0$ exists, such that $Ce^{tA}(x(0) - \bar{x}(0)) \neq 0$, which shows that the observability of time-invariant linear models is independent of the input which is applied to the system. This leads us to the Kalman criterion.

THEOREM (KALMAN CRITERION).– The system given by [4.1] is observable if and only if the matrix $[C, CA, ..., CA^{n-1}]^T$ is of maximal order (meaning the spatial dimension of the state space representation).

By using the result obtained from this theorem, it is therefore possible to show that the state space of model $x(t)$ can be deduced from the output $y(t)$ and input $u(t)$ by differentiating a linear combination of these functions a certain number of

times. But this is only a theoretical solution because, in practice, all measurements are biased by noise which makes this method unusable. Another method is to use an observer, which on the one hand, plays the role of a state space estimator, and on the other hand, will act as a filter to the outputs.

In the discrete case, i.e. when the inputs and outputs are sampled at the sampling frequency $f_e = \frac{1}{T_e}$ (T_e is the sampling period), the model is given by the equations:

$$\begin{cases} x_{k+1} = Ad_k x_k + Bd_k u_k \\ y_k = Cx_k + Du_k \end{cases} \quad [4.20]$$

with $x_k \in R^n; u_k \in R^m; y_k \in R^p$.

Among the different sampling methods, the most frequently used method is the zero-order hold method for the inputs u_k: the control applied to the system is constant during interval $[kT_e, (k+1)T_e[$ and is worth $u_k = u(kT_e)$. Between times kT_e and $(k+1)T_e$, by integrating the continuous time linear model [4.1], we then obtain:

$$x((k+1)T_e) = e^{AT_e} x(kT_e) + \int_{kT_e}^{(k+1)T_e} e^{A(t-kT_e)} Bu(kT_e)dt$$

$$= e^{AT_e} x(kT_e) + [(\int_0^{T_e} e^{At}dt)B]u(kT_e)$$

which gives the following for the discrete model matrices:

$$Ad_k = Ad = e^{AT_e} \text{ and } Bd_k = Bd = (\int_0^{T_e} e^{At}dt)B \quad [4.21]$$

Evidently, the discrete output equation is the same as the equation for the continuous output because there is no dynamic in this output.

The observability of sampled time-invariant linear systems is defined in the same way as for the continuous case, and the Kalman criterion, when applied to the matrices Ad and C, is a simple way of testing this observability.

This observability may be lost, however, due to this sampling, and therefore the following theorem may help avoid this problem.

THEOREM.– If the time-invariant linear system (TILS) is observable, then a sufficient condition for the sampled system to be observable is that if, for any pair of eigenvalues (λ_i, λ_j) such that $\mathrm{Re}(\lambda_i - \lambda_j) = 0$, then $\mathrm{Im}(\lambda_i - \lambda_j)$ is not a multiple of $\frac{2\pi}{T_e}$.

If the continuous TILS is observable, then there is a high chance that the corresponding discrete TILS is also observable.

This notion of observability for linear model systems can be extended to systems with non-linear models. However, if this is a global concept for linear models, then this is not the case for non-linear models.

Either the system is modeled by:

$$\begin{cases} \dot{x}(t) = \dfrac{dx}{dt}(t) = f(x(t), u(t)) \\ y(t) = h(x(t)) \end{cases}$$

Or, more simply by:

$$\begin{cases} \dot{x} = f(x, u) \\ y = h(x) \end{cases} \qquad [4.22]$$

For reasons of brevity, we will assume that $x(t) \in R^n$, $y(t) \in R^p$ and that $u(t) \in R^m$. The set of inputs $u(.)$ is such that for any initial condition x, the differential equation has a single solution written as $x_u(t)$, defined on a maximum interval $[0, T_{(u,x)}]$ (acceptable input). We thus propose the following definition for the observability of non-linear models:

DEFINITION.– (Observability):

1) two initial conditions $x \neq x'$ are said to be indistinguishable if, for any acceptable input $u(.)$, $h(x_u(t)) = h(x'_u(t))$ for any $t \in [0, T]$ with $T = \inf(T_{(u,x)}, T_{(u,x')})$;

2) if two initial conditions x and x' are such that $\exists u(.), \exists t \in [0,T]$ such that $h(x_u(t)) \neq h(x'_u(t))$, then we can say that $u(.)$ distinguishes x and x' over $[0,T]$;

3) the system is said to be observable if, for any pair with distinct initial conditions, it accepts an input which makes them distinguishable;

4) for any input which distinguishes any pair of initial conditions over an interval of $[0,T]$, then we say that it is an universal input over interval $[0,T]$ for the system, or that it makes the system observable over interval $[0,T]$.

We should note that the concept of system observability is initially linked to the input which is applied to the system, except for the following case:

DEFINITION.– A system is said to be observable for any input if any input makes it observable.

These types of systems, therefore, are said observable for any input.

4.3.2. *Different kinds of observers*

4.3.2.1. *Introduction*

Once we have obtained the system's observability, an observer can be synthesized. The nature of the observer depends on the chosen model type (linear, time-variant linear, affine state-space, affine control), on the structure chosen (for instance, uniform observability), on the type of observability obtained (high observability, in the sense of rank condition, local observability, uniform observability, for any input), and on the usable input (of course, a non-singular input, but also a regularly persistent input).

We will now present a few types of observers used in fault detection in squirrel-cage induction motors.

In all the examples, the observer algorithm can be broken down into two phases:

– an estimator reconstructs state X_{est} of the system by solving the state space equations modeling the system which has been established using equations in the machine's transient behavior:

$$\begin{cases} X_{k+1} = Ad_k X_k + Bd_k U_k \\ Y_k = CX_k + DU_k \end{cases} \quad [4.23]$$

– a correction phase. This is carried out using a term which depends on an error generated from measurable components. This gain is fixed according to the desired dynamics and robustness. It must be adapted to the properties of the system whose states we wish to observe:

$$X_{obs} = X_{est} + G.\left(y_{meas} - y_{est}\right) \qquad [4.24]$$

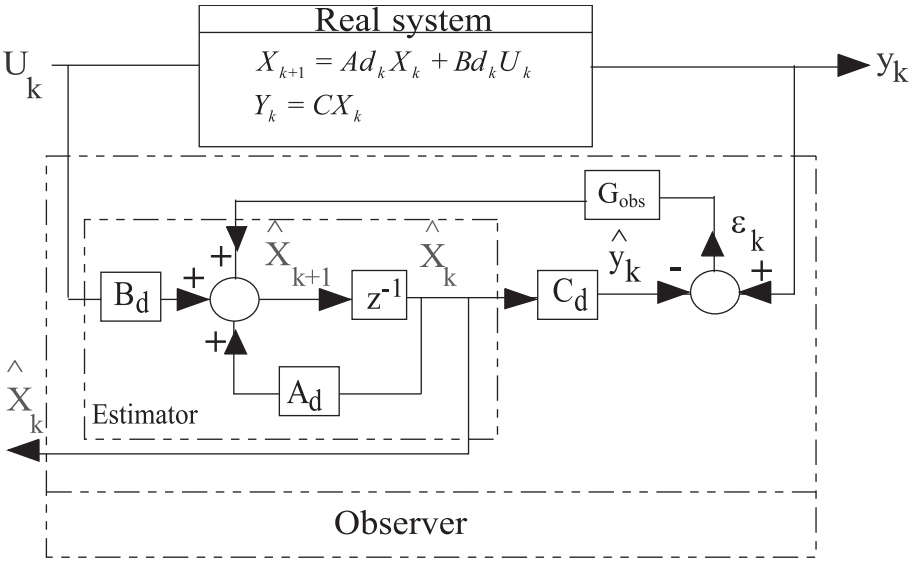

Figure 4.4. *General diagram of an observer*

Different types of observers can be distinguished by the gain synthesis method (term G of equation [4.24]) and the hypotheses given below. We will describe the most frequently used observers in diagnostics.

4.3.2.2. *The Luenberger observer*

The Luenberger observer [LUE 71] was, historically, the first observer to be developed. It can be used for time-invariant linear systems and continuous and discrete systems. It gives an estimation of the unmeasured states of a system's linear model. An observer for model [4.1] is given by:

$$\dot{\hat{x}} = A\hat{x} + Bu + K(C\hat{x} - y) \qquad [4.25]$$

where $\hat{x}$ is the state space observed by the observer[1], K is a gains matrix to be chosen in such a way that the eigenvalues of $A+KC$ have strictly negative real parts. This observer is therefore an exponential observer. In fact, a simple calculation shows that the error of estimation $e(t)=\hat{x}(t)-x(t)$ is controlled by the differential equation:

$$\dot{e}(t)=(A+KC)e(t) \qquad [4.26]$$

and if the eigenvalues of $A+KC$ have strictly negative real parts, then the error vector tends exponentially toward 0, and thus:

$$\lim_{t\to\infty} \hat{x}(t)=x(t) \qquad [4.27]$$

This observer, which allows us to understand the principle of system observation, is in fact little used in practice because it is very sensitive to modeling errors and measurement noise.

4.3.2.3. *Kalman observer*

For time-variant linear systems (if matrix A depends on time: $A(t)$), then the model is given by:

$$\begin{cases} \dot{x}=A(t)x+B(t)u \\ y=C(t)x \end{cases} \qquad [4.28]$$

and the Kalman observer [KAL 60, BOR 93 and DUV 02] is given by:

$$\begin{cases} \dot{\hat{x}}=A(t)\hat{x}+B(t)u+S^{-1}C^T(t)Q(y-C(t)\hat{x}) \\ \dot{S}=-\theta S-SA(t)-A^T(t)S-SRS+C^T(t)QC(t) \end{cases} \qquad [4.29]$$

1 We note here that an observer is, in fact, a copy of the model which we add a correction to, which depends on the deviation between the real output and the observer output. The observers are constructed in this way. Only the correction term varies from one observer to another.

The first equation gives the estimated state. The second is the Riccatti equation which calculates the observer correction gain. $\theta > 0$ and the matrices $S(0)$, Q, and R are chosen symmetrical definite positive to guarantee the existence and stability of the solution for this equation.

When the discrete model is described by:

$$\begin{cases} x_{k+1} = Ad_k x_k + Bd_k u_k + G_k w_k \\ y_k = Cx_k + D_k v_k \end{cases} \quad [4.30]$$

then $G_k w_k$ (respectively $D_k v_k$) is a model of the input noise (respectively output noise).

The Kalman observer is written as:

$$\begin{cases} \hat{x}_{k+1} = \hat{x}_{k+1/k} + K_{k+1}(y_{k+1} - C_{k+1}\hat{x}_{k+1/k}) \\ P_{k+1} = (P^{-1}{}_{k+1/k} + C^T{}_{k+1} R^{-1}{}_{k+1} C_{k+1})^{-1} \\ \hat{x}_{k+1/k} = Ad_k \hat{x}_k + Bd_k u_k \\ P_{k+1/k} = Ad_k P_k Ad_k^T + Q_k \\ K_{k+1} = P_{k+1/k} C^T{}_{k+1} (C_{k+1} P_{k+1/k} C^T{}_{k+1} + R_{k+1})^{-1} \end{cases} \quad [4.31]$$

In these equations, the notation $\amalg_{k+1/k}$ indicates the value of component $\amalg$ at time $k+1$ knowing instant k, otherwise known as the prediction of component $\amalg$ at time $k+1$.

$P_0 = \alpha.Id_n$ with $\alpha > 0$. Q_k and R_{k+1} are weighting matrices, both symmetric definite positive matrices, which are used to set the optimality of the Kalman filter (stability, observer convergence speed), and frequently chosen as being the covariance matrices of the measurement noise: $Q_k = G_k G_k^T$ and $R_{k+1} = D_{k+1} D_{k+1}^T$ (in the figure given below, $Q_k = R_{k+1} = Id_n$). Thus, $\hat{x}_{k+1}$ is the state space estimation x_{k+1} and $\hat{x}_{k+1/k}$ is its prediction.

For non-linear observable systems, it is possible to construct an extended Kalman observer (EKO). This observer comes from the Kalman filter. There are

three different versions of it: a continuous version, a discrete version, and a continuous-discrete version. The convergence of this observer is demonstrated in [LOH 98, LOH 00].

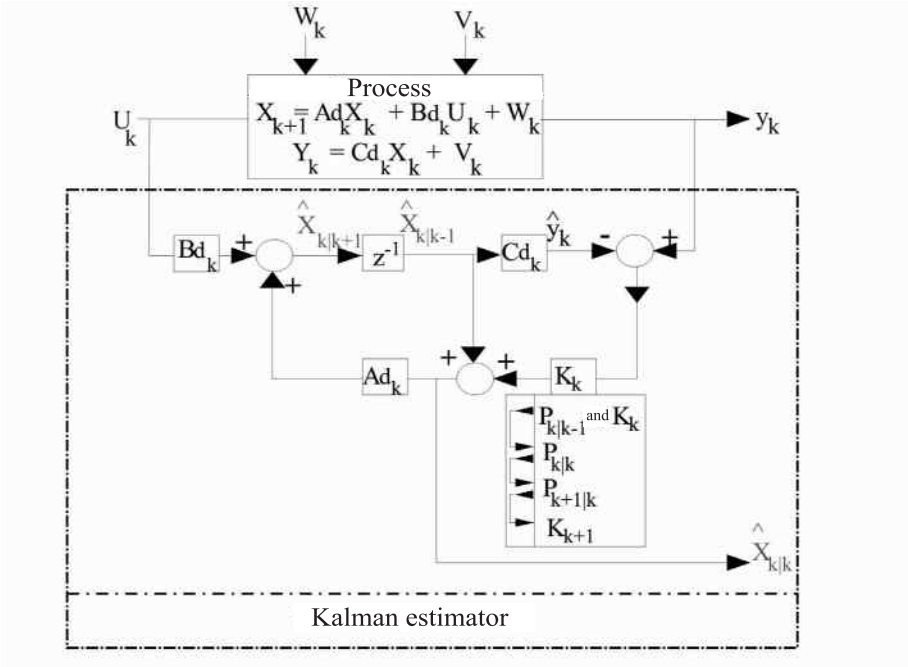

Figure 4.5. *Kalman observer*

In the continuous case, the observer is written as:

$$\begin{cases} \dot{\hat{x}} = f(\hat{x},u) + P\dfrac{\partial h}{\partial x}(\hat{x})R^{-1}(y - h(\hat{x})) \\ \dot{P} = \dfrac{\partial f}{\partial x}(\hat{x},u)P + P\dfrac{\partial f^T}{\partial x}(\hat{x},u) + Q - P\dfrac{\partial h^T}{\partial x}(\hat{x})R^{-1}\dfrac{\partial h}{\partial x}(\hat{x})P \end{cases} \quad [4.32]$$

where $\dfrac{\partial f}{\partial x}(\hat{x},u)$ (respectively $\dfrac{\partial h}{\partial x}(\hat{x},u)$) indicates the Jacobian matrix of f (respectively of h) calculated in $(\hat{x},u)$ (respectively in $\hat{x}$), and $\dfrac{\partial f^T}{\partial x}$ indicates the

transpose of the Jacobian matrix of f. $P(0)$, Q, and R are chosen symmetric definite positive matrices.

As for linear models, it is indeed possible to construct an extended Kalman observer in the discrete case. It has the same shape as the discrete observer for linear models, by replacing the matrices of the linear model by the Jacobian matrices of the model's non-linear vector field.

In the continuous/discrete case, the prediction is controlled by the corresponding differential equation, with the correction taking place at the time of sampling.

4.3.2.4. *High gain observer*

The models likely to be observed by high gain observers[2] must have the property of being observable for any input, and moreover, have a particular structure. Through a change in variables[3], at least a local change and not necessarily a single one, they must be written in the following form:

$$\begin{cases} \dot{z} = Az + \phi(u, z) \\ y = Cz \end{cases} \qquad [4.33]$$

With $z = \begin{bmatrix} z_1 \\ z_2 \\ \vdots \\ z_p \end{bmatrix} \in R^n$ and $z_k = \begin{pmatrix} z_{k1} \\ z_{k2} \\ \vdots \\ z_{kn_k} \end{pmatrix} \in R^{n_k}$ so that $\sum_{i=1}^{p} n_i = n$

$u \in R^m$, $y = \begin{pmatrix} y_1 \\ y_2 \\ \vdots \\ y_p \end{pmatrix} \in R^p$

2 See [HAM 02] for more details.

3 This variables change is given by a sequence of Lie derivatives $L_f^i h_k, k = 1,\ldots,p; i = 0,\ldots,n_k - 1$ having to verify certain conditions.

$$A=\begin{bmatrix} A_1 & 0 & \cdots & 0 \\ 0 & \ddots & \ddots & \vdots \\ \vdots & \ddots & \ddots & 0 \\ 0 & \cdots & 0 & A_p \end{bmatrix}, \text{ with each block: } A_k=\begin{pmatrix} 0 & 1 & 0 & & 0 \\ \vdots & 0 & \ddots & \ddots & \vdots \\ \vdots & & \ddots & \ddots & 0 \\ \vdots & & & 0 & 1 \\ 0 & \cdots & \cdots & \cdots & 0 \end{pmatrix}$$

$$C=\begin{bmatrix} C_1 & 0 & \cdots & 0 \\ 0 & \ddots & \ddots & \vdots \\ \vdots & \ddots & \ddots & 0 \\ 0 & \cdots & 0 & C_p \end{bmatrix}, \text{ with each block: } C_k=\begin{pmatrix} 1 & 0 & \cdots & 0 \end{pmatrix}, \ \phi=\begin{bmatrix} \phi_1 \\ \phi_2 \\ \vdots \\ \phi_p \end{bmatrix} \text{ and}$$

$$\phi_k=\begin{pmatrix} \phi_{k1} \\ \phi_{k2} \\ \vdots \\ \phi_{kn_k} \end{pmatrix} \text{ vector fields with values in } R^{n_k}.$$

In this form here, for a high gain observer to be built, then ϕ_k must verify the following hypothesis:

HYPOTHESIS H.– There are $2p$ integers $\{\sigma_1,\sigma_2,\ldots,\sigma_p\}$, $\{\delta_1,\delta_2,\ldots,\delta_p\}$, such that $\delta_k>0, k=1,\ldots,p$, satisfying: for $k,l=1,\ldots,p; i=1,\ldots,n_k$ and for $j=2,\ldots,n_l$, we have: if $\dfrac{\partial\phi_{ki}}{\partial z_{lj}}(u,z)\neq 0$ for a certain $j\geq 2$, thus:

$$\sigma_k+(i-1)\delta_k+\frac{\delta_k}{2}>\sigma_l+(j-1)\delta_l$$

Thus the observer is written as:

$$\dot{\hat{z}}=A\hat{z}+\phi(u,\hat{z})-S_{\Theta}^{-1}C^T(C\hat{z}-y) \qquad [4.34]$$

with $\hat{z}_{k1}=y_k$ for $k=1,\ldots,p$ (outputs injected into the observer) and $\hat{z}_{ki}=\hat{z}_k$ for:

$$k = 1,\ldots,p; i \neq 1 \text{, and } S_{\Theta} = \begin{bmatrix} S_{\theta^{\delta_1}} & 0 & \cdots & 0 \\ 0 & \ddots & \ddots & \vdots \\ \vdots & \ddots & \ddots & 0 \\ 0 & \cdots & 0 & S_{\theta^{\delta_p}} \end{bmatrix} \text{ and } S_{\theta^{\delta_k}}, k = 1,\ldots,p$$

is the single solution for:

$$\theta^{\delta_k} S_{\theta^{\delta_k}} + A^T S_{\theta^{\delta_k}} + S_{\theta^{\delta_k}} A = C_k^T C_k \qquad [4.35]$$

We thus have the following theorem:

Theorem [BOR 91, BOR 01].– If the above hypothesis, HYPOTHESIS H, is verified, and if the non-linear terms ϕ_i are globally Lipschitzian, then for each limited input $\exists\theta_0; \forall\theta > \theta_0$, equations [4.34] and [4.35] act as an exponential observer for system [4.33] whose convergence speed is controlled by the value of θ.

The solution for this equation, in light of the form of matrix A, gives the following values as the coefficients of these matrices $S_{\theta^{\delta k}}$ of the block matrix S_{Θ}:

$$S_{\theta^{\delta_k}}(i,j) = \frac{(-1)^{i+j} C_{i+j-2}^{j-1}}{\theta^{\delta_k (i+j-1)}} \text{ for } 1 \leq i,j \leq n_k \text{ and with } C_n^p = \frac{n!}{p!(n-p)!}$$

The advantages of this observer are that it only requires a few calculations (online use), and that it only has one level control coefficient (hence its simplicity). A disadvantage is that it is relatively sensitive to measurement noise.

4.3.3. *Extended observer*

4.3.3.1. *Linearization of non-linear systems*

Electrical machines in transient regime are described by non-linear state space equations. In fact, the state space matrices introduce angular frequencies (relative speed of the reference frame dp in relation to the rotor or stator).

They are put into the following form:

$$\frac{dX}{dt} = A(X,\theta,t)X + B(\theta)U + W(t)$$

$$\text{and } Y = C(X,\theta,t).X + V(t) \qquad [4.36]$$

with θ as a parameter vector, W is the noise on the state space, and V is the noise on the output.

Generally:

$$\begin{cases} \dfrac{dX}{dt} = f(X(t),U(t),t) + W(t) \\ Y(t) = h(X(t),t) + V(t) \end{cases} \quad [4.37]$$

The system is then linearized around a defined point of operation on the previous pitch by calculating the Jacobian matrices of functions F and H:

$$F(X(t),u(t),t) = \left(\frac{\partial f}{\partial X}\right)_{X=\hat{X}(t)} \text{ and } H(X(t),t) = \left(\frac{\partial h}{\partial X}\right)_{X=\hat{X}(t)}$$

and $\Phi(k+1,k) = e^{\left(\left(\frac{\partial f}{\partial X}\right)_{X=\hat{X}_{k|k}}\right).T_{ech}}$ as the transition matrix from X_k toward X_{k+1}.

The state space model thus obtained is then held to the 0 order (constant control during the sampling period Te), and is discretized:

$$\begin{aligned} X_{k+1} &= Ad_k X_k + Bd_k U_k \\ Y_k &= CX_k \end{aligned} \quad [4.38]$$

with:

$$Ad_k = e^{AT_e} \approx I + A.T_e + \frac{1}{2}(A.T_e)^2$$

$$Bd_k = \int_0^{T_e} e^{A\tau} Bd\tau \approx T_e\left(I + \frac{1}{2}T_e A\right)B$$

4.3.3.2. *Extended systems*

Our discretized system is represented by the following equations:

$$\begin{aligned} X_{k+1} &= Ad_k(\theta_k)X_k + Bd_k(\theta_k)U_k + W_{X_k} \\ Y_k &= C(\theta_k)X_k + V_k \end{aligned} \quad [4.39]$$

where W_{X_k} represents the noise on the state space, and V_k represents the noise on the outputs.

The state space vector can be extended to the parameters θ_k whose evolution we wish to trace.

By assuming that there is slow parameter evolution in relation to the system's dynamics, then a new state space vector is generated:

$$\breve{X}_k = \begin{bmatrix} X_k \\ \theta_k \end{bmatrix} \quad [4.40]$$

The extended system is, then, modeled by the state space equations.

By modeling the parameter variation by the noise W_{θ_k}, the equations for the augmented system are:

$$\begin{bmatrix} X_{k+1} \\ \theta_{k+1} \end{bmatrix} = \begin{bmatrix} Ad\ (\theta_k) & 0 \\ 0 & I \end{bmatrix} \begin{bmatrix} X_k \\ \theta_k \end{bmatrix} + \begin{bmatrix} Bd\ (\theta_k) \\ 0 \end{bmatrix} .U_k + \begin{bmatrix} W_{X_k} \\ W_{\theta_k} \end{bmatrix} \quad [4.41]$$

$$Y_{k+1} = [C(\theta_k)\,0] \begin{bmatrix} X_k \\ \theta \end{bmatrix} + V_k$$

This non-linear system is linearized around the following steady state:

$$F(X, u, kT_{ech}) = \begin{bmatrix} Ad\ (\theta_k) & \left(\dfrac{\partial \left(Ad\ (\theta_k) X_k + Bd\ (\theta_k) U_k \right)}{\partial \theta} \right)_{X_k} \\ 0 & I \end{bmatrix} \quad [4.42]$$

and:

$$H(X, kT_{ech}) = \begin{bmatrix} C(\theta_k) & \left(\dfrac{\partial \left(C(\theta_k) X_k \right)}{\partial \theta} \right)_{X_k} \end{bmatrix} \quad [4.43]$$

4.3.3.3. *Applying observers to extended systems*

Observers can be applied to linearized extended systems, thus making it possible to follow the parameters.

The observer is broken down into a prediction phase (the estimator) and a phase where the estimation is corrected using the deviation on an instrumental variable z_{k+1} which can be assessed using measurable quantities (we will write this assessment as z^m_{k+1}) and estimated quantities (we will write this estimation as z^c_{k+1}) generally in the following form:

$$z^c_{k+1} = H\hat{X}_{k+1} + J\hat{X}_k \qquad [4.44]$$

Often, the instrumental variable is reduced to measurable quantities y^m_k:

$$z^c_{k+1} = C.\hat{X}_k \qquad [4.45]$$

The observer algorithm is then broken down over each time step:

– re-calibration of matrices Ad, Bd, C, and matrices F and H;

– a prediction phase during which the state space vector predicted at time (k+1), written as $\widetilde{X}_{k+1}$, is calculated from the state space equations and the state space vector estimated at time k, written as $\hat{X}_k$:

$$\begin{aligned} \widetilde{X}_{k+1} &= Ad_k\hat{X}_k + Bd_kU_k \\ Y_k &= C.\widetilde{X}_k \end{aligned} \qquad [4.46]$$

– calculating the gain G_{k+1} according to the Jacobian matrices F and H, characteristics of the noise, etc.;

– a correction phase of the prediction vector $\widetilde{X}_{k+1}$ using the measurement vector y^m_{k+1} and gain G_{k+1} of the observer. We thus obtain the vector estimated at time k+1, $\hat{X}_{k+1}$:

$$\hat{X}_{k+1} = \widetilde{X}_{k+1} + G_{k+1}[z^m_{k+1} - z^c_{k+1}] \qquad [4.47]$$

4.4. Applying observers to diagnostics

4.4.1. *Using Park's model*

4.4.1.1. *Monitoring the rotor resistance*

In [BOU 00, BOU 01], an initial extended high gain observer was proposed, making it possible to follow the rotor resistance and rotor fluxes of axes d and q based on Park's two-phase model, described in section 4.2.1.

The algorithm was implanted into a DSP TMS320C31 data board by ©Dspace, with a sampling rate of 3 10-4 s. It was tested on a 5 kW motor test bench where squirrel-cage faults can be performed, as well as stator windings and bearings ones. The induction machine is loaded by a powder brake.

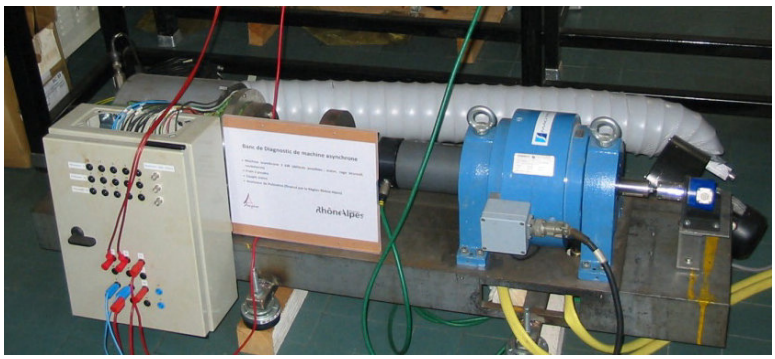

Figure 4.6. *Motor test bench*

The observer is constructed on a model extended to the parameters and then reduced.

The machine's model is the following:

$$\begin{cases} \dot{x}_1 = \dfrac{L_m x_3}{L_r} i_{ds} - \dfrac{x_3}{L_r} x_1 + (\omega_s - \omega_r) x_2 \\ \dot{x}_2 = \dfrac{L_m x_3}{L_r} i_{qs} - (\omega_s - \omega_r) x_1 - \dfrac{x_3}{L_r} x_2 \\ \dot{x}_3 = 0 \end{cases} \qquad [4.48]$$

with $[x_1 \quad x_2 \quad x_3]^T = [\varphi_{dr} \quad \varphi_{qr} \quad R_r]^T$.

The observer which is extended to the speed and the rotor resistance is thus given by:

$$\dot{\hat{x}} = f(\hat{x}) + g(\hat{x})u - \left(\frac{\partial \Gamma}{\partial \hat{x}}(\hat{x}(t))\right)^{-1} S_\theta^{-1}(h(\hat{x}) - y) \qquad [4.49]$$

with:

$$\dot{\hat{x}} = \begin{bmatrix} \dot{\hat{\varphi}}_{dr} \\ \dot{\hat{\varphi}}_{qr} \\ \dot{\hat{R}}_r \end{bmatrix}; h(\hat{x}) = \begin{bmatrix} \hat{\varphi}_{dr} \\ \hat{\varphi}_{qr} \end{bmatrix}; y = \begin{bmatrix} \varphi_{dr_e} \\ \varphi_{qr_e} \end{bmatrix}$$

$$S_\theta^{-1} \equiv \begin{bmatrix} 2\theta_1 & \theta_1^2 & 0 \\ \theta_1^2 & \theta_1^3 & 0 \\ 0 & 0 & 2\theta_2 \end{bmatrix}$$

We write $\Gamma(x) = \left[h_1(x), L_f h_1(x), h_2(x), L_f h_2(x)\right]^T$ with $L_f h_i$ as the first Lie derivative according to h_i in direction f.

We thus obtain:

$$\left[\frac{\partial \Gamma}{\partial \hat{x}}(\hat{x}(t))\right]^{-1} \equiv \begin{bmatrix} 1 & 0 & 0 \\ 0 & 0 & 1 \\ -\dfrac{\hat{R}_r}{\hat{\varphi}_{dr}} & -\dfrac{L_r}{\hat{\varphi}_{dr}} & \dfrac{(\omega_r - \omega_s)L_r}{\hat{\varphi}_{dr}} \end{bmatrix} \qquad [4.50]$$

The correction term $\left(\frac{\partial \Gamma}{\partial \hat{x}}(\hat{x}(t))\right)^{-1} S_\theta^{-1}(h(\hat{x}) - y)$ is obtained from the deviation between the fluxes estimated from the measurements, and the observed fluxes. We thus obtain a reduced observer.

The estimated fluxes φ_{dr_e} and φ_{qr_e} are obtained using the current measurements:

$$\begin{cases} \dfrac{d\varphi_{dr_e}}{dt} = \dfrac{L_r}{L_m}\left(V_{ds} - R_s i_{ds}\right) - \dfrac{\sigma L_r L_s}{L_m}\left(\dfrac{i_{ds}}{dt} - \omega_s i_{qs}\right) + \omega_s \varphi_{qr_e} \\ \dfrac{d\varphi_{qr_e}}{dt} = \dfrac{L_r}{L_m}\left(V_{qs} - R_s i_{qs}\right) - \dfrac{\sigma L_r L_s}{L_m}\left(\dfrac{i_{qs}}{dt} - \omega_s i_{ds}\right) + \omega_s \varphi_{dr_e} \end{cases} \quad [4.51]$$

The parameters θ_i are calibrated empirically using the process simulation.

The rotor resistance is initialized at 150% of its nominal value. To demonstrate the observer's performances, a resistance variation was simulated during operation (Figure 4.7).

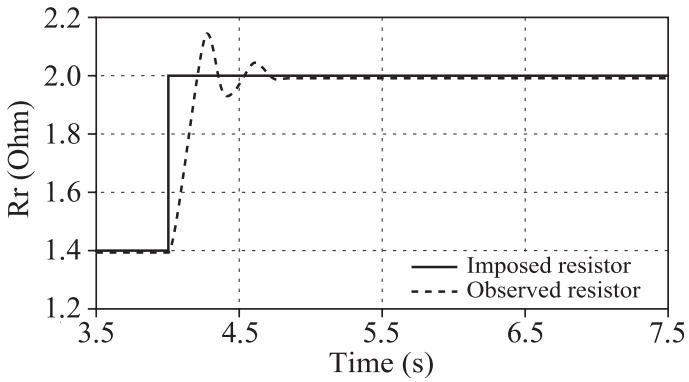

Figure 4.7. *Evolution of the rotor resistance (measured and observed)*

Figure 4.8 confirms the performances of this observer in a real test.

This easy-to-regulate observer (2 coefficients θ_i i) gives good results in real-time use.

A Kalman filter can also be used instead and in place of the high gain observer [SAI 00].

However, in each case, following a single parameter of model (R_r) does not allow us to discriminate an evolution due to a squirrel-cage fault or a normal evolution in the rotor resistance due to over-heating. It is therefore necessary to introduce a second parameter to avoid false alarms.

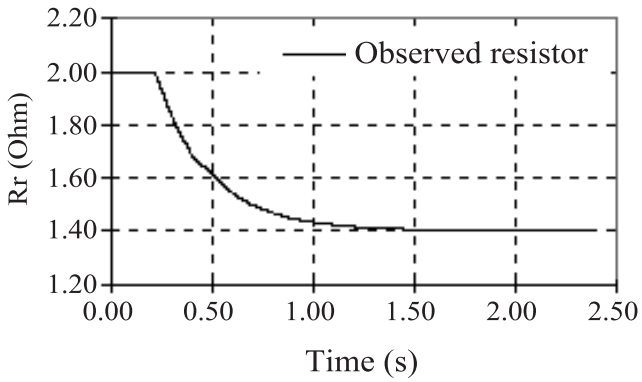

Figure 4.8. *Observation of rotor resistance on a motor test bench – Rr identified at 1.4Ω*

4.4.1.2. *Following the rotor resistance and magnetizing inductance*

[BOU 01] synthesized a Kalman observer extended to the rotor resistance and the magnetizing cyclic inductance based on the two-phase model in a reference frame linked to the rotating field. The estimation is based on the extended state space model, by assuming the slow parameter variations:

$$\begin{cases} \dot{i}_{ds} = -\left(\dfrac{R_r + R_s}{L_f}\right) i_{ds} + \omega_s i_{qs} + \left(\dfrac{R_r}{L_m L_f}\right)\varphi_{dr} + \left(\dfrac{1}{L_f}\right)\omega_r \varphi_{qr} + \dfrac{1}{\sigma L_s} V_{ds} \\ \dot{i}_{qs} = -\omega_s i_{ds} - \left(\dfrac{R_r + R_s}{L_f}\right) i_{qs} + \left(\dfrac{1}{L_f}\right)\omega_r \varphi_{dr} + \left(\dfrac{R_r}{L_m L_f}\right)\varphi_{qr} + \dfrac{1}{\sigma L_s} V_{qs} \\ \dot{\varphi}_{dr} = R_r i_{ds} - \dfrac{R_r}{L_m}\varphi_{dr} + \omega_{sl}\varphi_{qr} \\ \dot{\varphi}_{qr} = R_r i_{qs} + \omega_{sl}\varphi_{dr} - \dfrac{R_r}{L_m}\varphi_{qr} \\ \dot{R}_r = 0 \\ \dot{L}_m = 0 \end{cases} \quad [4.52]$$

Therefore, on a model in the following form:

$$\frac{d\hat{x}}{dt} = f(\hat{x}, u) \quad [4.53]$$

The Kalman observer is synthesized according to the method described in section 4.3.2.3.

A simultaneous variation in these two parameters was simulated in the presence of noise (Figures 4.9 and 4.10).

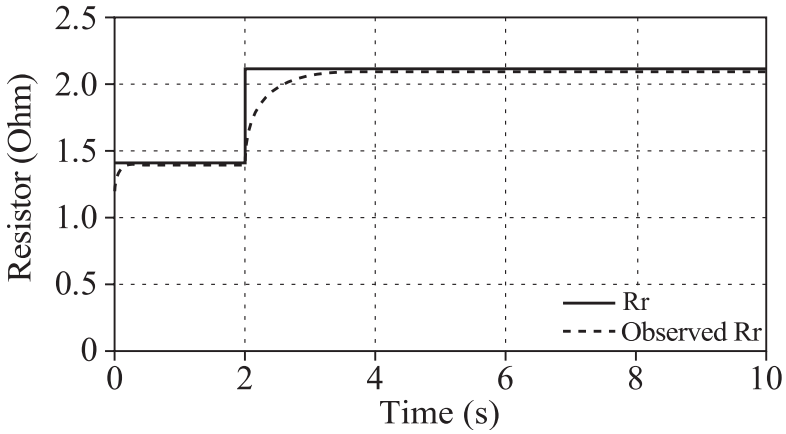

Figure 4.9. *Evolution of the rotor resistance (observed and simulated)*

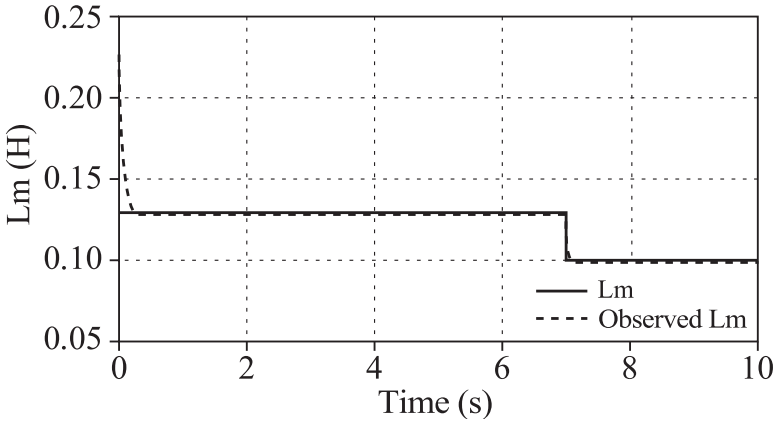

Figure 4.10. *Evolution of the magnetizing inductance (observed and simulated)*

The observer follows the variation of these two parameters perfectly. It thus enables us to discriminate the rotor fault in healthy operation. It can also be used for a mains supply or inverter supply.

4.4.2. *Use of the three-phase model*

[BOU 01] developed an extended Kalman observer, making it possible to detect an online asymmetrical evolution in the three rotor resistances of the two-phase model in the reference frame connected to the stator.

With this model, the system is *not* totally observable. On its own, the asymmetrical evolution is observable, but each resistance is not observable individually.

The estimator is constructed based on the model described in section 4.2.1.

The state space vector is composed of three stator phase currents, three rotor phase currents, and three rotor resistances.

The extended observer synthesis is described in section 4.3.3.

This observer was validated on the machine test bench described in section 4.4.1.1. The dissymmetry obtained on the three rotor resistances enables us to perfectly distinguish healthy operation and operation in the presence of a faulty rotor (4 broken bars obtained through a perforation in the squirrel-cage bars).

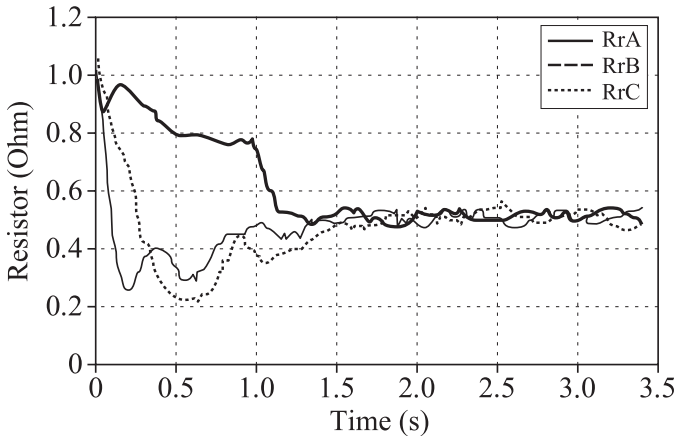

a) *Healthy rotor – motor test bench*

Figure 4.11. *Evolution of three rotor resistances (observed on real measurements)*

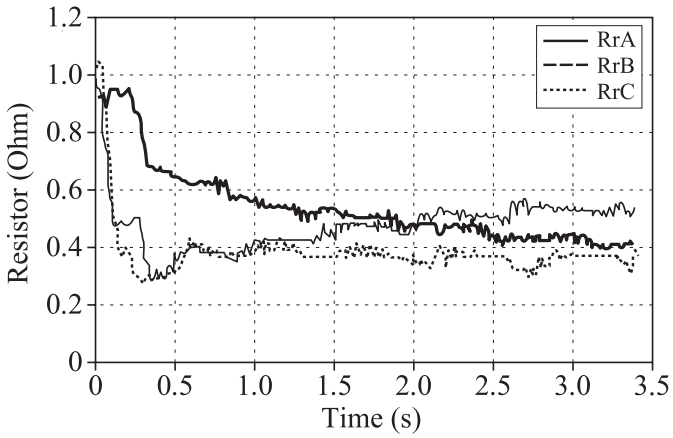

b) *Faulty rotor (4 broken bars) on the motor test bench*

Figure 4.11. *(continued) Evolution of three rotor resistances (observed on real measurements)*

This principle could be easily extended to detecting stator faults by following the three stator resistances.

However, the algorithmic complexity of this observer does not make operation compatible with online processing. The data is recorded then processed offline.

4.4.3. *Spectral analysis of the torque reconstructed by the observer*

[YAH 95] proposed diagnosing induction machine faults through a spectral analysis of the electromagnetic torque. [SAL 97] proposes a similar method for analyzing the load. As we will show, this method requires the use of a flux observer.

The torque can be assessed in Park's two-phase model, presented in section 4.2.1.2 by the following equation:

$$T_e = p\left(\psi_{ds} i_{qs} - \psi_{qs} i_{ds}\right) \qquad [4.54]$$

or:

$$T_e = \frac{pL_m}{L_r}\left(\psi_{dr} i_{qs} - \psi_{qr} i_{ds}\right) \qquad [4.55]$$

If the stator fluxes Ψ_{ds} and Ψ_{qs} are used, then they can be estimated from:

$$\psi_{ds} = \int (V_{ds} - R_s I_{ds})dt \text{ and } \psi_{qs} = \int (V_{qs} - R_s I_{qs})dt \quad [4.56]$$

But due to integration, this method may lead the algorithm to diverge if the current sensors show an offset. An observer ensures better reconstruction of the stator fluxes.

If the rotor fluxes Ψ_{dr} and Ψ_{qr} are used in an oriented flux vector control, then they are also reconstructed by an observer.

We can use the following state space model:

$$\frac{dX}{dt} = AX + BU \quad [4.57]$$

with:

$$U = \begin{bmatrix} v_{ds} \\ v_{qs} \end{bmatrix} \quad X = \begin{bmatrix} i_{ds} \\ i_{qs} \\ \Psi_{dr} \\ \Psi_{qr} \end{bmatrix}$$

$$A = \begin{bmatrix} -\left(\frac{1}{T_s\sigma} + \frac{1}{T_r}\frac{1-\sigma}{\sigma}\right) & \omega_e & \frac{1-\sigma}{\sigma}\frac{1}{L_m T_r} & \frac{1-\sigma}{\sigma}\frac{1}{L_m}\omega_m \\ -\omega_e & -\left(\frac{1}{T_s\sigma} + \frac{1}{T_r}\frac{1-\sigma}{\sigma}\right) & -\frac{1-\sigma}{\sigma}\frac{1}{L_m}\omega_m & \frac{1-\sigma}{\sigma}\frac{1}{L_m T_r} \\ \frac{L_m}{T_r} & 0 & -\frac{1}{T_r} & \omega_{sl} \\ 0 & \frac{L_m}{T_r} & -\omega_{sl} & -\frac{1}{T_r} \end{bmatrix}$$

and:

$$B = \begin{bmatrix} \frac{1}{\sigma L_s} & 0 \\ 0 & \frac{1}{\sigma L_s} \\ 0 & 0 \\ 0 & 0 \end{bmatrix}$$

This model is classically combined with a Kalman observer. As seen in section 4.3.2.3, this makes it possible to reconstruct the machine's state space and, therefore, the fluxes necessary for calculating the torque given by [4.55].

The obtained torque is thus analyzed in permanent regime in the frequency domain (by FFT), or in the slow variable regime, in the time/frequency plane (by using the Spectrogram, the Wigner-Ville distribution, etc.).

The following figure clearly shows that the component at 4 Hz (the machine is powered at 50 Hz) of the electromagnetic torque estimated with this method gives a rotor fault signature.

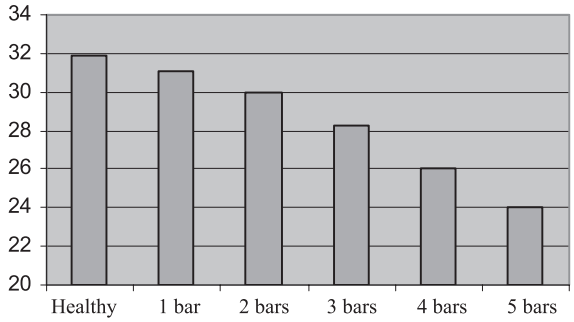

Figure 4.12. *Component at 4Hz of the torque for a rotor fault*

The electromagnetic torque is a relevant component for fault detection because it is the closest to the electromagnetic conversion and, therefore, the energy transfers. However, detecting rotor faults requires the machine to be loaded. Off-load detection is, therefore, not possible.

4.5. Conclusion

We have presented different techniques for diagnosing induction machines, based on observing the parameters of a healthy model or with a machine fault.

These approaches allow for real-time diagnosis of motors supplied by the distribution network or by using a converter. However, they remain much less sensitive than the modeless approaches (using frequency analysis of stator currents) in permanent regime, particularly for rotor faults [FIL 94].

They may, in addition, be accompanied by parametric identification methods which enable more accurate fault discrimination. The extended observer which alerts the presence of a potential fault can then be confirmed, analyzed, and quantified by an offline parametric identification method, or indeed by another approach.

They can be extended to other more complex systems. [GUN 09], for example, proposes monitoring the control of a high speed train drive.

4.6. Bibliography

[BAC 02] BACHIR S., Contribution au diagnostic de la machine asynchrone par estimation paramétrique, PhD Thesis, University of Poitiers, 2002.

[BAC 05] BACHIR S., CHAMPENOIS G., TNANI S., GAUBERT J.P., "Stator faults diagnosis in induction machines under fixed speed", *European Conference on Power Electronics and Applications*, 2005.

[BAC 06] BACHIR S., TNANI S., CHAMPENOIS G., "Diagnosis by parameter estimation of stator and rotor faults occurring in induction machines", *IEEE Transactions on Industrial Electronics*, vol. 53, no. 3, June 2006.

[BOR 01] BORNARD G., BUSAWON K., HAMMOURI H., *An Observer for a Class of Non-linear Systems*, LAGEP, Paris, 2001.

[BOR 91] BORNARD G., HAMMOURI H., "A high gain observer for a class of uniformly observable systems", *Proceedings of the Conference on Decision and Control*, Brighton, vol. 3, p. 1494-1496, 1991.

[BOR 93] BORNARD G., CELLE-COUENNE F., GILLES G., "Observabilité et observateurs", *Systèmes non linéaires*, *T1*, *Modélisation-Estimation*, p. 177-221, Masson, Paris, 1993.

[BOR 90] BORNE P., DAUPHIN-TANGUY G., RICHARD J.P., ROTELLA F., ZAMBETTAKIS I., *Commande et Optimisation des Processus*, Technip, Paris, 1990.

[BOU 00] BOUMEGOURA T., CLERC G., YAHOUI H., GRELLET G., SALLES G., "Rotor resistance estimation by non-linear observer for diagnostic and control systems", *European Journal of Automation*, vol. 34, no. 8, October 2000.

[BOU 01] BOUMEGOURA T., Recherche des signatures électromagnétiques des défauts dans une machine asynchrone et synthèse d'observateur en vue du diagnostic, PhD Thesis, Ecole centrale of Lyon, 2001.

[CAS 03] CASIMIR R., Diagnostic des défauts des machines asynchrones par reconnaissance de forme, PhD Thesis, Ecole centrale of Lyon, 2003.

[DUV 02] DUVAL C., Commande robuste des machines asynchrones, PhD Thesis, Ecole centrale of Lyon, 2002.

[FIL 94] FILIPPETTI F., FRANCESCHINI G., TASSONI C., VAS P., "Broken bar detection in induction machines: comparison between current spectrum approach and parameter estimation approach", *Industry Applications Society Annual Meeting*, proceedings vol. 1, p. 95-102, 2-6 October 1994.

[GRE 00] GRELLET G., CLERC G., *Actionneurs Electriques*, Eyrolles, Paris, 2000.

[GUZ 09] GUZINSKI J., DIGUET M., KRZEMINSKI Z., LEWICKI A., ABU-RUB H., "Application of speed and load torque observers in high-speed train drive for diagnostic purposes", *IEEE Transactions on Industrial Electronics*, vol. 56, no. 1, January 2009.

[HAM 02] HAMMOURI H., MARQUES J.C., "Observateurs de systèmes non-linéaires", *Systèmes non-linéaires*, p. 81-124, 2002.

[KAL 60] KALMAN R.E., BUCY R., "New results in linear filtering and prediction theory", *Journal of Basic Engineering*, no. 82, p. 35-40, 1960.

[KEY 86] KEYHANI A., MIRI S.M., "Observers for tracking of synchronous machine parameters and detection of incipient faults", *IEEE Transactions on Energy Conversion*, vol. EC-1, no. 2, June 1986.

[LOH 98] LOHMILLER J., SLOTINE J.-J., "On contraction analysis for non-linear systems", *Automatica*, vol. 34, no. 6, p. 683-696, 1998.

[LOH 00] LOHMILLER J., SLOTINE J.J., "Control system design for mechanical systems using contraction theory", *IEEE Transactions on Automatic Control*, vol. 45, no. 5, p. 984-989, 2000.

[LUE 71] LUENBERGER D.G., "An introduction to observers," *IEEE Transactions on Automatic Control*, no. 16, p. 592-602, 1971.

[MOR 99] MOREAU S., TRIGEASSOU J.C., CHAMPENOIS, GAUBERT J.P., "Diagnosis of induction machines: a procedure for electrical fault detection and localization", *SDEMPED'99*, 1-3 September 1999.

[SAÏ 00] SAÏD M., BENBOUZID M., ABDELKRIM BENCHAIB A., "Detection of broken bars in induction motors using an extended Kalman filter for rotor resistance sensorless estimation", *IEEE Transactions on Energy Conversion*, vol. 15, no. 1, March 2000.

[SAL 97] SALLES G., Surveillance et diagnostic des défauts de la charge d'un entraînement par machine asynchrone, PhD Thesis, Claude Bernard Univeristy, Lyon I, January 1997.

[SCH 99a] SCHAEFFER E., Diagnostic des machines asynchrones : modèles et outils paramétriques dédiés à la simulation et à la détection de défauts, PhD Thesis, Ecole centrale of Nantes, 1999.

[SCH 99b] SCHAEFFER E., LE CARPENTIER E., ZAÏM E.H., LORON L., "Diagnostic des entrainements électriques: détection de courts-circuits statoriques dans la machine asynchrone par identification paramétrique", *17e colloque GRETSI sur le traitement du signal et des images*, vol. 4, p. 1037-1040, Vannes, 13-17 September 1999.

[THO 93] THOLLON F., GRELLET G., JAMMAL A., "Asynchronous motor cage fault detection through electromagnetic torque measurement", *Proceedings of ETEP*, vol. 3, no. 3, September-October 1993.

[VAS 92] VAS P., *Electrical Machines and Drives*, *a Space Vector Theory Approach*, Oxford Science Publications, Oxford, 1992.

[YAH 95] YAHOUI H., SEETOHUL J., GRELLET G., JAMMAL A., "Detection of broken bar or end-ring fault in asynchronous machines by spectrum analysis of the observed electromagnetic torque through supply cable", *Revue Européenne de diagnostic et sûreté de fonctionnement*, vol. 5, no. 4, 1995.

Chapter 5

Thermal Monitoring of the Induction Machine

5.1. Introduction

This chapter analyzes the problem of temperature estimation in the stator and rotor electrical circuits of an induction machine. Its aim is not to give the best solution, but rather to present the main difficulties encountered by such a study. We will see that these problems can be found when implementing the estimation strategy, as well as in the experimental validation of the results.

Initially we will present the main reasons for the thermal monitoring of the induction machine, as well as the different available methods considered in scientific literature. We will then focus on approaches based on stator and rotor resistance estimations using the extended Kalman filter. Finally, we will examine a few experimental results obtained on a test bench carried in [FOU 05].

5.1.1. *Aims of the thermal monitoring on induction machines*

The thermal monitoring of an induction machine enables us to simultaneously meet several objectives, which can be classified in two groups depending on whether they relate to the availability of the machine or the tuning of its control.

Chapter written by Luc LORON and Emmanuel FOULON.

5.1.1.1. *Machine availability*

The first function of thermal monitoring is protection. This is especially significant as thermal overloads are one of the main initial causes of fault [GRU 08, SID 05, TAL 07].

This protection has several additional aspects:

– overload protection. Common protections rely on temperature probes positioned within the winding ends or equipment (fuses, thermal circuit breakers, digital systems etc.) which are based on very simple models [DU 08, GAO 06]. These two approaches have major disadvantages. The first category of solutions is relatively expensive for a low power machine, and requires additional wiring. The latter can be a source of fault (false alarm or non-detection). In addition, only part of the stator winding is monitored. The second approach may turn out to be inefficient, since the designers of the thermal protection systems generally focus on safety, at the risk of causing false alarms [GAO 06]. In return, users tend to eliminate these incidents by reducing the detection sensitivity, at the risk of making the protection ineffective. In this context, digital systems are more efficient, notably because of their configuration flexibility, which enables us to better adapt them to the machine operating conditions;

– thermal fault detection. In case of major modification of the thermal context of the machine, the latter risks fast overheating. This modification can be caused by breakdown, clogging of the ventilation system, rise in the room temperature or by the unexpected appearance of a new heat source (a fault in a neighboring machine, for example). The previously mentioned protection systems cannot detect this type of fault, since they only know the nominal thermal model of the machine;

– predictive monitoring and lifetime management. The windings accept a limited operating temperature corresponding to their class. When this temperature is exceeded, we consider the lifespan of the insulator to be divided by two for each rise in temperature by 10°C. By memorizing the thermal history of a machine, we can thus evaluate its residual lifetime and consider its predictive monitoring.

The induction machine has the reputation of being robust and inexpensive. We may then ask ourselves about the relevance of equipping it with a protection system. In fact, in some cases, it is not so much the destruction of the machine which is a penalizing factor, but rather its unavailability. We then need to install preventive or predictive maintenance, which will avoid any unscheduled intervention.

5.1.1.2. *Tuning of the machine control*

Thermal monitoring also enables us to tune the machine control, according to the evolution of its stator and rotor temperature:

– tuning the vector control. The rotor resistance R_r is one of the key-parameters of the indirect vector control, which is frequently used in industrial drives. Under the effect of the temperature, variations of R_r can mostly exceed 50%. To be at its optimum, a vector control must thus take these variations into account. Otherwise, we would notice on the one hand a deterioration in the dynamical performances of the response in the torque (but this is often concealed by the presence of a sufficiently robust speed loop), and on the other hand, which is more problematic still, an increase in machine losses, which increases its temperature further [NOR 85]. During the presentation of the experimental results, we observe the impact of the rise in the rotor temperature on the vector control;

– tuning the control without mechanical sensor. This type of control is very problematic at low speed, where the stator resistance R_s plays a predominant role [HOL 02]. Numerous control strategies without speed sensors thus incorporate an estimation mechanism of R_s.

5.1.2. *Main methods of thermal monitoring of the induction machines*

Thermal monitoring methods rely on the estimation of one or several temperatures within the machine. This estimation can be obtained with the help of a thermal model or through estimating the resistive parameters of an electrical model. We will classify the main methods, according to the type of model they operate: a thermal model, an electrical model, or both simultaneously. We will compare these strategies by highlighting their strengths and weaknesses.

5.1.2.1. *Methods based on a thermal model alone*

A thermal modeling of the machine is a complex multi-disciplinary problem and many approaches are possible [BOG 09, STA 05]. Nevertheless, to be exploitable in real-time without requiring excessive calculation power, a thermal model must have lumped constants and be of relatively low order. The most common models are of the first and second orders, and are generally represented by an equivalent R-C circuit. The order 2 seems to be the best compromise between complexity and efficiency. In addition, it enables us to separate stator and rotor monitoring.

We can consider an order reduction technique, to deduce a simplified model from a model obtained by fine nodal modeling (including up to several hundreds of nodes) [JAL 08]. But the most common approach is a black box approach, which relies on a relatively delicate experimental phase [MOR 01, STA 05], notably for a model of order 2 and a self-ventilated cage machine (the most common in the industry sector). The stator and rotor losses are then coupled and the thermal model is variable with the speed [SHE 05].

The model must also evaluate the main internal losses of the machine [DU 08, KRA 04, BOY 95]:

– Joule losses: they are the main term (more than 60% of the losses on low power machines) [DU 08, GRE 89]. These losses are easy to characterize, except for the fact that they depend on stator and rotor resistance, which themselves depend on temperatures;

– iron losses: they represent from 20% to 30% of the losses in low power and include the losses by hysteresis and the losses by eddy currents, which involve several factors (including the frequency, the amplitude and the waveform of the induction in the magnetic circuits). The iron losses are thus quite difficult to model [GRE 89];

– mechanical losses: these are the losses in the bearings and aerodynamic losses evolving according to the air density and thus once again, to the temperature. These losses are generally neglected, as they are the least significant ones (about 10% of the losses) and since their effect on temperature of the machine windings is negligible.

5.1.2.2. *Methods based on the estimation of resistive parameters*

We will now consider the estimation of the stator and rotor temperatures through one of the corresponding resistances R_s and R_r. This can be done by using an electric model alone or by coupling a thermal and an electrical model.

5.1.2.2.1. Methods based on an electrical model alone

The most frequent estimation techniques rely on a calculation of impedance in steady state [GAO 05a, GAO 05b, LEE 02, BEG 99] or on an extended Kalman filter, which is applied to a state model augmented with stator and rotor resistances [ALT 97, FOU 07, GAO 05c]. The latter are then considered as unknown parameters, randomly varying with slow dynamics. Some studies simultaneously propose an estimation of the speed [ALT 97, GAO 06].

Many authors highlight the problem raised by desensitizing R_s when the speed increases [DU 08, GAO 05c, LEE 02, WEI 07, WU 06]. This situation is all the more problematic as it is frequent and the stator is the most thermally fragile part. A similar difficulty appears with R_r when the machine is unloaded.

However, this is less critical, since in this case, the losses are low and the temperature tends to decrease. To sensitize R_s, we can consider periodically injecting a DC current into the machine [PAI 80, ZHA 08, ZHA 09]. Ideally, we would be able to do this during the stopping phases of the machine, in order not to interfere with its electromagnetic torque. To compensate for the desensitization of the stator and rotor resistances, we can also couple their variations, in an elementary way

(by a total coupling) or in a more subtle way with a thermal model (see following section). With a Kalman filter, during the adjustment of the covariance matrix of the state noise, we can possibly consider that the variations of R_s and R_r are strongly correlated. Finally, for low power machines which are supplied by the network and carry out frequent starting, it can be more convenient to only monitor the rotor temperature [BEG 99, GAO 05b].

In addition, as we will see later on, the other parameters of the electrical model and notably the L_m magnetization inductance must be known with sufficient accuracy [LEE 02]. We can then plan to take into account the variations of L_m by a saturation characteristic [FOR 06], as we will see in section 5.5, or to simultaneously estimate R_s, R_r and L_m [FOU 07].

5.1.2.2.2. Methods based on coupled electrical and thermal models

Another way of solving these desensitization problems would be to combine a thermal model with the electrical model. For this, several strategies have been proposed. The first one consists of writing a state model, associating electrical and thermal state variables. We then apply an extended Kalman filter to this global model [ALT 97, FOR 06, FOU 07].

As this approach is relatively sophisticated, other more simple solutions can be considered:

– [GAO 05c] uses an estimation of the rotor temperature, which is deduced from the estimation of R_r. It also uses a thermal model of the first order, to estimate the stator temperature using an extended Kalman filter;

– to estimate the rotor temperature, [KRA 04] alternately uses an estimation of R_r, deduced from the impedance measurement of the machine in steady state, and a first order thermal model, if the motor torque is too low;

– [GAO 05a] uses an adaptive thermal model of order 2 to estimate the stator temperature. In this model, the main term (the thermal conductance between the stator and its environment) is updated due to an estimation of the rotor temperature, deduced from estimation of R_r. This approach notably enables us to detect a ventilation fault.

5.1.2.3. *Comparison and assessment*

The main advantages of an approach based on a thermal model alone are related to its facility of implementation and to the low calculation power necessary for it. Indeed, the model only involves very slow dynamics. But this is an estimation of "open loop", which will be biased if the thermal model or the loss model is incorrect. This raises two major problems.

On the one hand, as previously stated, the main characteristic of this model is generally the thermal conductance between the stator and the outside. And yet, this conductance is not intrinsic to the machine, since it depends on its mechanical assembly. We thus need to consider an identification of the thermal model on site. But this is problematic and industrially unrealistic. On the other hand, this approach does not enable us to detect a modification of the room temperature or the thermal model after a ventilation problem, for example.

Methods based on resistive parameter estimations do not suffer from the previous disadvantages, since the modifications of the thermal environment no longer disturb the temperature estimation. It is even possible to detect them and diagnose a fault of the ventilation system. In addition, if we use a dynamic model of the machine, the flux can be estimated at the same time. This enables us to simultaneously carry out a direct adaptive vector control. However, these advantages come at a price, because the electrical model requires a high sampling frequency (often higher than 1 kHz) and thus a significant calculation power.

By exclusively relying on the electrical model, we can avoid all the problems related to determining the thermal model of the machine and the influence of room temperature. Short of having a long length of wiring which would affect the resistance and the leakage inductance at the stator, all the parameters of the electrical model are intrinsic to the machine. They can be determined in advance and are not specific to the machine operation. This approach thus seems to be the better suited one for an industrial context. However, the delicate problem of the resistance desensitization, and notably of R_s is yet to be solved. The methods based on the coupling of the electrical and thermal models aim at solving this problem, but they are relatively complex and rely on a thermal model, whose determination is not easy. However, the simultaneous exploitation of the electrical model enables us to reduce the impact of the errors made by the thermal model.

If we plan to build a global state model, it is better to rely on a reduced order electrical model, in order to eliminate the very fast dynamics of currents and to only preserve the dynamics of fluxes and that of the temperatures [FOU 05, FOU 07]. We can thus use a long sampling period and limit the numerical problems in the estimation algorithms.

In the following sections, we will consider the implementation of an extended Kalman filter, which is based on the electrical model alone. In a complementary way, we will find in [FOU 05], the implementation and the exploitation of an approach based on a global state model (electrical-thermal).

5.2. Real-time parametric estimation by Kalman filter

Our objective is thus to simultaneously estimate the magnetic state of the machine (in this case, its rotor flux) and the evolution of the mean stator and rotor temperatures. This is carried out mainly through estimating the resistances of the corresponding windings. We thus need to extract pieces of information, which are structured by a model, from experimental data which is more or less rich in information and more or less disturbed (due to noises, the inaccuracy of the measurements and the approximations of the model). When we work in real-time, this extraction requires recursive optimization techniques. The quality and the reliability of the obtained information depend on the pertinence of the model, as well as on the adequacy between the optimizer and the model. One of our priorities will thus be to define the pertinent models, as compared to the analyzed phenomena. The models would be fully compatible with the Kalman filter, which we will now present. The model definition will be discussed in section 5.3.

5.2.1. *Interest and specificities of the Kalman filter*

One of the main advantages of the Kalman filter is to jointly deliver estimations and their variance. We thus have at our disposal, not only the information but also its reliability. In some cases, the latter is equally as important as the estimation itself. Thus, in a fault detection system, the analysis of estimation variance can be a tool that would enable us to avoid false alarms. However, if we wish to have a realistic evaluation of the estimation variance, we need to be able to characterize the electronic noises and the model errors. But very often, it is a very delicate process. We will address the problems raised by the adjustment of the Kalman filter by suggesting a few reflection lines. We can adopt a diametrically opposite approach to the Kalman filter tuning and thus consider the covariance matrix of the noises as the tuning parameters of an optimum deterministic filter.

One of the main strengths of the Kalman filter is its robustness as its convergence is guaranteed when the system is observable. We often criticize the Kalman filter for being demanding in terms of calculation power. It is thus imperative, within the framework of a real-time implementation, to choose a sampling period with respect to the dynamics of the estimated quantities and not by constraints related to a clumsy discretization technique of a continuous model, as is often the case. We will revert to this in section 5.3.

Numerous variants of the filter have been suggested, notably in order to avoid the numerical problems linked to the evaluation of the ill-conditioned covariance matrix. Despite such variants, the most frequently used form in studies on the induction machine is the one that was initially suggested by Kalman [KAL 60]. Like

[CAV 89], we had preferred to use the Joseph algorithm, which is less sensitive to numerical errors, since it retains the symmetry of the covariance matrix better. In order to simultaneously estimate the state and the parameters of the machine, we use an extended Kalman filter. Since this filter poses a few divergence problems which are difficult to control, Ljung has suggested modifying it by introducing a corrective term, which involves the sensitivity of the Kalman gain on the estimated parameters [LJU 79]. However, this modification, which noticeably weighs on the algorithm, is rarely used. The extended Kalman filter uses a development of the first order of the non-linear expressions. Filters of higher order can be built on the basis of the Taylor expansion. We can thus find in literature filters of order two, or else iterative filters, which exploit several evaluations of the prediction and its variance by recalculating the tangent model around the last estimation. These approaches are generally too complex to be exploited in real-time.

5.2.2. *Implementation of an extended Kalman filter*

An extended Kalman filter is none other than a standard Kalman filter, in which the evaluations of the covariances are based on the tangent linearized model of a non-linear system. We will thus start by recollecting the standard Kalman filter algorithm.

5.2.2.1. *Kalman filter algorithm (Joseph form)*

Let us consider the discrete state model defined by:

$$\begin{cases} X_{k+1} = AX_k + BU_k + W_k \\ Y_k = CX_k + DU_k + V_k \end{cases} \quad [5.1]$$

where U_k, X_k and Y_k are the input, the state and the output of the model at time t_k respectively. W_k and V_k designate the state and output noises with the covariance matrix Q_k and R_k. In theory, these noises must be white, Gaussian, centered and de-correlated from the estimated state. We will revert to these restrictive hypotheses.

The Kalman filter is carried out by the following algorithm. The state prediction $X_{k+1|k}$ and the covariance matrix $P_{k+1|k}$ of its error are given by:

$$\begin{aligned} X_{k+1|k} &= AX_{k|k} + BU_k \\ P_{k+1|k} &= AP_{k|k}A^T + Q_k \end{aligned} \quad [5.2]$$

where $X_{k|k}$ is the optimum state estimation obtained at step k. The prediction of the output and its covariance are then:

$$\begin{aligned} Y_{k+1|k} &= CX_{k+1|k} + DU_{k+1} \\ \Sigma_{k+1} &= CP_{k+1|k}C^{T} + R_k \end{aligned} \quad [5.3]$$

Finally, the estimated optimum state at step $k+1$, as well as its covariance, are defined by:

$$\begin{aligned} X_{k+1|k+1} &= X_{k+1|k} + K_{k+1}\left(Y_{k+1} - Y_{k+1|k}\right) \\ P_{k+1|k+1} &= P_{k+1|k} - K_{k+1}\Sigma_{k+1}K_{k+1}^{T} \end{aligned} \quad [5.4]$$

with K_{k+1}, the Kalman gain given by:

$$K_{k+1} = P_{k+1|k}C^{T}\Sigma_{k+1}^{-1} \quad [5.5]$$

5.2.2.2. *Extended state model*

In order to simultaneously estimate the state X_1 of a system and a vector X_2 of parameters, we define the following extended state vector:

$$X = \begin{bmatrix} X_1 \\ X_2 \end{bmatrix} \quad [5.6]$$

Generally, the discrete time model involving the state noise W_k and the output noise V_k is written:

$$\begin{cases} X_{k+1} = \begin{bmatrix} X_{1,k+1} \\ X_{2,k+1} \end{bmatrix} = \begin{bmatrix} F_1(X_k, U_k) + W_{1,k} \\ F_2(X_k, U_k) + W_{2,k} \end{bmatrix} = F(X_k, U_k) + W_k \\ Y_k = G(X_k, U_k) + V_k \end{cases} \quad [5.7]$$

As previously discussed, we will respectively note Q_k and R_k, the covariance matrix of the state noises W_k and of the output noises V_k. When the initial state model (with the state vector X_1) is linear, we can use the classical matrix notations:

$$\begin{cases} X_{1,k+1} = A(X_{2,k})X_{1,k} + B(X_{2,k})U_k + W_{1,k} \\ Y_k = C(X_{2,k})X_{1,k} + D(X_{2,k})U_k + V_k \end{cases} \quad [5.8]$$

It is quite common not to have at our disposal an evolution model of the parameters. Their variations are then supposed to be purely random, by writing:

$$X_{2,k+1} = X_{2,k} + W_{2,k} \qquad [5.9]$$

In that case, only the correction stage of the Kalman filter enables us to estimate the evolution of the parameters. It is thus better to have a dynamic evolution model of the parameters. For the considered application, this means a thermal model of the machine.

5.2.2.3. *Algorithm of the extended Kalman filter*

The prediction stage henceforth includes the prediction of the $X_{2,k+1|k}$ parameters in the extended state prediction:

$$\begin{cases} X_{k+1|k} = \begin{bmatrix} X_{1,k+1|k} \\ X_{2,k+1|k} \end{bmatrix} = \begin{bmatrix} F_1(X_{k|k}, U_k) \\ F_2(X_{k|k}, U_k) \end{bmatrix} = F(X_{k|k}, U_k) \\ Y_{k+1|k} = G(X_{k+1|k}, U_{k+1}) \end{cases} \qquad [5.10]$$

In order to determine the covariance of the prediction, it is necessary to linearize the model which has become non-linear due to the extension of the state.

For this, we calculate the Jacobian of the extended state function:

$$\frac{\partial F}{\partial X\kappa}\left(X_{\kappa+1|k}, \mathrm{U}_\kappa\right) = \left[\begin{matrix} \frac{\partial F_1}{\partial X_{1,\kappa}} & \frac{\partial F_1}{\partial X_{2,\kappa}} \\ \frac{\partial F_2}{\partial X_{1,\kappa}} & \frac{\partial F_2}{\partial X_{2,\kappa}} \end{matrix}\right]_{X_{k+1|k}, U_K} \qquad [5.11]$$

We can thus express the covariance of the error on the prediction of the extended state:

$$P_{\kappa+1|\kappa} = \frac{\partial F}{\partial X_\kappa}\left(X_{\kappa+1|\kappa}, U_\kappa\right) P_{\kappa|\kappa} \frac{\partial F}{\partial X_\kappa}^T\left(X_{\kappa+1|\kappa}, U_\kappa\right) + Q_\kappa \qquad [5.12]$$

Concerning the correction stage, we need to define the Kalman gain, from the calculation of the Jacobian of the output function:

$$\frac{\partial G}{\partial X_k}\left(X_{k+1|k}, U_{k+1}\right) = \left[\frac{\partial G}{\partial X_{1,k}} \frac{\partial G}{\partial X_{2,k}}\right]\Bigg|_{X_{k+1|k}, U_{k+1}} \quad [5.13]$$

$$K_{k+1} = P_{k+1|k} \frac{\partial G}{\partial X_k}^T \left(X_{k+1|k}, U_{k+1}\right) \Sigma_{k+1}^{-1} \quad [5.14]$$

with the covariance of the error on the output prediction defined by:

$$\Sigma_{k+1} = \frac{\partial G}{\partial X_k}\left(X_{k+1|k}, U_{k+1}\right) P_{k+1|k} \frac{\partial G}{\partial X_k}^T \left(X_{k+1|k}, U_{k+1}\right) + R_k \quad [5.15]$$

Finally, after correction, we obtain the optimum estimation of the state and of the parameters:

$$X_{k+1|k+1} = \begin{bmatrix} X_{1,k+1|k+1} \\ X_{2,k+1|k+1} \end{bmatrix} = X_{k+1|k} + K_{k+1}\left(Y_{k+1} - Y_{k+1|k}\right) \quad [5.16]$$

The error covariance on the optimum estimation of the extended state is then defined by:

$$P_{k+1|k+1} = P_{k+1|k} - K_{k+1} \Sigma_{k+1} K_{k+1}^T \quad [5.17]$$

5.2.2.4. *Initialization of the Kalman filter*

Although this subject is rarely discussed, for some of the applications the initialization of the extended Kalman filter can be critical. This is notably the case for the estimation of the rotor parameters of the induction machine, since the rotor flux determines the sensitization of the rotor parameters: when the flux is null, these parameters are completely desensitized. The Kalman filter may certainly diverge if an null initial state is chosen, like in most cases. If we seek to only initialize the state of the model, we can apply a deterministic observer at the beginning of the test sequence and thus estimate the state before launching the extended Kalman filter.

However, it is clearly better to simultaneously evaluate the covariance matrix of the initial state, by taking into account the state noise $W_{1,k}$ and the structure noise induced by the initial variance of the parameters. It is best to use a specific Kalman filter, which is in fact the previous extended filter, in which the vector of the estimated parameters and its covariance matrix are frozen at their initial values. For this, we need to cancel the correction phase of the parameters in the extended filter [LOR 00].

Since this second filter does not estimate any parameters, its initialization does not pose any problem; this time, we can use a null initial state, to which we would

allocate a large variance. This filter is applied for a sufficient duration, in order to enable it to converge. We then change over to the extended Kalman filter, by keeping the last value of the state and the covariance matrix estimated by the filter. We thus obtain an optimum and coherent initialization (state and covariance) of the extended filter. This results in a good initial behavior and a fast convergence of the estimations of the parameters. This mechanism can also be used to temporarily fix the parameter estimation, if we are able to detect a loss of identifiability of this parameter. Thus, in the case of the induction machine, it is safer to stop the rotor resistance estimation, as soon as the reference torque becomes too low.

5.2.2.5. *Tuning of the covariance matrices*

The tuning of the covariance matrix of the state and output noises is a delicate matter, especially when we wish to obtain an evaluation of the estimation variance. Let us be realistic: unless we are in an ideal situation, i.e. if we have white and centered noises which are un-correlated with the estimated states, as well as a perfectly linear model, we will often only obtain a rough evaluation of the variances. This is especially true in the case of an extended Kalman filter. However, it is often worth trying to adjust at best the variances of the noises $W_{1,k}$ and V_k, by analyzing the different error sources, whether they are instrumental or due to modeling errors. This notably enables us to evaluate the impact of these different error sources on the estimations, and possibly reconsider a sensor choice or an excessive approximation.

On the contrary, the noises $W_{2,k}$ affecting the parameters generally do not have any physical reality. These are above all degrees of freedom, which characterize the dynamics of the parameters. By choosing a high variance, we favor significant dynamics. Conversely, a low variance produces a smoothing of the estimation. In practice, this adjustment is carried out by a trial and error approach, since the factors influencing the dynamics of the estimation are many (the informational content of the data, the discretization period, the other variances etc.). We will then revert to section 5.5 to the tuning of the covariance matrix in the case of the induction machine.

5.3. Electrical models for the thermal monitoring

As mentioned in the introduction, we will consider electrical models only, so as not to be confronted with the problems raised by the identification and exploitation of thermal models. Due to these models and an extended Kalman filter, we would estimate the stator and rotor resistances for deducing the corresponding temperatures.

The models that we will build must satisfy the constraints related to using an extended Kalman filter. We will notably need to linearize the extended model

around the current operating point. But the main problem would be posed by the real-time implementation, because of the significant difference of the dynamics of the state variables; typically the response time of the currents is counted in milliseconds, the response time of the fluxes in seconds and the response time of the temperatures in hours.

The currents are accurately measured. Thus, we would define a reduced order model which will only involve the fluxes and the resistances as state variables. We will thus be able to work with long discretization periods and lighten the algorithmic cost of the Kalman filter.

5.3.1. *Continuous time models*

In conformity to the previous remarks, we would define an electrical model optimized for estimating the resistances in real-time. For this, the dynamics of the stator currents won't be taken into account. To write this model, we will use the following usual assumptions:

– the electromotive force in the air gap has sinusoidal spatial distribution;

– the machine is not magnetically saturated;

– the neutral of the machine is isolated and the three-phase winding is symmetrical;

– the skin effect, the slot effects and, initially, the iron losses are neglected.

We would use a three-phase/two-phase transformation, which preserves the amplitudes and not the powers. This results in a factor of 3/2 in the expression of the electromagnetic torque of the machine. Finally, we would take advantage of the degree of freedom given by the distribution of the magnetic leakages between the stator and rotor, in order to group together these leakages on the stator. This conforms to the equivalent diagram of Figure 5.1a [LOR 07].

This leakage distribution will simplify the writing of the reduced order model, while making the model completely identifiable. We will note R_s, the resistance of the stator winding, R_r, the resistance of the rotor winding or cage, L_m, the magnetization inductance and L_{fs}, the global leakage inductance. These parameters appear in the equivalent steady state diagram of Figure 5.1a, where g represents the machine slip.

5.3.2. *Full-order model*

In complex notations ($j^2 = -1$), the electrical equations of the machine are expressed by:

$$\begin{cases} U_s = R_s I_s + j\omega_x \varphi_s + \dfrac{d\varphi_s}{dt} \\ 0 = R_r I_r + j(\omega_x - \omega_m)\varphi_r + \dfrac{d\varphi_r}{dt} \\ \varphi_s = L_s I_s + L_m I_r \\ \varphi_r = L_m I_r + L_m I_s \\ C_{em} = \dfrac{3}{2} p L_m \operatorname{Im}(I_s I_r^*) \end{cases} \quad [5.18]$$

These equations are expressed in any rotating frame at the angular frequency ω_x. U_s designates the stator voltage; I_r and I_s are respectively the rotor and stator currents; φ_r and φ_s are the rotor and stator fluxes; $L_s = L_{fs} + L_m$ and L_m designate the stator and magnetizing inductances. The machine has p pole pairs. It has a rotating mechanical part at the $\Omega_m = \omega_m / p$ speed and produces an electromagnetic torque C_{em}.

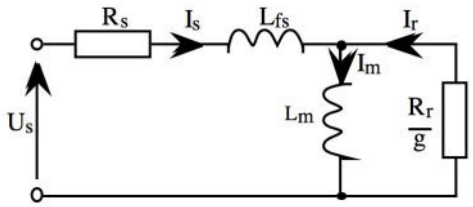

a)

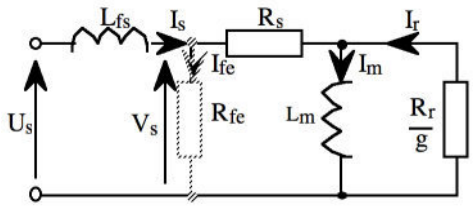

b)

Figure 5.1. *Equivalent diagram with leakages gathered at the stator (a) and reorganized diagram with optional iron losses (b)*

5.3.2.1. *Reduced order model*

By assuming the mechanical speed to be constant or slowly variable, the Park model of the induction machine leads to a state model of order 4, whose inputs and outputs are respectively the two-phase components of the stator voltages and currents. This model turns out to be very poorly adapted to real-time applications, due to the required computational cost.

Indeed, the discretization of the model supposes the calculation of the exponential of its state matrix. The exact value of this exponential can be obtained by diagonalizing this matrix. This requires a heavy calculation for a 4th order model. This is why many authors use 1st or 2nd approximations. In the case of a small sampling period, a 1st order approximation can respect the dynamics of the continuous model, but requires a high calculation level. If it is imperative to use periods longer than one millisecond, this implies a 2nd order approximation of the matrix exponential. In addition, the implementation of the extended Kalman filter requires the linearization of the discrete model with respect to the estimated parameters. This linearization is much heavier in the case of a 2nd order approximation. We will thus use a different approach, simultaneously enabling us to reduce the dimension of the state vector and to obtain an accurate discretization, for sampling periods longer than 10 ms.

From [5.18], we can write a pseudo-state-space model, where the stator current and rotor flux respectively represent the input and state variables. The output Y corresponds to the stator voltage U_s, from which we have subtracted the voltage drop in the leakage inductance L_{fs} (see Figure 5.1b).

For this, we would need to evaluate the derivative of the currents. In practice, this calculation does not pose any particular problems, since the current measurements are accurate and relatively little disturbed. The complex equations of the model in continuous time are then written:

$$\begin{cases} \dfrac{d\varphi_r}{dt} = \left(-\dfrac{R_r}{L_m} + j\left(\omega_m - \omega_x\right) \right) \varphi_r + R_r I_s \\ V_s = U_s - L_{fs}\left(\dfrac{dI_s}{dt} + j\omega_x I_s \right) = \left(-\dfrac{R_r}{L_m} + j\omega_m \right) \varphi_r + \left(R_s + R_r \right) I_s \end{cases} \quad [5.19]$$

By noting $U^T = \left[I_{s\alpha} \;\; I_{s\beta} \right]$, $X_1^T = \left[\varphi_{r\alpha} \;\; \varphi_{r\beta} \right]$ and $Y^T = \left[V_{s\alpha} \;\; V_{s\beta} \right]$, we obtain the following state-space model:

$$\begin{cases} \dot{X}_1 = A_c X_1 + B_c U \\ Y = C X_1 + D U \end{cases} \quad [5.20]$$

with:

$$A_c = -\frac{R_r}{L_m} \mathrm{I}_2 + (\omega_m - \omega_x) \mathrm{J}_2,\ B_c = R_r \mathrm{I}_2,\ C = -\frac{R_r}{L_m} \mathrm{I}_2 + \omega_m \mathrm{J}_2,\ D = (R_s + R_r) \mathrm{I}_2,$$

$$\mathrm{I}_2 = \begin{bmatrix} 1 & 0 \\ 0 & 1 \end{bmatrix} \text{ and } \mathrm{J}_2 = \begin{bmatrix} 0 & -1 \\ 1 & 0 \end{bmatrix}$$

Lastly, we have to select the reference frame. We generally avoid the stator reference frame, which leads to too large angular frequency signals and requires very small sampling periods. We could consider a synchronous reference frame linked to an electrical signal, notably the stator currents. This would be pertinent for an application without mechanical sensor. If we have at our disposal a mechanical sensor, the best choice seems to be the mechanical reference frame of angular frequency $\omega_x = \omega_m$.

In this case, not only do the signals have a small angular frequency in steady state (a few Hz due to the slip), but above all, the state matrix A_c becomes diagonal. This significantly simplifies the discretization of the state model. It then becomes possible to work with long sampling periods, all the more that the inputs of the reduced order model (the currents) have much lower dynamics during transients than the ones of the 4th order model (the voltages).

This model has been successfully used for the real-time estimation of the electrical parameters of the induction machine [LOR 00, LOR 07]. There are other approaches leading to a reduced order model. We can find in [THI 01] a summary of these different approaches. The one that we have chosen involves at least the electrical parameters of the machine in a very simple way. This will significantly facilitate the calculation of the linearized model.

5.3.2.2. *Modeling of the iron losses*

Any modeling error affecting the evaluation of the active power absorbed by the machine may have an impact on the real-time estimation of the stator and rotor resistances. Logically, we should take into account the iron losses of the machine; neglecting them could lead us to overestimate the Joule losses and thus the stator and rotor resistances.

Unfortunately, taking into account iron losses raises a delicate problem, because, to our knowledge, there is no dynamical model including them. The most common

approach consists of introducing a resistance in the equivalent diagram in parallel to the magnetization inductance. This solution is thus only exploitable in steady state. In addition, the additional resistance is variable with the operating point and is variable with the operating point defined by the stator frequency and the flux amplitude.

In [FOU 05], we have tried to take iron losses into account, by slightly modifying the state-space model [5.20], in order to preserve its simplicity. Thus, if we introduce a resistance R_{fe} conforming to the diagram in Figure 5.1b, we have only to modify the value of the stator current according to $I_s^{'} = I_s - I_{fe}$. This simplistic approach has provided disappointing results, sometimes leading to negative estimations of the stator resistance. This problem notably appears in high speed or during fast transients, because in both cases, the iron losses are overestimated. We will thus not take into account the iron losses in in the following sections.

5.3.3. *Discretized and extended model*

5.3.3.1. *Discretization*

The writing of an exact discrete-time model is only possible if we know the evolution of the input signals during the discretization period T_e. Thus, the control models assume that the inputs are constant. If, as in our case, this assumption is not verified, the previous studies [LOR 00] show that we are already quite significantly improving the accuracy of a discrete-time model by introducing a linear interpolation. This leads us to inject the average input, which is defined by $\bar{U}_k = \left(U_k + U_{k+1}\right)/2$, in the discrete-time model. The latter will have the following structure:

$$\begin{cases} X_{1,k+1} = A_d X_{1,k} + B_d \bar{U}_k \\ Y_k = C X_{1,k} + D U_k \end{cases} \qquad [5.21]$$

The dynamic matrix Ac is diagonal. Therefore, the writing of the discrete time model is very easily carried out and without approximation. This will allow long periods T_e:

$$A_d = e^{A_c T_e} = a_k \mathrm{I}_2$$

$$B_d = A_c^{-1}\left(A - \mathrm{I}_2\right) B_c = b_k \mathrm{I}_{22} \qquad [5.22]$$

with $a_k = e^{-\frac{R_{r,k}}{L_{m,k}} T_e}$ and $b_k = L_{m,k}\left(1 - a_k\right)$.

We can notice that the resistive parameters appear in all the matrix of the discrete-time model. It will thus be necessary to update the complete model in case of temperature variations. In addition, the output matrix C varies with the mechanical speed ω_m.

5.3.3.2. *Extended model for the estimation of R_s and R_r*

The objective of this extended model is to enable simultaneous estimation of the rotor flux and the stator and rotor resistances.

We thus have $X_{2,k}^T = \left[R_{s,k} \; R_{r,k} \right]$. The state and output functions are then given by:

$$F(X_k, \bar{U}_k) = \begin{bmatrix} a_k \varphi_{r\alpha,k} + b_k \bar{I}_{s\alpha,k} \\ a_k \varphi_{r\beta,k} + b_k \bar{I}_{s\beta,k} \\ R_{s,k} \\ R_{r,k} \end{bmatrix} \quad [5.23]$$

$$G(X_k, U_k) = \begin{bmatrix} \left(R_{s,k}+R_{r,k}\right) I_{s\alpha,k} - \varphi_{r\alpha,k} R_{r,k} L_{m,k}^{-1} - \varphi_{r\beta,k} \omega_{m,k} \\ \left(R_{s,k}+R_{r,k}\right) I_{s\beta,k} - \varphi_{r\beta,k} R_{r,k} L_{m,k}^{-1} + \varphi_{r\alpha,k} \omega_{m,k} \end{bmatrix} \quad [5.24]$$

with $\bar{I}_{s,k} = \left(I_{s,k} + I_{s,k+1}\right)/2$. The Jacobians of the extended state function and of the output are finally expressed by:

$$\frac{\partial F}{\partial X_k} = \begin{bmatrix} a_k & 0 & 0 & T_e a_k \bar{I}_{r\alpha,k} \\ 0 & a_k & 0 & T_e a_k \bar{I}_{r\beta,k} \\ 0 & 0 & 1 & 0 \\ 0 & 0 & 0 & 1 \end{bmatrix} \quad [5.25]$$

$$\frac{\partial G}{\partial X_k} = \begin{bmatrix} -R_{r,k} L_{m,k}^{-1} & -\omega_{m,k} & I_{s\alpha,k} & I_{r\alpha,k} \\ \omega_{m,k} & -R_{r,k} L_{m,k}^{-1} & I_{s\beta,k} & I_{r\beta,k} \end{bmatrix} \quad [5.26]$$

with $\bar{I}_{r,k} = \left(\bar{I}_{s,k} - \varphi_{r,k}/L_m\right)$ and $I_{r,k} = \left(I_{s,k} - \varphi_{r,k}/L_m\right)$ the average and instantaneous rotor currents.

5.3.3.3. *Evaluation of the stator and rotor temperatures*

The link between the resistance and temperature variations is carried out through temperature coefficients α_s and α_r of the stator (copper) and rotor (copper or aluminum) windings:

$$\begin{cases} R_r = R_{rRef}\left(1+\alpha_r\left(T_r - T_{Ref}\right)\right) \\ R_s = R_{sRef}\left(1+\alpha_s\left(T_s - T_{Ref}\right)\right) \end{cases} \quad [5.27]$$

with $\alpha_{Cu} = 3.93\ 10^{-3}\ °C^{-1}$ and $\alpha_{Al} = 4.03\ 10^{-3}\ °C^{-1}$. R_{sRef} and R_{rRef} designate the values of the stator and rotor resistances at the T_{Ref} temperature. These reference values can be determined in two ways. As they are intrinsic to the machine, we can determine them beforehand. We can also evaluate them on-site, at the starting of the converter-machine set. Thus, R_{sRef} will be determined during the magnetization of the machine and R_{rRef} will be determined as soon as the machine produces a significant torque. In most of the applications, we will be able to suppose that at this instant, the stator and rotor temperatures are equal to the easily measurable room temperature.

5.4. Experimental system

In the context of this study, the objective of a test bench is to allow the comparison of the temperature or resistance estimations with the corresponding measurements. This would pose many problems, which will be mentioned in this section. In fact, we will have to measure signals of very different natures (electrical, mechanical and thermal) in a disturbed environment, due to the static converter and sometimes moving elements (rotor). In addition, some quantities are local (temperatures) and others are global (resistances).

5.4.1. *General presentation of the test bench*

On the test bench presented in [FOU 05], we have three machines: two induction machines of 4 kW on which are carried out the measurements and one synchronous load machine (Figure 5.2).

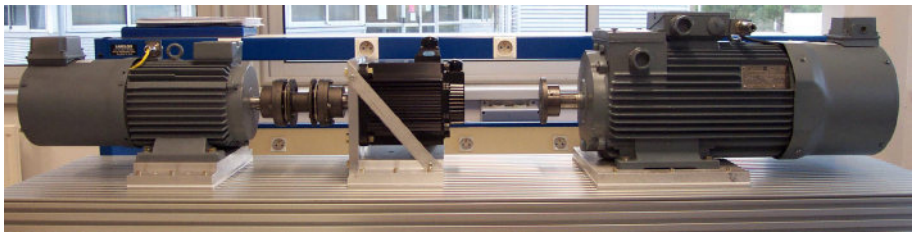

Figure 5.2. *Test bench machines*

The induction machines are supplied by a three-phase inverter piloted by a dSPACE DS1103 system. The synchronous machine is controlled by an industrial speed drive. The dSPACE board simultaneously ensures the vector control of the tested machine and the acquisition of the electrical and mechanical signals. The temperature and resistance measurements are carried out by a Fluke datalogger. The synoptic of the bench control is presented by Figure 5.3.

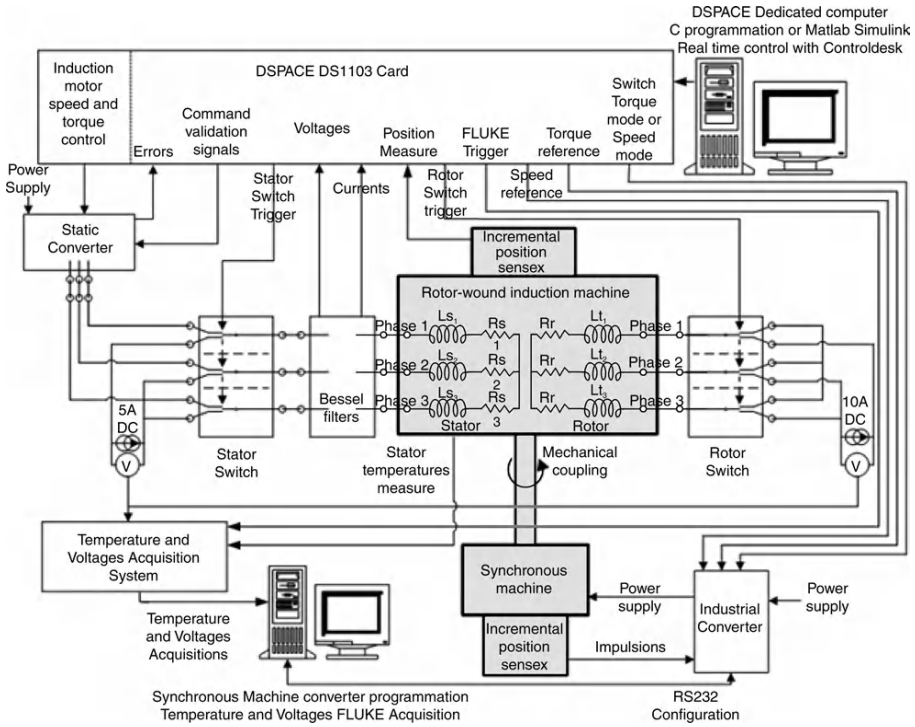

Figure 5.3. *Synoptic of the bench control*

5.4.1.1. *Machines*

The first induction machine (on the left of Figure 5.2) has a squirrel-cage rotor, which is typical for industrial machines. It thus represents the preferred scope. The second machine (on the right) is a slip-ring machine, which is much more expensive and whose use is more specific. By authorizing rotor resistance measurements, it enables us to carry out additional tests.

Each one of these machines can be coupled with the load machine. The nameplate of these machines and their main features are presented in Table 5.1. Each induction machine is equipped with an incremental encoder, which supplies 2,048 pulses/rev. This enables speed measurements.

With an aim to identify and operate the thermal model of a machine alone, it was necessary to minimize the thermal exchanges between the machines. We have connected them by a rigid coupling in torsion, but enabling a flexibility of layout and limiting the thermal exchanges between the machines. The three machines are placed on a metal support. We are therefore required to limit the thermal exchanges through the support. An insulation was provided with the help of a thermally insulating plate, which was inserted between the support of each machine and the bench (white plates visible in Figure 5.2, at the base of each machine).

5.4.1.2. *Power electronics*

The tested induction machine is supplied by a three-phase inverter manufactured by the ARCEL company. The power block is made up of four IGBT legs, of their drivers and protections. The fourth leg is devoted to the dissipation of the braking energy. The DS1103 board ensures all the control tasks: the generation of the MLI at 10 kHz, the control of the stator currents and the vector control of the machine. However, the control of the synchronous machine is put in charge of an industrial drive, which enables us to either control the torque or the speed of the machine. The change of operating mode (torque or speed) is piloted by the DS1103 board, as well as the corresponding reference value.

5.4.2. *Thermal instrumentation*

5.4.2.1. *On the induction machine stator*

We have installed thermocouples in the stator windings of the induction machines, within the slots and winding ends, so that we are able to carry out weighted averages. The layout of the thermocouples in the windings appear easy, but it is actually not easy to obtain a correct contact between the thermocouple and the winding in the slots. This is especially difficult in the case of the wound rotor machine, since the free space in the slots is much more restricted than for the

squirrel-cage machine. Concerning the winding ends, we would always find a place to insert the thermocouples. The main problem is to keep them there. Ideally, we should set the thermocouples at well-defined places, during the winding of the machine.

5.4.2.2. *On the squirrel-cage machine rotor*

Due to the restricted space available for instrumentation of the squirrel-cage machine rotor, we had decided to use an infrared sensor, so that a mean value of the rotor temperature could be obtained. In order to calibrate this measurement with respect to the emissivity of the rotor (painted in black), we had drilled upto a low depth in the rotor, so that we could insert a thermocouple in it. The measurements by the thermocouple are evidently only possible during rest. The infrared sensor enables us to make observations in different areas of the rotor through drilling in the back end flange of the machine. It gives the mean value of the temperature of the short-circuit ring, when the machine is rotating.

5.4.2.3. *At the rotor of the slip-ring machine*

The wound rotor of the second machine is more favorable for inserting the thermocouples. They allow us to continuously measure the temperatures during the locked rotor tests (for implementing a thermal model, for example). However, when tests are to be conducted when the machine is rotating, it is necessary to stop the machine for a short while, so that the thermocouples can be connected. This is a smaller problem, while waiting for an information transfer system, since the wound rotor induction machine already supplies an indication on its rotor temperature by measuring its rotor resistance.

5.4.2.4. *Acquisition of thermal measurements*

The acquisition of the temperature measurements has been carried out with the help of a Fluke datalogger coupled to a laptop (the transfer of the data in real-time, directly towards the DS1103 board not being possible). This would enable us to record 20 measurement channels in an almost unlimited way in time, with an acquisition period set at 20 s. The datalogger enables the exploitation of quite common thermocouples, as well as the measurement of DC voltages. The latter will be used for the determination of the stator and rotor winding resistances (on the slip-ring machine). We will revert to these measurements in the following section. In order to synchronize the measurements of the Fluke datalogger with the ones of the dSPACE board, the latter sends a trigger signal, which launches a sequence of automatic measurements of the activated channels.

5.4.3. *Electrical instrumentation*

Electrical instrumentation initially involves the stator current and voltage sensors. These measurements would be injected into the Kalman filter. We could manage without the voltage measurements and use their references, provided that we carry out an efficient compensation for the dead times of the inverter. And this is not an easy task.

In addition, considering the difficulties encountered during the thermal instrumentation of the machine and the definition of a thermal model, we have decided to measure the stator and rotor resistances during the test. This would enable us to evaluate the efficiency of the Kalman filter independently from the thermal aspects. We will thus be able to compare the measured and estimated global quantities (resistances) while the temperature measurements are local by nature.

5.4.3.1. *Measuring and filtering chain for stator voltages and currents*

In order to enable the measurement of the stator currents and voltages of the machines, we have used a measuring system intercalated between the inverter and the machine (Figure 5.3). This system measures two line currents and two voltages between phases, with the help of Hall effect sensors. These sensors guarantee galvanic insulation between the power part of the inverter and the instrumentation. To limit the aliasing phenomena due to pulse-width modulation at 10 kHz, we have used Bessel filters of order 5, with switched capacitors and a cut-off frequency of 1 kHz (this value offers a good compromise between the efficiency of the filter and its delay). This technology enables us to carry out high order filters with adjustable cut-off frequencies and with a good matching between filters.

We can thus minimize the phase differences between tracks, which would induce identification errors. However, the filters with switched capacitors have a slight offset. Unfortunately, no ideal filtering solution is currently available for a relatively low cut-off frequency of about 1 kHz.

5.4.3.2. *Measurement of the resistances*

With the aim of using the winding resistances as integrated sensors, we have established a real-time measurement method of the winding resistance during the tests. These measurements should be carried out quickly. During the whole evolution of the temperature, we have used a voltmeter-ammeter approach, which is simpler to implement and automatize than a bridge circuit. The voltmeter-ammeter approach has been restricted with a DC supply which is controlled and is placed in the current limitation mode, so that the supply currents are not measured. We would need ensure that the supply reaches its thermal steady state before commencing the measurements; otherwise, the current would slightly vary.

Finally, in order to be able to commute windings on the stator and the rotor in the case of the wound rotor induction machine, we have installed power relays (Figure 5.3). They commute at the stator the supply by the ARCEL inverter and a DC supply controlled in current. They also commute short-circuit on the rotor between the three phases and a second power supply controlled in the current. These relays are controlled by the dSPACE board.

Given the very low value of the measured resistances, notably at the rotor of the slip ring machine (of about 0.15 Ω), some precautions would have to be taken.

Thus, during the installation of these relays, we had carried out measurements of comparative resistances, in order to determine the resistance added by the relays, as well as the voltage drop, which has been introduced by the slip ring contact. It turned out that the resistance values, which were calculated by the voltmeter-ammeter method, were different from the ones estimated by the Kalman filter. This is later based on the data given by the measurement chain, which is presented in the previous section.

By observing the difference of the voltage measurements between the two devices under a same DC supply, we were able to correct the systematic bias on the measurement. At the rotor, the bias has been reduced by particularly taking care of the wiring: the use of an unsuitable connector technology (banana plugs) and the presence of a too long cable (2 m) doubled the rotor resistance. In addition, with the resistance of the slip-ring contact varying with the rotor position, it is quite delicate to carry out an accurate estimation of the rotor resistance. To reduce this problem, we have used an average measurement obtained on an integer number of turns carried out at 1 rev/s.

5.4.3.3. *Measurement protocol of the resistances*

The measurement of the resistances on the stator and rotor of the wound rotor machine requires a complex sequence. Indeed, it is necessary to briefly interrupt the normal course of the test, in order to launch a measurement sequence including the injection of the DC currents and the measurement of the resulting voltages.

In addition, we would need to take some precautions concerning the progressive stopping of the control of the induction machine. We need to monitor the flux of the induction machine, its speed loop, the control in torque or in speed of the load machine, and finally the complete stop of the inverter, to avoid the interference on the measurements of the resistances and temperatures caused by the pulse-width modulation.

The measurement sequence has been automated, in order to be as short and unintrusive as possible. The timing diagram associated with the measurement

sequence described above is visible on Figure 5.4. Despite the obvious sequence of the phases, it is necessary to provide several observations. The defluxing and fluxing operations of the machine are carried out at null speed, so that the vector control is not disturbed. During the voltmeter-ammeter measurements, it is necessary to insert a temporization between the closing of the relays and the voltage measurements, to give time to the supplies to change over to the current limitation mode.

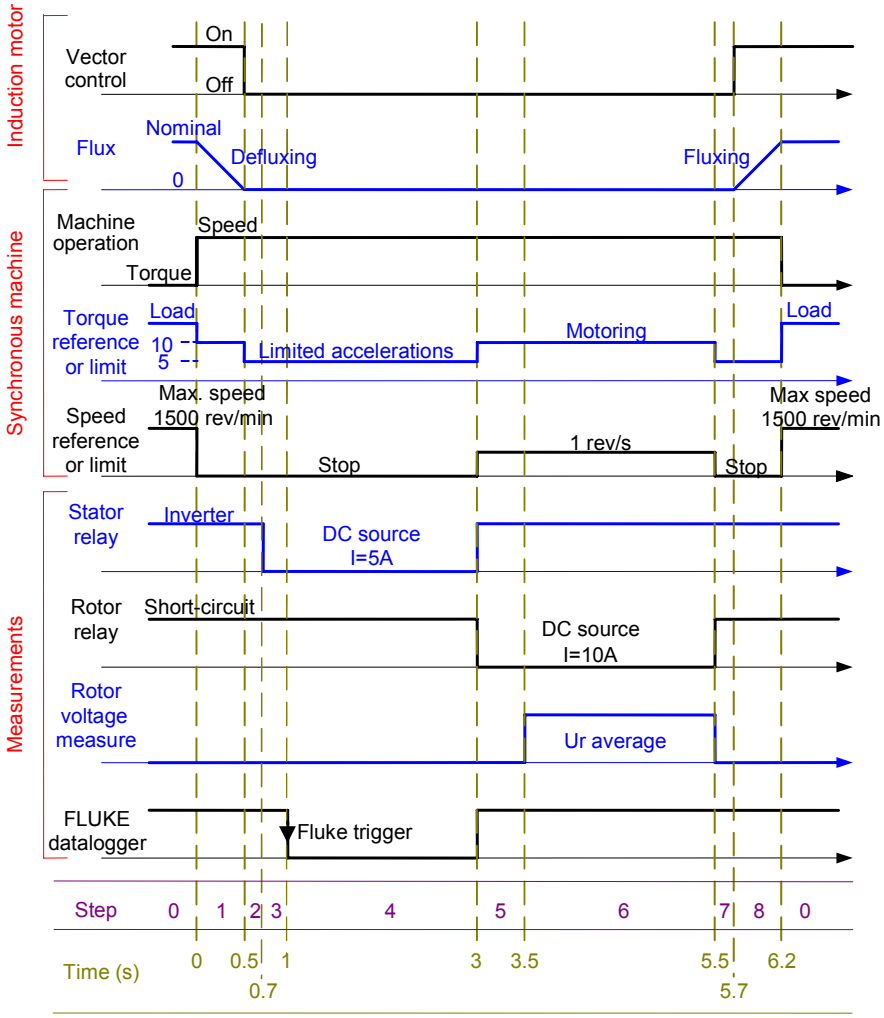

Figure 5.4. *Measurement sequence of the temperatures and resistances*

The relatively long time allocated to the measurement by the Fluke datalogger is due to the sequence backup of the channels. Despite the use of the fast mode which forces us to loose one digit of accuracy during the measurements, the measurement by this device remains the longest one. Finally, the measurement of the rotor voltage takes 2 s, so that we could carry out an average of two complete turns at slow speed, as previously mentioned.

5.4.3.4. *Temperature and resistance measurements*

Figure 5.5 shows the temperature and resistance measurements obtained during a test on the ring machine. The machine has been locked up in a box, in order to accelerate its rise in temperature. The upper diagram gathers the data supplied by the thermocouples set at the stator of the machine.

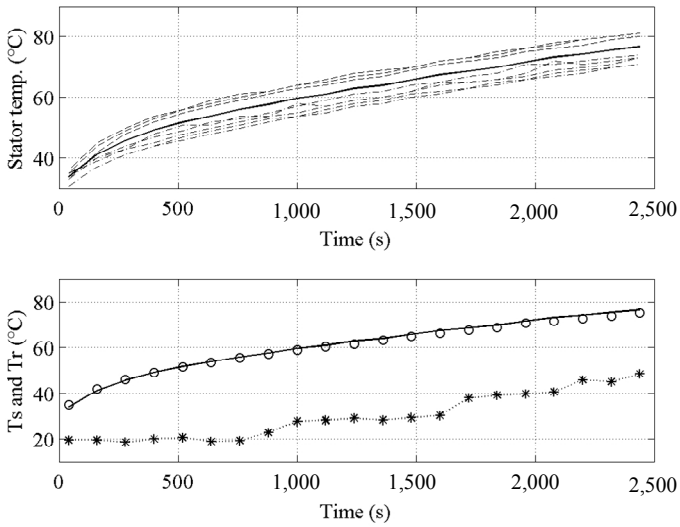

Figure 5.5. *Temperature measurements*

We observe that the average temperature of the thermocouples located in the winding ends (dotted lines) is higher than the temperature of the thermocouples located in the slots (mixed lines). The difference is of about 8°C.

Later on, we will use the average of these two temperatures (thick continuous line). The diagram below superimposes this last result on the temperature obtained from measurements of the stator resistance (circles). The correspondence is excellent. The second curve (stars) shows the rotor temperature deduced from the measurement of the rotor resistance.

We can note that despite all the precautions taken for the measurement of R_r, this remains disturbed. This results in temperature undulations.

5.5. Experimental results

The experimental results which we will analyze concern the comparison of the measurements and the estimations of the stator and rotor resistances. The tests have been carried out on the wound rotor machine giving access to R_r. The main advantage of this choice is that we can compare global pieces of information (resistances), and that the thermal aspects and their localization do not have to be taken into account. But if we estimate the resistances, we would have to deduce the temperature variations first.

5.5.1. *Tuning of the Kalman filter*

Initially, we will specify the tuning of the Kalman filter and observe the impact of this tuning and of the measurement protocol of the R_s and R_r resistance estimation. In fact, this protocol relies on the injection of a DC current at the stop and can affect the estimations given by the Kalman filter.

5.5.1.1. *Tuning of the covariance matrices*

To tune the covariance matrix of the state and output noises, we will use the approach presented in [LOR 00]. It consists of evaluating the Power Spectral Density (PSD) of the experimental noises, and of calculating PSD of the modeling errors by simulation.

To consider the colored noises without increasing the order of the model, we would use an upper bound model [LAR 81]. The variances are first evaluated in continuous time, before taking into account the discretization period T_e. We suppose the covariance matrix to be diagonal.

The covariance matrix of the state noises has two sub-matrix, corresponding to the real state X_1 (rotor flux) and to the parameters X_2 (resistances):

$$Q = T_e \begin{bmatrix} Q_1 & 0 \\ 0 & Q_2 \end{bmatrix} \quad \text{with} \quad Q_1 = \begin{bmatrix} 10^{-4} & 0 \\ 0 & 10^{-4} \end{bmatrix} \quad \text{and} \quad Q_2 = \begin{bmatrix} Q_{Rs} & 0 \\ 0 & Q_{Rr} \end{bmatrix} \qquad [5.28]$$

We obtain a tuning compatible with a slow dynamics of the temperatures with $Q_{Rs} = 10^{-3}$ and $Q_{Rr} = 10^{-4}$. This tuning will be carried out by default. If we wish to have higher estimation dynamics (Figure 5.7), we take $Q_{Rs} = 4\ 10^{-2}$ and $Q_{Rr} = 10^{-2}$.

The covariance matrix of the output noises (mainly related to the errors of voltage measurements) is given by:

$$R = \frac{1}{T_e}\begin{bmatrix} 10^{-1} & 0 \\ 0 & 10^{-1} \end{bmatrix} \qquad [5.29]$$

5.5.1.2. *First estimation of R_s and R_r*

The first test which we will exploit is a relatively low set speed test (100 rev/min), with a load torque of 25 nm. The speed is quite low and the torque is high; we are thus in favorable conditions with respect to the observability of the stator and rotor resistances.

However, Figure 5.6 shows that the estimations are not accurate. The estimate of R_s is particularly incorrect: although its initial value is correct, its evolution does not absolutely follow the measurement value. However, the R_r estimate has a bias remaining sensibly constant after a few minutes.

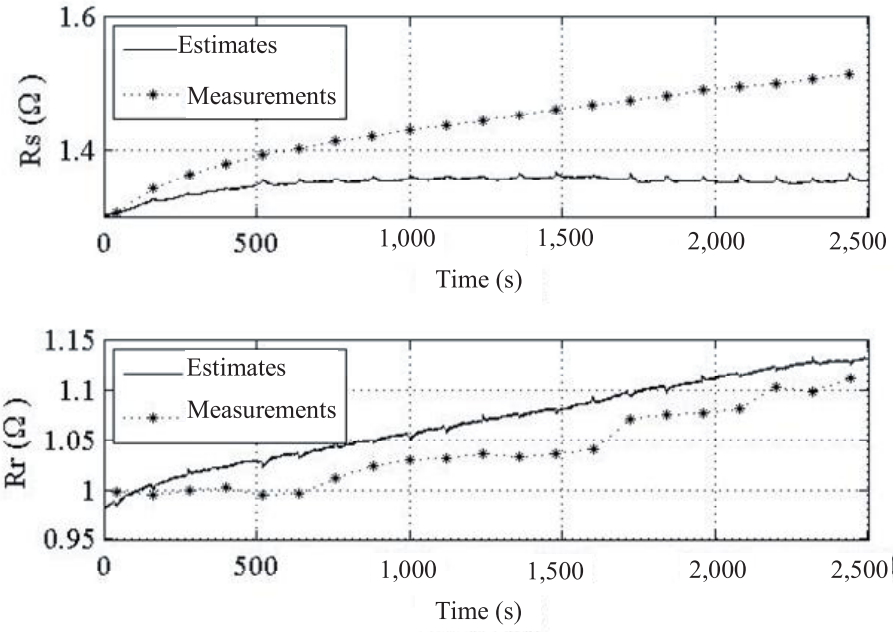

Figure 5.6. *Estimate of R_s and R_r during a steady state test*

5.5.1.3. *Impact of the DC current injection during the measurements of R_s and R_r*

Figures 5.7 and 5.8 highlight the behavior of the Kalman filter during the resistance measurement phase. In fact, the Kalman filter remains active during this phase: it is not possible to temporarily disable it. Figure 5.7 superimposes the estimations obtained with a variance of low noise and those obtained with a higher variance (see the adjustment of Q_2, section 5.5.1.1). We can note that the estimations are identical outside the measurement periods.

The latter has no effects on the estimations obtained with a low Q_2 variance. Figure 5.8 shows a zoom of one of the measurement periods. It shows the sensitizing effect of the DC current injection. Thus, with a high variance, the dynamics of the estimation of R_s is sufficient enough that it gets close to the measured value.

After the measurement phase, the two estimates converge. The Kalman gain cancels with the stator current, and the estimation is almost fixed. On the contrary, the estimate of R_r is disturbed during the injection of the DC current in the rotor.

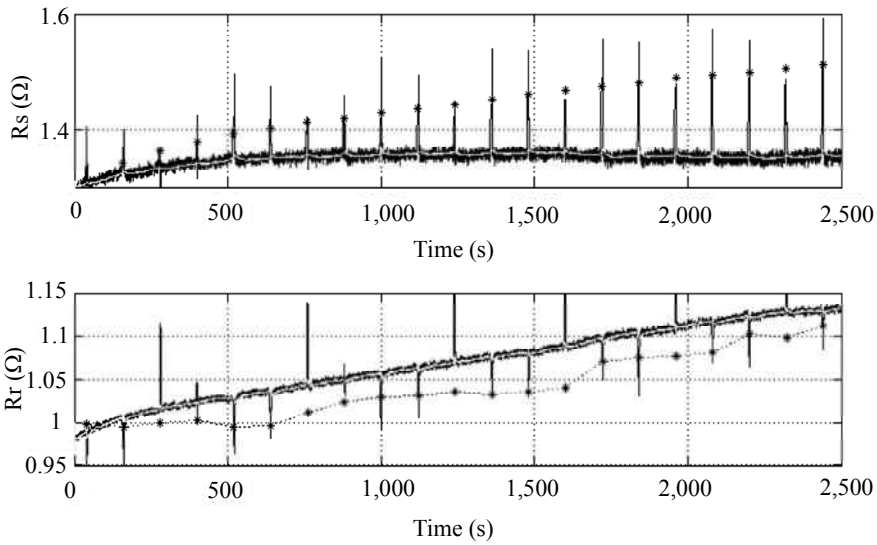

Figure 5.7. *Impact of the resistance measurements and of the Q_2 matrix tuning*

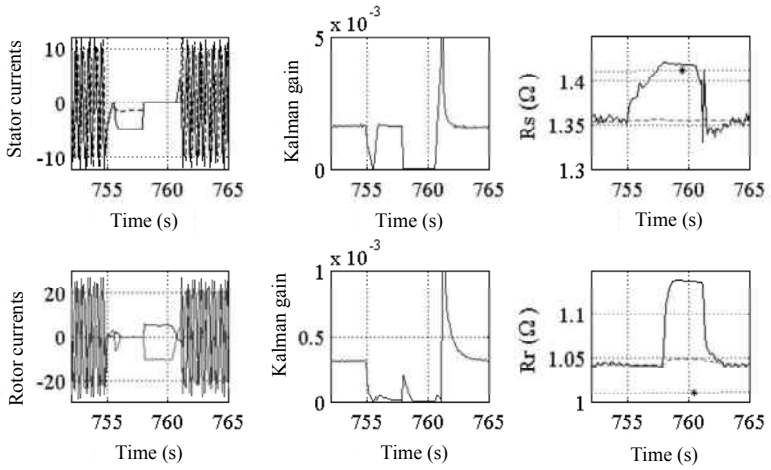

Figure 5.8. *Zoom of a sequence of resistance measurement*

5.5.2. *Influence of the magnetic saturation*

Senstivity studies have shown that an accurate value of the L_m magnetization inductance is necessary, in order to carry out a correct estimation of the resistances and notably of the stator resistance. This explains the bad results presented in the previous section. In fact, during the test we had used a non-adaptive vector control. The latter is thus progressively detuned by the temperature rise in the rotor, as we would observe.

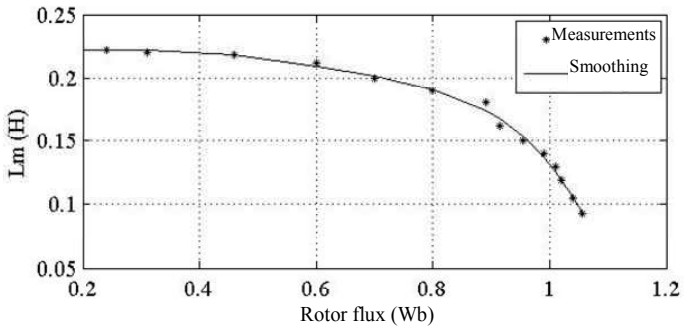

Figure 5.9. *Evolution of L_m with respect to the rotor flux magnitude*

To consider the variations of L_m, two approaches are possible. The first consists of exploiting the saturation characteristic of the machine, which is supposed to be

determined beforehand. The second plans to simultaneously estimate L_m by introducing it in the X_2 vector. In this case, we would increase the order of the extended model and the complexity of the Kalman filter. We would also increase the risk of identifiability loss. Thus, it is not possible to estimate three parameters from a test in a steady state. We will favor the first approach. Figure 5.9 shows the saturation characteristic of the machine. The measurement points (stars) have been obtained from the synchronism tests. The Kalman filter estimates the rotor flux. Thus, we would simply consider its evolution, in order to adapt L_m. Figure 5.10 shows the new resistances estimations, as well as the adaptation of L_m. For the latter, the peaks correspond to the moments when the rotor flux is cancelled during the measurement phases. We can check that the temperature rise in the rotor tends to disturb the vector control. The resistance estimations are notably improved. This time R_s has a constant bias. If we are only interested in the temperature, it is possible to cancel the bias on the temperature, by using an online initialization of the R_{sRef} and T_{sRef} reference magnitudes.

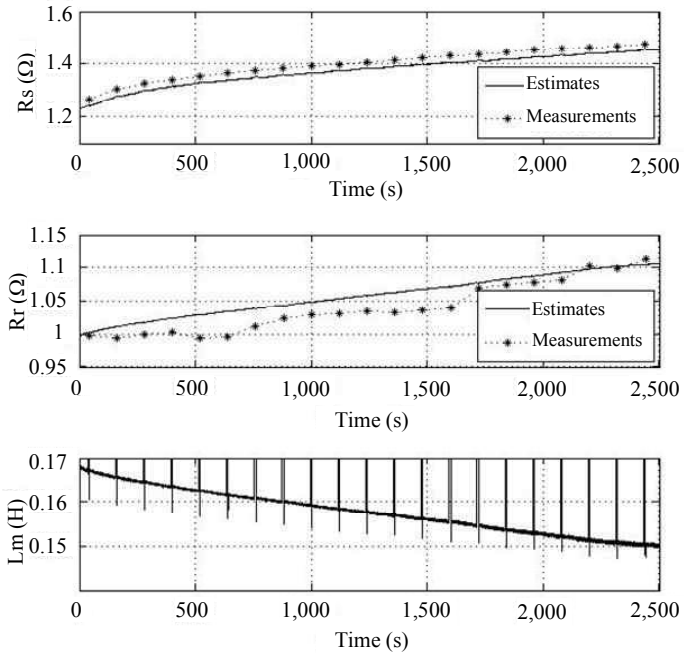

Figure 5.10. *Estimation of R_s and R_r, with adaptation of L_m*

The earlier tests have been carried out at low speed. We would now observe the influence of the speed on the estimations. Figure 5.11 shows a test during which the speed is changed by steps: 100, 200, 400, 800 rev/min, then back to 100 rev/min.

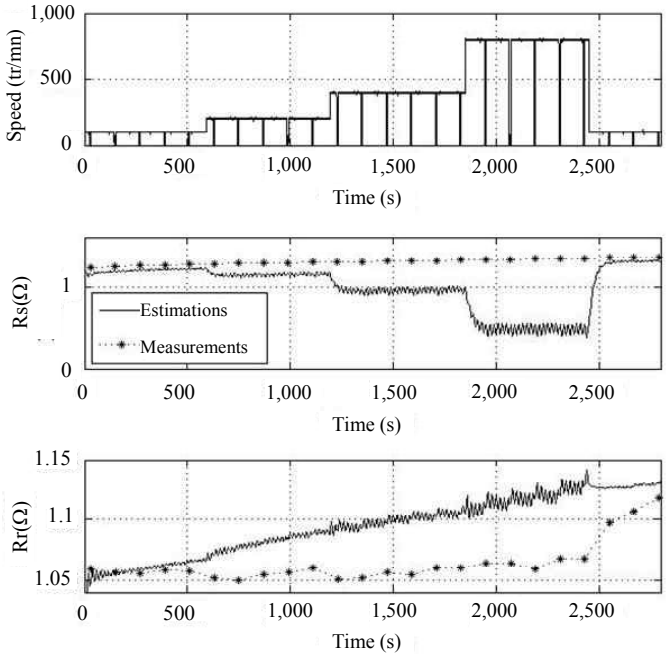

Figure 5.11. *Estimation of R_s and R_r, at various speeds*

The negative pulses appearing on the speed curve indicate the stopping phases of the machine, for the measuring the resistances. The load torque is also variable: it varies in steps between 10 and 20 nm with a period of 20 s.

Despite the fact that we had accounted for the magnetic saturation, the estimation error on R_s strongly increases when the speed increases. This highlights the impact of the desensitization of R_s at high speed. The estimate of R_r is also affected, though to a lesser extent.

5.6. Conclusion

The thermal monitoring of the induction machine is thus a relatively complex problem. On the one hand, the exploitation of a thermal model is relatively delicate in an industrial context, since this requires a perfect knowledge of the thermal environment of the machine, as well as its mechanical mounting. This approach is thus only possible in a well-defined context. In addition, even in this case, determining the thermal model is not easy. On the other hand, real-time monitoring of the stator and rotor winding temperatures through their resistances also poses

several problems. We have presented a technique that is based on an extended Kalman filter and a discrete-time model of reduced order, which authorizes a large sampling period (10 ms), in order to minimize the calculation power. This approach enables us to jointly estimate the resistances and the rotor flux. This has very simply enabled us to take into account the saturation of the machine. Ideally, we should be able to separate the rotor flux and resistance estimation, so that we can estimate them with an even larger temporal step, corresponding to their dynamics. Finally and above all, we have noticed how the stator resistance could be slightly sensitized, except at low speeds. This fundamental point is at the core of the problem. For some of the applications, it will be possible to use resting phases, in order to inject DC current. We have been able to check its efficiency. However, in most of the cases, we would certainly associate an estimation of the resistances with a thermal adaptive model, as suggested by [GAO 05a]. In addition, we have highlighted the problems raised by the implementation of a test bench which has been designed for this type of study. We have also suggested several measurement strategies for the temperatures and resistances.

5.7. Appendix: induction machine characteristics

	Squirrel-cage motor	**Slip-ring motor**
Rated power	$P_N = 4$ kW	$P_N = 4$ kW
Power factor	$\cos(\phi) = 0.78$	$\cos(\phi) = 0.8$
Phase-neutral rated voltage	$U_sN = 230$ V	$U_sN = 230$ V
Rated current (star)	$I_sN = 8.8$ A	$I_sN = 8.4$ A
Rated speed	$N_N = 1{,}435$ tr/mn	$N_N = 1{,}435$ tr/mn

Table 5.1. *Nameplates of the induction machines*

5.8. Bibliography

[ALT 97] AL-TAYIE J., ACARNLEY P., "Estimation of speed, stator temperature and rotor temperature in cage induction motor drive using the extended Kalman filter algorithm", *IEE Proceedings of Electric Power Applications*, no. 144, p. 301-309, 1997.

[BEG 99] BEGUENANE R., BENBOUZID M., "Induction motors thermal monitoring by means of rotor resistance identification", *IEEE Transactions on Energy Conversion*, no. 14, p. 566-570, 1999.

[BOG 09] BOGLIETTI A., CAVAGNINO A., STATON D., SHANEL M., MUELLER M., MEJUTO C., "Evolution and modern approaches for thermal analysis of electrical machines", *IEEE Transactions on Industrial Electronics*, no. 56, p. 871, 2009.

[BOY 95] BOYS J., MILES M., "Empirical thermal model for inverter-driven cage induction machines", *IEE Proceedings of Electric Power Applications.*, vol. 141, no. 6, p. 360-372, November 1995.

[DU 08] DU Y., HABETLER T., HARLEY R., "Methods for thermal protection of medium voltage induction motors – A review", *International Conference on Condition Monitoring and Diagnosis*, CMD 2008, p. 229-233, 2008.

[DU 09] DU Y., ZHANG P., GAO Z., HABETLER T., "Assessment of available methods for estimating rotor temperatures of induction motor", *Electric Machines and Drives Conference*, *IEMDC '09*, p. 1340-1345, 2009.

[FOR 06] FORGEZ C., FOULON E., LORON L., LY S., PLASSE C., "Temperature supervision of an integrated starter generator", *Industry Applications Conference 41st IAS Annual Meeting*, p. 1613-1619, 2006.

[FOU 05] FOULON E., Surveillance thermique de la machine asynchrone, PhD thesis, University of Nantes, 25 July 2005.

[FOU 07] FOULON E., FORGEZ C., LORON L., "Resistances estimation with an extended kalman filter in the objective of real-time thermal monitoring of the induction machine", *Electric Power Applications*, IET. 1, p. 549-556, 2007.

[GAO 05a] GAO Z., HABETLER T., HARLEY R., "An online adaptive stator winding temperature estimator based on a hybrid thermal model for induction machines", *International Conference on Electric Machines and Drives*, p. 754-761, 2005.

[GAO 05b] GAO Z., HABETLER T., HARLEY R., COLBY R., "A novel online rotor temperature estimator for induction machines based on a cascading motor parameter estimation scheme", *SDEMPED 2005*, p. 1-6, 2005.

[GAO 05c] GAO Z., HABETLER T., HARLEY R., COLBY R., "An adaptive kalman filtering approach to induction machine stator winding temperature estimation based on a hybrid thermal model", *Industry Applications Conference*, p. 2-9, vol. 1, 2005.

[GAO 06] GAO Z., Sensorless stator winding temperature estimation for induction machines, PhD thesis in School of Electrical and Computer Engineering, Georgia Institute of Technology, Atlanta, 2006.

[GRE 89] GRELLET G., "Pertes dans les machines tournantes", *Technique de l'Ingénieur*, D3450, 1989.

[GRU 08] GRUBIC S., ALLER J., LU B., HABETLER T., "A survey of testing and monitoring methods for stator insulation systems in induction machines", *International Conference on Condition Monitoring and Diagnosis*, *CMD 2008*, p. 196-203, 2008.

[HOL 02] HOLTZ J., "Sensorless control of induction motor drives", *Proceedings of the IEEE*, vol. 90, no. 8, p. 1359-1394, August 2002.

[JAL 08] JALJAL N., TRIGEOL J., LAGONOTTE P., "Reduced thermal model of an induction machine for real-time thermal monitoring", *IEEE Transactions on Industrial Electronics*, no. 55, p. 3535-3542, 2008.

[KRA 04] KRAL C., HABETLER T., HARLEY R., PIRKER F., PASCOLI G., OBERGUGGENBERGER H. *et al*., "Rotor temperature estimation of squirrel-cage induction motors by means of a combined scheme of parameter estimation and a thermal equivalent model", *IEEE Transactions on Industry Applications*, no. 40, p. 1049-1057, 2004.

[LAR 81] DE LARMINAT P., PIASCO J.-M., "Modèles majorants: application au filtrage de trajectoire de mobiles manœuvrants", *GRETSI*, Nice, 1981.

[LEE 02] LEE S.-B., HABETLER T., HARLEY R., GRITTER D., "An evaluation of model-based stator resistance estimation for induction motor stator winding temperature monitoring", *IEEE Transactions on Energy Conversion*, no. 17, p. 7-15, 2002.

[LOR 00] LORON L., "Identification paramétrique de la machine asynchrone par filtre de Kalman étendu", *Revue Internationale de Génie Electrique*, vol. 3, no. 2, p. 163-205, June 2000.

[LOR 07] LORON L., "Estimation en ligne des paramètres des machines asynchrones", in DE FORNEL B. and LOUIS J.-P. (eds), *Identification et observation des actionneurs électriques*, vol. 1, p. 141-199, Hermès, Paris, 2007.

[MOR 01] MORENO J., HIDALGO F., MARTINEZ M., "Realization of tests to determine the parameters of the thermal model of an induction machine", *IEE Proceedings of Electric Power Applications*, no. 148, p. 393-397, 2001.

[NOR 85] NORDIN K.B., NOVOTNY D.W., ZINGER D.S., "The influence of motor parameter deviations in feed-forward field orientation drive systems", *IEEE Transactions on Industry Applications*, vol. IA-21, no. 4, July-August 1985.

[PAI 80] PAICE D.A., "Motor thermal protection by continuous monitoring of winding resistance", *IEEE Transactions on Industrial Electronics and Control Instrumentation*, IECI-27, p. 137-141, 1980.

[SHE 05] SHENKMAN A., CHERTKOV M., MOALEM H., "Thermal behavior of induction motors under different speeds", *IEE Proceedings of Electric Power Applications*, no. 152, p. 1307-1310, 2005.

[SID 05] SIDDIQUE A., YADAVA G., SINGH B., "A review of stator fault monitoring techniques of induction motors", *IEEE Transactions on Energy Conversion*, no. 20, p. 106-114, 2005.

[STA 05] STATON D., BOGLIETTI A., CAVAGNINO A., "Solving the more difficult aspects of electric motor thermal analysis in small and medium size industrial induction motors", *IEEE Transactions on Energy Conversion*, no. 20, p. 620-628, 2005.

[TAL 07] TALLAM R., LEE S.-L., STONE G., KLIMAN G., YOO J., HABETLER T. *et al*., "A survey of methods for detection of stator-related faults in induction machines", *IEEE Transactions on Industry Applications*, no. 43, p. 920-933, 2007.

[THI 01] THIRINGER T., LUOMI J., "Comparison of reduced-order dynamic models of induction machines", *IEEE Transactions on Power Systems*, p. 119-126, 2001.

[WEI 07] WEILI H., XIANG Z., "An evaluation of wavelet network-based stator estimation for induction motor temperature monitoring", *8th International Conference on Electronic Measurement and Instruments*, *ICEMI 07*, p. 3-418-3-421, 2007.

[WU 06] WU Y., GAO H., "Induction-motor stator and rotor winding temperature estimation using signal injection method", *IEEE Transactions on Industry Applications*, no. 42, p. 1038-1044, 2006.

[ZHA 08] ZHANG P., DU Y., LU B., HABETLER T., "A remote and sensorless thermal protection scheme for soft-starter-connected induction motors", *Annual Meeting Industry Applications Society*, *IAS 08*, p. 1-7, 2008.

[ZHA 09] ZHANG P., LU B., HABETLER T., "An active stator temperature estimation technique for thermal protection of inverter-fed induction motors with considerations of impaired cooling detection", *Electric Machines and Drives Conference*, *IEMDC '09*, p. 1326-1332, 2009.

Chapter 6

Diagnosis of the Internal Resistance of an Automotive Lead-acid Battery by the Implementation of a model Invalidation-based Approach: Application to Crankability Estimation

6.1. Introduction

The ever-increasing draconian anti-pollution standards and the increase in fuel prices have forced car manufacturers to design new vehicles (stop & go, hybrid or electrical). The underlying idea behind these measures is to reduce the greenhouse gas emissions in the cities, either by stopping the internal combustion engine (ICE) when the vehicle is at a standstill, or by substituting electrical energy for fossil fuel. The latter involves an electric drive (AC motors), one or several electrical storage systems such as batteries and supercapacitors, and power electronics devices/systems (DC/DC and DC/AC converter).

To ensure the proper operation of these vehicles, car manufacturers must incorporate reliable management systems, which are related to the electrical energy domain [CHA 03]. These requirements have stipulated that state of charge (SOC) and state of health (SOH) estimators have to be designed.

Chapter written by Jocelyn SABATIER, Mikaël CUGNET, Stéphane LARUELLE, Sylvie GRUGEON, Isabelle CHANTEUR, Bernard SAHUT, Alain OUSTALOUP and Jean-Marie TARASCON.

Numerous characterization methods [COL 08] and reliable battery state estimators have been suggested throughout the world. However, most of them deal with the problem of the SOC estimation [PAN 01, PIL 01, COL 07] only.

The reader who is interested in this matter can also consult [MCA 96] for a presentation of some of the methods, and [MEI 03] for understanding a specific application that relates to the battery monitoring techniques of future vehicles.

However, the design of reliable and complete battery state estimator remains a difficult task, since on the one hand such an estimator must have the following advantages:

– good accuracy of the estimation;

– fast estimation;

– robustness with respect to the operating conditions.

On the other hand, a battery is a complex electrochemical system, whose behavior is:

– non-linear with respect to the stress current;

– with long memory due to the diffusion phenomena;

– sensitive to the temperature and the aging.

where the aging problem is increasingly being considered in the design of battery state estimators.

This chapter also discusses the battery state estimation. The study is restricted to the study of lead-acid batteries, since they are the most frequently used storage device in the present-day vehicles.

However, the suggested estimator is also applicable for other battery technologies, such as lithium-ion, Nickel Metal Hydride. In the case of lead-acid batteries, the aging notably results in an increase in resistance (by corrosion, sulfation, conductivity loss at the collector/active material interface).

Therefore, the measurement of the internal resistance of the battery is a frequently used indicator. In addition, it has been proved in this article that the power supplied by a battery is correlated with its own resistance. Due to the fact that a vehicle start-up requires mostly power (and not energy), the internal resistance can be used to evaluate the ability of the battery to start the vehicle (crankability).

However, we often mix up resistance measurement and impedance measurement, which can induce doubt on the relevance of the resistance values used in some

solutions. An “impedance measurement” is performed by calculating the resistance as the ratio of the voltage to the current variations on a (short or long) time interval.

This chapter suggests a new way of estimating the resistance and crankability of a lead-acid battery, from a start-up signal (and thus to design a crankability estimator), a fractional order model (non-integer order model), and a model invalidation-based approach.

The fractional behavior (resulting from the diffusive phenomena) of lead-acid batteries has long ago been demonstrated by electrochemists, but few methods take this behavior into account. This issue can be explained by the lack of tools for the analysis and modeling of fractional systems up to about 10 years ago.

At present, such tools are available [OUS 95, MEL 02, POD 99]. In addition, in the identification domain, several methods have been developed [COI 00, AOU 03], which enable us to consider and evaluate the battery systems, which have a long memory behavior (diffusive systems for example). One of the advantages of these methods is that they can be used to obtain low order models (which can help to use small number of parameters) of such systems. This property is considered in this chapter for the modeling of lead-acid batteries.

Since the number of parameters in the obtained models is small, we can develop simple and efficient estimation methods. The identification of the fractional model of the battery is carried out on a crancking signal, because this is a very interesting operating phase to evaluate the battery resistance and the battery lack of power (see also [SAB 10 and SAB 08a] for a description of the advantages of the cranking phase).

This chapter is organized in the following manner. Section 6.2 provides the fractional model used to characterize the behavior of the battery from a crancking signal. The identification method used is described and applied to a start-up signal in section 6.3. Section 6.4 shows the way in which the obtained fractional model can be used to estimate the battery resistance, as well as the power it can produce, and thus its crankability.

The model invalidation-based approach used to estimate the internal resistance is described and applied to section 6.5. The first estimator resulting from it is then simplified, in order to obtain an implementable version in a microcontroller. This version is validated on tests. Section 6.6 introduces the principles of a global state estimator of a battery that integrates an estimator of internal resistance.

6.2. Fractional model of a lead-acid battery for the start-up phase

It is possible to demonstrate the relation between the fractional systems and the systems described by a diffusion equation (parabolic partial differential equations).

This demonstration can be carried out by using the studies presented in [SAB 08b]. For the same reasons, Fick's 2nd law, which describes the diffusion phenomenon of the chemical species inside batteries, justifies the use of a fractional model for modeling the electrical behavior of batteries.

Therefore, the Randles' model [SAB 06] is frequently used in the literature for battery modeling. This model is represented in Figure 6.1. The model is developed by the simplified resolution of the electrochemical diffusion equations [SAT 79]. The Randles' model is fractional [MIL 93, OLD 74] since it comprises a Warburg impedance, which is defined by the transfer function [BAT 01]

$$W(s) = \frac{\sigma}{s^{\gamma}} \quad \sigma \in \mathrm{R},\ \gamma \in \mathrm{R} \qquad [6.1]$$

The transfer function of the Randles' model in Figure 6.1 is therefore given by:

$$H(s) = \frac{U(s)}{I(s)} = (Ls + R_l) + \frac{\frac{1}{Cs}\left(R + \frac{\sigma}{s^n}\right)}{\left(\frac{1}{Cs} + R + \frac{\sigma}{s^n}\right)} \qquad [6.2]$$

if L is considered null, this function is:

$$H(s) \underset{L=0}{=} \frac{R_l RCs^{n+1} + R_l \sigma Cs + (R_l + R)s^n + \sigma}{s^n\left(RCs + \sigma Cs^{1-n} + 1\right)} \qquad [6.3]$$

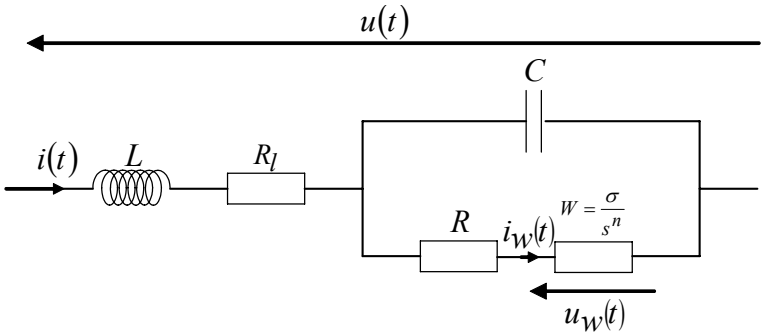

Figure 6.1. *Randles' model of a lead-acid battery*

Relation [6.3] thus shows that the Randles' model is fractional [SAM 93, MIL 93]. However, if the study of a lead-acid battery is limited in the frequency

domain [8 Hz; 1 kHz] corresponding to the spectrum of a start-up signal (see Figure 6.2), a simpler model can then be used to describe its dynamical behavior.

As shown in Figure 6.2, for a lead-acid battery at 20°C (but this is also true for a temperature varying from -10°C to 50°C, [SAB 06]), and irrespective of the state of charge, the phase diagram of the battery frequency response has an almost constant value in this frequency range, which is not a multiple of 90°.

Such a frequency response can be reproduced by a model that is simpler as compared to the Randle's model:

$$H_F(s) = K\left(\frac{1+\frac{s}{\omega_h}}{1+\frac{s}{\omega_b}}\right)^{\gamma} \qquad [6.4]$$

Akin to the Randles' model, the model with relation [6.4] is also fractional, but is made up of four parameters, instead of six (a gain K, two transitional frequencies ω_b and ω_h and the fractional order γ).

6.3. Identification of the fractional model

The parametric estimation of the $H_F(s)$ model of the relation [6.4] involves determination of the numerical values of the parameter vector:

$$\theta = \begin{bmatrix} K & \omega_b & \omega_h & \gamma \end{bmatrix}^T \qquad [6.5]$$

This parametric estimation is based on an output error approach summarized by the diagram in Figure 6.3 and detailed in [COL 07]. Such an approach has also been successfully applied to the modeling of thermal systems [SAB 06].

6.3.1. *Output error identification algorithm*

The set of sampled data is assumed to be made up of K pairs $\{i(kh), u*(kh)\}$ (h being the sampling period) and where:

$$u*(kh) = u(kh) + b(kh) \qquad [6.6]$$

b indicates a white output noise.

since $\hat{\theta}$ is an estimation of θ, the prediction of the output error is given by:

$$\varepsilon\left(kh,\hat{\theta}\right)=u*\left(kh\right)-\hat{u}\left(kh,\hat{\theta}\right) \qquad [6.7]$$

The optimum value of $\hat{\theta}$ is noted as θ_{opt}, and is then obtained by the minimization of the quadratic criterion:

$$J\left(\hat{\theta}\right)=\sum_{k=0}^{K-1}\varepsilon^{2}\left(kh,\hat{\theta}\right) \qquad [6.8]$$

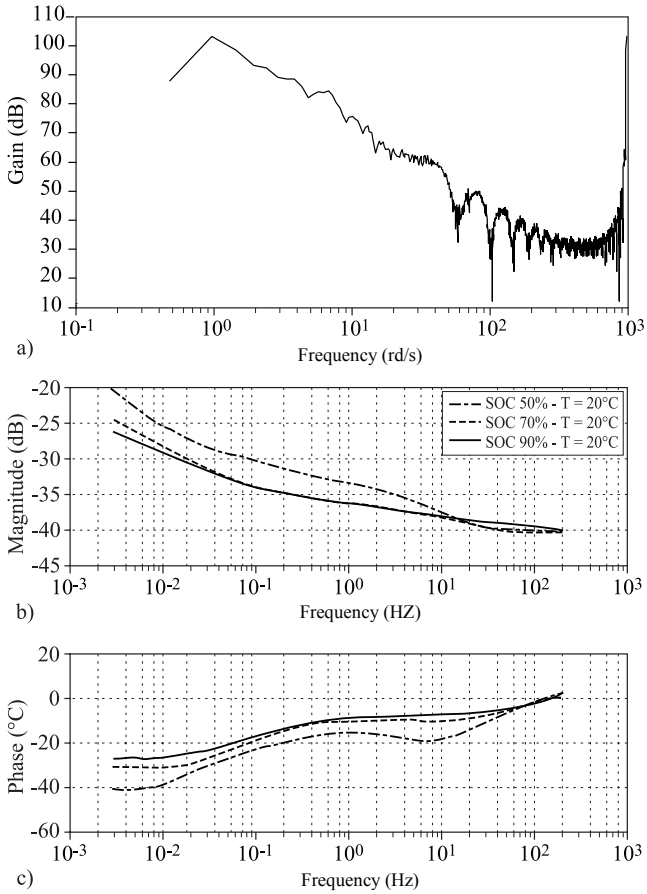

Figure 6.2. *Fast Fourier Transform of a start-up signal (a), Bode magnitude plot (b) and Bode phase plot (c) of the frequency response of a lead-acid battery for several states of charge (at 20° C)*

Since the $\hat{u}\left(kh,\ \hat{\theta}\right)$ prediction output vector is non-linear in $\hat{\theta}$, the Marquardt algorithm is used to estimate $\hat{\theta}$ in an iterative way:

$$\theta_{i+1} = \theta_i - \left\{\left[J_\theta^{"} + \xi I\right]^{-1} J_\theta^{'}\right\}_{\hat{\theta}=\theta_i} \quad [6.9]$$

where:

$$\begin{cases} J_\theta^{'} = -2\sum_{k=0}^{K-1} \varepsilon(kh) S(kh,\hat{\theta}) : gradient \\ J_{\theta\theta}^{"} \approx 2\sum_{k=0}^{K-1} S(kh,\hat{\theta}) S^T(kh,\hat{\theta}) : hessian \\ S(kh,\hat{\theta}) = \dfrac{\partial \hat{u}(kh,\hat{\theta})}{\partial \theta} : sensitivity\ output\ function \\ \xi : control\ parameter \end{cases}$$

This algorithm, often used in non-linear optimization, ensures a robust convergence, even if $\hat{\theta}$ is initialized at a value far from the optimum value.

6.3.2. *Calculation of the output sensitivities*

The output sensitivity of each parameter of the $H_F(s)$ model is calculated by the partial derivative of the output prediction:

$$\frac{\partial\, \hat{u}\left(t,\hat{\theta}\right)}{\partial \hat{\theta}_i} = \mathrm{L}^{-1}\left(\left[\frac{\partial H_F(s)}{\partial \theta_i}\right]\theta_i = \hat{\theta}_i\right) * i(t) \quad [6.10]$$

where:

$$\frac{\partial H_F(s)}{\partial K} = \frac{1}{K} H_F(s) \quad [6.11]$$

$$\frac{\partial H_F(s)}{\partial \omega_b} = \frac{n\, s}{\omega_b^n}\left(1+\frac{s}{\omega_b}\right)^{-1} H_F(s) \quad [6.12]$$

$$\frac{\partial H_F(s)}{\partial \omega_h} = -\frac{n\,s}{\omega_h^n}\left(1+\frac{s}{\omega_h}\right)^{-1} H_F(s) \qquad [6.13]$$

$$\frac{\partial H_F(s)}{\partial n} = \ln\left(\frac{1+\frac{s}{\omega_h}}{1+\frac{s}{\omega_b}}\right) H_F(s) \qquad [6.14]$$

Relations [6.11] to [6.13] can be simulated by using an integer approximation [OUS 95] and relation [6.14] can be simulated by using the appendix of [SAB 06].

6.3.3. *Validation of the estimated parameters*

By assuming that the prediction error is a white-noise sequence with null average, the covariance matrix of the estimated parameters is given by [LJU 87, SOD 89]:

$$\mathrm{cov}\left(\hat{\theta}\right) = \sigma^2\left(\sum_{k=0}^{K-1} S\left(kh,\hat{\theta}\right) S^{\mathrm{T}}\left(kh,\hat{\theta}\right)\right)^{-1} \qquad [6.15]$$

By using this matrix, the variance of the parameters (located on the diagonal) and the correlation coefficients between parameters (non-diagonal terms) can be obtained.

6.3.4. *Application to start-up signals*

Model [6.4] and the parametric estimation method previously described have been applied to voltage and current signals measured at the terminals of a 60 Ah (216,000 C) battery during a start-up, where the current signal corresponds to the input signal, in the framework of this study.

Figure 6.4 shows a comparison between the measured voltage signal and the signal produced by the model after its parametric estimation. This comparison will enable us to validate the model and the chosen parametric estimation method.

In addition, we will note that a comparison with a model with integer derivatives has also been carried out in [SAB 10] and [SAB 08a].

This model is made up of five parameters and is defined by:

$$H_E(s) = K \frac{\left(1+\frac{s}{\omega_{h_1}}\right)\left(1+\frac{s}{\omega_{h_2}}\right)}{\left(1+\frac{s}{\omega_{b_1}}\right)\left(1+\frac{s}{\omega_{b_2}}\right)} \quad [6.16]$$

This comparison is summarized in Figure 6.4, which shows that the fractional model leads to an error three times smaller with only four parameters. On the other hand, the integer model has five parameters (and this in order to ensure that the asymptotic behaviors in low and high frequencies are the same). It is therefore possible to conclude that a fractional model, in fact, improves the simplicity/accuracy compromise, when it is used for modeling of a lead-acid battery during the start-up phase.

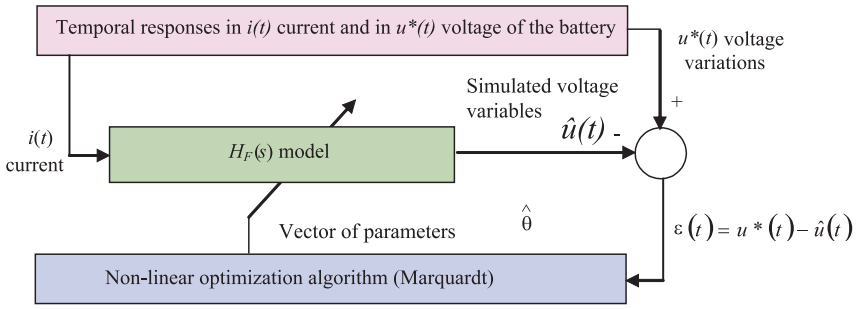

Figure 6.3. *Parametric estimation of the $H_F(s)$ model by an output error-based approach*

6.4. Battery resistance as crankability estimator

The start-up of an ICE (Internal Combustion Engine) vehicle relies on the power which can be supplied by the battery. The start-up function is ensured if:

– the current proportional to the torque supplied by the starter is higher than the permanent resisting torque of the ICE;

– the voltage linked to the starter speed is higher than the reset value of the microcontroller, which monitors the vehicle functions.

Several start-up tests carried out on three new batteries (designated by NJS2, NJS1, and NJS0) and three used batteries (designated by VCN101, VCN102, and

VCN103) have shown the impact of battery resistance on its power performance, as illustrated in Figure 6.5.

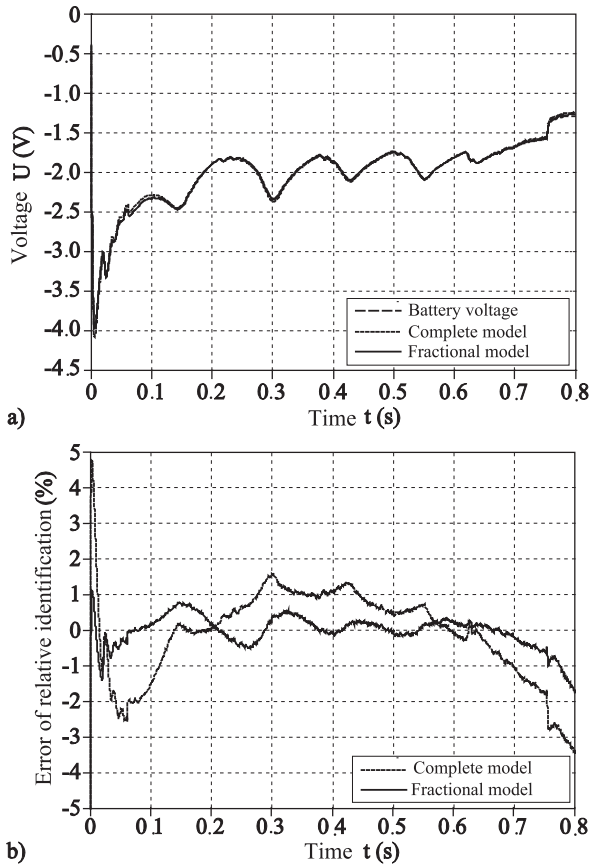

Figure 6.4. *Performance comparison of an integer and a fractional model from measurements carried out on a vehicle during a start-up*

The analysis of Figure 6.5 shows that the vehicle does not start if the power supplied by the battery is lower than 4 kW, or if its resistance is higher than 8.5 mΩ. The cause of the non-start-up is not due to a lack of energy, but due to a lack of power.

The frequency characteristics of several models are obtained through data collected from several used batteries at different SOF_C (SOF_C designates the ratio of the available capacity to the nominal capacity and is defined by the battery manufacturer). These frequency characteristics are represented in Figure 6.6.

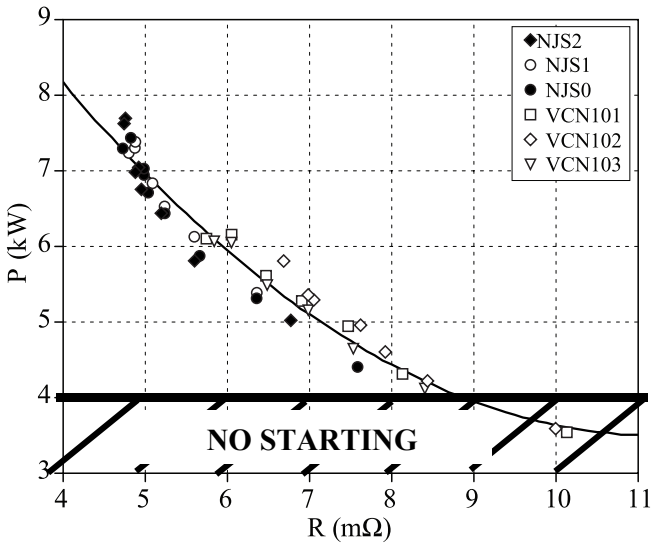

Figure 6.5. *Evolution of the power supplied by the batteries with respect to their resistances at an ambient temperature of about 20°C*

We notice from these curves that the battery resistance corresponds to the high frequency gain of the $H_F(s)$ fractional model (given its null imaginary part in high frequency). Consequently, it is possible to estimate the battery resistance from a $H_F(s)$ model, which has been identified with a start-up signal.

However, we need to notice that the battery resistance varies with respect to the temperature, according to the Arrhenius equation [BOD 77, p. 76], where characterization of the latter will allow us to update the resistance value, irrespective of the temperature.

We can also notice in Figure 6.6 that the high frequency gain and thus the resistance are directly connected to the SOF_C, so that the lower the SOF_C, the higher will be the resistance.

These observations lead to the conclusion that identification of an $H_F(s)$ model from start-up signals, combined with an SOF_C estimator and an equation of the resistance change with respect to the temperature, will enable us to evaluate, not only the battery resistance for the next start-up, but also the available power, if we refer to our previous comments related to Figure 6.6. Consequently, this approach provides an estimation of the crankability.

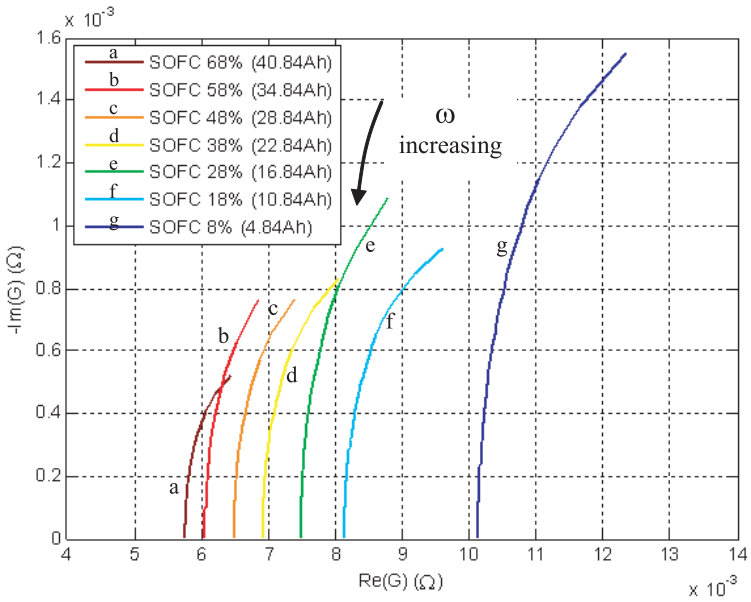

Figure 6.6. *Nyquist plot of the VCN101 battery models identified during the start-up at 20°C*

6.5. Model validation and estimation of the battery resistance

6.5.1. *Frequency approach of the model validation*

The model validation method used in the sequel will now be summarized. This method is the outcome of the works presented in [SMI 92, MOU 04, NEW 98]. In these studies, it is assumed that the identification of a P_{sys} real system has resulted in creation of a $P_{nom}(s)$ nominal model.

The gap between the real system and the nominal model can originate from two sources: the model uncertainties Δ and the exogenous disturbances or noises w.

By assuming that these two sources are additive, the residue r corresponding to the difference between the measured and simulated data is defined by the relation:

$$r = y - y_{nom} = \left(P_{sys} - P_{nom}\right) u \qquad [6.17]$$

Let L_2 be the set of signals, whose norm 2 is bounded (see also [BAT 02] for a definition of the norm 2 $\|\cdot\|_2$ and of the infinite norm $\|\cdot\|_\infty$). Introducing the weighing

matrices P_z and P_w used to normalize the frequency signal w, such that $w \in L_2$, $\|w\|_2 < 1$, and to normalize the perturbation Δ, so that $\|\Delta\|_\infty < 1$, the P_{sys} system admits the representation of Figure 6.7.

In order to define the model validation problem, the LFT (*Linear Fractional Transformation*) representation is used and applied to the model in Figure 6.7.

From the resulting model of Figure 6.8, the following 4 equations can be obtained:

$$r = y - P_{22}\,u\ ,\ v = \Delta z\ ,\ z = P_{11}\,v + P_{12}\,u\ ,\ y = P_{21}\,v + P_{22}\,u + P_w\,w \qquad [6.18]$$

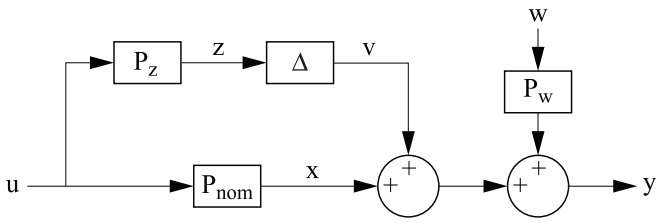

Figure 6.7. *Representation of the system*

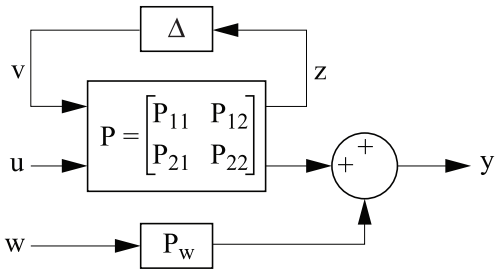

Figure 6.8. *LFT (Linear Fractional Transformation) representation of the system*

The model validation problem can now be formulated as follows [6.21], [6.22].

PROBLEM 1.– Let a set of models defined by the LFT $F_u(P,\Delta)$, so that $\sup_\omega \mu\left(P_{11}\left(e^{j\omega}\right)\right) < 1$ (μ designates the structured singular value [BAT 02]) and (u, y) the experimental data set. Is there a (Δ, w) pair with $w \in L_2$, $\|w\|_2 < 1$ and $\|\Delta\|_\infty < 1$ so that $y = F_u(P,\Delta)\,u + P_w w$?

If no (u, y) pair satisfies the conditions of problem 1, then the model is said to be "invalidated" by the experimental data; the latter cannot be reproduced by any models considered.

We shall also consider that a model can never be validated (this is thus a misnomer), but only not invalidated. To validate a model, strictly speaking, we should be able to test all the possible conditions, which cannot be done in practice.

A model validation problem can be solved by the implementation of an optimization problem. The problem 1 can thus be reformulated in the following manner [MOU 04].

PROBLEM 2.– What is the smallest value of β, so that $\|\Delta\|_\infty \le \beta$ and $\|w\|_2 \le \beta$ satisfies the following equality, $y = F_u(P, \Delta)u + P_w w$?

If the condition $\beta < 1$ is met, then the model is not invalidated. Mathematically, it involves solving the following optimization problem:

$$\|\Delta\|_\infty^{opt} = \|w\|_2^{opt} = \min_{\substack{w \in \boldsymbol{L}_2 \\ \|\Delta\|_\infty < 1}} \left\{ \beta \;\middle|\; \begin{array}{l} \exists \|\Delta\|_\infty \le \beta, \|w\|_2 \le \beta \,/ \\ y = F_u(P, \Delta)u + P_w w \end{array} \right\} \quad [6.19]$$

Let β_{opt} be the optimum value of β, so that:

$$\beta^{opt} = \min_{w,\Delta} \beta \quad under \begin{cases} y = F_u(P, \Delta)u + P_w w \\ \|\Delta\|_\infty \le \beta \\ \|w\|_2 \le \beta \end{cases} \quad [6.20]$$

In this study, the validation problem is formulated in the frequency domain (so that they will allow us to make some simplifications as described later). The frequency response of the signals required for its implementation is obtained by the Discrete Fourier Transform (DFT) of input and output data applied to the system.

The input-output experimental data originating from the real system and made up of N samples $\{(u_k, y_k); k = 0, \ldots, N-1\}$ are thus replaced by their DFT $\{(U_n, Y_n); n = 0, \ldots, N-1\}$.

The P_{sys} system is characterized by its frequency response, and Δ_n designates the complex matrix of perturbation for the *nth* considered frequency $\omega_n = 2\pi n/N$.

Equation [6.5] thus becomes:

$$\begin{aligned} R_n &= Y_n - P_{22}\left(e^{j\omega_n}\right)U_n \quad V_n = \Delta_n\left(e^{j\omega_n}\right)Z_n \\ Z_n &= P_{11}\left(e^{j\omega_n}\right)V_n + P_{12}\left(e^{j\omega_n}\right)U_n \\ Y_n &= P_{21}\left(e^{j\omega_n}\right)V_n + P_{22}\left(e^{j\omega_n}\right)U_n + P_w\left(e^{j\omega_n}\right)W_n \end{aligned} \qquad [6.21]$$

If the norm L_2 on w is replaced by the Euclidean norm, the problem 2 can then be reformulated in the frequency domain in the following way.

PROBLEM 3.– What is the smallest value of β_n so that $\|V_n\| \le \beta_n \|Z_n\|$, $\|W_n\| \le \beta_n$ and $R_n = P_{21}V_n + P_w W_n$?

The associated optimization problem is thus $\forall n = 0, \ldots, N-1$:

$$\beta_n^{opt} = \min_{V_n, W_n} \beta \quad under \begin{cases} R_n = P_{21}V_n + P_w W_n \\ V_n^* V_n \le \beta_n^2 Z_n^* Z_n \\ W_n^* W_n \le \beta_n^2 \end{cases} \qquad [6.22]$$

This optimization problem is made up of a convex criterion, two quadratic inequality constraints and one linear equality constraint. It thus admits a LMI (*Linear Matrix Inequality*) formulation [NEW 98].

6.5.2. *Application to the estimation of the battery resistance*

When we are given the relationship between the high frequency gain of the $H_F(s)$ model (equation [6.4]) and the internal resistance of a battery (see the comments related to Figure 6.5), it is possible to design a resistance estimator based on the evaluation of the high frequency gain of the $H_F(s)$ model. This can be done by applying the model invalidation-approach presented in the previous section.

The application of this approach to the resistance diagnosis of a lead-acid car battery requires one or several nominal models, depending on the aim one is trying to achieve. If this aim is to check whether the resistance is below a minimum value, and prevents the start-up. In this case a single model is sufficient.

However, if the goal is to evaluate the resistance of the battery with an absolute error of $\pm\,\varepsilon$ over the ΔR range, then the N minimum number of models to be used is defined by the relation:

$$N = \left[\Delta R / 2\varepsilon \right] \qquad [6.23]$$

In this application, the objective is to determine the value of the resistance (and its evolution) during every start-up, in order to define if the power required for the next start-up may be supplied and thus create a crankability indicator.

For a new battery, as for a used one, many tests carried out on vehicles (Peugeot 407 SW 2l HDI) have shown that the battery was able to start the vehicle when the resistance varied from 4.5 to 8.5 mΩ. The choice of a relative error of ± 0.25 mΩ in a 4.25 mΩ to 8.75 mΩ interval, would require that a battery be represented by a series of 9 uncertain models, as shown in Figure 6.9.

The nominal models are represented by the following transfer functions $\forall i = 1, \ldots, 9$:

$$P_{nom}(i) = r(i) + K(i) \frac{\left(1 + \frac{s}{\omega_h(i)}\right)^{\gamma(i)}}{\left(1 + \frac{s}{\omega_b(i)}\right)^{\gamma(i)}} \qquad [6.24]$$

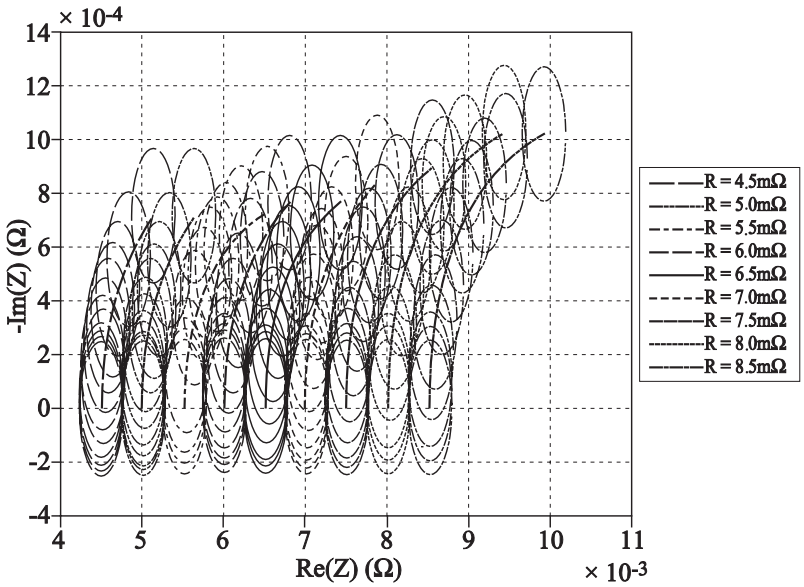

Figure 6.9. *Nyquist plots obtained for each resistance value from a set of nominal models and their associated perturbation domains*

It is important to understand that the parameter values of these models must be identified again for any application in which start-up signals would have a different amplitude (for example in the case of the same battery used with another vehicle).

The weighting $P_W = 0.03$ weighting is obtained from the analysis of noise in the battery cranking voltage signal.

Model perturbation P_z has been established to define the range of resistance permissible variation around a nominal model. It is defined by:

$$P_z(s) = 0.002 \frac{\left(1 + \frac{s}{100}\right)}{\left(1 + \frac{s}{2000}\right)} \qquad [6.25]$$

The model validation-approach has been applied to start-up data obtained with a 60 Ah-battery (i.e. 216,000 C). The aim is here to check if the P_{nom} nominal model and the P_w and P_z weightings, which characterize the different battery models, are well calibrated in order to validate the measured signals.

Initially, the validation method is applied to a signal measured on a new battery at SOC of 90%, whose resistance is equal to 4.75 mΩ. The obtained result is represented in Figure 6.10.

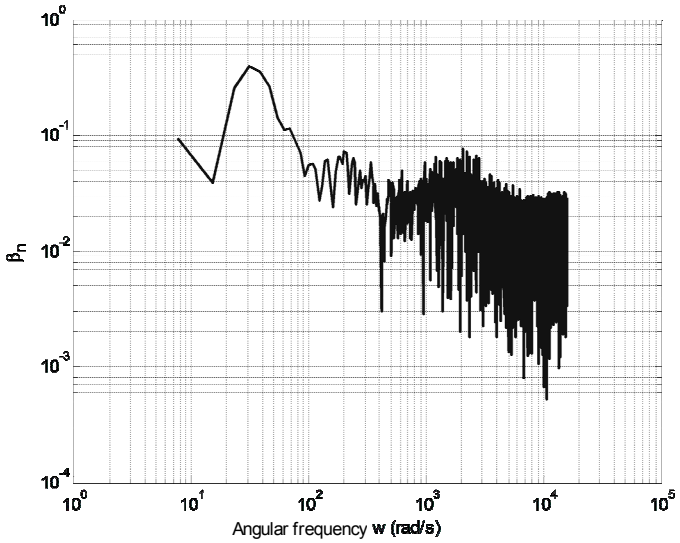

Figure 6.10. β_n^{opt} *resulting from the data of the NJS2 battery at SOC 90%*

We can notice in this figure that for each frequency considered, the value of β_n^{opt} is less than 1. The model of a battery, whose resistance is 5 mΩ, is not invalidated by the data, where the data measured on a battery whose resistance is 4.75 mΩ.

The validation method has also been applied outside the domain ± 0.25 mΩ. As shown in Figure 6.11, data from the used battery VCN101 at SOC 90%, whose resistance is equal to 6.05 mΩ, invalidates the 5 mΩ battery model.

A similar test has been carried out by using the data coming from a used battery at SOC 40%, whose resistance is equal at 10.13 mΩ. These data again invalidate the model corresponding to a battery with a 5 mΩ resistance.

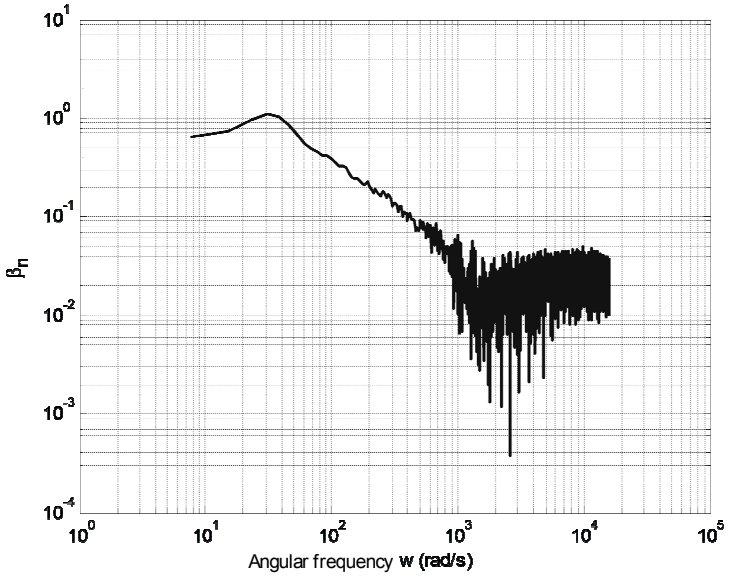

Figure 6.11. β_n^{opt} *resulting from data of the VCN101battery at SOC 90%*

6.5.3. *Simplified resistance estimator*

The major problem of the solution presented in section 6.5.2 is the double optimization on the perturbation and the noise (w, Δ). This leads us to solve a problem based on LMI, which cannot be implemented in a car microcontroller. The simplified version of the battery resistance estimator presented in Figure 6.12 has therefore been suggested.

This simplified version can now be implemented in a microcontroller, since, as shown in Figure 6.12, only a limited number of basic operations are necessary for the implementation.

In order to facilitate the description of this simplified method, it has been assumed that $P_w = 1$ and that w is a white noise of b_{max} maximum amplitude and null mean value. Let be $y(t) = u_{crank}(t)$ (voltage) and $u(t) = i_{crank}(t)$ (current) in Figure 6.7.

According to this figure, for each nominal model of i index:

$$u_{crank}(t) = x_i(t) + v_i(t) + w(t) \qquad [6.26]$$

the v_i signal is given by:

$$v_i(t) = u_{crank}(t) - x_i(t) - w(t) \qquad [6.27]$$

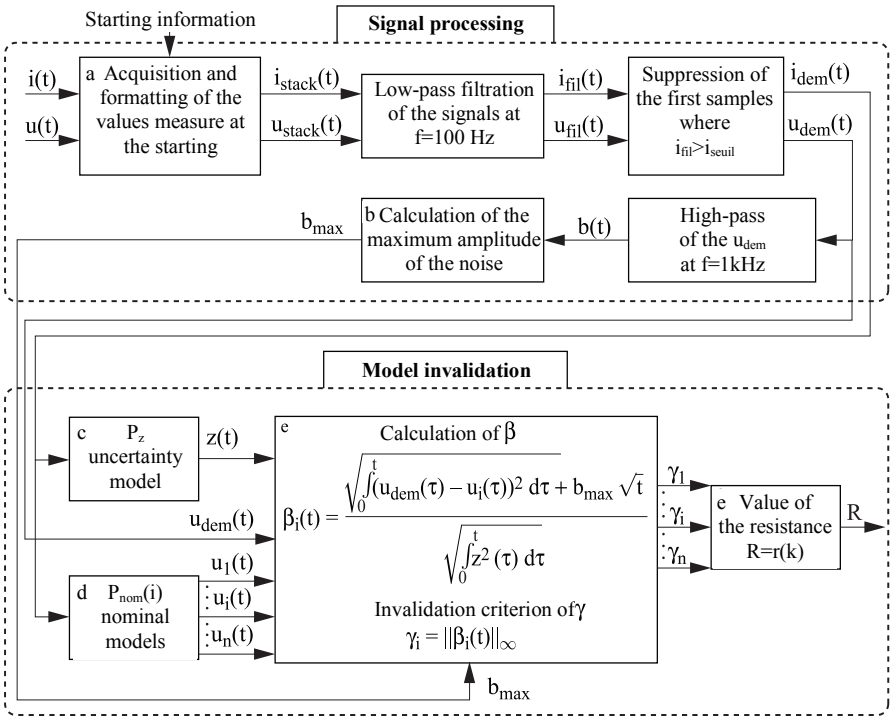

Figure 6.12. *Simplified battery resistance estimator based on an approach of model validation*

The v_i signal energy is given by (t_d designates the start-up instant and t_{max}- t_d, its duration):

$$\sqrt{\int_0^{t_{\max}-t_d} v_i^2(t)\,dt} = \sqrt{\int_0^{t_{\max}-t_d} \left(u_{crank}(t) - x_i(t) - w(t)\right)^2\,dt} \qquad [6.28]$$

In practice, the disturbance v_i cannot be calculated because the noise signal w is unknown. However, an upper bound of the energy of w is known and an upper bound of relation [6.29] can be obtained:

$$\sqrt{\int_0^{t_{\max}-t_d} v_i^2(t)\,dt} \le \sqrt{\int_0^{t_{\max}-t_d} \left(u_{crank}(t) - x_i(t)\right)^2\,dt} + \sqrt{\int_0^{t_{\max}-t_d} w^2(t)\,dt} \qquad [6.29]$$

An upper bound of β_i related to Δ_i is thus:

$$\left\| \Delta_i(t) \right\|_2 = \frac{\left\| v_i(t) \right\|_2}{\left\| z(t) \right\|_2} \le \beta_i(t) = \frac{\sqrt{\int_0^t \left(u_{crank}(\tau) - x_i(\tau)\right)^2\,d\tau} + b_{\max}\sqrt{t}}{\sqrt{\int_0^t z^2(\tau)\,d\tau}} \qquad [6.30]$$

Thus, the validation criterion is defined as the maximum value of $|\beta_i|$, which verifies the constraint:

$$\gamma_i = \left\| \beta_i(t) \right\|_\infty \le 1 \qquad [6.31]$$

Let $R = r(i)$ be a function associating the i index (index of the $P_{nom}(i)$ nominal model) with a value of battery resistance R. The nominal models are assumed to be classified in ascending order of the resistance values characterizing them. Therefore, $r(1)$ designates the smallest resistance which ensures the start-up and $r(n)$, the highest. To determine R, it is necessary to answer the question: is there a model of k index which can verify relation [6.31]? Let N be the number of not invalidated models, which verify this condition. The method used to estimate the resistance of the battery depends on N, as indicated in Table 6.1.

As an example, this simplified method is applied on the data generated by a battery, whose internal resistance is 6 mΩ. For this set of data, Figure 6.13 shows

the evolution time of the limit of β (upper bound of Δ according to condition [6.30]).

N	**Estimation of the battery resistance**
$N = 0$, $\gamma_1 < \gamma_n$	Battery in short-circuit: $R < r(1)$
$N = 0$, $\gamma_1 > \gamma_n$	Discharged or old battery: $R > r(n)$
$N = 1$	$\exists ! k \in [1;n] / \gamma_k \leq 1 \Rightarrow R = r(k)$
$N > 1$ (1st method)	Minimum value of γ : $\exists ! k \in [1;n] / \gamma_k = \min_i \gamma_i \Rightarrow R = r(k)$
$N > 1$ (2nd method)	Weighted mean: $\forall j = \{ i \mid \gamma_i \leq 1 \} \quad R = \left(\sum_j \frac{r(j)}{\gamma_j} \right) \left(\sum_j \frac{1}{\gamma_j} \right)^{-1}$

Table 6.1. *Method to determine the R value of the resistance of a battery*

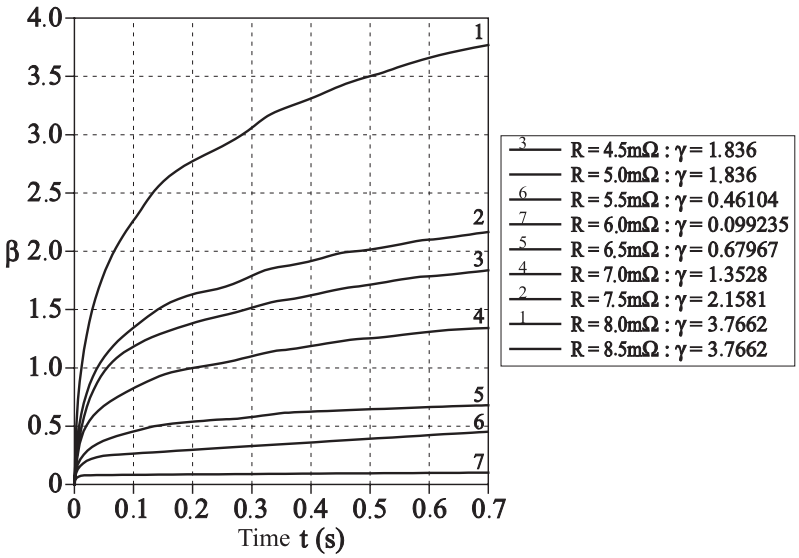

Figure 6.13. *Values of β obtained for each model*

According to this figure, three models are not invalidated, since, β is less than 1. According to Table 6.1 and since this is the case $N > 1$, two solutions can be used in

order to estimate the resistance. The first solution consists of keeping the model which has produced the lowest value of β.

The value of the obtained R resistance is then $R = 6$ mΩ. The second solution takes into account, through a weighted mean, all the values of β which are equal to or less than 1. This solution leads to $R = 5.99$ mΩ.

The good results obtained in the previous example show that the simplified solution of the resistance estimator (version implementable in a car microcontroller) produces accurate results.

6.6. Toward a battery state estimator

An advantage of the previously described estimator is that it can be included in a more complex system, which is able to supply information related to the global state of a battery in terms of SOC (state of charge), SOH (state of health), and SOFc (state of functioning). This estimator is presented in Figure 6.14. By using only three measured magnitudes (voltage, current and temperature), this estimator is able to provide us with the necessary indications for the monitoring of the energy and the battery power.

From a series of starts-up carried out on new and used batteries, the identification of their dynamical behavior has enabled us to evaluate their resistances (as shown in section 6.4), besides the evolution of this resistance in the function of the SOC and the SOH, with the help of fractional models.

These characteristics are used in the estimator in Figure 6.14, in order to predict the performances in power of the battery and its ability to start the vehicle. The operation of this estimator is described in [CUG 09, CUG 07, CUG 09] and will be illustrated in a subsequent chapter.

6.7. Conclusion

This study has shown that the electrical signals measured at the terminals of a battery during the start-up of a thermal motor are, in fact, exploitable in order to design an internal resistance estimator. The start-up capacity of a battery only depends on the power which it can release. This power can also be estimated from its internal resistance, as it has been shown previously.

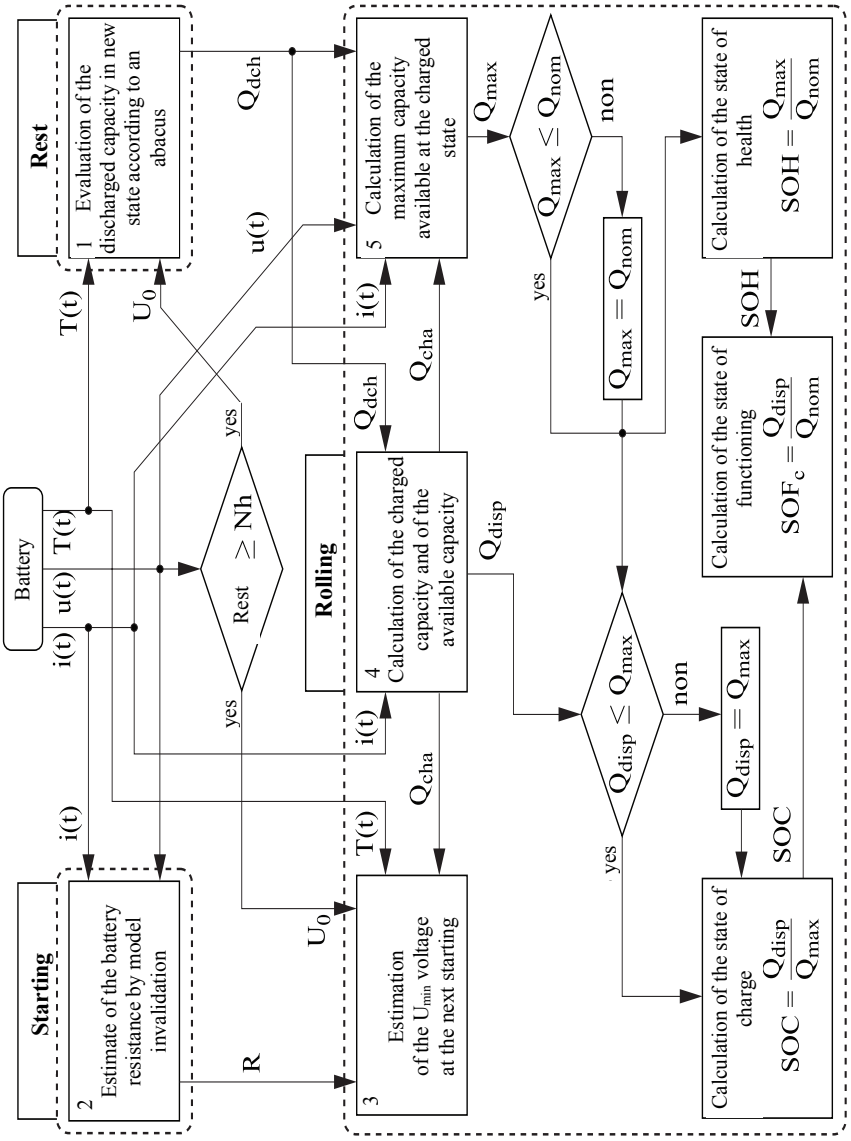

Figure 6.14. *Block diagram of the battery state estimator*

The internal resistance of a battery can therefore be considered as a crankability indicator (associated with an indicator of SOFc and a law of resistance variation with the temperature). Determination of an efficient mean of measuring the resistance of a battery involves evaluating the high frequency gain of a simple fractional model (which has only four parameters) from measured electrical signals at the battery terminals. The use of a technique of model validation will then enable us to create a new estimator of battery resistance.

However, due to its calculation complexity, this estimator cannot be implemented in a car microcontroller. Due to this reason, a simplified version has been developed and validated by using experimental data, in order to consider and evaluate the requirements of the industrial sector.

Due to the fact that the resistance of the battery varies with its age, such a solution can be used, coupled with a temperature measurement (due to the dependence of the battery resistance with the temperature), in order to diagnose not only the crankability, but also the battery state of health.

This issue has been discussed by the authors in a new article, in which they have proposed a more complex tool [CUG 09, CUG 07, CUG 09], which integrates the estimator (the subject of this work), in order to enable a global estimation of the battery state.

6.8. Bibliography

[AOU 03] AOUN M., MALTI R., LEVRON F., OUSTALOUP A., "Orthonormal basis functions for modeling continuous-time fractional systems", *Proceedings of the 13th IFAC SYSID'03*, Rotterdam, 2003.

[BAT 01] BATTAGLIA J.-L., COIS O., PUIGSEGUR L., OUSTALOUP A., "Solving an inverse heat conduction problem using a non-integer identified model", *International Journal of Heat and Mass Transfer*, no. 44, 2001.

[BAT 02] BATES D.G., POSTLETHWAITE I., *The Structured Singular Value and μ–Analysis*, Lecture Notes in Control and Information Sciences, vol. 283, Springer, Berlin, 2002.

[BOD 77] BODE H., *Lead-Acid Batteries*, John Wiley & Sons, New York, 1977.

[CHA 03] CHATZAKIS J., KALAITZAKIS K., VOULGARIS N.C., MANIAS S.N., "Designing a new generalized battery management system", *IEEE Transactions on Industrial Electronics*, vol. 50, no. 5, p. 990- 999, October 2003.

[COI 00] COIS O., OUSTALOUP A., BATTAGLIA E., BATTAGLIA J.-L., "Non-integer model from model decomposition for time domain system identification", *Proceedings of the 12th IFAC SYSID'2000*, Santa-Barbara, 2000.

[COL 07] COLEMAN M., LEE C.K., ZHU C., HURLEY W.G., "State-of-charge determination from EMF voltage estimation: using impedance, terminal voltage, and current for lead-acid and lithium-iron batteries", *IEEE Transactions on Industrial Electronics*, vol. 54, no. 5, p. 2550-2557, October 2007.

[COL 08] COLEMAN M., HURLEY W.G., LEE C.K., "An improved battery characterization method using a two pulse load test", *IEEE Transactions on Energy Conversion*, vol. 23, no. 2, p. 708-713, June 2008.

[CUG 07] CUGNET M., SABATIER J., BOUYGUES I., Estimateur d'état batterie par invalidation de modèle, patented by INPI, reference # FR0759784, 2007.

[CUG 09] CUGNET M., SABATIER J., LARUELLE S., GRUGEON S., CHANTEUR I., SAHUT B., OUSTALOUP A., TARASCON J.M., "A solution for lead-acid battery global state estimation", *ECS Transactions*, vol. 19, October 2009.

[LJU 87] LJUNG L., *System Identification: Theory for the User*, Prentice-Hall, New York, 1987.

[MCA 96] MCANDREWS J.M., JONES R.H., "A valve regulated lead-acid battery management system (VMS)", *Proceedings of the 18th IEEE INTELEC*, p. 507-513, 1996.

[MEI 03] MEISSNER E., RICHTER G., "Battery monitoring and electrical energy management precondition for future vehicle electric power systems", *Journal of Power Sources*, no. 116, p. 79-98, 2003.

[MEL 02] MELCHIOR P., LANUSSE P., COIS O., DANCLA F., OUSTALOUP A., "Crone toolbox for matlab: fractional systems toolbox", *Proceedings of the 41st IEEE CDC 02*, Las Vegas, 2002.

[MIL 93] MILLER K.S., ROSS B., *An Introduction to the Fractional Calculus and Fractional Differential Equations*, Wiley-Interscience, New York, 1993.

[MOU 04] MOUHIB O., (In-)validation de modèles de systèmes incertains, PhD thesis, Automatics department of Supélec, University of Paris XI, 2004.

[NEW 98] NEWLIN M.P., SMITH R.S., "A generalization of the structured singular value and Its application to model validation", *IEEE Transactions on Automatic Control*, vol. 43, no. 7, p. 901-907, 1998.

[OLD 74] OLDHAM K.B., SPANIER J., *The Fractional Calculus*, Academic Press, New York, London, 1974.

[OUS 95] OUSTALOUP A., *La dérivation non entière*, *théorie*, *synthèse et applications*, Hermès, Paris, 1995.

[PAN 01] PANG S., FARRELL J., DU J., BARTH M., "Battery state-of-charge estimation", *Proceeding of the American Control Conference*, p. 1644-1649, Arlington, 2001.

[PIL 01] PILLER S., PERRIN M., JOSSEN A., "Methods for state of charge determination and their applications", *Journal of Power Sources*, no. 96, p. 113-120, 2001.

[POD 99] PODLUBNY I., "Fractional differential equations", *Mathematics in Sciences and Engineering*, no. 198, Academic Press, San Diego 1999.

[SAB 06] SABATIER J., AOUN M., OUSTALOUP A., GRÉGOIRE G., RAGOT F., ROY P., "Fractional system identification for lead-acid battery state of charge estimation", *Signal Processing*, no. 86, p. 2645-2657, 2006.

[SAB 08a] SABATIER J., CUGNET M., LARUELLE S., GRUGEON S., SAHUT B., OUSTALOUP A., TARASCON J.M., "Estimation of the lead-acid battery cranking capability by fractional model identification", *3rd IFAC Workshop on "Fractional Differentiation and its Applications"* (*FDA'08*), Ankara, 5-7 November 2008.

[SAB 08b] SABATIER J., MERVEILLAUT M., MALTI R., OUSTALOUP A., "On a representation of fractional order systems: interests for the initial condition problem", *3rd IFAC Workshop on "Fractional Differentiation and its Applications"* (*FDA'08*), Ankara, 5-7 November 2008.

[SAB 10] SABATIER J., CUGNET M., LARUELLE S., GRUGEON S., SAHUT B., OUSTALOUP A., TARASCON J.-M., "A fractional order model for lead-acid battery crankability estimation", *Communications in Non-linear Science and Numerical Simulation*, vol. 15, no. 5, p. 1308-1317, 2010.

[SAM 93] SAMKO S.G., KILBAS A.A., MARICHEV O.I., *Fractional Integrals and Derivatives*, Gordon and Breach, New York, 1993.

[SAT 79] SATHYANARAYANA S., VENUGOPALAN S., GOPIKANTH M.L., "Impedance parameters and the state-of-charge I: Ni-Cd battery", *Journal of Applied Electro-Chemistry*, no. 9, p. 125-139, 1979.

[SMI 92] SMITH R.S., DOYLE J.C., "Model validation: a connection between robust control and identification", *IEEE Transactions on Automatic Control*, vol. 37, no. 7, p. 942-952, 1992.

[SOD 89] SÖDERSTROM T., STOÏCA P., *System Identification*, Prentice Hall, London, 1989.

Chapter 7

Electrical and Mechanical Faults Diagnosis of Induction Machines using Signal Analysis

7.1. Introduction

At present, the usage of fast and accurate digital processors is very important, whether for controlling driven processes or for monitoring electrical actuators alone or in their environment. Although processes are more frequently operated at variable speeds, we will limit our study to monitoring and diagnosing the induction machine powered by the electrical network. In fact, there are still many applications, where the machine is directly connected to the electrical network. Irrespective of this operational safety, monitoring, diagnosis or prognosis of the power supply and motor set are highly important in some cases, so-called *sensitive* applications. When a fault begins to occur, it is virtually invisible. In spite of this, its evolution may propagate and become a source of other problems and lead to the shutting down of the process. Let us note here that an off-centering fault may generate a homopolar current in the induction machine, problematic for the ball bearings or bearings. Because of this, a change in behavior may be invisible at the beginning and would make diagnosis difficult or even impossible. This is a real challenge and is thus difficult to overcome.

Due to this problem, while using signals we must conclude with a faulty or faultless operation, and thus the process is programmed to shut down. This is either to replace the failing element or part, or simply to program an overhaul of the whole process. Scientific activities in the diagnosis and prognosis domain, as well as indirect financial interests, still hold enough importance to bring together and motivate our community of researchers.

Chapter written by Hubert Razik and Mohamed El Kamel Oumaamar.

Among the existing faults, we can cite rotor bar breakage or squirrel-cage end-ring breakage, which induces premature aging in the transmission component of the mechanical torque due to fluctuations in the torque and propagates this fault to its adjacent bars [BON 88]. The current amplitudes change and increase, which unfortunately increases electrodynamic strains. These strains, although secondary, may be dangerous for the operator and the production chain process.

There are relatively few statistical studies, and the articles used relate to data recorded 20 years ago. Irrespective of the case, we have taken most of the following figures from [THO 01] which are listed in Table 7.1. Others such as [BON 92, HEI 98, FIS 99, MEL 99] propose different data, putting the rotor fault in second or even third place.

Area of fault	Distribution according to the number of faults (%)
Bearing fault	41
Stator fault	37
Rotor fault	10
Other	12

Table 7.1. *Fault statistics*

However, we must be skeptical since the progress is continuous and, consequently, interferes with this data. We may emphasize here, for example, that the problems concerning faults on inter-bar connections between the rotor and the squirrel-cage have now been partly solved. Thus, the existing statistical tables in available literature may not be updated and would not be useful.

Irrespective of the above facts, the main causes leading to failure must be detected as early as possible. For diagnosis or prognosis, it is indeed necessary to carry out one or many analyses on site in order to interpret the signals coming from sensors, in terms of frequency and time. The signals that facilitate a diagnosis can be acquired by measuring the current absorbed by the electrical motor, the square of this current, the instantaneous power, Park's vector, axial or radial vibrations and, to a certain extent, the audible noise.

In this chapter, we will also approach the diagnosis of a process driven by an induction machine. We will explore different types of failure and educate our readers of the difficulty of establishing a reliable diagnosis.

7.2. The spectrum of the current line

Mostly, rotor failures develop gradually over a period of time. They are slow evolving phenomena, which enable the induction machine to guarantee a lower quality

operation. In fact, an oscillating torque may be generated, resulting in vibrations and causing an increased level of fatigue in the motor and during the drive process producing. Detecting a break down due to a rotor fault is classically achieved by using the spectral analysis of a signal coming from a sensor, which may be an accelerometer, a current sensor, etc. To achieve this purpose, we have represented the spectral content of a current absorbed by an induction motor (working at mid-load), when there is no fault (Figure 7.1), and when in the presence of a broken rotor bar (Figure 7.2). A quick

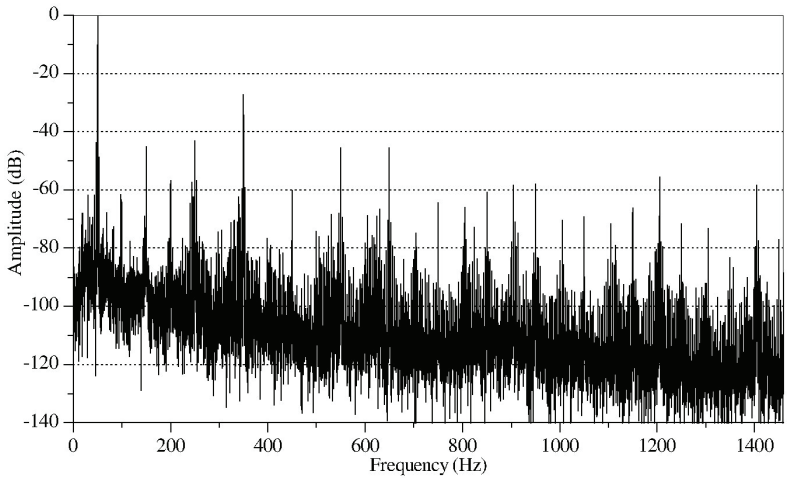

Figure 7.1. *Stator current spectrum around the fundamental machine: the rotor is healthy*

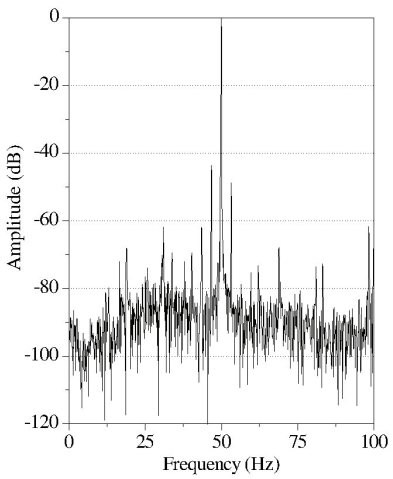

Figure 7.2. *Stator current spectrum around the fundamental machine: the rotor has 1 broken bar*

analysis of these spectra demonstrates the depth of these contents and the difficulty of obtaining a safe and reliable diagnosis.

7.3. Signal processing

At present, we are noticing a growing need to monitor the behavior of driven systems which evolve in a "healthy" operating mode towards a known mode of operation (or even unknown), whose mode can be dangerous and disastrous. Therefore early detection of this evolution towards an undesired mode must enable us to anticipate diagnosis by using monitoring techniques, before the process reaches this point. Thus, the methodology consists of favoring an online monitoring which implements the most rudimentary algorithm, known as the Fourier transform (whose spectrum will not be continually updated), or even better, the sliding discrete Fourier transform (SDFT). We will also briefly return to a few concepts and limitations – conditions of use.

7.3.1. *Fourier's transform*

One of the main disadvantages of the discrete Fourier transform is the need to possess all the samples of an acquisition sequence, in preparation for estimating the spectral content of the measured signal. This type of algorithm requires a number of acquisitions equal to the power of 2 (more precisely 2^N, where N is the number of samples). In addition, the desired spectral resolution is equal to $\Delta F = \frac{F_e}{N} = \frac{1}{T_e}$, where ΔF is the spectral resolution, F_e is the sampling frequency and T_e is the acquisition time of the signal to be studied. This naturally imposes extreme conditions on the process's operations, the most restrictive condition being operation in stationary regime.

The discrete Fourier transform of a final sequence of N samples $x(p-n)T_e$ at a time $t = p.T_e$ can be obtained by the following expression:

$$X_p\,[k] = \frac{1}{N}\sum_{n=0}^{N-1} x\,(p-n)\,.W_N^{nk} \qquad [7.1]$$

with:

$$W_N^{nk} = \exp\left(-\frac{\jmath 2\pi nk}{N}\right) \qquad [7.2]$$

with n as k = 0, 1, 2, …, $N-1$.

When the number of available samples is less than the required length N, then the number of missing samples will be reduced to zero, according to the "zero-padding" technique.

7.3.1.1. *The sliding discrete Fourier transform (SDFT)*

The need to constantly update the spectrum of the signal to be analyzed has led to the design of an algorithm based on a "sliding" approach. This enables each new sample to update the estimated spectral content of the signal. This is clear that, for "real-time" and online application means, the calculation time must be lower than the sampling duration.

By writing equation [7.1] in the following form:

$$X_p[k] = \frac{1}{N}\sum_{n=0}^{N-1} x(p-n).W_N^{nk} \pm \frac{1}{N}x(p-N).W_N^{Nk} \qquad [7.3]$$

then it is easy for us to introduce the induction expression as follows:

$$X_p[k] = \left(\frac{x(p)-x(p-N)}{N}\right) + W_N^k.X_{p-1}[k] \qquad [7.4]$$

knowing that $X_{p-1}[k]$ is the previously calculated discrete Fourier transform (DFT) at time $t=(p-1)T_e$. We thus have the expression of the SDFT, rendering it possible to update the spectral content of the signal to be analyzed at each sampling moment.

7.3.1.2. *Zoom effect for the sliding discrete Fourier transform*

The zoom effect observes a part of the initial spectrum obtained at a sampling frequency of F_e with a defined number of samples, N in a more accurate and detailed way. No specific problems are caused in the case of the SDFT carrying out the zoom function. As the spectral resolution is low, the number of samples required will go from N to N_2 and, on the other hand, the spectral analysis on a desired band frequency $[f_1; f_2]$ is now possible by limiting the exploration range, i.e.: $k \in [k_1; k_2]$.

$$X_p[k] = \left(\frac{x(p)-x(p-N_2)}{N_2}\right) + \exp\left(\frac{-\jmath 2\pi k}{N_2}\right).X_{p-1}[k] \qquad [7.5]$$

The spectral resolution will therefore be equal to $\Delta F = \frac{F_e}{N_2}$. [ABE 02] gives a simple example of the layout of this sliding discrete Fourier transform.

7.3.2. *Periodogram*

The power spectral density (PSD) of a signal is based on the following relation:

$$\hat{P}_x(f) = \frac{1}{N}\left|\sum_{n=0}^{N-1} x(n)\, e^{-\jmath 2\pi f n}\right|^2 \qquad [7.6]$$

Irrespective of the case, such estimation of the PSD may be considered as to come from a signal filtered through a filter bank with a bandwidth at -3 dB close to $\frac{1}{N}$. To guard against an effect linked to raw signal processing, it is recommended to use a weighting window such as the Hanning window, etc. [DID 04]. In addition, the expression of the equation for estimating the PSD thus becomes:

$$\hat{P}_x(f) = \frac{1}{N} \left| \sum_{n=0}^{N-1} \omega(n)\, x(n)\, e^{-\jmath 2\pi f n} \right|^2 \qquad [7.7]$$

where $\omega(n)$ corresponds to the weighting window equation.

An initial characteristic of the periodogram is the independence of the PSD variance with the number of samples. The second feature is that the PSD estimation is biased. In addition, the increase in N will influence the bias alone but not the variance. This leads us to use methods which reduce this variance, and therefore the noise of the estimated spectrum. For this, we can consider the Bartlett or the Welch method which is better.

7.3.2.1. *Bartlett method*

Based on the knowledge that the spectrum noise is independent of the length N of the number of samples to be analyzed, the Bartlett method divides an "average" estimation of the signal, into S sections of M samples. In addition, the PSD is thus obtained as follows:

$$\hat{P}_x(f) = \frac{1}{S} \sum_{s=0}^{S-1} \left\{ \frac{1}{M} \left| \sum_{n=0}^{M-1} \omega(n)\, x(n)\, e^{-\jmath 2\pi f n} \right|^2 \right\} \qquad [7.8]$$

7.3.2.2. *Welch method*

The Welch method is distinguished from the Bartlett method by the fact that sections S overlap. An overlapping of 50% reduces the PSD noise obtained by the Bartlett method by nearly 50%. This method is expressed in the following way:

$$\hat{P}_x(f) = \frac{1}{S} \sum_{s=0}^{S-1} \left\{ \frac{1}{M} \left| \sum_{n=0}^{M-1} \omega(n)\, x(n + (s-1)\, C)\, e^{-\jmath 2\pi f n} \right|^2 \right\} \qquad [7.9]$$

with $1 \leq s \leq S$, and C as the number of samples which overlap ($1 \leq C \leq M$).

Of course, there are other types of estimators.

7.4. Signal analysis from experiment campaigns

Two test benches were required for the experimental study of different faults which may affect an induction machine. These benches were MAS_1 and MAS_2 whose characteristics are highlighted in Table 7.7. The first one was located in the GREEN laboratory (Groupe de Recherche en Électrotechnique et Électronique de Nancy) and was composed of an induction machine coupled with a DC motor as a load. The signal for diagnosis was acquired by using a GaGe data board (CS 1602), to which the current, vibration and audible noise sensors were connected. For the inter turn short-circuit tests in the induction machine, the second test bench was from the Laboratoire d'électrotechnique de Constantine (LEC). The tests were carried out on a MAS_2 induction machine, re-wound for this purpose, whose characteristics are displayed in the Table 7.7. The short-circuit current was recorded using the LeCroy oscilloscope (WR60500). The data was processed using the MATLAB[1] software in order to analyze the signals.

7.4.1. *Disturbances induced by a broken bar*

Rotor failure may mainly occur at the short-circuit bar/end-ring intersection. This failure is analyzed by comparing it with a signature/a witness of healthy state. In addition, the current spectrum measured *in situ* will be affected by markers which are specific to the fault.

7.4.1.1. *Stator current analysis*

Breakage in a section of the rotor bar, of the bar/end-ring intersection of the short-circuit, or a break in a section of the end-ring, leads to the occurrence of lines given by the following relation:

$$f_{brk} = [1 \pm 2ks] f_s \qquad [7.10]$$

where s is the slip, f_s is the power supply frequency, k = 1, 3, 5 ....

Other signatures for broken bar faults are given by Deleroi [DEL 84]:

$$f_{sh} = [h(1-s) \pm s]\, f_s \qquad [7.11]$$

with h as the order of harmonics, h = 1, 5, 7 ....

If we consider the effects induced by speed oscillations of the mechanical shaft, then frequency lines appear according to the following relation:

$$f_{sh} = [h(1-s) \pm s \pm 2ks]\, f_s \qquad [7.12]$$

1 Matlab is a commercial product: www.mathworks.com.

However, the spectral content of the current is also affected by high frequency harmonics. In particular, they are located around the rotor slot harmonics (RSH) whose relation will be shown here:

$$f_{sh} = f_s \left[\frac{\lambda N_r}{p} (1 - s) \pm 1 \pm 2ks \right] \quad [7.13]$$

where k = 1, 3, 5 ... and N_r is the number of rotor bars.

Evidently, an oscillation in the load torque with a multiple of the rotation speed f_r will induce lines in the stator current spectrum on the frequency:

$$f_{load} = f_s \pm k f_r = \left(1 \pm k \frac{1 - s}{p} \right) f_s \quad [7.14]$$

with k = 1, 3, 5 ... and N_r as the number of rotor bars. Let us note here that these frequencies also correspond to those induced by an eccentricity fault. However, their increased amplitude is more sensitive in the case of eccentricity than for a case of load oscillation. Due to this, these lines will not be monitored without its problems when using classic techniques.

For this purpose, we have represented many current spectra absorbed by the induction motor, whether it is failing on the rotor or not, and on different frequency ranges.

In Figure 7.3, we show two stator current spectra around the fundamental harmonic with the spectral content on the left when the motor is healthy (Figure 7.3a). In fact, there is no alteration here, since there are still natural imperfections in the machine. On the right (Figure 7.3b), we show the spectral content when the rotor displays a failure, more precisely, when there is a broken bar in the squirrel-cage. We may notice the presence of lines indicating the bar fault and in addition the presence of lines relating to an eccentricity in the rotor in relation to the stator.

In Figure 7.4, we illustrate two spectra on the frequency range around the 3rd harmonic as well as the 5th harmonic in Figure 7.5. We can clearly see the lines generated by a speed oscillation caused by a rotor broken bar. Hence we could see a clear manifestation of significant lines (markers) which can offer an efficient diagnosis.

In Figure 7.6, we show two spectra on the frequency range around the frequencies indicating that the rotor is composed of a certain number of slots (28 in this application). Yet again, lines appear due to the rotor slotting. These lines indicate the presence of a rotor squirrel-cage fault at high frequency.

We therefore have a certain number of frequency ranges which could give an efficient diagnosis. Hence, we can choose our own range to decide on the type of

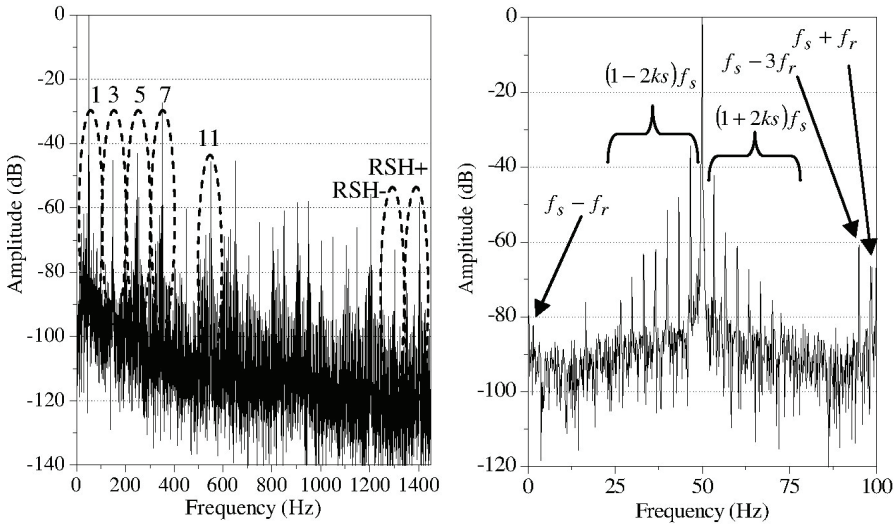

(a) No broken bars (b) 1 broken bar

Figure 7.3. *Stator current spectrum around the fundamental: a) the rotor is healthy; b) the rotor has 1 broken bar*

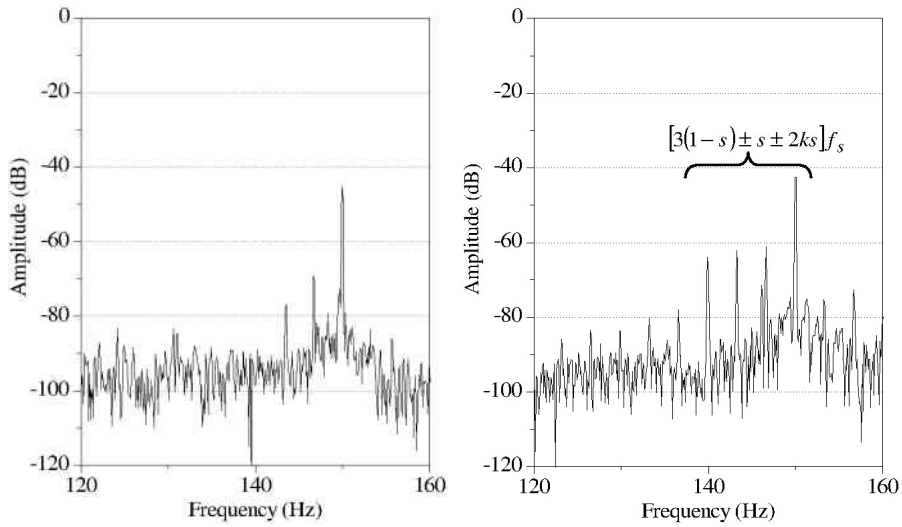

(a) No broken bars (b) 1 broken bar

Figure 7.4. *Stator current spectrum around the 3rd harmonic: a) the rotor is healthy; b) the rotor has 1 broken bar*

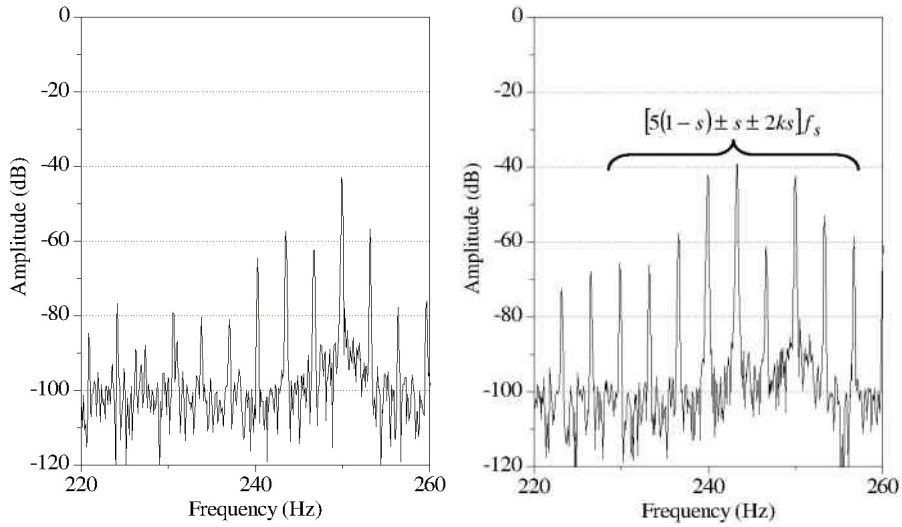

(a) No broken bars (b) 1 broken bar

Figure 7.5. *Stator current spectrum around the 5th harmonic: a) the rotor is healthy; b) the rotor has 1 broken bar*

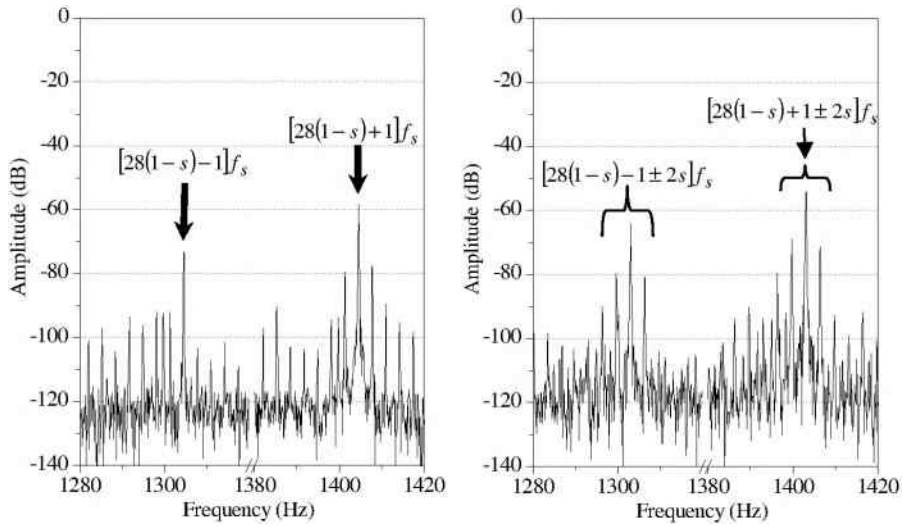

(a) No broken bars (b) 1 broken bar

Figure 7.6. *Stator current spectrum around the RSH: a) the rotor is healthy; b) the rotor has 1 broken bar*

fault. Most of the articles from the scientific or industrial community are limited on exploitation of the spectral content around the power feed frequency of the induction metal. In fact, the capacitive and inductive effects may alter the diagnosis by reducing the sensitivity of the amplitude variations of the emission lines according to the level of fault studied.

7.4.1.2. *Vibration and audible noise analysis*

A broken bar may cause unbalanced radial forces. These forces rotate with the rotor at a constant load, plus a load which evolves at twice the speed of the sliding. Consequently, as [SCH 04] underlines, the forces acting on the bearings will have frequency components given by:

$$f_{vbc} = hf_r \pm f_p \qquad [7.15]$$

where $f_p = P.f_{sl}$ corresponds to the pole pass frequency (PPF), $f_{sl} = f_s - f_r$ is the slip frequency, and P is the number of poles.

We may see other frequencies in the vibration spectrum which are indicated by the lateral lines $\pm 2f_s$ around the rotor bar pass frequency (RBPF), which is given by $RBPF = N_r.f_r$ [SCH 04]. They are thus expressed as:

$$f_{vbc} = N_r f_r \pm 2f_s \qquad [7.16]$$

Figure 7.7 shows the fundamental harmonic of the stator current spectrum of the induction machine operating at a charge of 50%. On the one hand, we can distinguish a significant increase in the component amplitudes whose frequencies are $f_s - f_r$ and $f_s + f_r$ (Figure 7.7b), which are already present in the spectrum of the healthy machine and are due to natural dynamic eccentricity (Figure 7.7a). On the other hand, considering that the rotor is faulty, the frequency lines relating to this type of fault are clearly seen in the spectrum. In the same way, observing the harmonics induced in the current under the speed ripple complies perfectly with the generalized formula given by [7.10]. The component at a frequency of $f_s - 3f_r$ given by equation [7.14] does not appear in the healthy spectrum, and appears when there is a fault. This is the consequence of having a particular form of eccentricity which is introduced by the broken bar fault. Let us note that there can be lateral bands around the fundamental, even when the machine is healthy.

Figure 7.7 shows the presence of lateral bands around the 3rd harmonic in the case of a healthy and faulty rotor. According to equation [7.12], the main difference is the significant increase in the amplitude of these components in the case of a fault.

Figure 7.8 mainly concerns the frequency band around the RSH in the healthy case, and also the lateral bands induced by a broken bar fault [7.15].

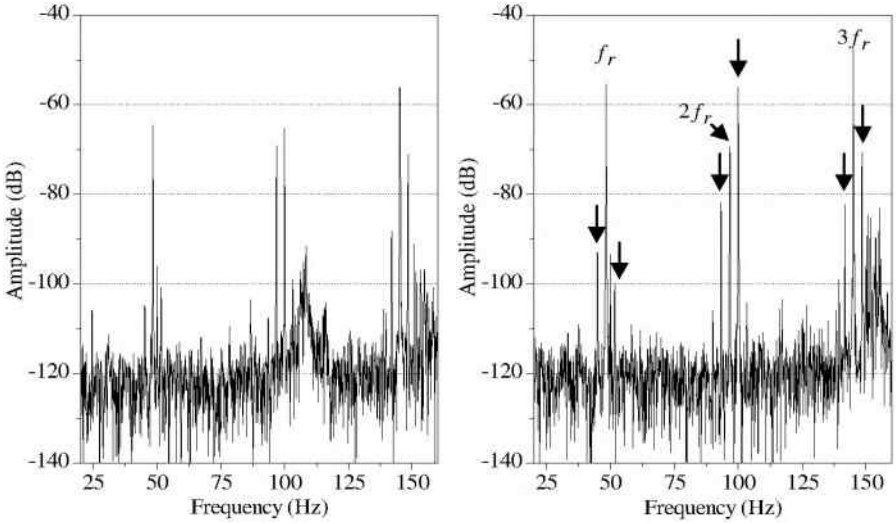

(a) No broken bars (b) 1 broken bar

Figure 7.7. *Radial vibrations spectrum on the first three harmonics: a) the rotor is healthy; b) the rotor has 1 broken bar*

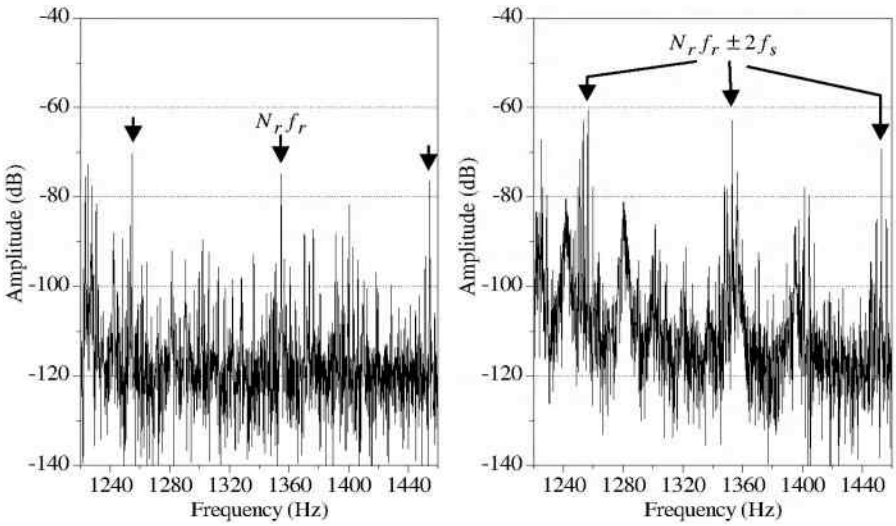

(a) No broken bars (b) 1 broken bar

Figure 7.8. *Radial vibration spectrum on the RBPF: a) the rotor is healthy; b) the rotor has 1 broken bar*

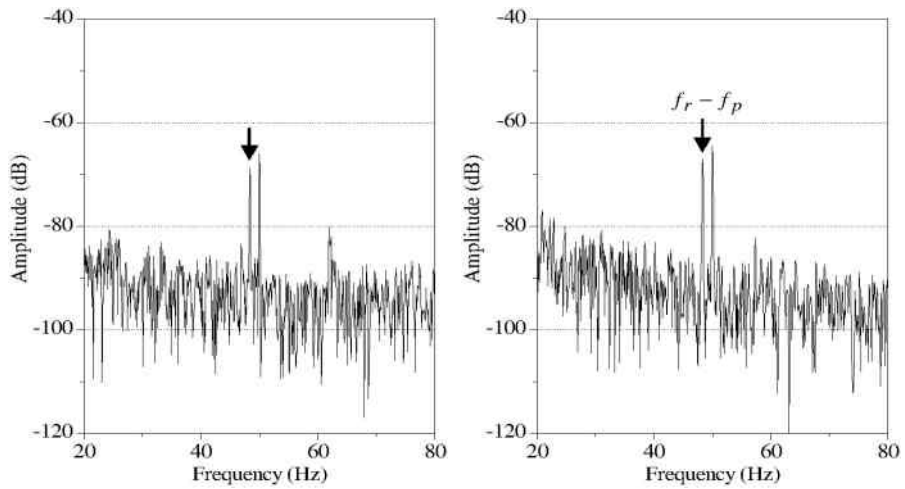

(a) No broken bars (b) 1 broken bar

Figure 7.9. *Noise spectrum around the fundamental: a) the rotor is healthy; b) the rotor has 1 broken bar*

With respect to vibratory and acoustic analyses, Figures 7.7 to 7.10 show the frequencies induced by the bar fault which complies with the previous formulae, such as the multiples of the rotation frequency surrounded by lateral bands $\pm f_p$. This explains the frequencies and amplitudes of the components introduced by the fault and for the different types of signals which are recorded in Table 7.2.

7.4.2. *Bearing faults*

Ball bearings may be subjected to faults due to assembly problems, or indirectly due to mechanical strain in the motor and drive process. Deterioration may also be induced by currents when a power feed uses a power inverter (speed variation). Fault detection can be considered either by vibration analysis, analyzing the spectral content of the absorbed current, or modifying the audible noise.

7.4.2.1. *Signatures in the stator current*

On the one hand, Schoen *et al*. [SHO 95] show that the relationship of the bearing vibration to the stator current spectrum can be determined by remembering that any eccentricity in the air-gap will produce anomalies in its flux density, and consequently gives the following relation:

$$f_{bng} = |f_s \pm m f_v| \qquad [7.17]$$

where m = 1, 2, 3 . . . and f_v is a characteristic vibration frequency.

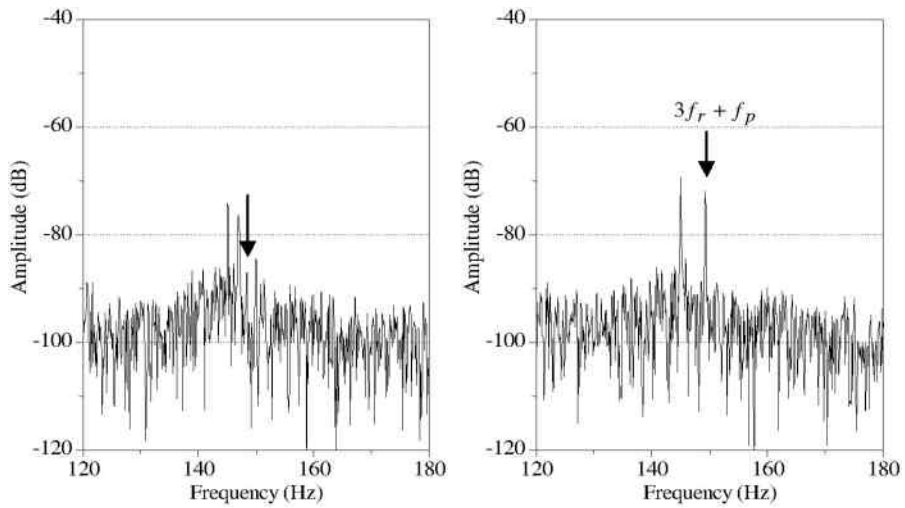

(a) No broken bars (b) 1 broken bar

Figure 7.10. *Noise spectrum around the 3rd harmonic: a) the rotor is healthy; b) the rotor has 1 broken bar*

On the other hand, Blödt, [BLÖ 08] suggests a characteristic expression with three fault types, as follows:

Outer race fault: $f_{bng} = |f_s \pm m f_o|$ [7.18]

Inner race fault: $f_{bng} = |f_s \pm f_r \pm m f_i|$ [7.19]

Ball bearing fault: $f_{bng} = |f_s \pm f_{cage} \pm m f_b|$ [7.20]

Irrespective of the case, the characteristic vibration frequencies will be calculated based on the bearing size (Figure 7.11). These bearing fault frequencies include the outer race frequency f_o, the inner race frequency f_i, the ball bearing frequency f_b, and finally the cage frequency f_{cage}:

$$f_i = \frac{N_b}{2}.f_r.\left(1 + \frac{Bd}{Pd}\cos\beta\right) \quad [7.21]$$

$$f_o = \frac{N_b}{2}.f_r.\left(1 - \frac{Bd}{Pd}\cos\beta\right) \quad [7.22]$$

$$f_b = \frac{Pd}{Bd}.f_r.\left[1 - \left(\frac{Bd}{Pd}\cos\beta\right)^2\right] \quad [7.23]$$

$$f_{cage} = \frac{f_r}{2}.\left(1 - \frac{Bd}{Pd}\cos\beta\right) \quad [7.24]$$

Formula	Frequency (Hz)	Signal/amplitude (dB)					
		Current		Vibration		Noise	
		Healthy	Fault	Healthy	Fault	Healthy	Fault
$f_s - f_r$	1.61	−87	−82				
$[1 \pm 2s]f_s$	46.7	−44	−34				
	53.3	−49	−34				
$f_s - 3f_r$	95.12	−83	−61				
$f_s + f_r$	98.35	−61	−66				
$(3 - 4s)f_s$	143.4	−77	−62				
$(3 - 2s)f_s$	146.7	−69	−61				
$(5 - 6s)f_s$	240.1	−65	−42				
$(5 - 4s)f_s$	243.4	−57	−39				
$[28(1 - s) - 1 \pm 2s]f_s$	1,299	−94	−80				
	1,306	−105	−80				
$[28(1 - s) + 1 \pm 2s]f_s$	1,399	−80	−69				
	1,406	−77	−70				
$f_r \pm f_p$	44			−105	−92		
	52			−102	−99		
$2f_r \pm f_p$	93			−108	−82		
	100			−65	−56		
$3f_r \pm f_p$	141			−89	−83		
	148			−71	−70		
$28f_r \pm 2f_s$	1,253			−68	−63		
	1,453			−77	−70		
$f_r - f_p$	45					−69	−67
$3f_r + f_p$	148					−84	−71

Table 7.2. *Line amplitudes relating to a fault*

We could see that 5 physical parameters must be known to determine the characteristic frequencies of the bearing fault, namely: ball bearing diameter Bd, the average diameter or the diameter of the cage Pd, the number of ball bearings N_b, the angle of contact β in radians, and the rotation frequency f_r.

The faulty components in the bearing produce a single frequency in relation to the dynamic of the bearing motion, and the mechanical vibrations produced are a function of the rotation speeds of each component.

However, we could not determine the exact fundamental frequencies of the bearing faults when the geometric dimensions of the bearings installed in the induction motor were unknown. In addition, Schoen has shown in [SHO 95] that the vibration frequencies can be brought closer for most of the bearings with 6-12 balls by the following formulae:

$$f_o = 0.4N_b f_r; \quad f_i = 0.6N_b f_r \qquad [7.25]$$

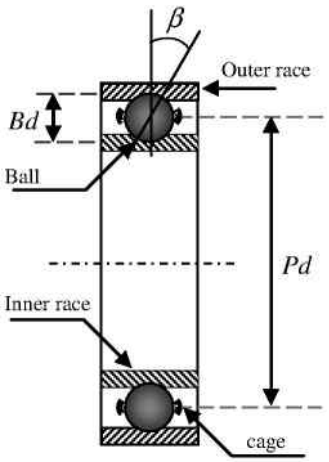

Figure 7.11. *Ball bearing dimensions*

Due to this fact, these approximations are valid for bearings in the 6200 series alone and not for the 6300 series [STA 04]. However, [CRA 92] has proposed approximations to estimate the frequencies f_{cage}, f_i and f_o (Table 7.8). Thus, for the 6300 series, his approximations give the following:

$$f_{cage} = \left(\frac{1}{2} - \frac{1.2}{N_b}\right).f_r \qquad [7.26]$$

$$f_i = \left(\frac{N_b}{2} + 1.2\right).f_r \qquad [7.27]$$

$$f_o = \left(\frac{N_b}{2} - 1.2\right).f_r \qquad [7.28]$$

7.4.2.2. *Outer race fault*

Figures 7.12 to 7.15 respectively show the frequency components that relate to the bearing's outer race faults in the induction machine, which is operating at 50% charge. In the current spectrum, we see that the component's amplitude increases according to equation [7.18], and thus the frequency of the outer race. With respect to the radial vibration spectra and the noise, there is a clear increase in the frequencies given by equation [7.22]. Finally, the frequencies and amplitudes of the components introduced by the fault, and for different types of signals, have been highlighted in Table 7.3.

7.4.2.3. *Ball bearing fault signatures*

The ball bearing fault test was carried out under the same load conditions as the bearing's outer race test.

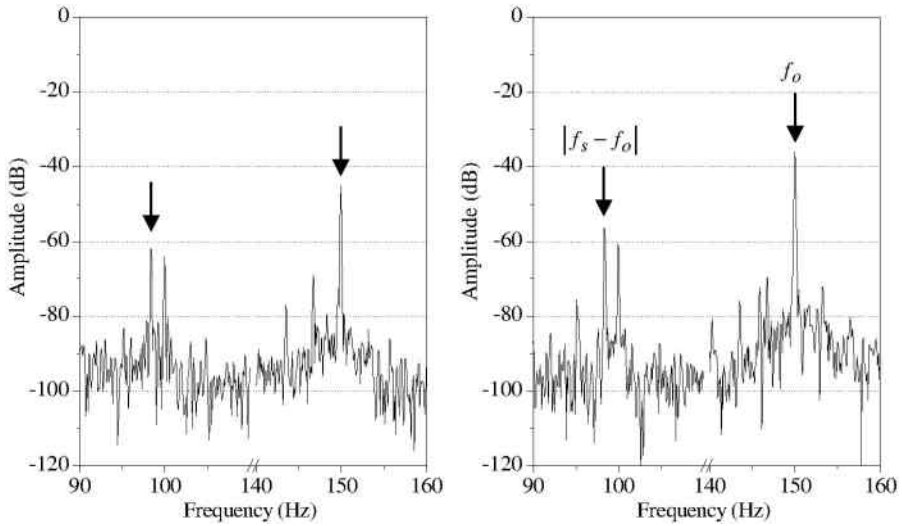

(a) Healthy outer race (b) Faulty outer race

Figure 7.12. *Stator current spectrum: a) the bearing is healthy; b) the bearing has an outer race defect*

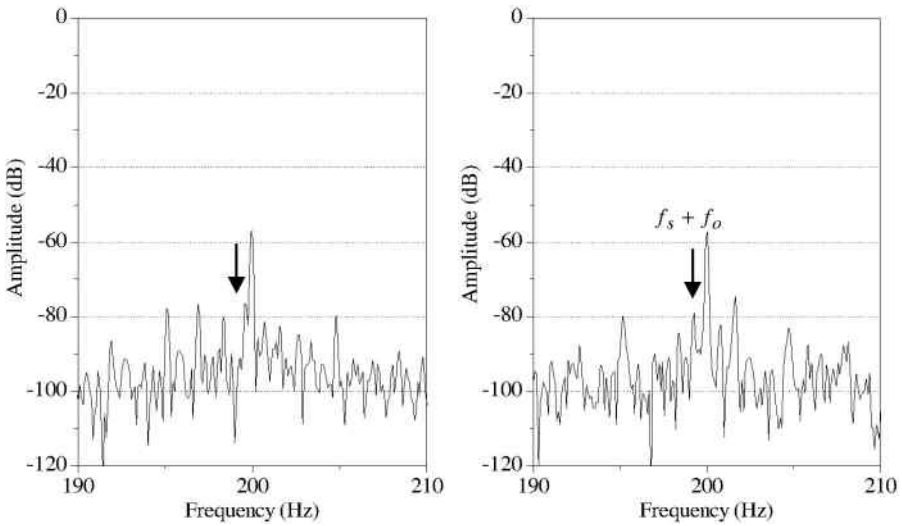

(a) Healthy outer race (b) Faulty outer race

Figure 7.13. *Radial vibration spectrum: a) the bearing is healthy; b) the bearing has an outer race defect*

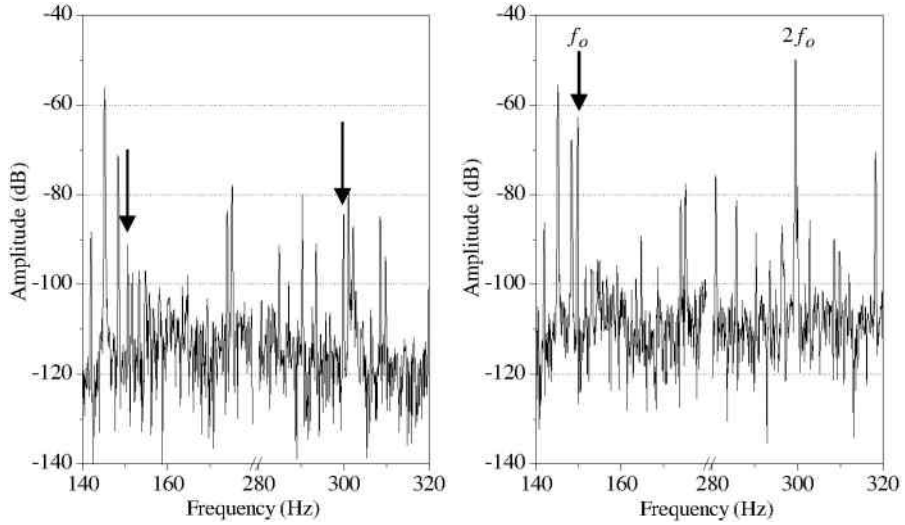

(a) Healthy outer race (b) Faulty outer race

Figure 7.14. *Radial vibration spectrum: a) the bearing is healthy; b) the bearing has an outer race defect*

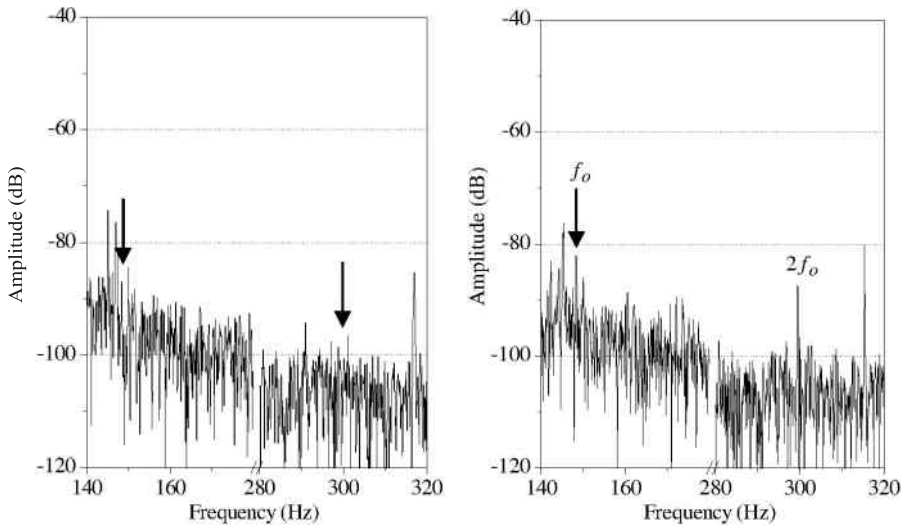

(a) Healthy outer race (b) Faulty outer race

Figure 7.15. *Radial audible noise spectrum: a) the bearing is healthy; b) the bearing has an outer race defect*

Formula	Frequency (Hz)	Signal/amplitude (dB)					
		Current		Vibration		Noise	
		Healthy	Fault	Healthy	Fault	Healthy	Fault
$f_s - f_o$	98	−76	−69				
$f_s + f_o$	199	−91	−79				
f_o	148			−117	−63	−87	−81
$2f_o$	296			−121	−50	−97	−87

Table 7.3. *Line amplitudes relating to an outer race fault*

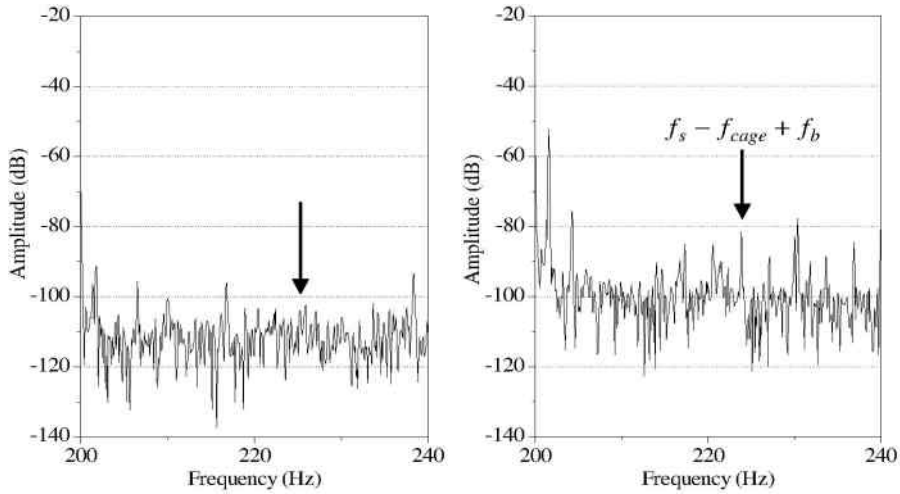

(a) Healthy balls (b) Faulty balls

Figure 7.16. *Stator current spectrum close to* $f_{bng} = f_s - f_{cage} + f_b$*: a) the bearing is healthy; b) the bearing has 2 damaged balls*

Figures 7.16 to 7.20 show the frequencies relating to the ball fault. For the current spectrum, there is a slight increase in the frequency amplitude of the fault given by equation [7.19] respectively at $f_s - f_{cage} - f_b$. However, in the vibration spectrum, we note an increase in the frequency amplitude, given by equation [7.23], on f_b as well as $2f_b$. We also note a slight increase in the amplitude of $3f_b$ in the noise spectrum. The frequencies and amplitudes of the components introduced by the fault and for different types of signals are set out in Table 7.4.

7.4.3. *Static eccentricity*

Off-setting is an anomaly which appears benign. It occurs naturally during the construction of an electric motor (assembly), and also by a ball bearing in particular. Once again, lines will emerge in the spectral content, as much from the current absorbed

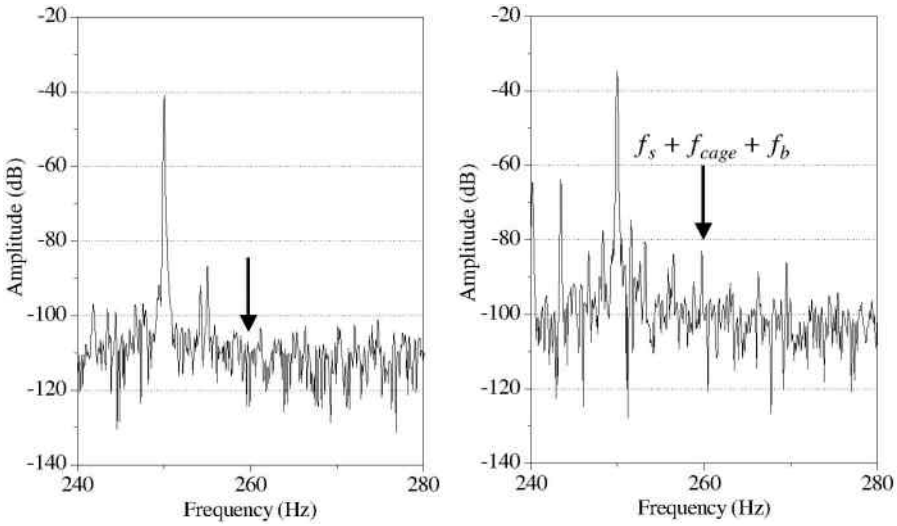

(a) Healthy balls (b) Faulty balls

Figure 7.17. *Stator current spectrum close to* $f_{bng} = f_s + f_{cage} + f_b$*:*
a) the bearing is healthy; b) the bearing has 2 damaged balls

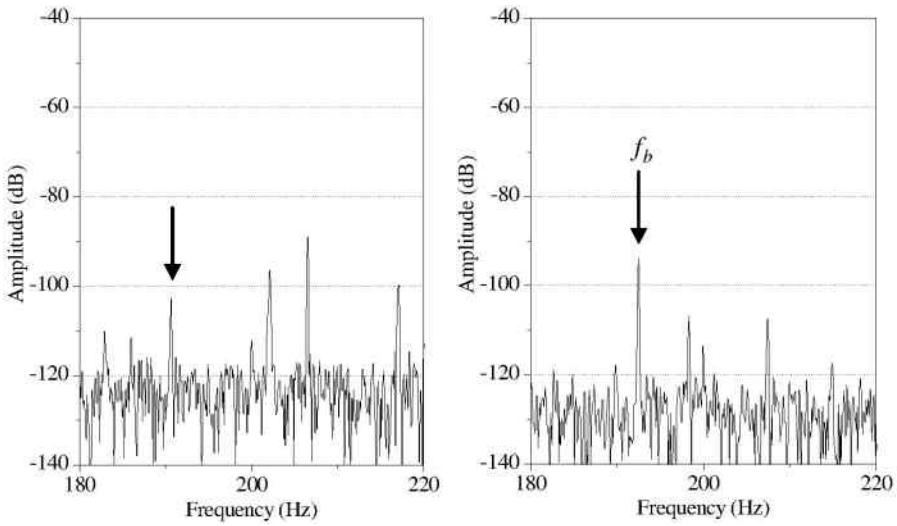

(a) Healthy balls (b) Faulty balls

Figure 7.18. *Radial vibration spectrum surrounding* f_b*:*
a) the bearing is healthy; b) the bearing has 2 damaged balls

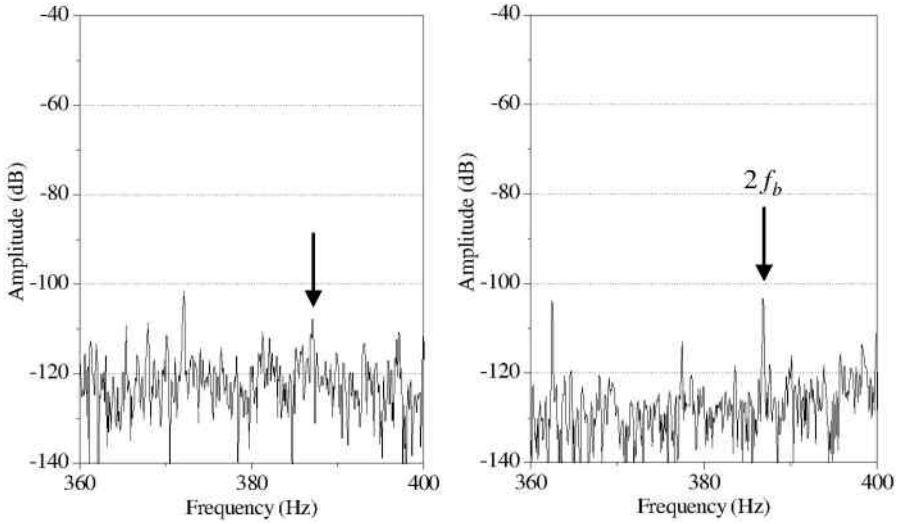

(a) Healthy balls (b) Faulty balls

Figure 7.19. *Radial vibration spectrum surrounding* $2f_b$*:*
a) the bearing is healthy; b) the bearing has 2 damaged balls

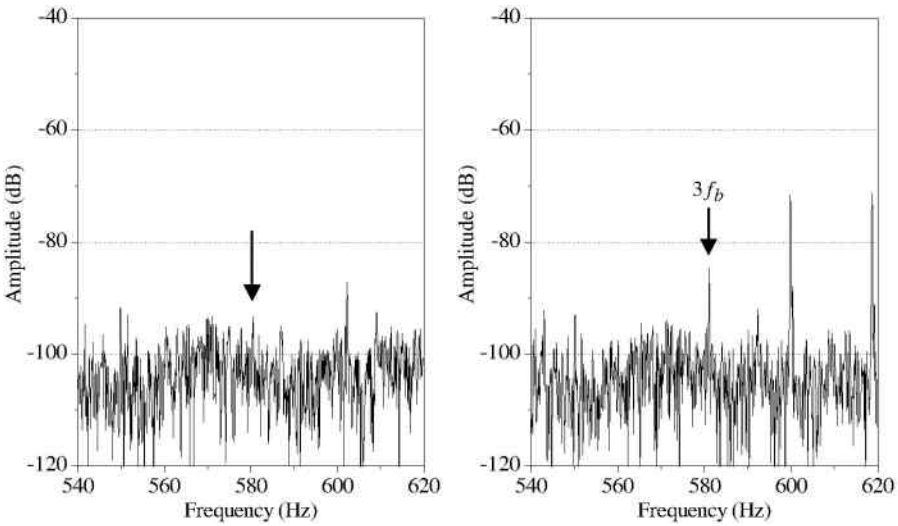

(a) Healthy balls (b) Faulty balls

Figure 7.20. *Radial vibration spectrum surrounding* $3f_b$*:*
a) the bearing is healthy; b) the bearing has 2 damaged balls

Formula	Frequency (Hz)	Signal/amplitude (dB)					
		Current		Vibration		Noise	
		Healthy	Fault	Healthy	Fault	Healthy	Fault
$f_s - f_{cage} + f_b$	225	−83	−73				
$f_s + f_{cage} + f_b$	262	−108	−82				
f_b	192			−102	−92		
$2f_b$	384			−108	−102		
$3f_b$	576					−92	−85

Table 7.4. *Line amplitudes relating to a ball bearing fault*

by the electrical motor as in the generated vibrations. Let us note that when there is an off-set of more than 20%, then it is recommended that the bearings/ball bearings are replaced. This eccentricity may be the source of a homopolar current which, closed by the bear bearings, will cause premature aging in the bearings.

7.4.3.1. *Stator current spectral content*

Naturally, the spectral content of the current absorbed by the induction machine will be altered by the lines specific to the off-set fault. As there is even dynamic as well as combined excentration, we will only refer to the case of static excentration due to experimental reports. The frequencies of these lines induced by static excentration are shown hereafter:

$$f_{s,ecc} = \left[kN_r \left(\frac{1-s}{p} \right) \pm 1 \right] f_s \qquad [7.29]$$

with k = 1, 2, 3 ....

When we consider the harmonics contained in the motor's power supply voltages, then the frequencies induced by the excentration in the absorbed current spectrum are expressed as below:

$$f_{s,ecc} = \left[kN_r \left(\frac{1-s}{p} \right) \pm n \right] f_s \qquad [7.30]$$

with n being the time-harmonic rank (n = 1, 3, 5 ...).

Figures 7.21 and 7.22 show the characteristic frequencies of the static eccentricity. The frequency range corresponds to high frequencies (RSH). We may note a relative lack of sensitivity of the line amplitudes in relation to the eccentricity rate. Figure 7.21 is limited to the fundamental harmonic of the power supply voltage [7.29], whereas Figure 7.22 show the spectrum induced when the 3rd harmonic is considered in the voltage [7.30].

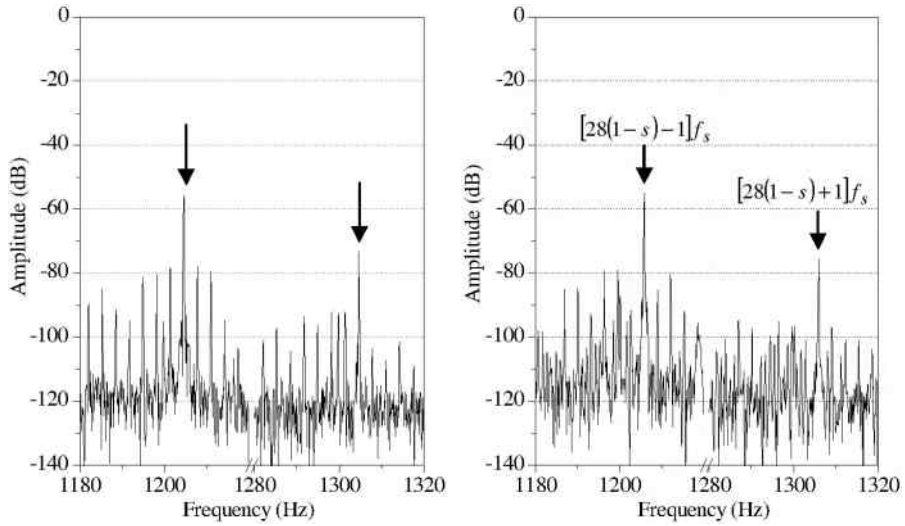

(a) No off-set (b) Off-set

Figure 7.21. *Stator current spectrum, static eccentricity ($n = 1$): a) healthy machine; b) eccentricity*

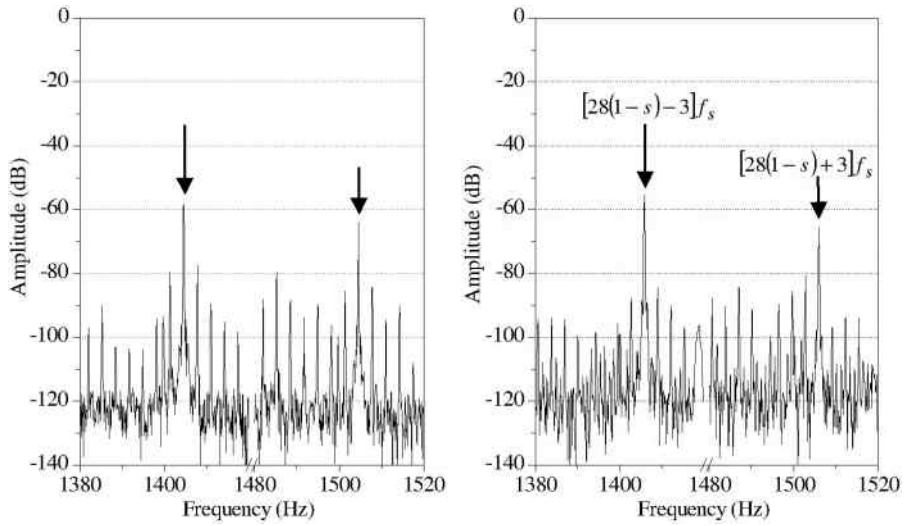

(a) No off-set (b) Off-set

Figure 7.22. *Stator current spectrum, static eccentricity ($n = 3$): a) healthy machine; b) eccentricity*

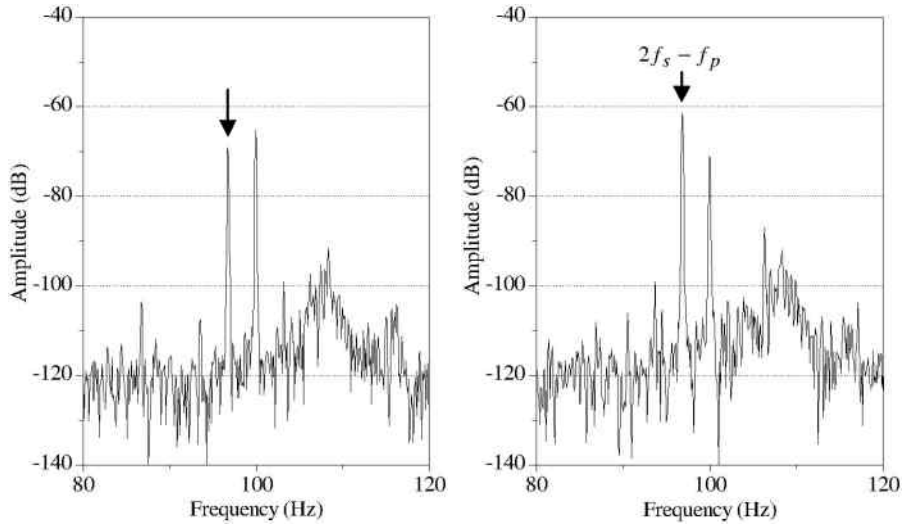

(a) No off-set (b) Off-set

Figure 7.23. *Radial vibration spectrum of static eccentricity at $F_{ecc} = 2f_s - f_p$: a) healthy machine; b) machine with off-set*

7.4.3.2. *Spectral content of vibrations and audible noise*

The rotor eccentricity generates frequencies which are twice that of the power supply frequency $2f_s$, at more or less the passing frequency per pole, written as f_p. The expression of frequency is given by:

$$F_{ecc} = k(2f_s \pm f_p) \qquad [7.31]$$

with k = 1, 2, 4 ....

Figures 7.23 to 7.28 show the vibration spectra for a healthy motor and, an off-set motor.

From Figure 7.23, we can see a low increase in the frequency amplitudes introduced by the eccentricity, given by equation [7.31] (with k = 1) at: $2f_s - f_p$. This amplitude variation is infact deed significant, but well beyond those observed when k is equal to 2, or even 4 (Figures 7.24 and 7.25).

In the same way, in Figures 7.26 to 7.28 we show the spectral content of the audible noise produced by the induction motor when it is healthy and also when there is excentration. The line frequencies are identical to those expected, as well as those obtained in the radial vibration spectra. The amplitude variations of these lines demonstrate the presence of significant excentration in order to express the presence (or not) of an excentration fault.

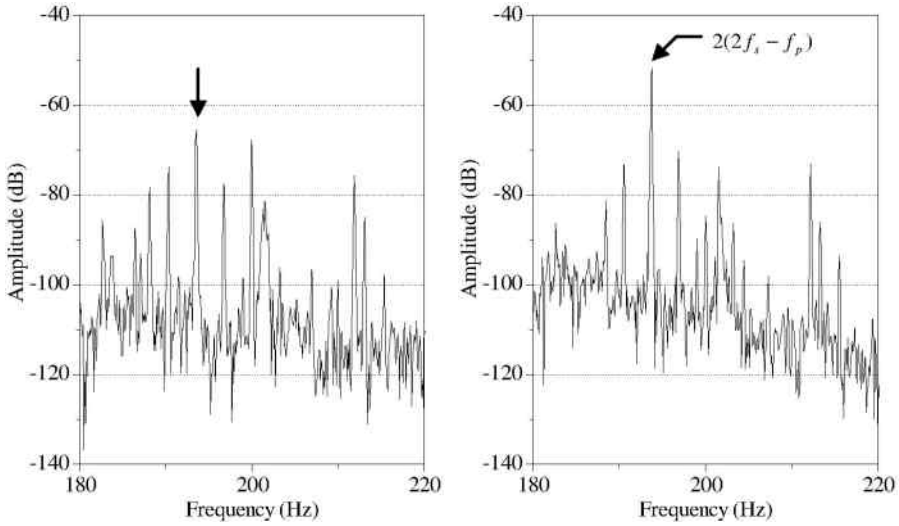

(a) No off-set (b) Off-set

Figure 7.24. *Radial vibration spectrum of static eccentricity at $F_{ecc} = 2(2f_s - f_p)$: a) healthy machine; b) machine with off-set*

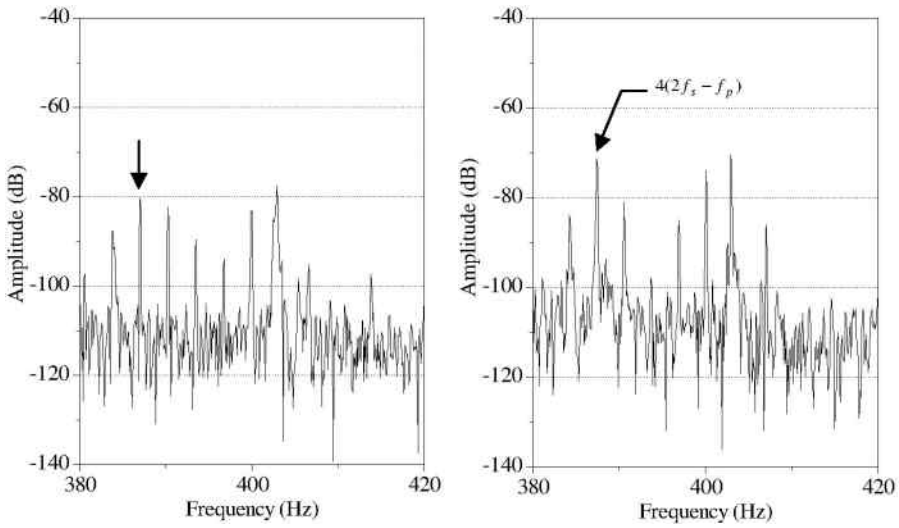

(a) No off-set (b) off-set

Figure 7.25. *Radial vibration spectrum of static eccentricity at $F_{ecc} = 4(2f_s - f_p)$: a) healthy machine; b) machine with off-set*

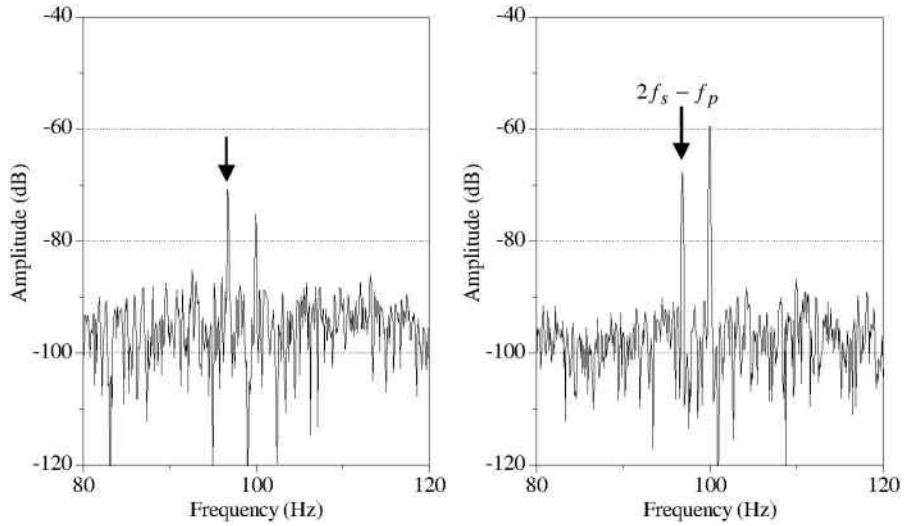

(a) No off-set (b) off-set

Figure 7.26. *Audible noise spectrum of static eccentricity at $F_{ecc} = 2f_s - f_p$: a) healthy machine; b) machine with off-set*

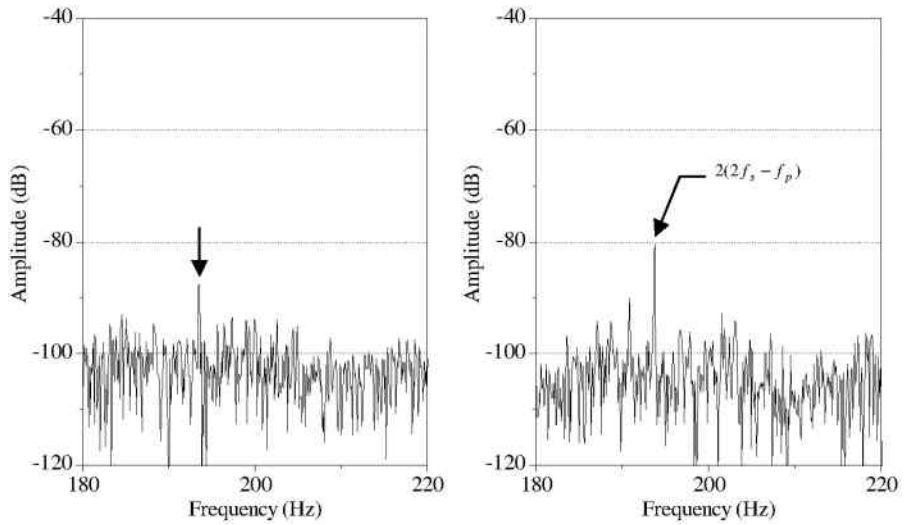

(a) No off-set (b) off-set

Figure 7.27. *Audible noise spectrum of static eccentricity at $F_{ecc} = 2(2f_s - f_p)$: a) healthy machine; b) machine with off-set*

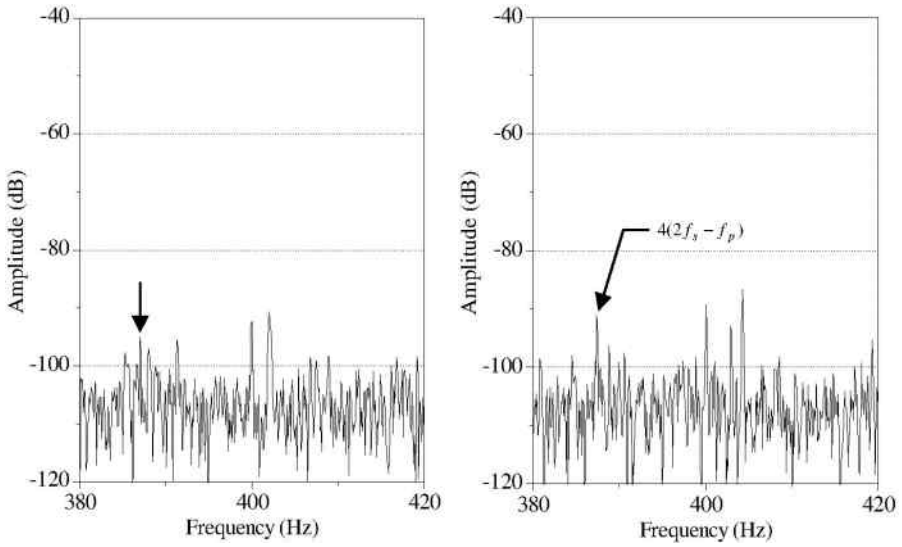

(a) No off-set (b) off-set

Figure 7.28. *Audible noise spectrum of static eccentricity at $F_{ecc} = 4(2f_s - f_p)$: a) healthy machine; b) machine with off-set*

Finally, we have reported the frequencies and amplitudes of the components introduced by this type of fault and for different types of sensors. These are highlighted in Table 7.5. This allows us to confirm the relative non-sensitivity of the line amplitudes close to the RSH in relation to an excentration. Consequently, these lines cannot be reasonably used in monitoring or diagnosis. However, the lines given in [7.31] for k equal to 2 or 4 are completely relevant for diagnosis. Their increased amplitude is high enough to recommend them for monitoring the motor's health state.

Formula	**Frequency (Hz)**	**Signal/amplitude (dB)**					
		Current		**Vibration**		**Noise**	
		Healthy	**Fault**	**Healthy**	**Fault**	**Healthy**	**Fault**
$[28\,(1-s)-1]\,f_s$	1303.4	−56	−55				
$[28\,(1-s)+1]\,f_s$	1403.4	−72	−76				
$[28\,(1-s)-3]\,f_s$	1203.4	−58	−55				
$[28\,(1-s)+3]\,f_s$	1503.4	−62	−65				
$2f_s - f_p$	96.7			−69	−62	−70	−68
$2(2f_s - f_p)$	193.66			−66	−50	−88	−80
$4(2f_s - f_p)$	387.32			−80	−72	−95	−91

Table 7.5. *Amplitude of observed lines, relating to off-set*

7.4.4. *Inter turn short-circuits*

As stated at the beginning of this chapter, we have tested inter turn short-circuits in the stator phase of an MAS_2 induction machine, whose technical details can be found in appendix A. We had carried out "no-load motor" tests. The machine was re-wound with intermediate sockets. They were distributed across the three phases, aiming to short-circuit a number of pre-selected turns. Wires soldered onto the sockets are brought down to the terminal board.

7.4.4.1. *Stator current analysis*

There are two equations which are frequently found in literature, and are suggested as relevant indicators for inter turn short-circuit fault detection. The first equation described in [PEN 94] relates to low frequencies, as expressed below:

$$f_{st} = f_s . \left[n \frac{(1-s)}{P} + k \right] \Bigg|_{k=1,3,5}^{n=1,2,3..} \qquad [7.32]$$

with f_{st} as the frequencies induced by a coil short-circuit on the stator, n = 1, 2, 3, ..., k = 1, 3, 5, and ..., P is the number of pole pairs and s is the slip.

An inter turn short-circuit will cause an increased current amplitude in the rotor bars, proportional to the seriousness of the fault. This justifies the observation of short-circuit frequencies around the slot harmonics (RSH), hence a second equation given by [JOK 00]. The equation is the following:

$$f_s . \left[1 + \lambda N_r \frac{(1-s)}{P} \right] \Bigg|_{\lambda=1,2,3...} \qquad [7.33]$$

with λ as a whole number, and N_r as the number of rotor bars.

Figure 7.29 shows the fundamental harmonic of the stator current spectrum of the induction machine operating at no-load. On the one hand, we could see components with frequencies at $f_s - f_r$ and $f_s + f_r$, which are already present in the healthy machine spectrum, and due to natural dynamic eccentricity.

On the other hand, Figure 7.30 shows the increase in the same components given by the equation [7.32] and generated by the coil short-circuit in the induction machine.

As the induction machine is not loaded, in Figure 7.30 we notice a slight increase in the frequencies given by equation [7.33] in relation to the healthy case. On the other hand, in Figure 7.31, even if the machine is operating at no-load and with a machine phase which is short-circuited at 60%, we notice a significant increase in the frequency amplitude on the RSH, above all on the first RSH for $\lambda = 1$. As for low frequencies, the amplitudes are the same as the previous ones, hence we do not find it relevant to show them here. This explains the frequencies and amplitudes of the components introduced by the short-circuit, which are listed in Table 7.6.

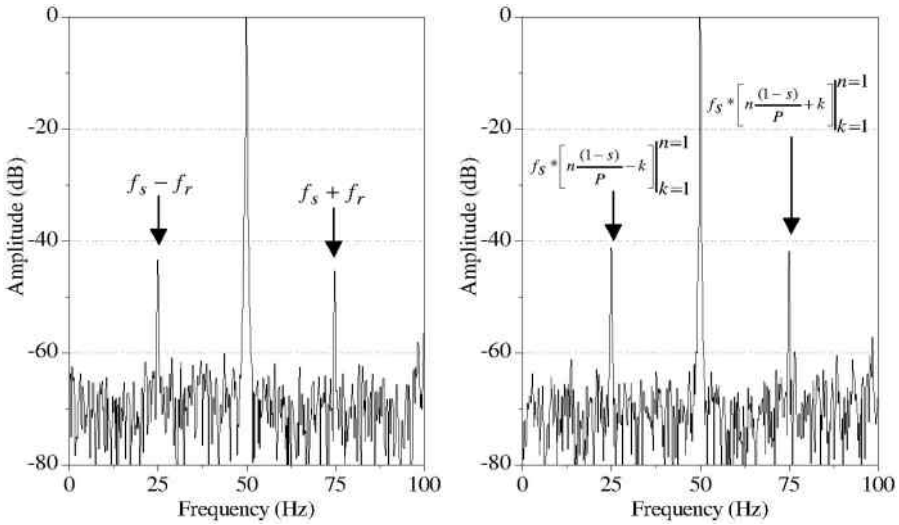

(a) No short-circuit (b) With short-circuit

Figure 7.29. *Stator current spectrum around the fundamental harmonic: a) healthy machine; b) machine with 30% of the coils in the short-circuited phase*

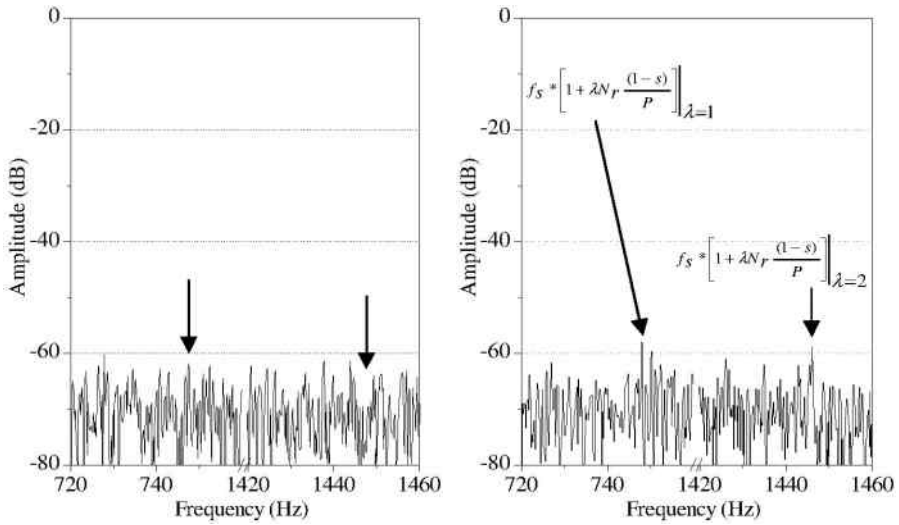

(a) No short-circuit (b) With short-circuit

Figure 7.30. *Stator current around the RSH: a) healthy machine; b) machine with 30% of the coils in the short-circuited phase*

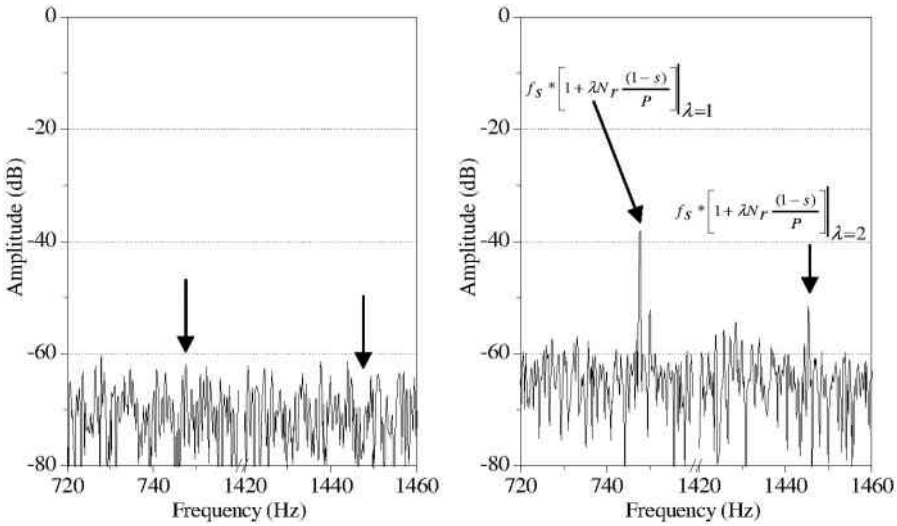

(a) No short-circuit (b) With short-circuit

Figure 7.31. *Stator current spectrum around the RSH: a) healthy machine; b) machine with 60% of the coils in a short-circuited phase*

Formula	Freq. (Hz)	Amplitude (dB)		
		Healthy	Fault	
			30%	60%
$f_s.\left[n\frac{(1-s)}{P} - k\right]\Big\|_{k=1}^{n=1} = f_s[\frac{(1-s)}{2} - 1]$	24.70	−44	−41	−39
$f_s.\left[n\frac{(1-s)}{P} + k\right]\Big\|_{k=1}^{n=1} = f_s[\frac{(1.s)}{2} + 1]$	74.66	−46	−42	−42
$f_s * \left[1 + \lambda N_r \frac{(1-s)}{P}\right]\Big\|_{\lambda=1} = f_s[1 + 28\frac{(1-s)}{2}]$	748	−62	−57	−38
$f_s.\left[1 + \lambda N_r \frac{(1-s)}{P}\right]\Big\|_{\lambda=2} = f_s[1 + 28(1-s)]$	1446	−70	−59	−51

Table 7.6. *Line amplitudes relating to a short-circuit fault*

7.5. Conclusion

With the advent of vector control, the induction machine is widely used in the industrial environment, and maintaining the serviceability causes aging in this machine. The aim of this chapter was to establish the state-of-the-art diagnosis techniques through signal processing, and it was for this purpose that we carried out our work which was generated around experiments on machine faults with the aim to diagnose them. This chapter was split into two parts, the first was dealing with rotor faults such as bar

breakage and bearing fault. Part 2 was dedicated to inter turn short-circuits in a stator phase. In a non-exhaustive way, we have shown the different techniques and hypothesis published in the field of diagnostics. All faults were created artificially in order to bring together the approaches presented previously, namely, drilling a rotor bar in order to simulate bar breakage, slotting in the outer race, abrasion in the two ball bearings, and a second machine was wound in order to demonstrate inter turn short-circuiting. We then analyzed these signals to follow the evolution of the spectrum obtained by using the FFT. We showed the frequencies inherent to each fault which should occur in the spectra of each signal. After having scanned a wide range of electrical and mechanical faults in the induction machine, we can easily conclude that vibratory and acoustic techniques offer the best results for diagnosing mechanical faults. As for electrical faults, we have noticed that the current analysis gives good results. Let us point out here that this type of fault is problematic to diagnose, as a fault between successive coils will affect the behavior of the electrical motor differently, as much in terms of abnormal over-heating and the motor's destruction speed, as following a fault between coils which are more distanced from each other.

7.6. Appendices

7.6.1. *Appendix A*

We have shown some of the characteristics of the motors used. The motor branded SEW USOCOME was subjected to several failures. However, for short-circuited coil faults on the stator winder, the FIMET branded motor was used.

Description	**MAS$_1$**	**MAS$_2$**
Brand	SEW USOCOME	FIMET
Power	3 kW	3 kW
Current	5.9 A	6.13 A
Number of poles	2	4
Number of rotor bars	28	28
Number of stator slots	36	36
Nominal speed	2,800 rpm	1,380 rpm

Table 7.7. *Characteristics of the induction machines used*

7.6.2. *Appendix B*

Here, we have given some of the characteristics of ball bearings used, knowing that bearing 6205 is positioned next to the ventilator and that bearing 6306 presents failures in this study.

Description	6306	6205
Brand	KG	KG
Number of balls	8	9
Average diameter	51 mm	46 mm
Ball diameter	12 mm	10 mm
Contact angle β	0˝	0˝

Table 7.8. *Ball bearing dimensions*

7.7. Bibliography

[ABE 02] ABED A., Contribution à l'étude et au diagnostic de la machine asynchrone, thesis, Henri Poincaré University, Faculté des Sciences de Nancy 1, 2002.

[BLÖ 08] BLÖDT M., GRANJON P., RAISON B., ROSTAING G., "Models for bearing damage detection in induction motors", *IEEE Transactions on Industrial Electronics*, vol. 55, no. 4, p. 1813-1822, April 2008.

[BON 88] BONNETT A.H., SOUKUP G.C., "Analysis of rotor failures in squirrel-cage induction motors", *IEEE Transactions on Industry Applications*, vol. 24, no. 6, p. 1124-1130, November/December 1988.

[BON 92] BONNETT A.H., SOUKUP G.C., "Cause and analysis of stator and rotor failures in three-phase squirrel-cage induction motors", *IEEE Transactions on Industry Applications*, vol. 28, no. 4, p. 921-937, July/August 1992.

[CRA 92] CRAWFORD A.R., CRAWFORD S., *The Simplified Handbook of Vibration Analysis Vol I: Introduction to Vibration Analysis Fundamentals*, Computational Systems Incorporated, 1992.

[DEL 84] DELEROI W., "Broken bar in squirrel-cage rotor of an induction motor. Part I: Description by superimposed fault-currents", *Archiv Fur Elektrotechnik*, vol. 67, p. 91-99, 1984.

[DID 04] DIDIER G., Modélisation et Diagnostic de la machine asynchrone en présence de défaillances, thesis, Henri Poincaré University, Faculté des Sciences de Nancy 1, 2004.

[FIS 99] FISER R., FERKOLJ S., "The progress in induction motors fault detection and diagnosis", *Proceedings of EEDEEQ '99 4th International Symposium Maintenance of Electrical Machines*, Zagreb, Croatia, November 15-16, 1999.

[HEI 98] HEIN D., Identification de la machine asynchrone en vue du diagnostic de pannes, thesis, CNAM de Paris, Centre Associé de Metz, 1998.

[JOK 00] JOKSIMOVIC G.M., PENMAN J., "The detection of inter turn short circuits in the stator windings of operating motors", *IEEE Transactions on Industrial Electronics*, vol. 47, no. 5, October 2000.

[MEL 99] MELERO M., CABANAS M., FAYA F., ROJAS C., SOLARES J., "Electromagnetic torque harmonics for online inter turn short circuits detection in squirrel cage induction motors", *EPE'99*, Lausanne, Switzerland, p. 9, 1999.

[PEN 94] PENMAN J., SEDDING H.G., LLOYD B.A., FINK W.T., "Detection and location of inter turn short circuits in the stator winding of operating motors", *IEEE Transactions on Energy Conversion*, vol. 9, no. 5, December 1994.

[SCH 04] SCHEFFER C., GIRDHAR P., *Practical Machinery Vibration Analysis and Predictive Maintenance*, Elsevier, 2004.

[SHO 95] SHOEN R.R. *et al.*, "Motor bearing damage detection using stator current monitoring", *IEEE Transactions on Industry Applications*, vol. 31, November-December, 1995.

[STA 04] STACK J.R., HARLEY R.G., HABETLER T.G., "An amplitude modulation detector for fault diagnosis in rolling element bearings", *IEEE Transactions on Industrial Electronics*, vol. 15, no. 5, October, 2004.

[THO 01] THOMSON W., FENGER M., "Current signature analysis to detect induction motor faults", *IEEE Transactions on Industry Applications*, vol. 7, no. 4, July-August, 2001.

Chapter 8

Fault Diagnosis of the Induction Machine by Neural Networks

8.1. Introduction

The induction machines are more frequently used due to their robustness. But as with any other machine, the induction machine is not protected from malfunctioning. It can be affected by electrical or mechanical faults at the level of the stator, the rotor, or both at the same time. In order to increase the availability of this machine, it is important to detect the faults that are likely to appear in this machine at an early stage. This chapter focuses on two electrical faults of the induction machine: the stator fault type inter turns the short-circuit of the stator windings and the rotor fault type is a result of the broken bars of the rotor cage. The requirements of operation safety and productivity of the industrial installations have resulted in significant research efforts for the detection and the diagnosis of the faults; hence several approaches in this domain are developed.

The artificial neural networks (ANN) have given good performances to solve the problems of fault diagnosis and the automation of the monitoring process. In addition, the ANN has proven their pertinence for the fault detection by recognition of the shapes. For this reason, this chapter suggests a monitoring system based on the application of the neural networks for the detection and the diagnosis of the faults of the induction machine.

Chapter written by Monia Ben Khader BOUZID, Najiba MRABET BELLAAJ, Khaled JELASSI, Gérard CHAMPENOIS and Sandrine MOREAU.

The system is composed of a circuit for the detection of the two stator and/or rotor faults, along with another circuit for the localization of the phase at fault in case of stator fault, and of a third circuit for the identification of the number of broken bars in the rotor, in the case of rotor fault.

The ANN performances in the fault diagnosis domain are directly related to the quality and the nature of the pertinent inputs of the network, which are also called fault indicators. For the detection process, a direct approach involves using the amplitudes of the currents as inputs of the neural network. This approach has been found to be unsuitable, in particular with respect to load variations. Other, more sophisticated indicators resulting from a prior processing have therefore been used.

We have chosen to use the residues of a parametric estimation method, which are null during healthy operation and non-null in presence of faults. To improve the discrimination of the faults found in the residues, a second preprocessing is carried out by Fourier transform. The Fourier transform gives an image of the fault in specific frequency lines, which are perfectly discriminable by the ANN. In addition, the identification technique provides a robust detection with respect to the parametric variations due to the external causes (temperature or magnetic state) without considering that the parameter variation as a fault. For the localization circuit of the stator fault, the chosen fault indicators are the three phase shift between each phase voltage and its line current. These phase shifts are very efficient for a correct localization of the faulty phase, in the case of an inter turns short-circuit fault. In order to identify the number of broken bars in the rotor, the amplitude and the frequency of the spectrum line of the stator current, which characterize the fault, are used as fault indicators by the neural network. This network is used to determinate automatically the number of broken bars.

This chapter starts with a presentation of the neural networks and their different architectures. Then, the chapter describes the experimental validations of the detection process of the stator and rotor faults by the neural networks. Finally, the complete monitoring system is described with performance tests.

8.2. Methodology of the use of the ANN in the diagnostic domain

At present, the ANN are a well-understood data processing and monitoring technique, which should be a part of the toolbox of any engineer concerned with extracting the maximum pertinent information from the data at his disposal: carrying out predictions and data mining, developing models, as well as recognizing forms or signals. In this chapter, the ANN are used for the detection and the diagnosis of the faults of the induction machine, based on the recognition of the signatures of the faults extracted from the measurable signals.

Similar to the biological neural systems, an ANN is a strongly connected assembly of formal neurons, which are linked between each other by synaptic connections. The ANN has a natural propensity for storing the empirical knowledge and making it available for usage. They primarily operate on the basis of a learning process. This process involves the estimation of the parameters of the network neurons, by adjusting the interconnection weights between the neurons, so that these neurons are able to complete their task. The following properties enable the ANN to provide an interesting solution for surveillance problems of the industrial equipment: capabilities to solve the problems related to classification and form recognition, high learning and generalization ability, and rapidity of non-linear data processing [DRE 02].

Depending on the nature of the data at the output of the network, the ANN can be used for monitoring in two different ways: as main classification and form recognition (classifiers) tool or as a tool, so that we can rebuild a given variable (estimators) with, for example an output of the sensor [CAS 03]. This estimation can be used, for example to evaluate a variable, which is difficult to measure, and whose value is important for the decision-making process, or for the prediction of its future evolution. In fault diagnosis, the ANN are used as form recognition tools. Thus, the diagnosis problem is replaced by a recognition problem, where the forms represent the set of observations or measurements of the system (qualitative or quantitative data), and where the classes correspond to the different operating and failure modes of the system.

In this study, the fault diagnosis relies on the design of an ANN playing the role of automatically designing each operating signature of the machine to its corresponding (healthy or faulty) operation state. In order to better understand the use of the ANN in the diagnosis domain, it is advisable to recollect the different stages adopted for the implementation of an ANN in this domain.

8.2.1. *Choice of the fault indicators*

For an efficient exploitation of the ANN, a preliminary analysis of the different simulated variables of the machine during faulty and normal operations must be carried out as carefully as possible. It must be performed by diagnosis experts of the induction machine. This analysis will enable us to choose, in a significant and discriminating manner, the most representative fault indicators. The latter are used as the pertinent inputs of the neural network.

The development of a discriminating representation of the fault indicators is an extremely significant stage, which largely conditions the efficiency of the classification by ANN. The choice of the suitable fault indicators enables us to fix

the number of inputs for each ANN. Therefore, there will be as many ANN inputs as fault indicators.

The current strategy is adopted for the fault diagnosis of the induction machine. In this strategy, the ANN are considered as the essential tools for the automatic recognition of the normal and abnormal operation state of the machine. However, the choice and the processing of the pertinent inputs of the network is primarily important for an essential work, in order to develop an efficient diagnosis. The inputs of the network are extracted from the machine signals, where the faults are revealed by these signals. Consequently, the surveillance is mainly based on the continuous monitoring of these signals.

In order to have a clear and accurate idea of the effect of the faults on the behavior of the induction machine, without destroying the machine, the simulation study is carried out initially with a model. This model represents at best the real behavior of the machine. A deep analysis of the simulated variables of the machine (currents, speed, torque) will enable us to establish the signature of each of the two faults [BOU 09].

In fact, the stator fault is depicted by an increase of the line current of the phase where the fault occurred, and by an imbalance on the level of the phase shift between the line current and the phase voltage. On the contrary, the rotor fault results in a low frequency modulation of the amplitude of the three stator currents, while the displacement of the each phase to the other remains 120°. Following these considerations, the choice of the inputs is primarily based on the monitoring of the stator current, since it reflects the existence of two stator and rotor faults, in a significant and discriminating way. In addition, the current sensor is simple, inexpensive and utilized in all speed variators.

8.2.2. *Choice of the structure of the network*

In the literature, there are several types of ANN architecture [DRE 02]. The MLP (Multi-Layer Perceptron) neural structure of feed forward type is the most frequently used structure in the classification domain [RAJ 08]. In this chapter, the fault diagnosis is carried out by MLP networks of feedforward type.

The architecture of a feed forward type of MLP ANN incorporates an input layer, of one or several hidden layers and an output layer. The example of a structure with two hidden layers is represented in Figure 8.1. The designer can fix the inputs and the outputs of a network, as well as the type of transfer function and the connectivity of the neurons. The number of the inputs corresponds to the number of fault indicators, and the number of neurons of the output layer corresponds to the

chosen k classes (or modes). The number of neurons in the hidden layers cannot be *a priori* fixed and no law is still applicable for its determination. Generally, it is determined according to an iterative method, following the learning and test performances.

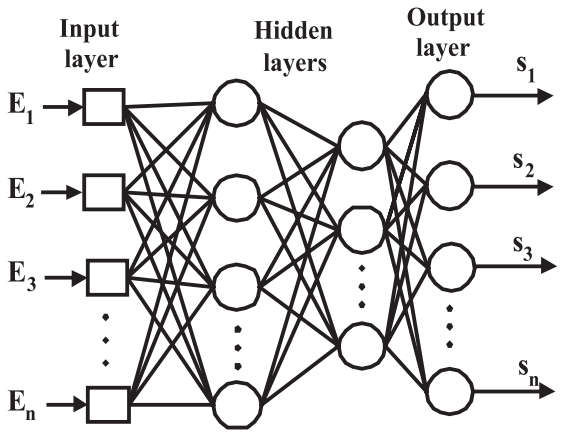

Figure 8.1. *Structure of the MLP networks*

8.2.3. *Construction of the learning and test base*

After the choice of the fault indicators and the network structure, the third stage consists of an acquisition of the data coming from a simulator or from a machine of a test bench. These data are then processed and classified in a database, which is made up of N examples and is divided into 2 parts: one part for the learning base made up of (N-No) examples, and the other part for the test base, made up of No examples.

The learning database must be quite representative in terms of quality and quantity of different operating modes of the machine. The vector of the inputs, namely $E = [E_1\ E_2\ E_3\ \ldots\ E_n]^T$ is represented to the ANN as examples. As previously mentioned, the task of the ANN is to try to associate with each input variable, and a (healthy or faulty) operating mode. These modes represent the vector of the desired outputs, called Target $T = [T_1\ T_2\ \ldots\ TN]^T$. In this case, the input-output relation directly represents the diagnostic operation [RAJ 08]. Therefore, the [E; T] vector represents the learning database of the ANN.

8.2.4. *Learning and test of the network*

Once the database is ready, the network understands and learns the examples provided in the learning base, as part of the learning process. In that case, the ANN is made to develop a non-linear relation between its inputs and outputs, by adjusting its weights from the examples. These examples are supplied to them during the learning phase. The success of such an application is dependent on the quality of the information found in the learning base. In situations where the database is experimental, preprocessing of the database is an important element to comprehend its quality.

The role of learning is to minimize the cost function, which is the "mean square error" (MSE) between the desired output and the real output of the network. This output is calculated on the basis of different examples provided in the learning base, by using an iterative algorithm. It is iteratively calculated after each alteration of the synaptic weights, during each presentation of the learning examples to the ANN. The iterative learning algorithm used in this chapter is the back-propagation technique of the gradient. This technique is the most frequently used in order to carry out the learning of the feedforward MLP networks [VEN 03].

The test or "generalization" phase consists of measuring the performances of the network tested by examples not learned in the learning base. The test procedure is carried out successively with the learning process, in order to avoid the problem of over- and under-learning [DRE 02]. The back-propagation algorithm can lead to local minimums and in that case, the MSE has not reached its absolute minimum. We thus need to repeat the learning process until we achieve the desired performances. The learning and the test enable us to seek the optimum structure of the ANN, i.e. for the number of neurons in the hidden layers of the ANN. The chosen optimum architecture is the one that maintains a compromise between the minimization of the learning mean square error (LMSE) and the test mean square error (TMSE).

8.3. Description of the monitoring system

The aim of this chapter is to explain the design of a monitoring system of the state of the machine, in order to avoid its total deterioration, and consequently increase its availability. The global term of monitoring involves the detection and the diagnosis functions. Due to this reason, the suggested monitoring system is designed to detect and diagnose the induction motor faults: stator type fault of inter turns short-circuit, rotor fault type of broken bars of the rotor cage, and the simultaneous stator/rotor faults.

The synoptic diagram of Figure 8.2 represents the neural architecture of the monitoring system considered. This system is made up of three neural networks: a (RN_d) network designed for the detection of the two faults, a (RN_{cc}) network for the localization of the short-circuit fault at the stator, and a (RN_{bc}) network for the determination of the number of broken bars at the rotor [BOU 09]. The RN_d network is the primary network of the monitoring system. This network ensures an intelligent detection of a fault in its initial stage of appearance. The network classifies the faults into the stator and/or the rotor. The localization, identification, and confirmation functions of the fault are carried out by the two networks RN_{cc} and RN_{bc}. In the case of stator fault detected by the first output S_{1d} of RN_d, the RN_{cc} circuit indicates the phase where the short-circuit fault has occurred (Figure 8.2). In the same way, if RN_d detects a rotor fault, which is indicated by the activation of its second output S_{2d}, in this case, the RN_{bc} network indicates the number (N) of broken bars in the rotor cage.

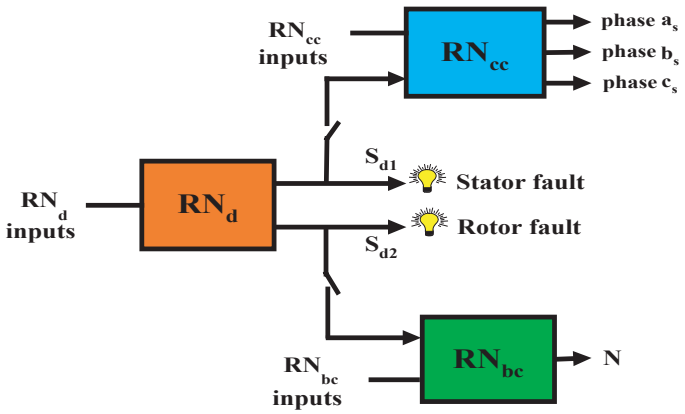

Figure 8.2. *Global neural architecture of the monitoring system of the induction machine*

We will show in the latter part of this chapter that this system is sufficiently sensitive to enable an efficient detection of the faults, and is also sufficiently robust to avoid false alarms in the presence of disturbances, such as noise, and the variations of the electrical parameters under the effect of heat, or of saturation of the magnetic circuit of the machine.

8.4. The detection problem

The detection of early faults which originate in the induction machine is a very significant task. To ensure that the detection function is efficient and reliable, it must

be sufficiently sensitive in order to allow secure fault detection. However, the function should also be sufficiently robust, in order to avoid false alarms, which can slow down the production in industrial processes. The RN_d network is used for the simultaneous detection (existence or not of a fault) and classification (type of fault) of the two machine faults. However, during normal operation, the structural parameters of the machine (magnetizing resistances and inductances) are subjected to variations in the temperature and the magnetic saturation functions. Under the effect of heat, the resistance values vary according to the following law [CAS 03]:

$$R = R_0 \left(1 + \alpha \,.\, \Delta T\right) \qquad [8.1]$$

with:

– R_0: the value of R at $T_o = 25°$;

– α: the temperature coefficient of the resistance;

– ΔT: the temperature variation.

In addition, the increase in temperature results in an increase of the rotor volume. This results in the decrease of the "e" thickness of the air gap between the rotor and the stator. According to equation [8.2] extracted from the ampere theorem, under a constant magnetic field H, the decrease of the course "1" of the field results in the corresponding decrease of the magneto-motive force $\left(n.i\right)$ and consequently, the current i, which is necessary to magnetize the stator, where the stator winding coil has n number of turns:

$$H.1 = n.i \qquad [8.2]$$

According to equation [8.3], if the magnetizing current decreases under the increase of the temperature, then, at constant φ flux, the L magnetizing inductance of the stator windings will increase [SAI 76].

$$L = n.\varphi / i \qquad [8.3]$$

During normal operation, the electrical parameters of the machine are therefore subject to changes. This operating mode must not be considered as a fault mode, although the line currents are subjected to variation. In that case, the monitoring by ANN based on the evolution of the residues of the machine currents would involve the risk of having false alarms. To avoid this problem, an approach with robust detection has been carried out. It is described in the next section.

8.5. The proposed method for the robust detection

Figure 8.3 represents the display of the detection method of the two faults based on double preprocessing, before the use of the RN_d network. The first preprocessing allows a robust detection concerning the normal variations of the parameters of the machine, which are caused for example by heating or a modification of the level of magnetization (operation in defluxing). For this, we will permanently adjust the parameters of a Park model with the help of a parametric estimation process, which is based on the output error method [MOR 99a].

Thus, we will have:

– approximately null residues since the identified model is very close to the machine model, even in presence of normal variations of the parameters of the machine (due to the parametric matching technique);

– non-null residues in the presence of fault: in fact, the fault is viewed as a modeling error, which increases the value of the residues (on the d and q axes).

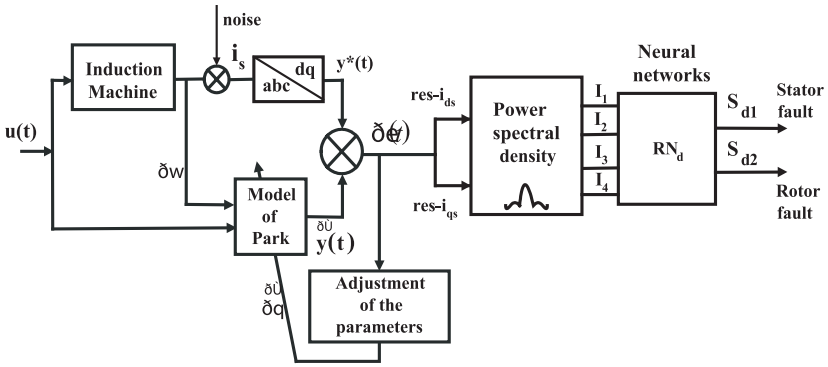

Figure 8.3. *Synoptic of the detection principle of the two faults by the RN_d network*

The speed of the machine is used as input of Park's model, which allows us to free ourselves from the variation of the loading conditions. In addition, to ensure realism during the simulation study of the fault detection, a noise is incorporated to the measured currents. This noise is made up of white noise, which has power 10-5, to which we add three sine waves whose frequencies are 20 Hz, 140 Hz and 5,030 Hz. respectively. The amplitudes of these sine waves are 0.2, 0.1 and 0.15 (A) respectively.

Once the res-i_{ds} and res-i_{qs} d-q current residues are generated, a second preprocessing carries out a spectral analysis, in order to extract four fault indicators

(I_1, I_2, I_3, I_4). These indicators are the inputs of the RN_d network. The meaning of each one of these inputs will be described later on.

As indicated by Figure 8.3, the RN_d network is composed of two outputs, in order to indicate the two faults. The stator fault will be indicated by its first output S_{d1}, and the rotor fault by its second output S_{d2}.

8.5.1. *Generation of the estimated residues*

The estimation of the four electrical parameters (R_s, R_r, L_r, L_f) of the Park's model of the machine (whose reference mark is linked to the rotor, and the totalized leakages to the stator) is carried out by the output error method. The latter consists of minimizing the following quadratic multivariable criterion:

$$J = \sum_{k=1}^{K} \left(i_{ds}^{*} - \hat{i}_{ds} \right)^2 + \sum_{k=1}^{K} \left(i_{qs}^{*} - \hat{i}_{qs} \right)^2 \qquad [8.4]$$

with:

$$i_{ds}^{*} - \hat{i}_{ds} = \text{res} - i_{ds} \text{ and } i_{qs}^{*} - \hat{i}_{qs} = \text{res} - i_{qs}$$

The advantage of the multivariable criterion is that it supplies richer information to the estimator, as compared to the case of a criterion based on the minimization of only one output magnitude.

The minimization of the criterion [8.4] is carried out by a non-linear programming technique of the Levenberg-Marquardt type, which iteratively leads to the estimation of the parameters vector $\underline{\theta^T} = [R_S \; R_r \; L_r \; L_f]$.

In addition, to ensure that the identification algorithm converges and provides the optimum parameters, where the optimum parameters are as near as possible to the parameters of the machine, it is necessary to use a rich excitation [MOR 99b]. The excitation protocol, which can give the best identification results of the healthy regime, is the one which can enable voltage excitation.

This excitation consists of adding four other sinusoidal voltages of respective frequencies 10 Hz, 20 Hz, 30 Hz and 40 Hz to the main voltage (for example 50 Hz). The amplitudes of these voltages are, for example 1.2 V, 1.5 V, 1.8 V and 2.2 V respectively. These amplitudes have been chosen, so that the currents generated by these voltages can excite the machine without disturbing the normal operation of the machine, i.e. where current amplitudes of excitation are lower than 10% of the main current.

NOTE.– The identification process is necessary for the definition of Park's model. In fact, Park's model is fundamental which enables the generation of the residues. If the machine operates under the same conditions (the same parameters), we can possibly free ourselves from the matching phase of the parameters, but with an unavoidable deterioration of the performances. On the contrary, if the operation conditions vary, the matching phase of the parameters becomes indispensable due to the identification algorithm.

8.6. Signature of the stator and rotor faults

The spectral analysis of the residues of the Park's currents will enable us to determine the operating mode of the machine (faulty or healthy operation), and indicate the type of the fault and its severity. In fact, this analysis will also enable us to develop discriminating spectral signatures, which are also quite characteristic of the fault, and are useful for good detection by the RN_d network [MOR 99a].

8.6.1. *Analysis of the residue in healthy regime*

It is obvious that to study the spectra of the faulty machine, we first need to analyze the spectrum of the healthy operating mode, in order to determine the presence of new spectral lines during the appearance of a fault. The power spectral density (PSD) of the simulated residue of noisy estimation of res-i_{ds} and res-i_{qs}, under a nominal load torque (C = 7 nm) is represented in Figure 8.4. Under healthy operating conditions, there is no specific spectral line in the studied frequency range.

8.6.2. *Analysis of the residue in presence of the stator fault*

8.6.2.1. *Study of the effect of the stator fault on the spectrum of the residue*

In order to study the effect of the inter turns short-circuit fault on the content of the spectrum of the estimation residue, the load has been fixed at the nominal value (C = 7 nm), and a variation in the (n) number of short-circuited turns on the phase a_s has been carried out [BAC 03]. Figures 8.5 and 8.6 illustrate the spectra of the estimation residue of the Park currents for different cases of short-circuited turns on the phase a_s (1, 5 and 10 turns by knowing that each phase is formed by 464 turns). This inter turns short-circuit fault gives rise to a spectral component at the 97.4 Hz frequency, which is equal to $(2.f_s - g.f_s)$. This confirms the results found in [BOU 09]. This spectral line has an amplitude that evolves in proportion to the number of short-circuited turns (about 2dB by turns). Even the fault of only one shorted turn represents a significant level of this line. By generalizing, for n shorted turns, the line amplitude with the fault follows the relation:

$$\text{for } n \geq 1\text{: the amplitude of the spectral line (dB)} = -1.85 + \log(n) \qquad [8.5]$$

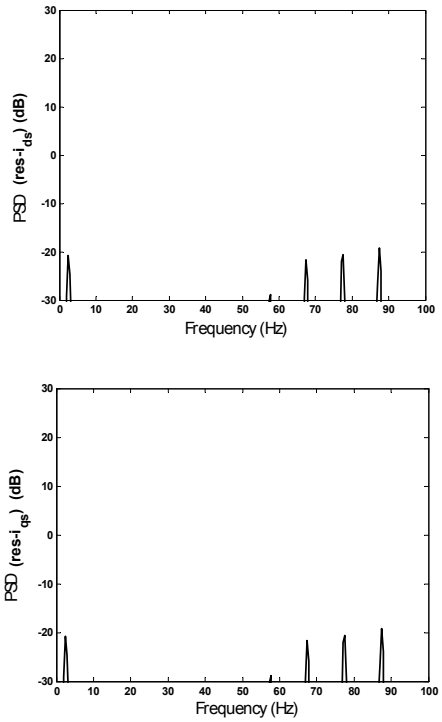

Figure 8.4. *PSD of the estimation residue of the Park currents in healthy operating*

It is important to mention that the same spectral characteristics are obtained when a fault appears in phase b_s or c_s. According to Figures 8.5 and 8.6, the influence of the stator fault on the $(2.f_s - g.f_s)$ component is felt almost in the same evolution for the two spectra of res-i_{ds} and res-i_{qs}. It will thus be adequate if we restrict our study to one PSD only; for example the res-i_{ds}.

8.6.2.2. *Study of the effect of the load on the spectrum of the residue*

The effect of the load variation on the spectrum of the estimation residue has also been studied. Figure 8.7 shows the evolution of the aforementioned spectral behavior in the presence of a 5 shorted turns on the phase a_s, under different loads: case of a machine with nominal load (a) and no load (b). The variation in load results in variation of the frequency of the spectral line, without modifying its amplitude, which is the characteristic of inter turns short-circuit fault in the spectrum of (res-i_{ds}) residue. The frequency of the line increases with the decrease of the load according to the relation:

$$F_{line} = 2.f_s - g.f_s \qquad [8.6]$$

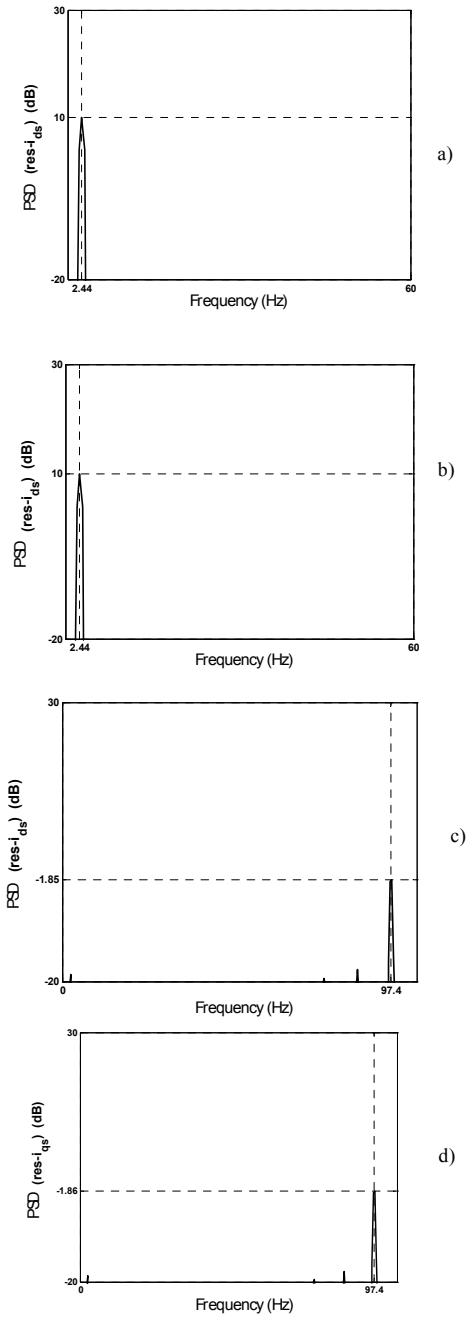

Figure 8.5. *PSD of the residues with a short-circuit fault of 1 turn on the phase* a_s

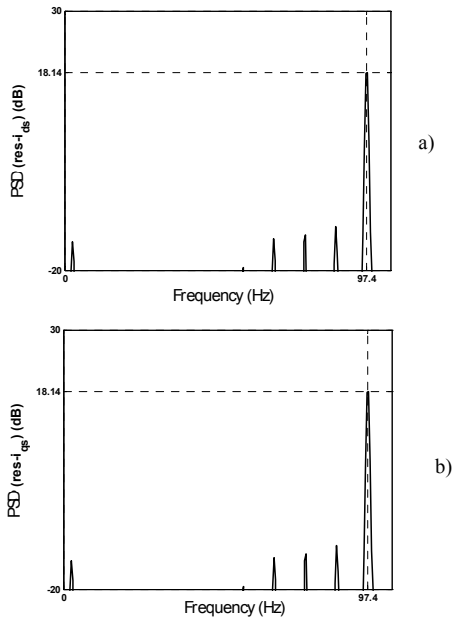

Figure 8.6. *PSD of the residues with a short-circuit fault of 10 turns on the phase* a_s

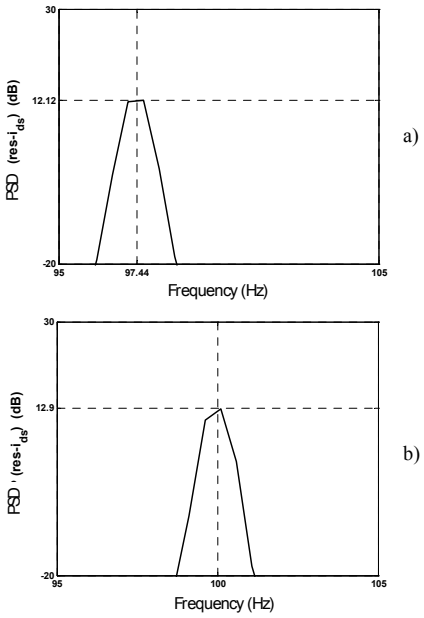

Figure 8.7. *PSD of res-*i_{ds} *in function of the variation of the load a) nominal load; b) no load*

To summarize, according to this analysis, the inter turns short-circuit fault is characterized by the appearance of a line at the f_{line} frequency in the spectrum of the residue of the Park currents. The amplitude of this line provides information related to the importance of the fault (almost an increasing of 2 dB due to the shorted turn on one of the three phases of the machine). Its frequency informs about the loading conditions of the machine.

8.6.3. *Analysis of the residue in presence of the roto fault*

8.6.3.1. *Study of the effect of the rotor fault on the spectrum of the residue*

The content of the spectrum of the residue of the estimated Park currents is also used to characterize the spectral signature of the rotor fault of a machine operating in load under broken rotor bars fault [BAC 03]. Figures 8.8 and 8.9 illustrate the PSD of the residue of the estimated Park currents res-i_{ds} and res-i_{qs} respectively for a fault of (N = 1, 2 and 3) broken bars at the rotor in the presence of a nominal load of 7 nm.

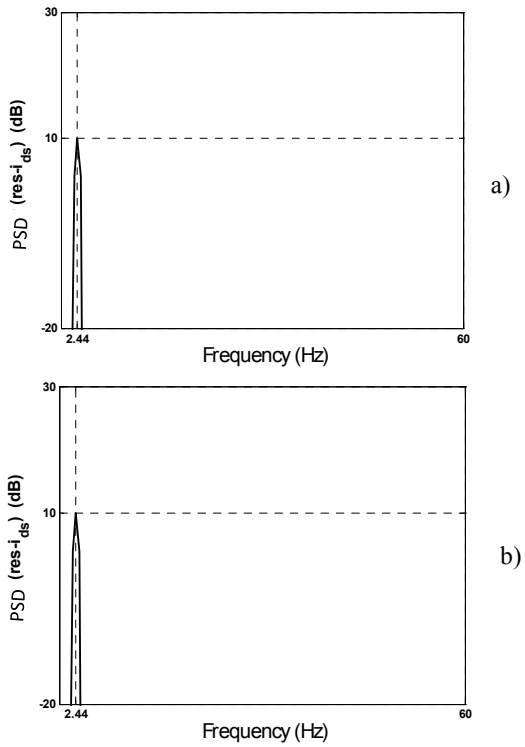

Figure 8.8. *PSD of the estimation residues for the case of one broken bar at the rotor*

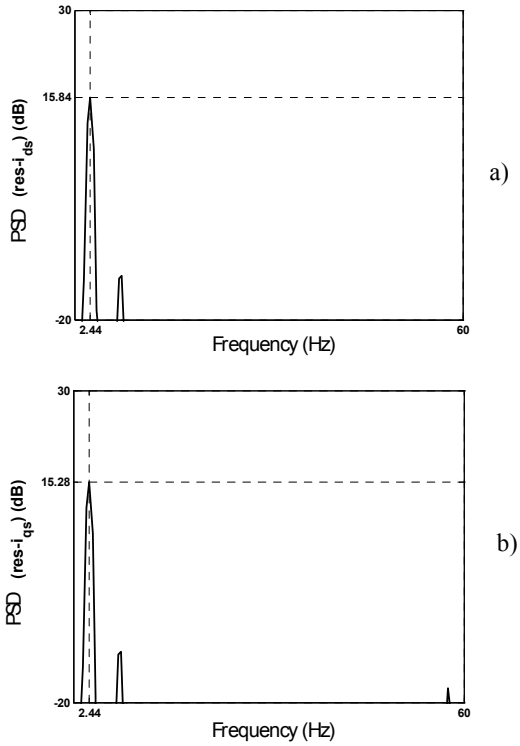

Figure 8.9. *PSD of the estimation residues for the case of two broken bars at the rotor*

These figures highlight, on the one hand, the appearance of a new spectral line, which is introduced by the rotor fault at a very low frequency equal to 2.44 Hz, which is none other than:

$$f'_{line} = g.f_s \qquad [8.7]$$

(with g, the slip of the machine) and on the other hand, the dependence of the amplitude of this line on the N number of broken bars with an almost proportionality of the amplitude in function of the N number of bars compared to the amplitude of one broken bar.

8.6.3.2. *Study of the effect of the load on the spectrum of the residue*

After the study of the effect of the number of broken bars on the spectrum of the residue, it is advisable to study the effect of the load on the PSD of res-i_{ds}. Figure 8.10 shows the PSD of the simulated i_{ds} residue of the machine with a fault of a broken bar at the rotor for several load conditions (no load and full load). The variation of the load alters the frequency of the characteristic line of the rotor fault

according to f'_{line}, which verifies equation [8.7]. Contrary to the stator fault, the amplitude of the line is proportional to the load effect.

By combining these last results, the amplitude of the main line which indicates the fault of broken bars can be written under the following form:

for $N \geq 1$: amplitude of the spectral line (dB) = $20.(\log(k.f_{line}) + \log(N))$ [8.8]

with $k = 1.4$ for the test machine.

After this study, we can conclude that the rotor fault is characterized by the appearance of a line at a low $g.f_s$ frequency (dependent on the load), with an amplitude that represents the severity of the fault, all the while taking into account the load conditions of the machine.

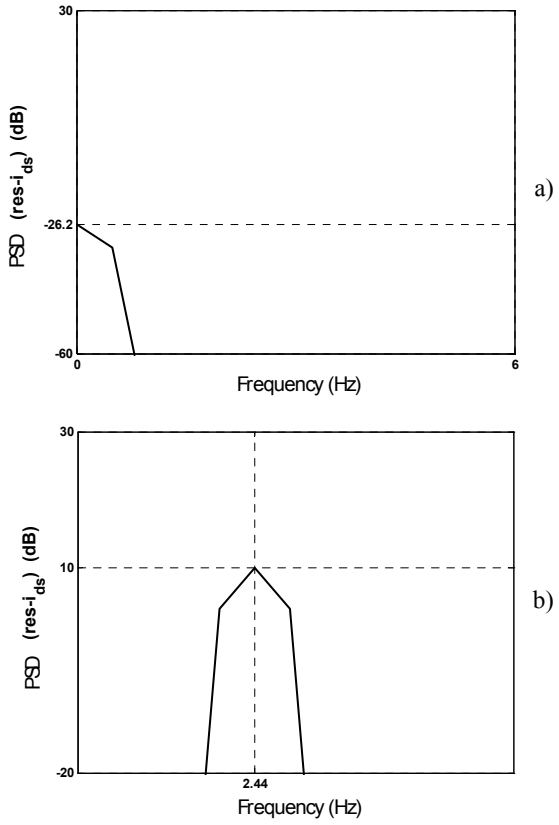

Figure 8.10. *PSD of the res-i_{ds} residue for the case of a fault of one broken bar at the rotor a) no load; b) nominal load*

8.6.4. *Analysis of the residue in presence of simultaneous stator/rotor fault*

After the analysis of the spectra of the residue of the estimated Park currents for the two cases of stator and rotor faults, this section tackles the spectra of the estimation residue of the Park currents for the case of a simultaneous stator/rotor fault which affects the induction machine.

The spectra of the estimation residue in nominal load for several cases of simultaneous stator/rotor faults contain the two frequency components relative to each fault. Indeed, these spectra show the appearance of a line at the $g.f_s$ frequency, which reveals the presence of a rotor fault, and the appearance of a line at the $(2.f_s - g.f_s)$ frequency, which indicates the presence of a stator fault. The variations of the amplitude of these two lines depend on the importance of these two faults which are given by the two equations [8.5] and [8.8] for separately considered faults. The effect of the load variation is the same as the effect pointed out in the case where each stator and rotor fault is considered separately.

8.7. Detection of the faults by the RN_d neural network

8.7.1. *Extraction of the fault indicators*

The frequency study has already been carried out on the simulated signals. This study shows that the spectra of the estimation residue contain rich and useful information which enable us to detect and discriminate between the two stator and rotor faults. In fact, these spectra enable us to highlight the existence or not of a stator fault, a rotor fault and a simultaneous stator/rotor fault by the generation of lines linked to the characteristic frequencies of each fault. These lines in relation to each fault have the advantage of being different from one another and do not present any overlap.

The indicators in relation to each fault are extracted from the spectra. They will be used as inputs of the RN_d network, which is dedicated to the detection of the two faults [BOU 07]. For this, four fault indicators are chosen for the detection of stator and rotor faults, which are gathered in a "E" vector. The latter is the input vector of the RN_d network. The expression of E is:

$$E = [I_1\ I_2\ I_3\ I_4]^T \qquad [8.9]$$

where:

– I_1 and I_2: the surfaces of the respective line of the PSD of res-i_{ds} and res-i_{qs} around the frequency equal to 2 Hz;

– I_3 and I_4: the surfaces of the respective line of the PSD of res-i_{ds} and res-i_{qs} around the frequency equal to 98 Hz.

8.7.2. *Learning sequence of the RN_d network*

The useful database for the learning process is made up of a pair of vector (E, T), which are defined as follows:

– the vector of the E inputs of the RN_d network is formed of a series of examples of the surfaces of the PSD line of the residue of the estimated Park currents, which characterize several cases of healthy and faulty operation, at nominal and no load. This series is presented to the RN_d network in the following order: two samples of healthy operation, 8 samples of inter turns short-circuit fault in phase a_s, 6 samples of operation under rotor fault and 12 samples of operation under simultaneous stator/rotor fault. The input vector of the learning sequence is thus formed of 28 samples, as illustrated in Figure 8.11a. This database only contains the examples of fault in phase a_s considering that the stator fault manifests itself in the same way for the other phases b_s or c_s. In addition, examples of bar crack at the rotor are introduced with the aim of making the ANN learn an early rotor fault. Consequently, the monitoring system will have to be able to detect an early rotor fault;

– the vector of the desired outputs $T = [T_1 \; T_2]^T$ is formed by the two classes to which the learning examples will be allocated (Figure 8.11b). The first output T_1 represents the stator fault, and the second output T_2 represents the rotor fault. Therefore, each operation example of the E input vector is allocated the state of the two desired outputs (T_1 and T_2) of the RN_d network, so that the T vector has a value:

$$T = \begin{bmatrix} 0 \\ 0 \end{bmatrix} \text{ for an healthy operation,}$$

$$T = \begin{bmatrix} 1 \\ 0 \end{bmatrix} \text{ case of a stator fault,}$$

$$T = \begin{bmatrix} 0 \\ 1 \end{bmatrix} \text{ case of a rotor fault,}$$

$$T = \begin{bmatrix} 1 \\ 1 \end{bmatrix} \text{ case of a simultaneous stator/rotor fault.}$$

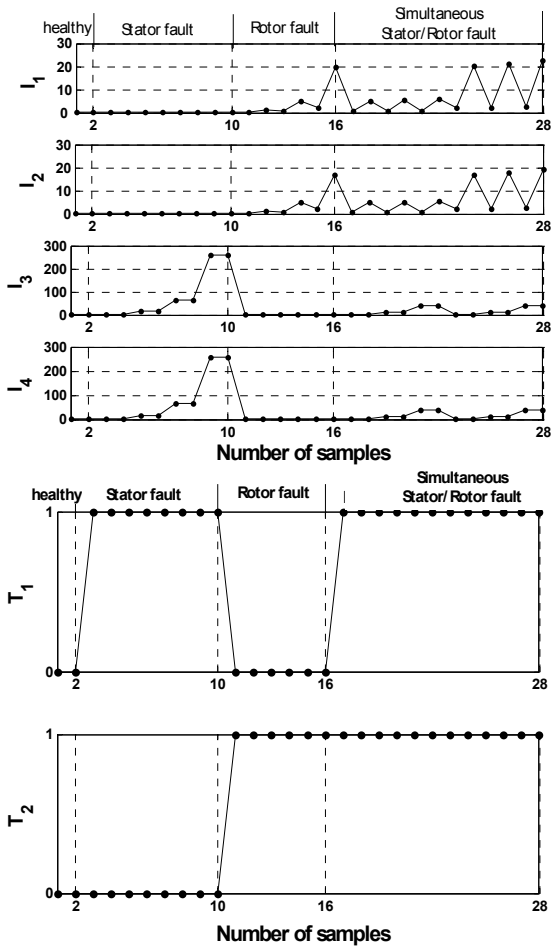

Figure 8.11. *Learning sequence of the RN_d for the detection of the faults a) inputs of the RN_d network; b) desired outputs of the RN_d network*

8.7.3. *Structure of the RN_d network*

The choice of the fault indicators and the outputs of the RN_d network will enable us to set the external architecture of the network. In addition, the RN_d neural network designed for the detection of the two faults is a feedforward MLP network, where its inputs are set at four and its outputs at two. To seek the number of hidden layers, as well as the number of the neurons constituent of them, several learning sequences are carried out successively and are followed by test sequences in order to avoid over- and under-learning.

The optimum structure of the RN_d network is the one that provides the best learning and test performances. This structure is represented in Figure 8.12. It is formed of only one hidden layer, which is made up of four neurons. The activation function of the neurons of the hidden layer is sigmoid type "tangsig", whereas one of the neurons of the output layer is of the "logsig" type.

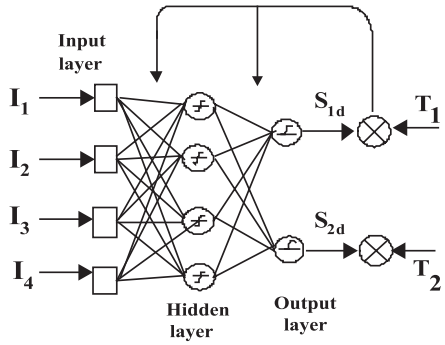

Figure 8.12. *Architecture of the RN_d network of fault detection*

8.7.4. *Results of the learning of the RN_d network*

The evolution of the LMSE highlights the good learning performances of the network (Figure 8.13). In fact, after 780 iterations the LMSE of the RN_d network reaches a very low value, which is worth 3.793×10^{-22}.

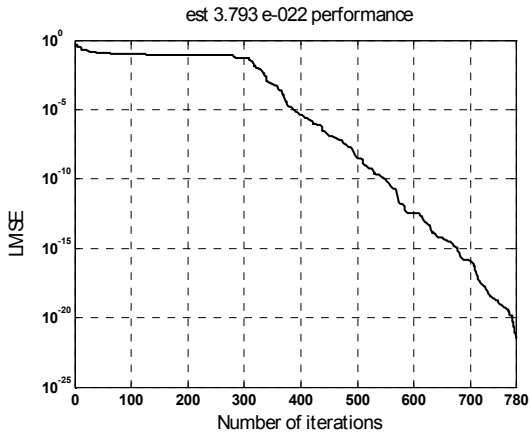

Figure 8.13. *Evolution of the learning MSE of RN_d*

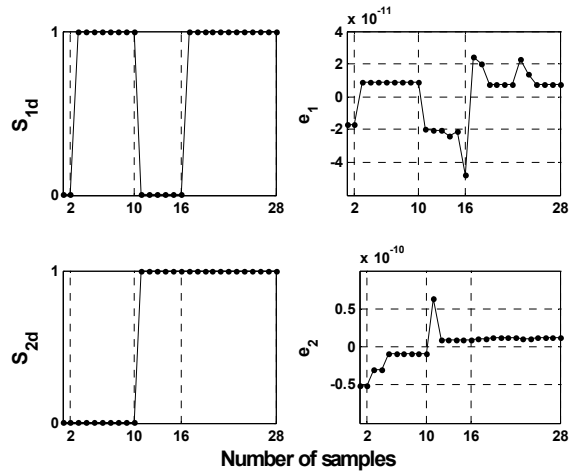

Figure 8.14. *Learning outputs and errors of the RN_d*

The outputs, as well as the learning errors of the network are represented on Figure 8.14. The learning error is almost null (of about 10^{-10}). This proves that the network has learned the presented fault sequences quite well, and has been able to correctly reproduce the desired outputs.

8.7.5. *Test results of the RN_d network*

In order to evaluate the generalization performances of the RN_d network, the latter has been tested for several examples not learned during the learning process. A few test examples are presented for each fault.

8.7.5.1. *Test of the RN_d network for stator faults*

In order to test the behavior of the network, we can consider an example, where a database is not learnt during the learning process. This database is formed of seven samples: two healthy operation samples and five operation samples with a short-circuit fault under several load conditions.

The performances of this test are represented in Figure 8.15, i.e. the errors and the state of the two outputs (S_{1d}, S_{2d}) of the RN_d network. The latter indicates (0,0) for a healthy operation and (1,0) for a stator fault with a very low error. Consequently, the RN_d network correctly detects the healthy operation and the inter turns short-circuit fault in one of the phases of the stator. We also have to note that the network is able to detect a short-circuit fault with any load torque and with a high number of short-circuited turns.

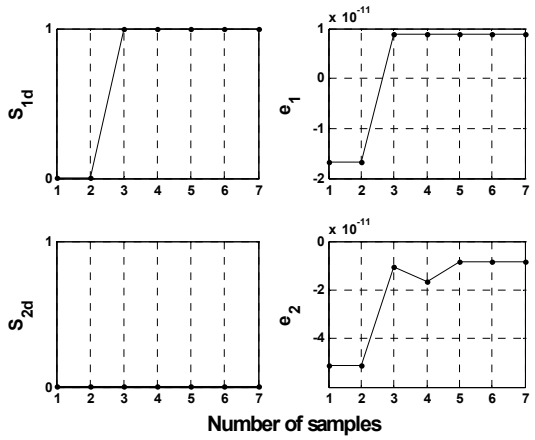

Figure 8.15. *Test outputs and test errors of the RN_d network for stator fault*

Thus, the evaluation test of the performances of the stator fault detection of the RN_d neural network has shown that it has a good generalization ability of the stator fault.

8.7.5.2. *Test of the RN_d network for rotor faults*

The test of the RN_d network in the presence of several rotor faults has also provided satisfying results. The test result of the RN_d network presented in Figure 8.16 is an example of a test sequence, which is composed by faults different from those of the learning.

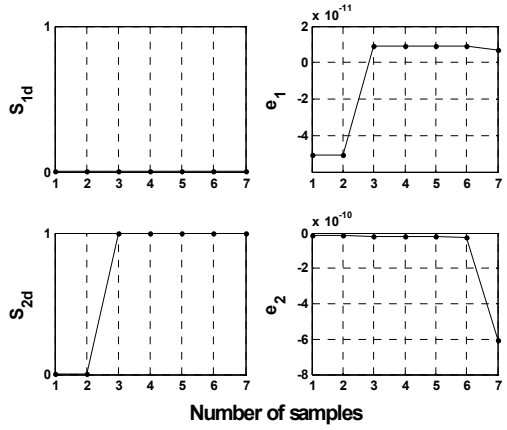

Figure 8.16. *Test outputs and test errors of the RN_d network for rotor fault*

The test sequence is made up of two healthy operation samples, two samples with cracked bars at the rotor and three operation samples with a fault of one, two and three broken bars at the rotor under different load conditions. The network accurately detects the different examples by indicating (0,0) at its two outputs (S_{1d}, S_{2d}), for the healthy operating and (0,1) for a rotor fault. The RN_d network can, on the one hand, differentiate between a healthy operation and the one with a rotor fault, and, in the other hand, correctly detect a rotor fault at the beginning of the appearance (a cracked bar ($N = 0.5$)).

8.7.5.3. *Test of the RN_d network for simultaneous stator/rotor faults*

The RN_d network has also been tested for several cases of simultaneous stator/rotor faults. The test results of the network are presented in Figure 8.17 for a not learned sequence, which is made up of two healthy operation samples and four operation samples with simultaneous stator/rotor faults under different load conditions. The outputs of the network (S_{1d}, S_{2d}) have indicated (0,0) for a healthy operation and (1,1) for a simultaneous (stator/rotor) fault with a low error. Thus, the RN_d network also accurately detects the simultaneous stator/rotor faults.

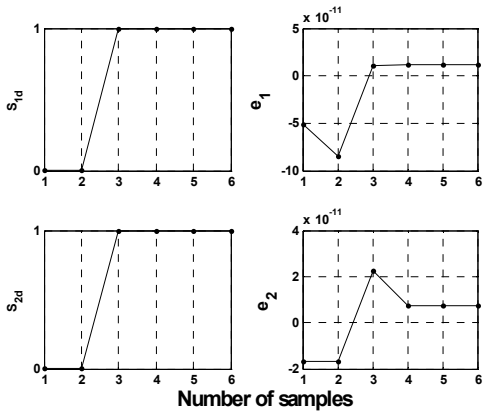

Figure 8.17. *Test outputs and test errors of the RN_d for simultaneous stator/rotor faults*

8.7.5.4. *Test of the robustness of the RN_d network*

The suggested detection approach consists of carrying out a robust detection process with respect to the parametric variation. Therefore, the behavior of the RN_d network has been tested for an operation with a variation of the electrical parameters of the machine. Examples with variable stator and rotor resistance values have been applied to the input of the RN_d network. The behavior of the RN_d network is represented in Figure 8.18 for a sequence including operation cases with a 100% increase in the value of the rotor resistance. This sequence is made up of a successive

series of two samples of healthy operation, two samples of operation with a rotor fault and two operation samples with a 100% increase of the value of the R_r rotor resistance. The network has indicated (0,0) for the healthy operation, (0,1) for the rotor fault and (0,0) for an operation with a parametric variation [BOU 07]. This network is thus able to correctly distinguish between a true fault and a normal operation with a variation of the values of one of the electrical parameters of the machine.

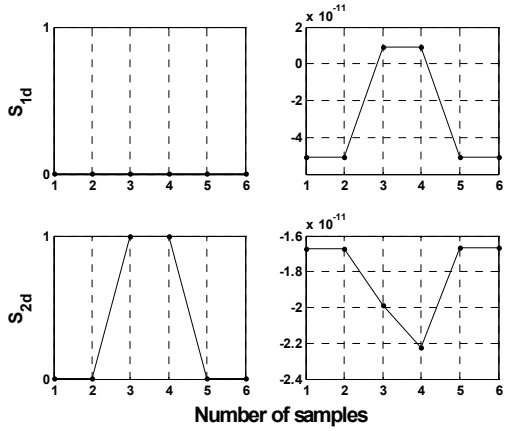

Figure 8.18. *Test outputs and test errors of the RN_d with respect to variation of the machine parameter*

8.8. Diagnosis of the stator fault

The RN_{cc} network of the suggested monitoring system (Figure 8.2) is the localization of the phase, where the short-circuit fault has occurred when a stator fault is detected by the RN_d network. However, the RN_{cc} network can only be activated when the first S_{1d} output of RN_d is activated. A detailed study of the diagnosis of the stator fault has been carried out in this section.

8.8.1. *Choice of the fault indicators for the RN_{cc} network*

It has been mentioned in section 8.6.2 that in the frequency domain, a short-circuit fault on each phase (a_s or b_s or c_s) is similarly manifested.

This renders the localization of the faulty phase difficult and consequently justifies the advantage of more efficient fault indicators. We have observed that the best performances of the diagnosis of the stator fault have been obtained by using as fault indicators the three phase shifts between the line current and the phase voltage of the machine. In fact, during an inter turns short-circuit in one of the three phases,

an imbalance occurs at the level of the amplitude and during the phase shift of the line currents, by assuming that the supply voltage is balanced. According to different studies carried out, the phase shift is a good discriminated indicator of the faulty phase [BOU 08].

8.8.1.1. *Study of the phase shift in presence of a stator fault*

Figure 8.19 represents the characteristics of the three simulated phase shift (Phi_a, Phi_b, Phi_c) for faults on the a_s (a), b_s (b), c_s (c) phases, as function of the number (n) of the shorted turns for a constant load torque (C = 3 nm), in order to study the effect of the fault on these phase shifts [BOU 08].

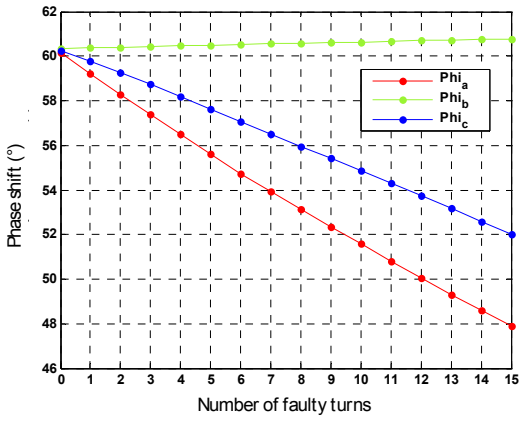

a)

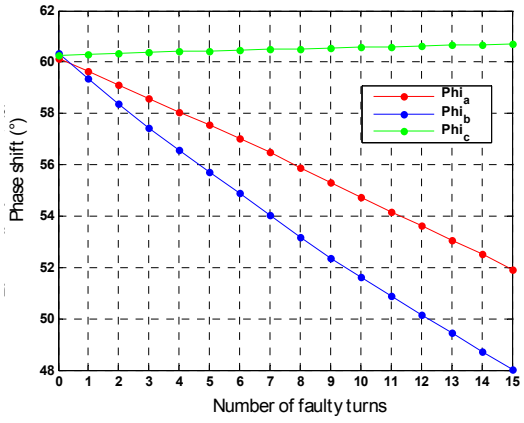

b)

Figure 8.19. *Evolution of the phase shifts in function of the shorted turns in phase a) a_s; b) b_s*

The analysis of these characteristics shows that:

– a fault with a "n" number of faulty turns on the a_s or b_s or c_s phase, and the three phase shifts are perfectly distinct and do not have any crossing between them;

– the phase shift of the faulty phase is the lowest;

– the higher the number of turns, the more will be the increase in gap between the phase displacements;

– for a three-phase supply in the direct direction, the evolution of the three phase shifts in case of a fault on one of the phases (a_s, b_s or c_s) is carried out based on a circular permutation in the indirect rotation direction, in an ascending order (Phi_a, Phi_c, Phi_b), (Phi_b, Phi_a, Phi_c) and (Phi_c, Phi_b, Phi_a) respectively.

8.8.1.2. *Study of the phase displacement in function of the load*

In order to study the effect of the load on the behavior of the three phase shifts, Figure 8.20 shows the behavior of phase shifts under different load torques (C = 3 and 7 nm). We need to point out that the phase shifts do not present any overlap, even during the variation of the load.

The study of the phase shifts as function of the fault and of the load has shown that the three simultaneous values of the phase displacements can be considered as an efficient fault signature for the diagnosis of the stator fault. In fact, the three phase shifts provide rich information on the presence of the fault, the localization of the phase at fault and even the severity of the fault (quantization of the number of shorted turns). They are thus considered as a non-invasive probe for the localization of the faulty phase [BOU 08].

8.8.2. *Learning sequence of the RN_{cc} network*

The input vector is made up of three components (Phi_a, Phi_b, Phi_c) as shown by Figure 8.21a, and it is composed of 75 samples under different load conditions. These samples are successively presented to the input of the network as follows: three healthy operation samples, 24 samples of short-circuit fault on each of the three phases.

We should note that the simultaneous stator/rotor faults are not in the learning database, since the rotor fault does not generate any imbalance at the level of the phase shifts [BOU 09]. The learning database of the RN_{cc} network is represented in Figure 8.21.

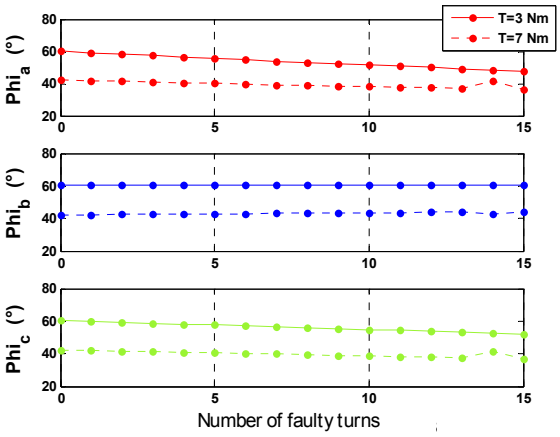

a)

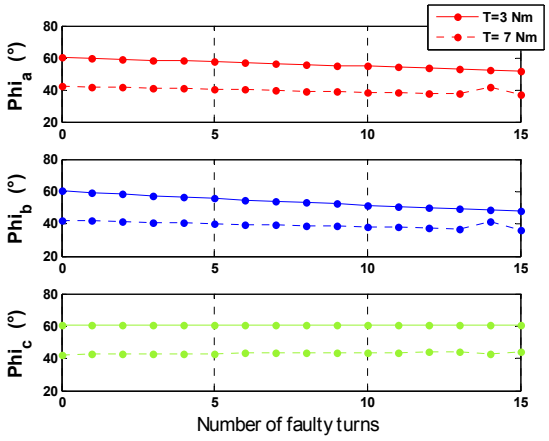

b)

Figure 8.20. *Behavior of the phase shift under different load conditions for the faults on the phase a) a_s; b) b_s*

8.8.3. *Structure of the RN_{cc} network*

The RN_{cc} network which enables the localization of the faulty phase is a feedforward MLP network with three inputs, which are the three phase shifts, and three outputs, and indicate the state of the three stator phases. The optimum structure chosen for the diagnosis of the stator fault is represented in Figure 8.22. It is made up of only one hidden layer formed of five neurons. The activation functions of the neurons of the hidden layer and of the output layer are “tangsig” and “logsig” respectively.

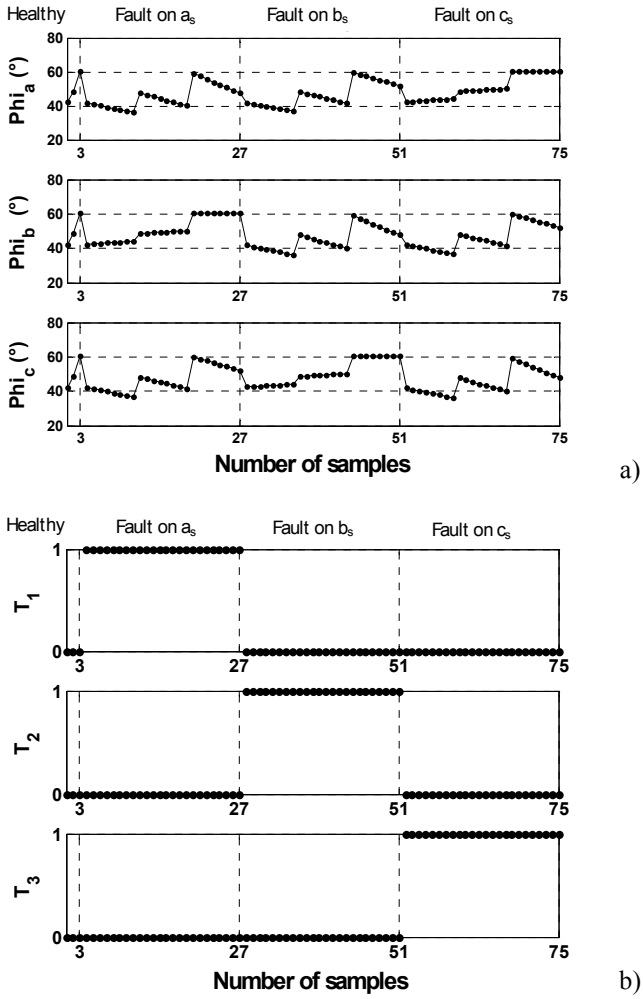

Figure 8.21. *Learning sequence of the RN_{cc} a) inputs of RN_{cc}; b) outputs of RN_{cc}*

8.8.4. *Learning results of the RN_{cc} network*

The learning of the RN_{cc} network is carried out by the back-propagation algorithm of the gradient error. The evolution of the learning performances is shown in Figures 8.23 and 8.24. After 5,000 iterations, the LMSE has attained a very low value (7.28×10^{-21}). The network has localized the phase at fault very accurately.

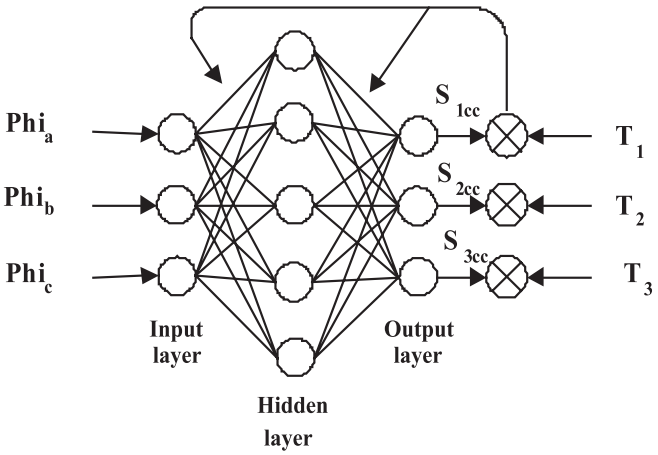

Figure 8.22. *Architecture of the RN_{cc} network*

8.8.5. *Results of the test of the RN_{cc} network*

In order to ensure the good operation of the RN_{cc} network when it is integrated in the monitoring system, several cases of stator fault and simultaneous stator/rotor fault have been tested. The test results are satisfying. Figures 8.25 to 8.27 show the test performances of the RN_{cc} network, for the short-circuit faults on the phase a_s, b_s and c_s, respectively.

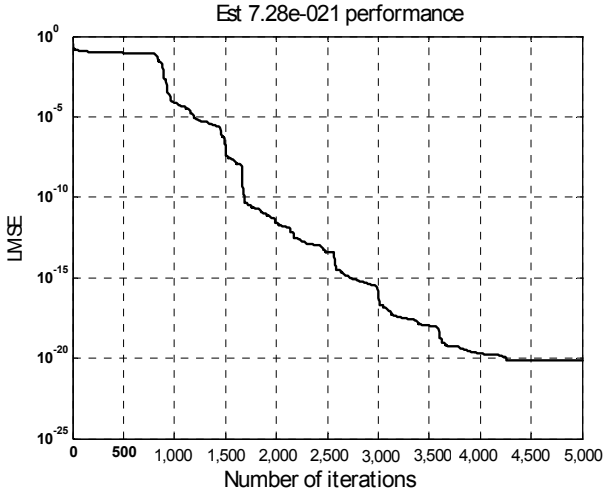

Figure 8.23. *Evolution of the LMSE of the RN_{cc} network*

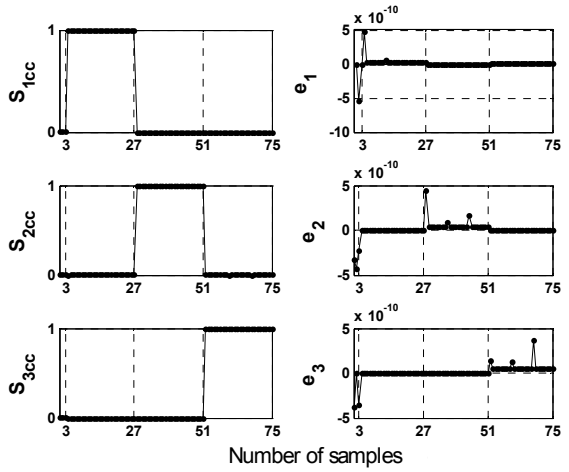

Figure 8.24. *Learning outputs and learning errors of the RN_{cc} network*

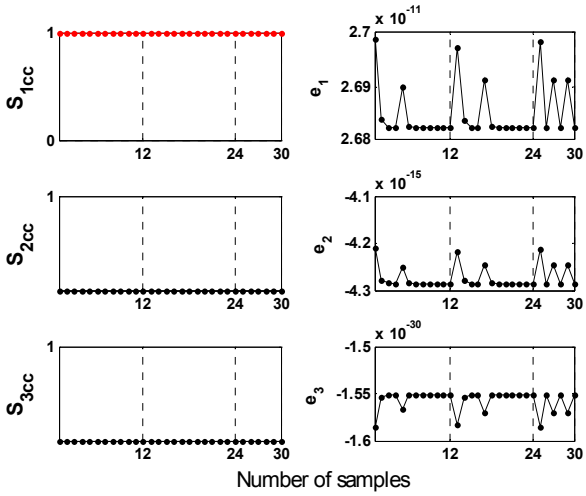

Figure 8.25. *Test outputs and test errors of the RN_{cc} network for stator fault in the phase a_s and rotor faults simultaneously*

The network displays (S_{1cc}, S_{2cc}, S_{3cc}) (1, 0, 0), (0, 1, 0) and (0, 0, 1) at its outputs, in order to indicate a short-circuit fault on the phase a_s (Figure 8.25), on the phase b_s (Figure 8.26) and on the phase c_s, respectively (Figure 8.27). In each case, the output error of the network is low, which proves that it has good generalization ability. The three phase shifts are thus reliable fault indicators which allow the RN_{cc}

network to accurately locate the faulty phase, in the presence of noise and under different loading conditions, in presence or not of broken rotor bars fault.

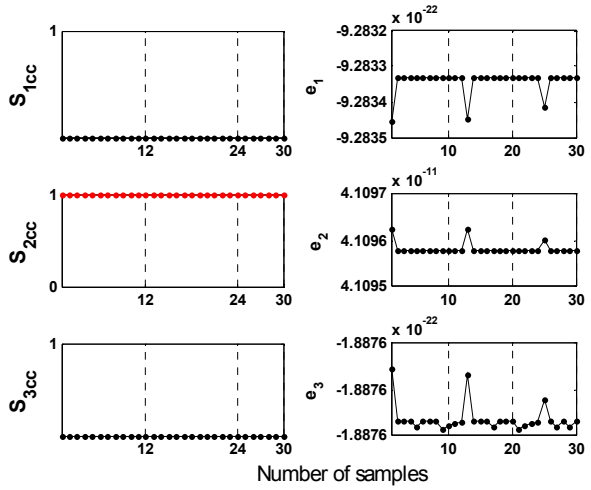

Figure 8.26. *Test outputs and test errors of the RN_{cc} network for stator faults in the phase b_s and for rotor fault simultaneously*

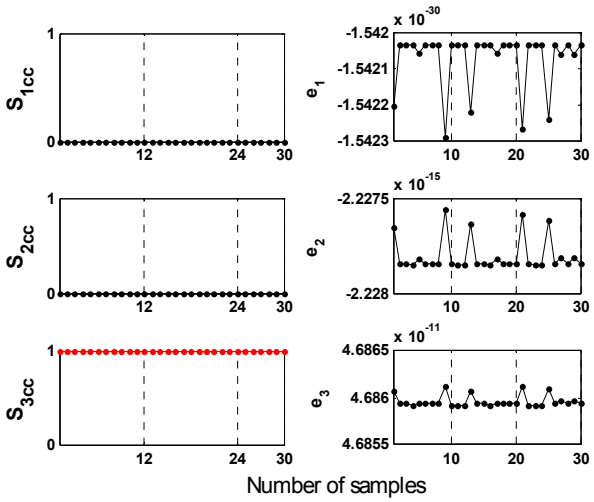

Figure 8.27. *Test outputs and test errors of the RN_{cc} network for stator faults in the phase c_s and for rotor fault simultaneously*

8.8.6. *Experimental validation of the RN_{cc} network*

During simulation, the RN_{cc} network shows good learning and test performances. The experimental examples generated from an effective machine always remain more true to the reality than the ones coming from a simulator. Consequently, it is necessary to evaluate its performances with respect to real signals coming from an induction machine.

8.8.6.1. *Description of the test bench*

To experimentally validate the RN_{cc} network, two identical test benches have been used for the acquisition of the practical signals. These two benches are considered for the study of the behavior of the induction machine in the presence of short-circuit, for low and high numbers of shorted turns. The configuration of the two benches is shown in Figure 8.28. Each of them is equipped with a squirrel cage induction machine, and they are respectively noted as M_1 and M_2. They are also directly supplied by the network. Their characteristics are shown in Table 8.1.

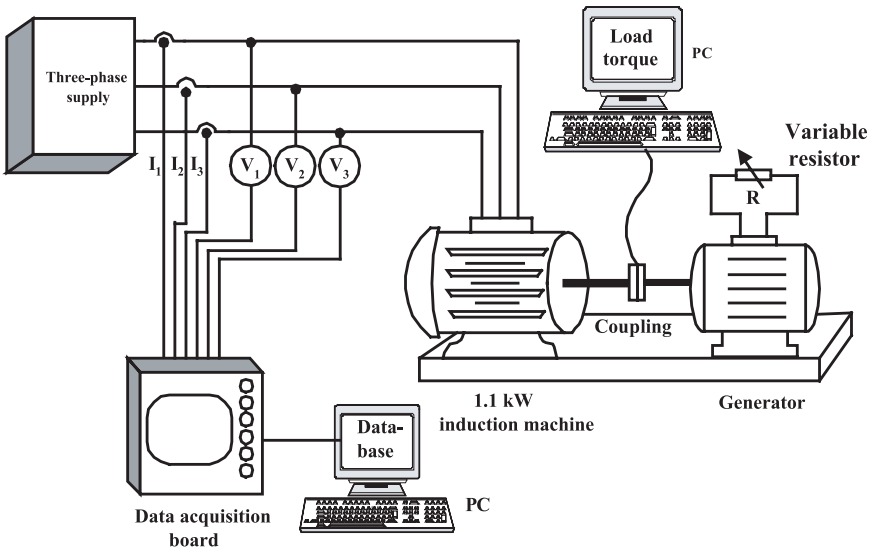

Figure 8.28. *Block diagram of the experimental test bench (Generator, data acquisition board, 1.1 kW Induction machine)*

To carry out tests with several load torques, each motor is coupled to a direct current generator. The variation of the load of the motor is carried out through the variation of the resistor connected to the generator.

Power	1.1 kW
Rated voltage	400/230 V
Rated current	2.6/4.3 A
Cos (φ)	0.85/0.82
Rated speed	1,425 tr/min
Number of pairs of poles	2
Number of stator slots	48
Number of bars at the rotor	28
Number of turns per phase	464

Table 8.1. *Characteristics of the M1 and M2 motors of the test benches*

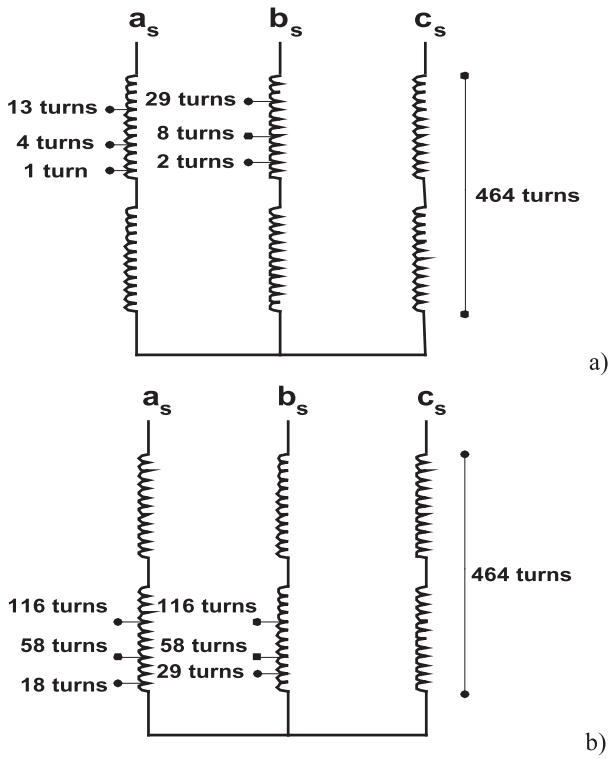

Figure 8.29. *Configuration of the access points of the stator windings of the motor a) M_1 motor; b) M_2 motor*

The first M_1 motor is designed with intermediate terminals of the winding, in order to emulate (or introduce) short-circuit faults with a low number of shorted turns: (3, 9, and 12) turns on the phase a_s and (6, 21, and 27) turns on the phase b_s (Figure 8.29a). The short-circuit faults with a high number of faulty turns can be carried out on the second motor M_2 and are of (18, 40, 58, 98 and 116) turns on the phase a_s and (29, 58, 87 and 116) turns on the phase b_s (Figure 8.29b). For the two motors, the phase c_s does not have any additional terminals in order to introduce faults. To limit the current in the turns at fault to four times the nominal current, all the short-circuits are carried out through a resistor. While different tests are introduced, the three currents and the three voltages are recorded and processed for several (healthy and faulty) operating modes of the machine. An algorithm written with Matlab, which is based on the interpolation of the position of the maximum in the discrete convolution product of two signals, calculates the three phase shifts, in order to obtain the experimental database necessary to test the behavior of the RN_{cc} network with experimental data [BOU 08].

8.8.6.2. *Study of the experimental phase displacements*

Before experimentally validating the operation of the RN_{cc} network, it is interesting to experimentally verify the behavior of the phase shift as a function of the fault and the load. This behavior has already been studied by simulation in section 8.8. For this, with the help of a three-phase network analyzer, the three phase shifts have been measured in case of healthy operation, an operation with faults of (3, 6, and 12) short-circuited turns in the phase a_s and an operation of fault of (9, 21 and 27) short-circuited turns in the phase b_s.

The three curves of the experimental phase displacements Phi_a, Phi_b and Phi_c, as a function of the number of turns at fault on each of the three phases represented on Figure 8.30, are obtained from three measurements of the faults on the phase a_s, from the three measurements of the faults on the phase b_s and by carrying out circular permutation for the faults on the other phases. The experimental phase shifts have the same behavior (point of view of the shape and of the order of circular permutation of the three phase shifts) as the ones of the simulated phase shifts, which are represented in Figure 8.19. It is very important to point out that the values of the experimental and simulated phase shifts have a slight difference, even when a fault is absent. This is due to the inevitable manufacturing faults which the machine can have, as well as to the imbalance of the voltage supply network, to the probe and quantization errors, etc.

The curves of the experimental phase shifts are not strictly monotonic. This is due to the fact that some of the values of experimental phase shifts are obtained by permutation. In addition, in practice, the machine has slight manufacture asymmetry (magnetic imbalance, low eccentricity of the stator and rotor etc.). Therefore, the

phase shifts obtained experimentally are a bit different from the ones found by simulation for the same fault on two different phases. Thus, ideally we would have at our disposal a machine with the same sockets on the three phases, where we would carry out the test of all the faults on the three phases (a_s, b_s and c_s) and then we would take the mean value of each phase displacement, in order to minimize the effects mentioned above [BOU 08].

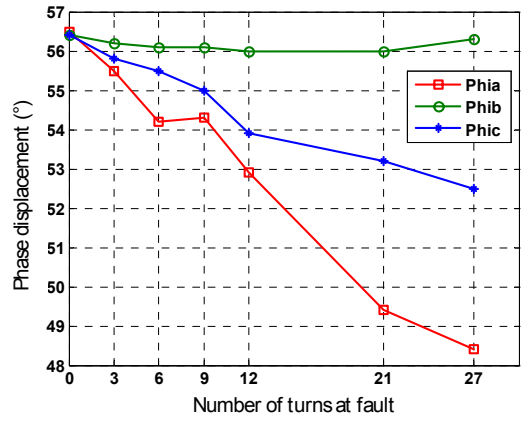

Figure 8.30. *Curves of experimental phase shifts in function of the number of shorted turns in the phase a) a_s; b) b_s*

8.8.6.3. *Validation results*

In order to experimentally validate the operation of the RN_{cc} network structure, which is represented in Figure 8.22, a database has been developed by experimental tests carried out on the M_1 motor with healthy operations and operations with stator

faults. Table 8.2 describes the operation conditions of the 48 samples used for the learning of the RN_{cc} network. The learning results are quite satisfactory (LMSE of about 10^{-22}). The output errors of the network are very low (Figure 8.31).

Initially, the test of the RN_{cc} network has been conducted with several faults on the same M_1 motor. This has given good results. To better evaluate the performances of the network, the tests have also been conducted on another motor, with the same characteristics (M_2 motor), with faults made up of 12 samples of (18, 29, 40 and 58) short-circuited turns on each one of the three phases and according to the three values of the load torque (C = 0, 2 and 4 nm). The test results are represented on Figure 8.32. In this case, the network has accurately identified the significant faults; while it has learned some faults delivered from another motor. According to this result, it is thus possible to make learn to an ANN the faults from a test machine and then to use it in order to locate a fault on other machines of the same design and power. These results experimentally validate the localization method of the phase at fault by neural network, by monitoring the three phase displacements of the machine [BOU 08].

No of samples	Phase at fault	Torque (nm)	Turns in DC
1 to 3	healthy	7, 5, 3	healthy
4 to 8	Phase a_s	7	3, 6, 9, 12, 21
9 to 13	Phase a_s	5	3, 6, 9, 12, 21
14 to 18	Phase a_s	3	3, 6, 9, 12, 21
19 to 23	Phase b_s	7	3, 6, 9, 12, 21
24 to 28	Phase b_s	5	3, 6, 9, 12, 21
29 to 33	Phase b_s	3	3, 6, 9, 12, 21
34 to 38	Phase c_s	7	3, 6, 9, 12, 21
39 to 43	Phase c_s	5	3, 6, 9, 12, 21
44 to 48	Phase c_s	3	3, 6, 9, 12, 21

Table 8.2. *Experimental conditions of the learning samples of the RN_{cc} network*

8.9. Diagnosis of the rotor fault

The third RN_{bc} network has the role of determining the N number of broken bars at the rotor during the activation of the second output S_{2d} of the RN_d network. This case is only possible when the RN_d network detects a rotor fault or a simultaneous stator/rotor fault.

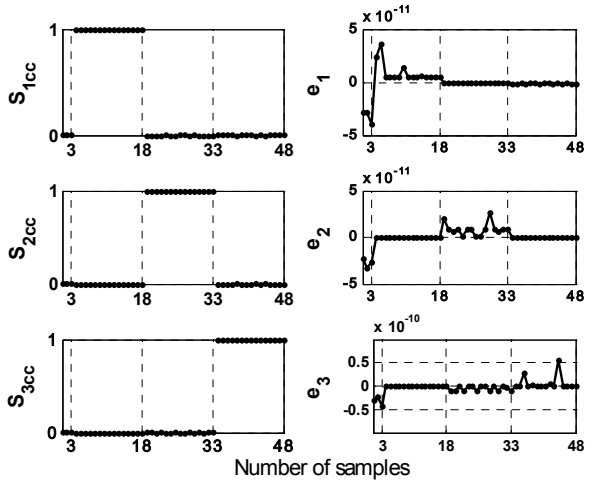

Figure 8.31. *Learning outputs and learning errors of the RN_{cc} network for experimental faults carried out on the M_1 motor*

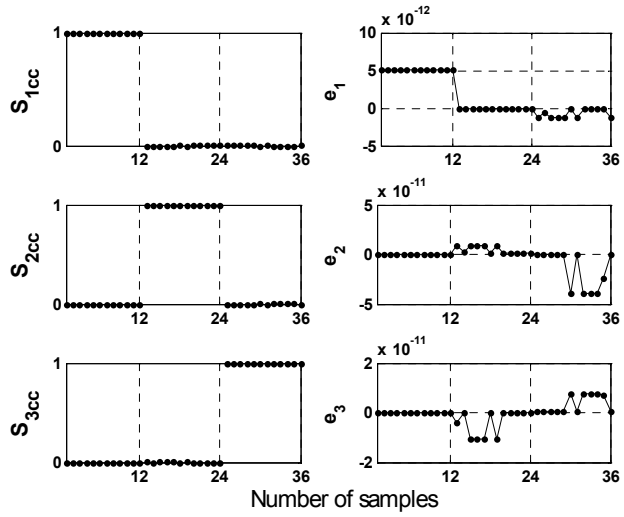

Figure 8.32. *Test performances on M_2*

The determination of the number of broken bars at the rotor is very important, since it helps the decision-making process concerning the operation of the machine with rotor fault. The diagnosis of the rotor fault is carried out with the same strategy used in the stator fault. Due to this reason, we have only presented the database and

the structure of the RN_{bc} network in the following section, where the network is used to identify the number of broken bars at the rotor.

8.9.1. *Choice of the fault indicators of the RN_{bc} network*

The rotor fault indicators which are useful for the determination of the number of broken bars at the rotor by the RN_{bc} network are extracted from the PSD of the res-i_{ds} residue. In fact, the frequency study carried out in section 8.6.3 has shown that the amplitude and the frequency of the g.f_s line of the residue of the estimated Park currents have significantly depicted the existence of a rotor fault and have provided information about its importance, as well as about the load conditions of the machine. From this, the inputs of the RN_{bc} network will be set to the amplitude and the frequency of the g.f_s line of the spectrum of res-i_{ds}.

8.9.2. *Learning sequence of the RN_{bc} network*

Since the RN_{bc} network only operates during the activation of the second output S_{2d} of the RN_d network, operation examples with rotor fault and simultaneous stator/rotor fault must be learnt by the RN_{bc} network. For this, the E vector is made up of 48 samples under different load conditions and of healthy or faulty operating modes, which are successively presented to the inputs of the RN_{bc} network. The following table describes the 48 samples, which are used for the learning process of this network.

No of samples	Operation state	Torque (nm)	Shorted Turns
1 to 3	healthy	3, 5, 7	0
4 to 8	1 cracked bar at 50%	3, 4, 5, 6,7	0
9 to 18	1 cracked bar at 50% + stator faults	3, 4, 5, 6, 7	1 and 15
19 to 23	1 cracked bar	3, 4, 5, 6, 7	0
24 to 33	1 cracked bar + stator faults	3, 4, 5, 6, 7	1 and 15
34 to 38	2 cracked bars	3, 4, 5, 6, 7	0
39 to 48	2 cracked bars + stator faults	3, 4, 5, 6, 7	1, 15

Table 8.3. *Operation conditions of the learning samples of the RN_{bc} network*

Figure 8.33 shows the learning sequence, which is formed by the desired input and output vectors.

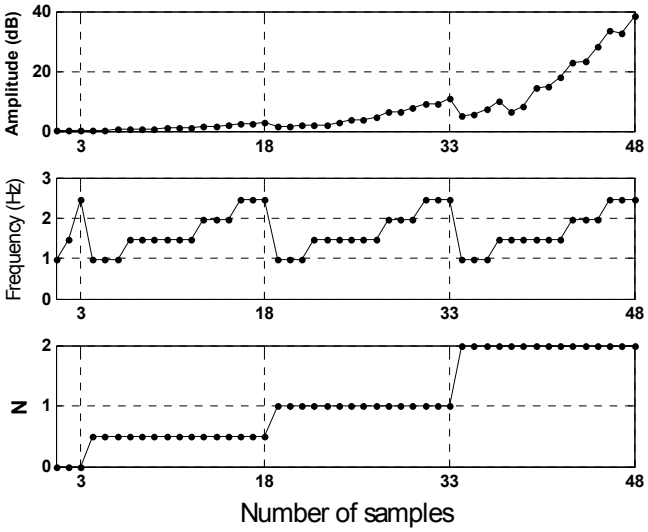

Figure 8.33. *Learning sequence of the RN_{bc} network*

NOTE.– For the crack of one bar at the rotor, the output vector designates it by the number N = 0.5.

8.9.3. *Learning, test and validation results*

The external structure of the RN_{bc} network is made up of an input layer, which is itself made up of two inputs (amplitude and frequency of the PSD line of the res-i_{ds}), and an output layer, which is itself made up of only one neuron; this neuron indicates N, number of broken bars at the rotor. After several learning sequences, the optimum structure which has given good learning and test performances is represented in Figure 8.34 [BOU 09]. It is made up of only one hidden layer of 13 neurons. The activation functions of the neurons of the hidden layer and of the output layer are "tangsig" and "purelin" respectively.

The RN_{bc} network has provided good learning performances, where the LMSE has achieved a low value (1.15×10^{-16}) after 10,000 iterations. The network has also been tested for several cases of rotor faults.

It has shown good generalization ability and has been able to accurately determine the number of broken bars in the rotor and even the crack of a bar. The network and the chosen method have been experimentally validated on a test bench.

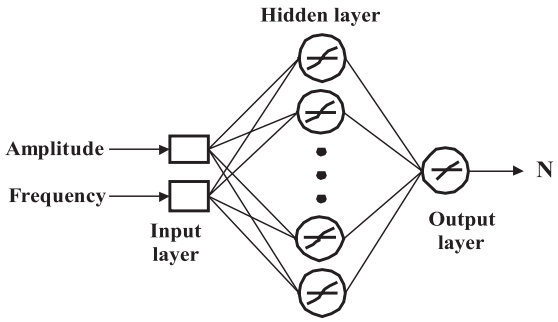

Figure 8.34. *Architecture of the RN_{bc} network*

8.10. Complete monitoring system of the induction machine

Once the performances of each network have been separately studied, it is necessary to evaluate the performances of the global system by gathering the three networks: RN_d, RN_{cc} and RN_{bc}. The external structure of the system is made up of nine inputs and six outputs, as illustrated by Figure 8.35. The outputs (S_{1d}, S_{1cc}, S_{2cc}, S_{3cc}) are designed for the monitoring of the stator fault. On the contrary, the outputs (S_{2d} and S_{bc}) are earmarked for the monitoring of the rotor fault.

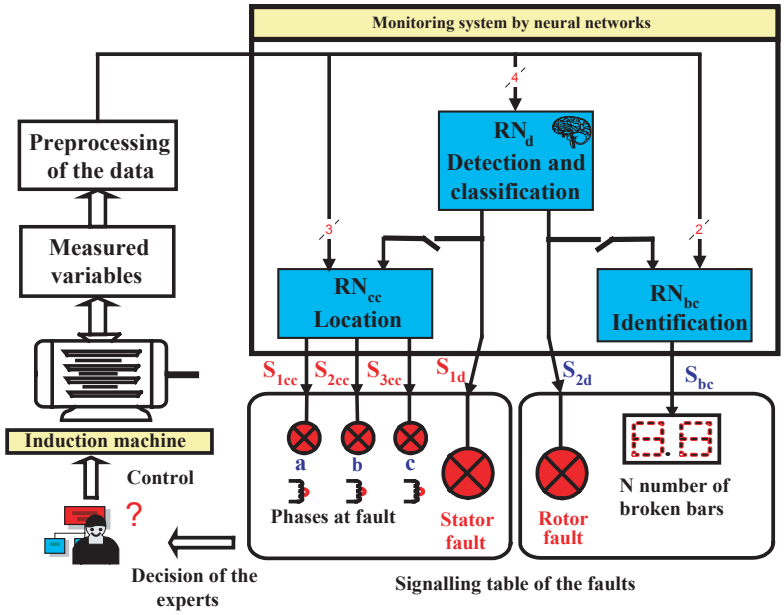

Figure 8.35. *Monitoring system of the stator and rotor faults of the induction machine*

The system has been tested with several cases of faults under different load conditions. Figure 8.36 shows the test results of a sequence, which is presented to the inputs of the system. This test sequence is made up of 15 examples of operation of the machine, which are described in Table 8.4 with the state of the outputs corresponding to each group of samples.

The output error of the three networks is low (Figure 8.36). This depicts the efficiency of the system. In fact, the suggested monitoring system can automatically point out, in an efficient and reliable way, the stator and rotor faults in an early stage, as well as the simultaneous stator/rotor faults [BOU 09].

No of samples	Stator fault	Rotor fault	Torque (nm)	S_{1d}	S_{2d}	S_{1cc}	S_{2cc}	S_{3cc}	S_{bc}
1 to 3	healthy	healthy	3, 5, 7	0	0	0	0	0	0
4 to 6	phase a_s	healthy	3, 5, 7	1	0	1	0	0	0
7 to 9	phase b_s	healthy	3, 5, 7	1	0	0	1	0	0
10 to 12	healthy	1 broken	3, 5, 7	0	1	0	0	0	1
13 to 15	phase a_s	1 broken bar	3, 5, 7	1	1	1	0	0	1

Table 8.4. *Operation conditions of the test samples and the corresponding outputs of the diagnosis system*

8.11. Conclusion

By considering the importance and the frequency of use of the induction machines in the inductrial sector, early detection of the faults in these machines has become a predominant economical stake. It is essential to develop detection and diagnosis tools, in order to automatically monitor the operation state of the machine.

In this chapter, an automatic monitoring system of the state of the induction machine based on the ANN has been suggested. This system is designed, so that it can carry out an early detection of the fault of the inter turns short-circuit fault and the fault of broken bars at the rotor of the induction machine. In addition, the system can diagnose these two faults, by locating the phase where the short-circuit fault has occurred when a stator fault has been detected. It is also able to identify the number of broken bars at the rotor, in case of the detection of a rotor fault. The detection and the diagnosis of the two faults are rendered reliable and robust by using a parametric estimation method, in order to avoid false alarms, which are caused by a variation of the electrical parameters of the machine due to temperature variations and/or the modification of the magnetic state of the machine. The detection of the faults is also carried out in the presence of noise and by taking into account the variation of the

load of the machine. This shows that the choice and the processing of the pertinent inputs of the network is a preliminary work, which is necessary for the development of an efficient and robust diagnosis.

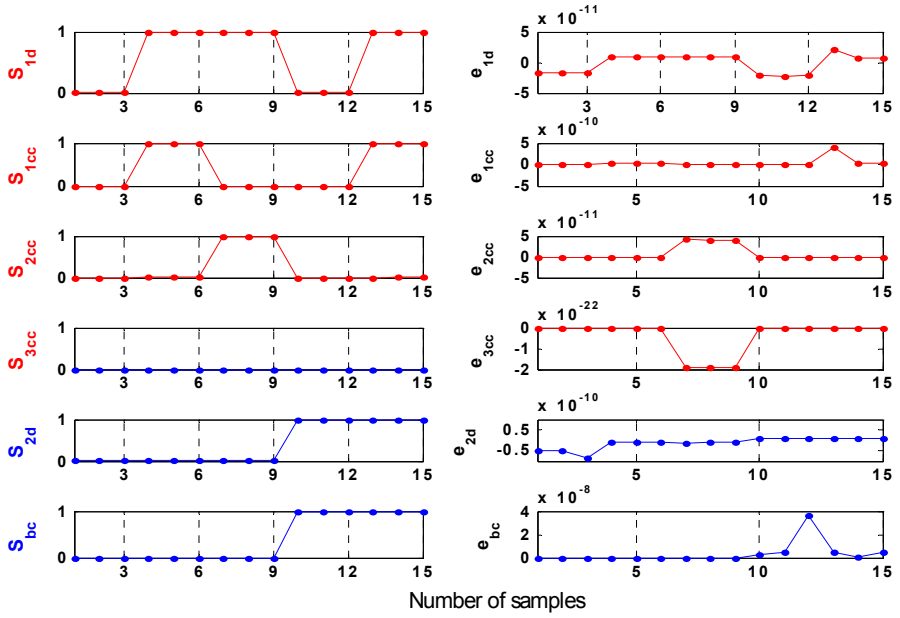

Figure 8.36. *Outputs and errors of the monitoring system of the induction machine*

This study has highlighted the efficiency of the ANN of the feedforward MLP type in the fault diagnostic domain. The ANN thus remain as an essential tool to automatically recognize the normal or abnormal operation state of the machine. Therefore, we have focused in this chapter on the global structure of the diagnosis and on the pertinence of the inputs of the ANN as a function of the objectives of each ANN for the detection and the localization of the faults chosen in the study.

8.12. Bibliography

[BAC 03] BACHIR S., TNANI S., CHAMPENOIS G., TRIGEASSOU J.-C., "Méthodes de commande des machines électriques", *Diagnostic de la machine asynchrone*, p. 253-257, Hermès, Paris, 2003.

[BOU 07] BOUZID M., MRABET N., MOREAU S., SIGNAC L., "Accurate detection of stator and rotor faults by neural network in induction motor", *IEE Multi-conference on System Signal and Devices*, SSD'07, Tunisia, 21 March 2007.

[BOU 08] BOUZID M., CHAMPENOIS G., BELLAAJ N., SIGNAC L., JELASSI K., "An effective neural approach for the automatic location of stator inter turn faults in induction motor", *IEEE Transactions on Industrial Electronics*, vol. 55, no. 12, p. 4277-4289, December 2008.

[BOU 09] BOUZID M., Diagnostic de défauts de la machine asynchrone par réseaux de neurones, PhD Thesis, El Manar University, National School of Engineering of Tunis, 2009.

[CAS 03] CASIMIR R., Diagnostic des défauts des machines asynchrones par reconnaissance de formes, PhD Thesis, Ecole centrale de Lyon, December 2003.

[CHE 02] CHEN Y.M., LEE M.L., "Neural networks-based scheme for system failure detection and diagnosis", *Mathematics and Computers in Simulation*, vol. 58, no. 2, p. 101-109, 2002.

[DRE 02] DREYFUS G., MARTINEZ J.M., SAMUELIDES M., GORDON M.B., BADRAN F., THIRIA S., HERAULT L., *Réseaux de neurones: Méthodologie et applications*, Eyrolles, Paris, 2002.

[MOR 99a] MOREAU S., Contribution à la modélisation et à l'estimation paramétrique des machines électriques à courant alternatif: Application au diagnostic, PhD Thesis, University of Poitiers, Ecole supérieure d'ingénieurs de Poitiers, 1999.

[MOR 99b] MOREAU S., TRIGEASSOU J.C., CHAMPENOIS G., "Diagnosis of electrical machines: a procedure for electrical fault detection and localization", *Proc. IEEE SDEMPED'99 – Symposium on Diagnostics for Electric Machines*, *Power Electronics and Drives*, p. 225-229, Gijon, Spain, September 1999.

[RAJ 08] RAJAKARUNKARAN S., VENKUMAR P., DEVARAJ K., RAO K.S.P., "Artificial neural network approach for fault detection in rotary system", *Applied Soft Computing*, vol. 8, no. 1, p. 740-748, January 2008.

[SAI 76] SAINT-JEAN B., *Electrotechnique et Machines Electriques*, Eyrolles, Paris, 1976.

[VEN 03] VENKATASUBRAMANIAN V., RENGASWAMY R., KAVURI S.N., YIN K., "A review of process fault detection and diagnosis Part III: Process history based methods", *Computers & Chemical Engineering*, vol. 27, p. 327-346, 2003.

[ZWI 95] ZWINGELSTEIN G., *Diagnostic des défaillances, théorie et pratique pour les systèmes industriels*, Hermès, Paris, 1995.

Chapter 9

Faults Detection and Diagnosis in a Static Converter

9.1. Introduction

Since the 1970s, power electronics has witnessed a staggering growth due to the progress made in the knowledge of components, converter topologies and control. Static power converters have gained popularity in energy conversion and their applications range from DC to AC and in many applications such as:

– variable speed torque industrial drives (railway traction, mills, lifting devices, pumping, etc.);

– new architectures of autonomous electrical energy conversion systems (electric or hybrid vehicles, production networks and electricity distribution networks using renewable energy sources – wind farms or photovoltaic panels, for example);

– large electrical energy transport systems (FACTS[1], HVDC[2], SVC[3]…);

– low power mobile applications (cell phones, computers, etc.).

Using converters in these applications, for example, has improved the quality and efficiency of energy in networks, the development of variable speed in railway traction, and more recently, the development of traction chains (propulsion) in

---

Chapter written by Mohamed BENBOUZID, Claude DELPHA, Zoubir KHATIR, Stéphane LEFEBVRE and Demba DIALLO.

1 FACTS: *Flexible Alternating Current Transmission System.*

2 HVDC: *High Voltage Direct Current.*

3 SVC: *Static Var Compensator.*

electric vehicles. However, we must ensure that such benefits are not gained at the expense of reliability, availability, and the safety of goods and people. Moreover, the equipment obtained through high investments must be preserved.

Tables 9.1 and 9.2 show that more than 90% of failures are due to the converter or the control circuits. Apart from natural aging of the components, some of the extreme operational conditions, malfunctioning or difficult environments (confinement or electromagnetic disturbance, for example) induce stresses on the system and its different components (electrical and thermal strains on the power switches, mechanical strains on moving parts or premature wear on passive components). They lead to intermittent faults or failures, which result in converter failure, and consequently, the interruption of the energy transfer.

Part 1 of this chapter focuses on the methods for detecting and diagnosing faults which affect the control circuits, wherein detection and diagnostic actions are performed by only using current measurements available on the static converters.

Part 2 will focus on describing and understanding the mechanisms that generate the fault or failure in the semi-conductor components of the converter. The composition of the converter's components is in fact complex, with many phenomena taking place, all of which are multiphysical with very different time scales. This preliminary study must enable us to obtain representation models, to determine the relevant measures for carrying out a diagnosis (or prognosis), and to extract design methods for increasing converter reliability.

Converter failure	38%
Control circuit failure	53%
Failure of external and auxiliary components	9%

Table 9.1. *Failure rate in the energy conversion chain*

Among the converter components, the electrolytic capacitors and transistors are the elements that experience most of the failures.

Continuous bus capacitor	60%
Power transistors	31%
Diodes	3%
Inductive elements	6%

Table 9.2. *Failure rate of converter components*

The major difficulty in power electronics diagnosis is having a model that sufficiently represents the component or the converter, where there is adequate availability of measurement-related information.

Diagnosing the components, and therefore the converter, will depend on the availability of measurements, and the ability to interpret them in order to analyze their behavior. The main difficulty lies in the limited number of sensors used, due to cost constraints and packaging problems. Thus, we mainly find current sensors and, more rarely, voltage and (global) temperature sensors, whose information is useful in controlling the actuator chain.

The methods presented here are based on the current vector trajectory (instantaneous or average) by using analytical models or pattern recognition methods to detect faults in the control circuits, or switch opening faults. The time taken for diagnostics must be less than the stipulated time. Recalibration of the control system and/or the installation of a protection device would ensure that successive faults or failures are avoided.

9.2. Detection and diagnosis

9.2.1. *Neural network approach*

9.2.1.1. *Introduction*

Developing a model from physical laws (knowledge model) requires very precise process knowledge, which restricts its usage in complex systems, except for assuring strong hypothesis that will reduce its validity and the accuracy of the obtained evolutions. It can, however, be used to describe a sub-system in a modeling procedure, which combines many methods. Knowledge models provide access to component parameters through the analytical relationships between the inputs and outputs, and even internal variables. Control techniques (identification and observation, for example), therefore, will enable us to follow the evolution of variables and parameters, to establish diagnostic procedures.

A priori or representation models will enable us to establish links between inputs and outputs, without the need for a precise knowledge of the laws that govern the system's operation. However, they must have a level of expertise obtained through simulation or experiment reports. Representation models assume the availability of knowledge models to develop the simulation or the experimental device to perform the experiments, where we are aware of the fact that the fault situations are not always possible to simulate for obvious safety reasons. The advantage of representation models is that they are well adapted to the usage of artificial intelligence techniques, namely artificial neural networks (ANN) or fuzzy logic (FL) [MUR 06, MOH 09]. These techniques have adequate capacity to process a large amount of data or imitate

human reasoning. The learning potential of ANNs (formalization of the acquired knowledge base) renders it an interesting tool for detecting and diagnosing faults. Many studies related to the applications of neural networks to diagnose electrical machine and power systems have been developed (see Chapter 8). They have demonstrated the feasibility of ANN's and their capacity to recognize faults in electrical systems.

The natural robustness of fuzzy logic (FL) due to its ability to manage uncertainties also makes it a useful diagnosis tool.

In the following section, we present a technique for detecting and diagnosing an intermittent opening fault in one of the switches of a three-phase voltage inverter, which powers an induction drive. This fault can be due to a failure in the control circuit (see Table 9.1).

The inverter is controlled in an open loop, by applying a *V/f* type law. We only have 2 current sensors which measure the a and b machine's phase currents to guarantee a follow-up of the system's state. There is no mechanical sensor, whose cost and maintenance will often hold up the investment. We will admit here that malfunctions are processed in mechanical steady state (Figure 9.1).

The aim is to detect the fault by using the trajectory of the mean current vector value in Concordia's two-phase reference frame. The advantage of this approach for monitoring is based on the use of pre-measured currents of the drive, where using the mean value enables us to reduce the amount of data to obtain synthetic information [DIA 05].

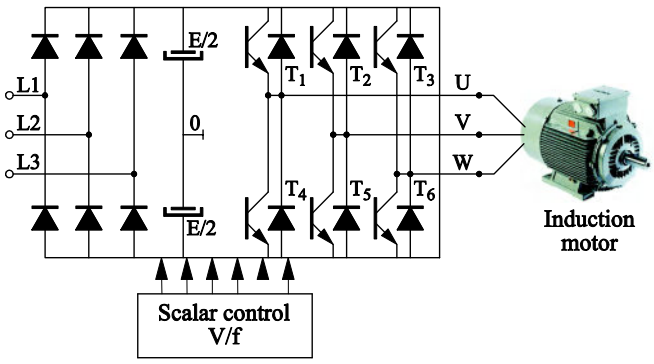

Figure 9.1. *Drive structure*

9.2.1.2. *Concordia transformation*

In three-phase induction machines, the neutral wire is often inaccessible and unconnected. The stator currents, therefore, do not have a homopolar component.

We can, then, substitute the three-phase system with a two-phase one, to represent the electrical components. The chosen representation is based on the Concordia transformation. Under these conditions, the components (i_α, i_β) may be expressed in terms of the three-phase currents (i_a, i_b, i_c), by:

$$i_\alpha = \sqrt{\frac{2}{3}} i_a - \frac{1}{\sqrt{6}} i_b - \frac{1}{\sqrt{6}} i_c$$

$$i_\beta = \sqrt{\frac{1}{2}} (i_b - i_c)$$

If the currents are sinusoidal (perfect conditions), then this relationship becomes:

$$\begin{cases} i_\alpha = \dfrac{\sqrt{6}}{2} I \sin(\omega t) \\ i_\beta = \dfrac{\sqrt{6}}{2} I \cos(\omega t) \end{cases}$$

where I is the power supply peak current, ω is the power supply frequency, and t is the time variable. Under these conditions, the Concordia outline is a circle centered at the origin, as illustrated in Figure 9.2. This simple example will enable us to detect anomalies in the three-phase system by monitoring its deviations. When the system is healthy, analyzing the transformed currents will allow us to notice that the outline is circular, and is centered around zero with a constant radius in steady state [NEJ 00, ZID 03].

9.2.1.3. *Detection and localization area*

Here we will focus on failure in the control circuitry of one of the power switches on the inverter arm. We will assume that the fault only affects the control of one of the inverter arms, and that the control of the extra switch on the same arm remains unchanged.

When a fault occurs on a switch, the voltage in the corresponding phase loses a certain number of pulses, resulting in an increase in the DC component ΔV. This variation is the reason for the current vector contour displacement. The direction of the displacement is decided by the sign of the current variation, which makes will enable us to locate the faulty switch. For switch T_1, the contour moves in direction $(-\alpha)$ (Figure 9.2b). The contours corresponding to other switches, which are faulty, can be easily deduced by 120° rotations.

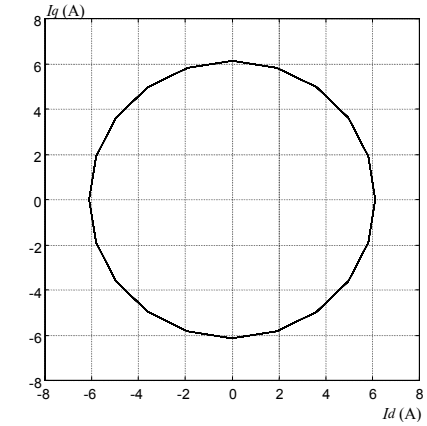

a) Perfect conditions

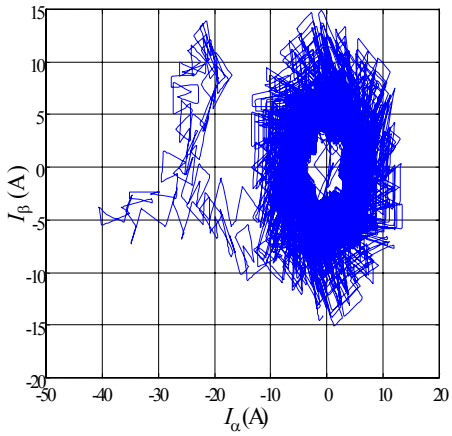

b) Fault T1

Figure 9.2. *Concordia contour*

If we assume that the sinusoidal currents have constant amplitude, then the current vector trajectory will be a circle with constant radius. When there are no imbalances, and we work out the mean, then we will obtain a point at the origin of the reference frame. However, in a real system, a slight imbalance remains between the phases of the machine. Therefore, the trajectory of the current vector's mean value over all the points of operation will be presented by a set of point clouds around the reference frame origin.

This trajectory is thus limited to a circle whose radius is calculated by considering the dispersion of these obtained points. The inner area of the circle will

be considered as the zone of healthy operation, and any point or set of points outside the circle will be associated with malfunction. Determining the radius R of this circle is very important, as it defines the detection threshold. It must be small enough for the diagnosis to be reliable, but not too small to prevent detection of false alarms.

The dispersion of these points, leads us to define them by their membership probability.

We are thus describing the probability of any measuring point belonging to one of two categories of the area corresponding to either the inside or outside of the circle.

If we accept a Gaussian law for the normal operation category, then the probability will be written as:

$$p(I) = \frac{1}{2\pi\sigma_0^2} \exp\left(-\frac{\|I\|^2}{2\sigma_0^2} \right)$$

where $\|I\|$ indicates the norm of the mean value of the vector current in the Concordia reference frame, and the standard deviation is written as σ_0. If we find that $\|I\| \geq R$ and that, in truth, these measurements do not relate to a fault, then this has to be a false alarm. This case can be attributed to a low occurrence probability, so that the diagnosis is reliable. This minimum, but not zero, probability is written p_0.

In the low power domain (<1 kW), it is only mildly beneficial to locate the fault when the converter power moduli are integrated into the same casing. In these cases, it is enough to just detect the converter's malfunctioning. To do so, the normal operating domain must be determined for all the operatory modes. The flexibility and capacity of these neural networks to educate us, will render these networks as suitable design tools in this domain.

In the following section, as an example we will illustrate a method for determining the healthy operation domain, known as the Radial Basis Function (RBF).

The RBF network has an evolutionary architecture with three layers: an input layer with components (I_α, I_β) of the mean current vector I, a layer of concealed neurons, and an output neuron which calculates the probability density under-lying the learning base distribution.

The probability density is a sum which is weighted by the weights ω_k of the activation functions $G_k(I, \mu_k, \sigma)$:

$$P(I) = \sum_{k=1}^{K} \omega_k G_k (I, \mu_k, \sigma)$$

Weights ω_k are defined by:

$$\omega_k = \sum_{k=1}^{K} G_k$$

The hidden neurons have identical Gaussian activation functions G_k defined as the following:

$$G_k (I, \mu_k, \sigma) = \frac{1}{2\pi\sigma^2} \exp\left(\frac{-1}{2\sigma^2} (I - \mu_k)^T (I - \mu_k) \right)$$

The *isocontour* of the Gaussian function is composed of a set of points such as:

$$(I - \mu_k)^T (I - \mu_k) = \sigma^2$$

In the case of a two-dimensional space, the isocontours are circles C_k with a center μ_k and a radius of $\tilde{\sigma}$.

The *activation region* of a Gaussian neuron is within the isocontour. The neuron will have a significant response if the observation presented on the network is located in the neuron's activation region.

Building the network and its learning process are carried out by a placement algorithm at the centers of the activation regions. At the end of the algorithm, we obtain the structure of the layer hidden in the network, where each circle C_k relates to a Gaussian neuron. Figure 9.3 is an example taken from a learning data base of 200 points, which results in a 45-neuron architecture in the hidden layer.

For reasons of simplicity, this domain will be circumscribed in a circle with radius R, whose equation is described by the following equation:

$$R^2 = \|I\|^2 = -2\sigma_0^2 \ln\left(2\pi\sigma_0^2 p_0\right)$$

This will appear in the hexagon of the location space, as shown in Figure 9.4. The thick straight lines which define the boundaries of the 6 domains (T_1, T_2…, T_6) are obtained by using an analytical approach. For example, for T_3, we have equation $i_\beta = \sqrt{3} i_\alpha \pm i_0$ where i_0 indicates the maximum offset.

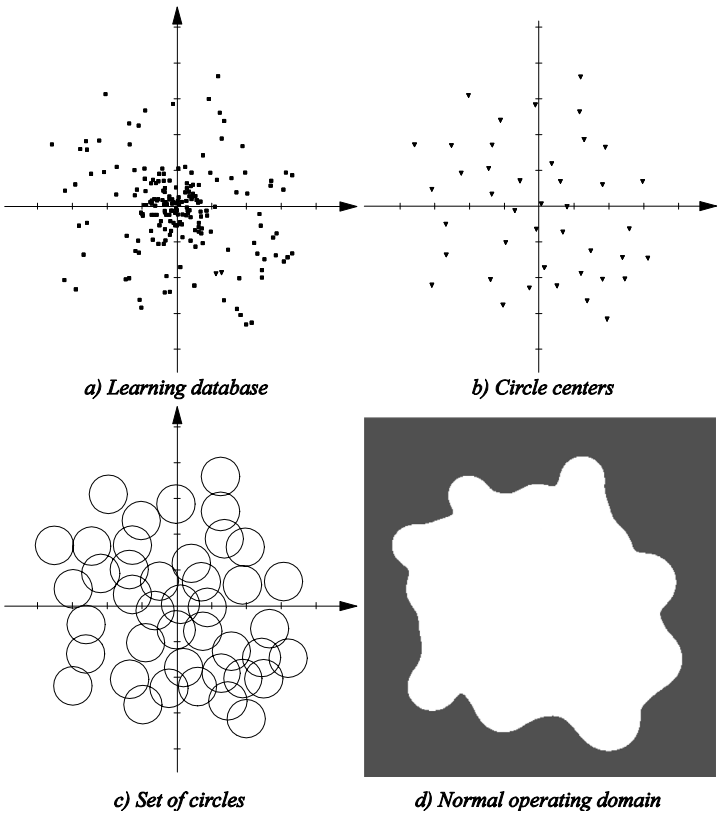

Figure 9.3. *Definition of the normal operating domain*

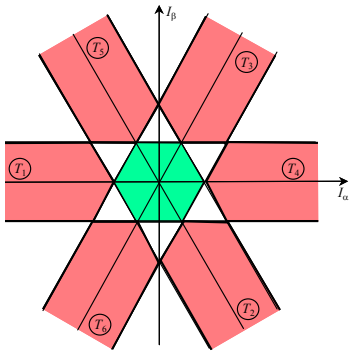

Figure 9.4. *Detection and localization space*

A combination of a representation model and a knowledge model would lead to an approach that would help us to construct the localization space. According to the direction and amplitude of the current vector trajectory displacement, we can therefore detect the occurrence of a fault, and locate the faulty switch, which is relevant in high power applications where the power moduli per phase are well defined.

9.2.1.4. *Discussion*

This diagnosis technique that uses the mean value of the measured currents represented in the Concordia reference frame gives interesting results. Defining the localization space based on the mean current vector and a probability of belonging to the healthy operating zone, would render it possible to consider the imperfections inherent to the power supply and the machine. However, it also enables us to take into account any variation in the operating point. However, precision of the location is still not enough, primarily due to the difficulty in adjusting the size of the healthy operating zone, and the possible overlapping of the domains for each switch. We must also point out that using the mean value is disadvantageous due to two reasons:

– when we want to collect adequate points to properly determine the healthy operating zone, at low speed, the duration of the diagnosis algorithm would be at least equal to an electrical period, which may not be compatible with safety requirements;

– on the one hand, we must implement methods that rely more on representation models developed by using expertise acquired on static converters, and on the other hand, consider the direct use of instantaneous components whose operating point must be taken into account.

In the following section, we will present another approach based on fuzzy logic.

9.2.2. *A fuzzy logic approach*

9.2.2.1. *Introduction*

As we have just seen, the diagnostics expert often uses signals or signatures to study the state of the electrical system, and consequently, determines the occurring faults. However, these experts are often required to interpret measurement data, which are often not very conclusive. Using fuzzy logic can help us to diagnose faults (the location of the faulty switch in our case).

In fact, fuzzy logic, which has evolved from human reflection and natural language processes, will enable us to make decisions with vague information [ZAD 65, BUH 94, KAU 87].

Fuzzy logic allows elements to be described as having a certain degree of membership to a set. This allows a computer process, which is normally forced to work in a binary mode to "0" and "1", to be used within the continuous domain.

In fact, by moving onto fault diagnosis in a converter, there are many situations where the state of this converter is neither "good" nor "bad", but somewhere in between.

Moving on from the fact interpreting the condition of an electrical actuator is a fuzzy concept, many approaches dedicated to fuzzy diagnosis of the induction machine have been proposed over the last few years. The retained method is based on the phase currents and the same location space as the ANN-based method. Its operational diagram is illustrated in Figure 9.5 [ZID 08].

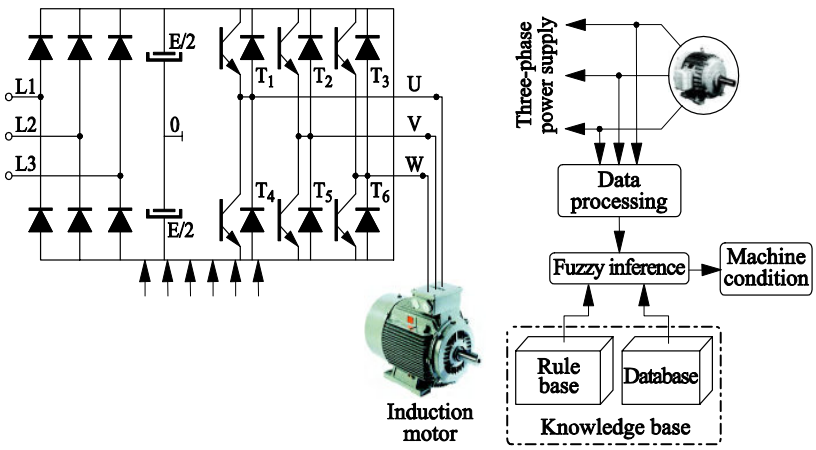

Figure 9.5. *Operational diagram for detection and location using fuzzy logic*

9.2.2.2. *Detection and localization space*

The detection and localization space illustrated in Figure 9.6 is obtained from an *a priori* analysis of the failure modes of the inverter switches based on the Concordia contour displacement according to the failing switch.

The detection and localization block, which uses fuzzy logic, has two inputs calculated according to the following expressions:

$$\begin{cases} E_d = d_H - d_F \\ I_\theta = \sum_{i=1}^{6} N_i \end{cases}$$

where d_H and d_F respectively indicate the diameter of the healthy operation zone and the zone obtained in case of a stator current vector fault in the Concordia reference frame. I_θ represents the angular sector and therefore enables us to locate the switch (Figure 9.7).

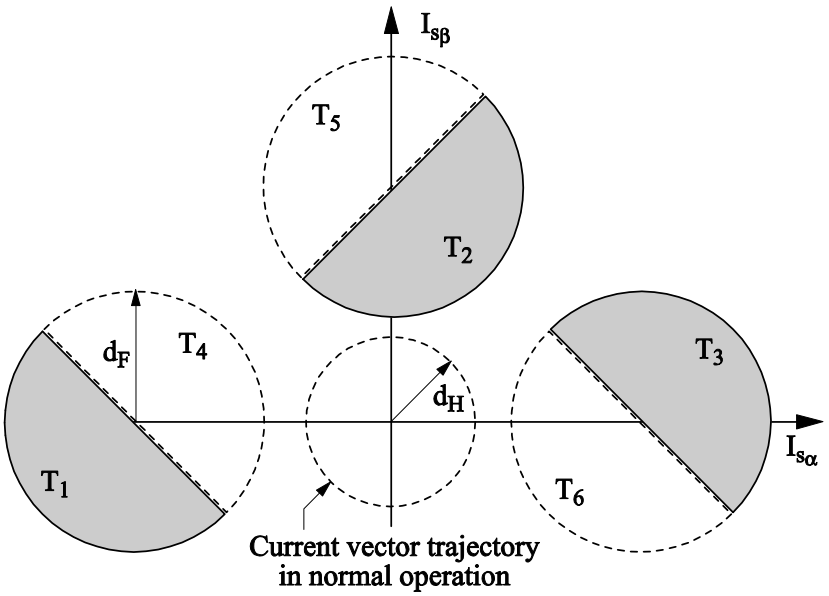

Figure 9.6. *Detection space*

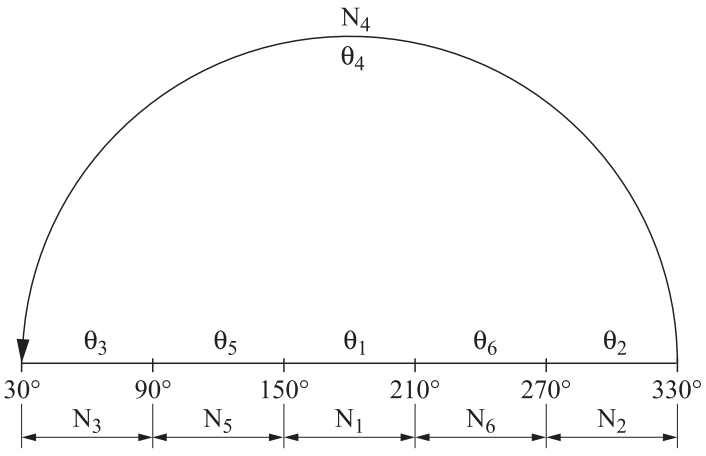

Figure 9.7. *Representation of the angular sector*

The standardized membership functions for the inputs and output are defined in Figure 9.8.

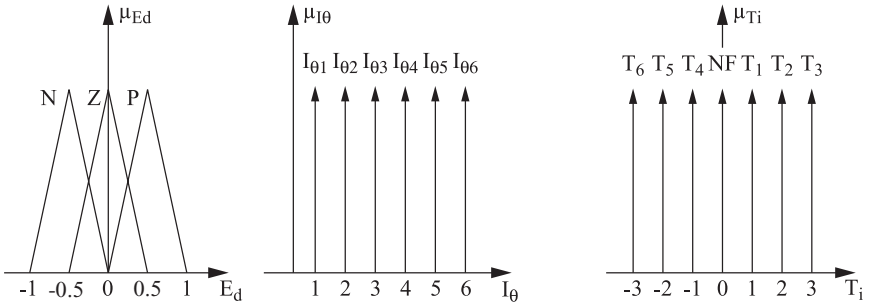

Figure 9.8. *Membership functions*

The rules used are described in Table 9.3.

E_d	I_θ	$I_{DL\text{-}FS} \Rightarrow$ Failing switch
Z or P	$I_{\theta i}$; $i = 1\ldots, 6$	$I_{0\text{-}DL\text{-}FS} \Rightarrow NF$ (No failure)
N	$I_{\theta 1}$	$I_{1\text{-}DL\text{-}FS} \Rightarrow T_1$
	$I_{\theta 2}$	$I_{2\text{-}DL\text{-}FS} \Rightarrow T_2$
	$I_{\theta 3}$	$I_{3\text{-}DL\text{-}FS} \Rightarrow T_3$
	$I_{\theta 4}$	$I_{4\text{-}DL\text{-}FS} \Rightarrow T_4$
	$I_{\theta 5}$	$I_{5\text{-}DL\text{-}FS} \Rightarrow T_5$
	$I_{\theta 6}$	$I_{6\text{-}DL\text{-}FS} \Rightarrow T_6$

(N: negative, Z: zero, P: positive, NF: no failure)

Table 9.3. *Linguistic rules*

9.2.2.3. *Application*

Experiments were carried out on an induction machine powered at 1.5 kW, where the induction machine was loaded with a DC machine connected to a variable resistance. The torque is regulated to provide a load torque of 2.5 nm, and the switch control is inhibited for 3.3 msec every two periods.

The phase currents *a* and *b* are sampled and processed offline by the detection and localization algorithm.

In Figure 9.9, we can observe the current vector projected in the Concordia reference frame. It is difficult to detect the contour displacement. On the other hand, after processing these contours, we obtain the result represented in Figure 9.10. We can see that the output is close to 1, which indicates that the switch T_1 is failing. The lower values (close to 0.5) represent normal biases due to the imbalances inherent in the induction motor.

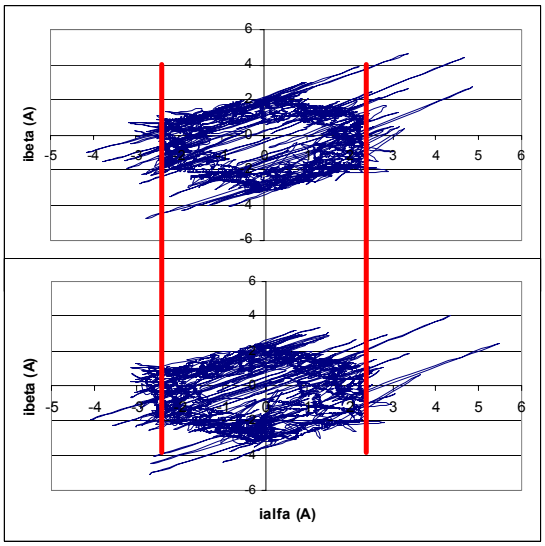

Figure 9.9. *Current vector trajectory (top: no fault, bottom: faulty)*

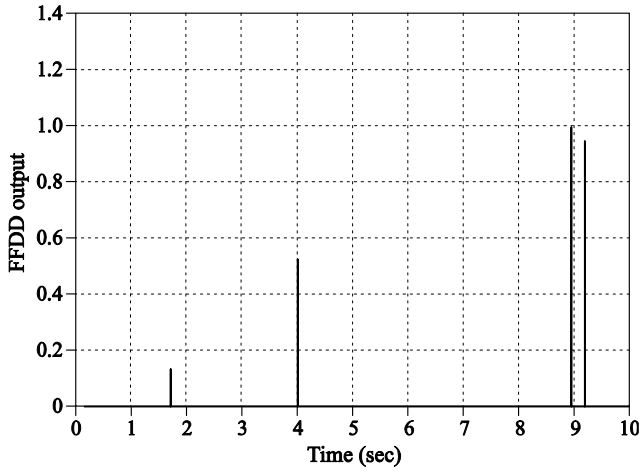

Figure 9.10. *Detection block output and fuzzy localization*

9.2.2.4. *Discussion*

These results give an increased robustness to the diagnosis through false alarms being reduced. Additionally, this fuzzy logic approach means that we neither have to calculate the mean of the current vector, nor the electrical period. As a result, the calculation and processing time is linked to the target material used, and corresponds to a few sampling periods.

To extend the work, we could consider increasing the rule base in order to detect double breakdowns. Moreover, for diagnosing failures in a multilevel inverter, we could consider the same approach by subdividing the angular domain into as many angular spaces as there are switches.

9.2.3. *Multi-dimensional data analysis*

In this section, we will focus on analyzing data collected in its multi-dimensional form, with the objective of using for diagnosis and fault detection applications.

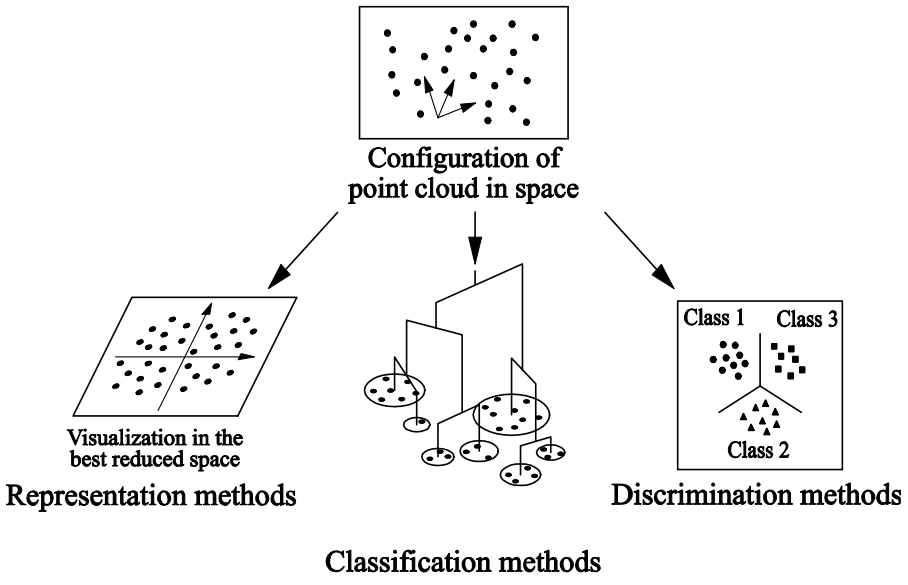

Figure 9.11. *Method groups in multi-dimensional data analysis*

In general, there are many methods in data analysis. They are grouped together according to three different objectives: representation, classification, and discrimination.

For representation methods, the main idea is to project the data (initially in multi-dimensional form) into a plane, in order to reduce the size of the problem. Next, the data is allocated to *a priori* groups from which we wish to separate the data. During the discrimination phase, a law for separating the data is proposed, so that we can identify unknown samples. In the following sections, we will focus on a representation method, which is known as principal component analysis (PCA), a method of supervised categorization and discrimination: the discriminant analysis [MOR 88, JAM 99, SAP 90].

For all these methods, whether they are methods of representation, classification or discrimination, the choice of variables representing the phenomena to be observed, is in fact, fundamental. In fact, the performances of the analyses carried out will depend on these characteristics. In our case, the choice involves electrical characteristics which are easily accessible, without having to change the physical structure of the device under study, thus making the procedure widely applicable to any industrial, electrical machine. The results that we will present here, as examples or illustrations, are based on the different phase currents from a polyphase machine. For each method, we indicate how the data must be organized, so that the collected data can be analyzed.

9.2.3.1. *Principal component analysis* (PCA)

The Principal Component Analysis (PCA) is a representation method, which involves seeking directions in space, which represent the best correlations between n random variables [MOR 88, JAM 99, SAP 90]. Also known as the Karhunen–Loève transform (KLT), the PCA is an unsupervised analysis method (i.e. where *a priori* knowledge of the samples is not taken into account in the method's calculations), which enables a visual approach to a multi-dimensional problem in a smaller space, called the principal plane. The main idea here is to highlight the major similarities and differences between $\boldsymbol{k}$ observations of a database, by projecting these data onto axes called principal components.

For this study, the data will be distributed into a base where $\boldsymbol{k}$ observations are described by using $\boldsymbol{n}$ variables.

For example, if we only wish to use physical components, which are available with no major interventions on the converter, then we propose using the currents from each phase in the case of a polyphase machine. These currents can be combined with all other signals (voltages, speeds etc.), which could significantly describe and represent the phenomena to be observed.

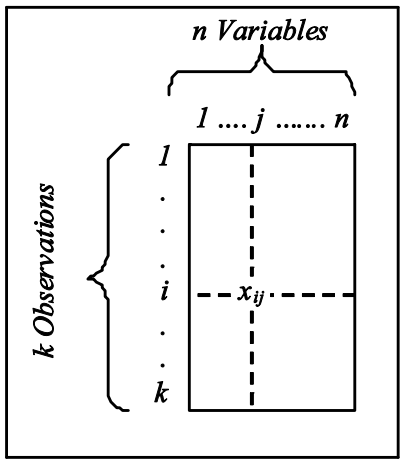

Figure 9.12. *Database structure for PCA*

The signals studied may be considered as realizations of a random vector ***X*** of the vector space $\Re^n$. For this approach, we are working with a zero-mean vector. To do so, we use the reduced centered matrix X_c whose elements are such that: $x_{c_{n,k}} = \frac{x_{n,k} - \overline{x}_n}{\sigma_n \sqrt{k}}$. $x_{c_{n,k}}$ can be seen as the kth centered reduced element described by the nth representative variable. We thus write $\overline{x}_n$ and σ_n respectively as the mean value and the variance of variable ***n***.

We then calculate the covariance matrix ***C*** such that:

$$C = X_c{}^T . X_c$$

Using this correlation matrix, to find the new factorial axes which are linear combinations of X_c whose variances are maximized, we must calculate the matrix V of the eigenvectors, which diagonalizes the covariance matrix as follows:

$$V^{-1} C V = \lambda V$$

λ is thus the diagonal matrix containing the eigenvalues of ***C***. It represents the energy distribution of the original data for the corresponding eigenvectors. These eigenvectors ***V*** of the covariance matrix correspond to the principal orthogonal components sought. They represent the best projection space for the database where most of the information is represented. To obtain coordinates **Y** of the data in the new projection space, we calculate: $Y = V^T . X$.

In this applied framework which attracts our attention, we generate an initial database made up of 2,500 observations, and described with 3 variables representing the observed phenomena, i.e. the currents of the 3 phases of a converter which feeds a three-phase machine [DEL 07, DEL 08]. These observations have been raised to characterize the healthy behavior of the converter.

By applying the PCA to this database, with the first 2 factorial axes we reach a representation that contains 99.98% of the information from the original database (see Table 9.4). The cumulated variance for these first 2 axes and the eigenvalues clearly show that the first 2 axes are sufficiently representative to describe the studied database.

	Variances	**Cumulated variances**	**Eigenvalues**
PC 1	53.358	53.358	1.601
PC 2	46.621	99.979	1.399
PC 3	0.021	100	0.001

Table 9.4. *Principal components for the PCA results with healthy samples*

The representation obtained by using the PCA describes a healthy operating contour similar to that obtained by using the Concordia transform. The advantage of the PCA is that the representation space uses principal axes, which are uncorrelated and orthogonal.

To complete this study, we have included other samples in the database, which correspond to faults in phase a and phase c. The analysis database which contains 6,800 samples (healthy and unhealthy) is analyzed by using the PCA. We obtain a representation, which, with the first 2 principal axes, can describe 98.83% of the information contained within the database. In fact, as the eigenvalues prove it in Table 9.5, a small amount of information is carried by the 3rd principal axis.

	Variances	**Cumulated variances**	**Eigenvalues**
PC 1	58.03	58.03	1.74
PC 2	40.80	98.83	1.22
PC 3	1.17	100	0.035

Table 9.5. *Principal components for the PCA results with healthy and faulty samples*

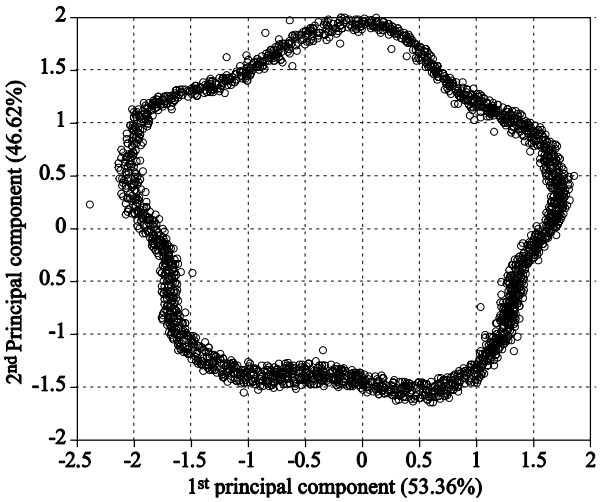

Figure 9.13. *PCA in a healthy sample case*

All the same, we draw the same 3D representation of the set of information from the database on the 3 obtained factorial axes. The corresponding representation shows strong correlations between the data according to their nature (healthy case, fault in phase *a*, fault in phase *c*). A small amount of different data is overlapped, which leaves us to think in light of these dispersions that the faults can be correctly separated into distinct categories, thus helping us to diagnose phase faults in the converter.

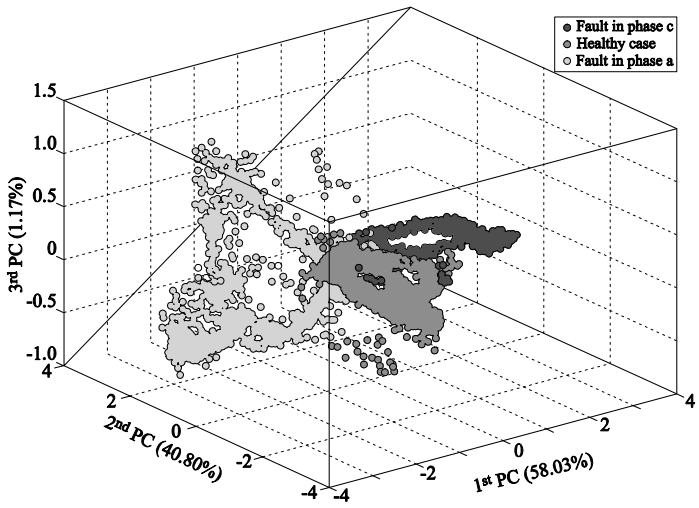

Figure 9.14. *PCA for healthy and faulty samples*

We then carry out a linear discriminant analysis to categorize the faults, as well as discriminating or identifying new unknown test samples.

9.2.3.2. *Linear Discriminant Analysis*

The Linear Discriminant Analysis (LDA) method relates to the multivariable variance analysis and multiple regression methods [MOR 88, JAN 99, SAP 90]. This is a supervised analysis method, i.e. has a learning phase during which the *a priori* knowledge of the data membership groups is taken into account while generating the method. In fact, when the analysis database is being generated, the observations must be allocated into *a priori* groups. These observations are, in the case of the PCA, collected for several variables which represent the phenomena to be observed. Still, the choice of variables that represent the data is fundamental in relation to the categorization results. Often, preprocessing is applied to these variables to improve the relevance of the information representing the phenomena to be observed.

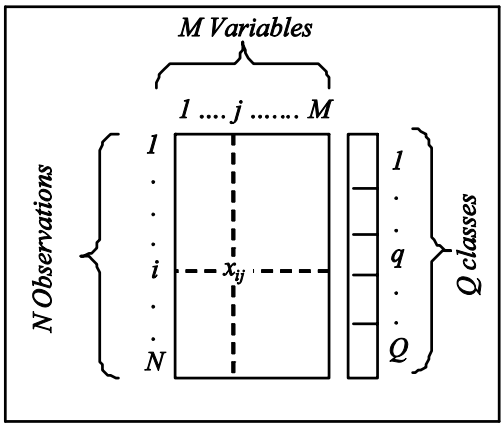

Figure 9.15. *Database structure for the LDA*

The discriminant analysis is both a descriptive (categorization phase) and decisive (discrimination phase) method. In its descriptive phase, it aims to reduce the data representation dimension, and also separates the data according to their *a priori* allocated groups. In its decision phase, it generates a law of discrimination as linear combinations of predictive variables, which characterize the differences or similarities among the *a priori* defined groups. With the help of this law, it will then be possible to identify samples with no *a priori* knowledge of their group.

For multi-dimensional analysis, the idea is to group the individuals (or observations) characterized by a certain number ***M*** of explicative variables. In this

case, classification means grouping together the individuals characterized by the explicative variables into a certain number of classes/groups $\boldsymbol{Q}$. The explicative variables space, also called the feature space, is generally identified as $\Re^M$. Each explicative variable corresponds to a magnitude of interest, extracted from the objects that we wish to discriminate.

In the applicative example relevant to our study, the explicative variables are the currents, and the observations (individuals) relating to these currents are allocated into *a priori* groups corresponding to the types of case studied (healthy case, fault in phase *a*, fault in phase *b*…). No specific preprocessing was applied to the data besides filtering, which allows us to maintain valuable information in the signal measurements on the currents. For our illustration, the classes, which characterize the samples will be the 3 categories ($\boldsymbol{Q}$ = 3) proposed to allocate the individuals (healthy case, fault in phase *a*, fault in phase *c*). For our analysis, a database of 6,800 individuals was created [DEL 08].

The objective of the LDA is to find one or several discriminant hyperplanes in R^M, which is the best for differentiating groups of similar individuals into disjointed classes. The first stage of the method (descriptive) consists of looking for discriminant functions in a sample of individuals of size *N*, with each function being a linear combination of *M* explicative variables whose values separate the *a priori* defined class *Q* in the best way. The second stage (decision-making) consists of knowing the class that an anonymous individual is allocated to, described by the same explicative variables using the discrimination rule established with the learning sample of size *N*.

Let us consider the data matrix $\tilde{X}$, of size $M \times N$, made up of centered reduced explicative variables. The total variance matrix of the centered reduced point cloud written V and of size $M \times M$, can be written as $V = \tilde{X} . \tilde{X}^T$.

This total variance matrix can be re-written as the sum of two terms: the intraclass variance linked to the dispersion of individuals belonging to the same class around their center of gravity, and the interclass variance linked to the dispersion of centers of gravity belonging to the classes around the origin. Thus, if we write the intraclass variance matrix as W, and the interclass variance matrix as B, then we may express *V* in the following form: $V = W + B$.

We are therefore looking for the best linear combinations, so that we could discriminate the individuals in the best manner, which amounts to transforming the feature space of size *M*, so as to obtain a maximum interclass variance and a minimum interclass variance. Generally, maximizing the interclass variances will highlight the differences between these classes, and minimizing the intraclass

variance amounts to limiting the range of individuals in the same class. Next, to calculate a linear combination, we must look for the combination that discriminates the classes from those that are not correlated to the previous ones. The different linear combinations obtained will then be among $\boldsymbol{Q}$ – 1 and will then constitute the discriminant linear functions.

To calculate the first linear combination, we must maximize the interclass variance. Knowing that the sum of the interclass and intraclass variance is constant, we thus choose the vector u_1 which maximizes the ratio between the interclass variance and the total variance, such that:

$$u_1 = \arg\max_{u \in R^M} \frac{u^T B u}{u^T K u}$$

We thus resolve the equation $V^{-1}Bu = \lambda u$ such that the eigenvectors u are called discriminant factors, and the corresponding eigenvalues λ represent the discriminant power.

Using the realized discrimination, we can propose a discrimination rule to identify the test samples. Thus, we can allocate an anonymous individual, characterized by its vector with characteristics $x \in R^M$, from the linear functions of x, written $f_q(x)$, relating to each group $q \in \{1,.....Q\}$. Thus, we can write the following relation:

$$f_q(x) = \left\| x - \bar{x}_q \right\| x^t V^{-1} x$$

where $\left\| x - \bar{x}_q \right\|$ is the distance from x to the center of gravity $\bar{x}_q$ of class q. The anonymous individual will be assigned to group q where $f_q(x)$ is the smallest:

$$x \in q \; si \; f(x) = \min\left\{ f_q(x) \right\}$$

In the example for classifying the faults which we are interested in, we show that by using the discriminant analysis, we are able to correctly separate the faults in phase *a*, in phase *c*, and the healthy case [DEL 08].

Validating the *a priori* classification which we have obtained shows that the choice of member groups of the selected individuals is correct. In fact, classification errors that we may observe are mainly due to the fact that the faults studied are intermittent.

Consequently, the phases where the fault occurs and disappears again create an ambiguous zone where the samples should be considered as healthy.

As a result, this limit must be defined with a maximum level of accuracy during the sample characterization phase (during which the evolution of the currents and the characteristic quantities of the phenomena were studied) to reduce uncertainties in the classification process.

		A posteriori		
		Class 1 (healthy case)	**Class 2 (fault in phase a)**	**Class 3 (fault in phase c)**
A priori	Class 1 (healthy case)	99.94%	0%	0.06%
	Class 2 (fault in phase a)	24.22%	75.78%	0%
	Class 3 (fault in phase c)	32.74%	0%	67.26%

Table 9.6. *Results from classifying samples in different groups*

The discriminant plane that we have obtained, defined by the two factorial axes, means that we can correctly classify the data from the moment where the beginning and the end of the zone of the intermittent fault is clearly identified.

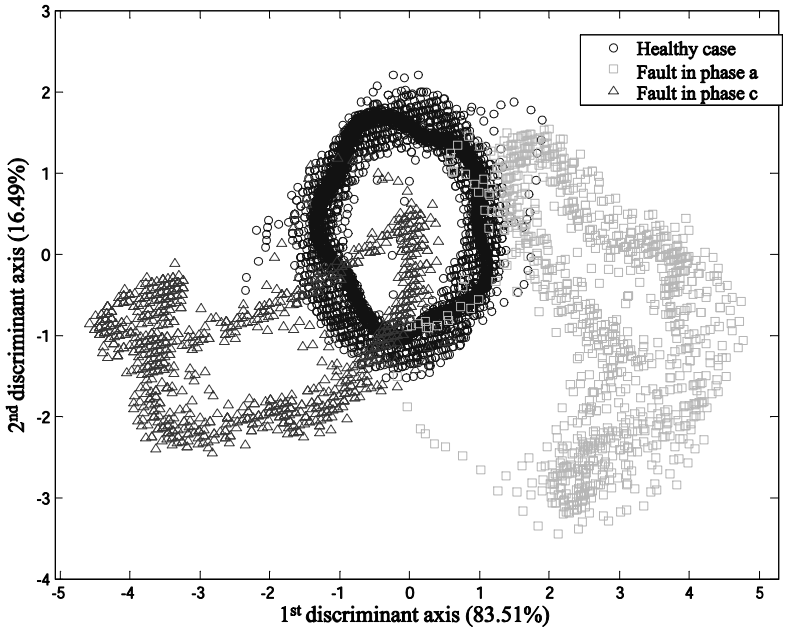

Figure 9.16. *Representation of the classification of samples in the discrimination space*

The results achieved in this classification stage would lead us to believe during the discrimination phase that the unknown sample tests can be correctly identified and classified within their corresponding groups.

With these methods, the learning phase must be performed offline. In fact, it is based on a database, where the database is fed with various operation states, which must be characteristic of the phases to be discriminated. In addition, it enables us to generate laws of discrimination, which will be used during the diagnosis to identify the real state of the device with no *a priori* knowledge of the samples. During operation, the decision step which is otherwise known as the classification phase, relies on these laws that are linear combinations of the input variables. These are simple operations whose implementation on a material target (a microcontroller, signal processor) is compatible with real time constraints. It is also possible to develop a material architecture for diagnosis (FPGA[4] type digital circuit) to implement a mobile diagnosis solution in the system involved. Obviously, the classification results (newly identified samples) can be stored in order to broaden the database and refine the laws of discrimination.

9.3. Thermal fatigue of power electronic moduli and failure modes

In this section, we will recollect the main degradations found in components and semi-conductor power moduli during operation. The outcomes presented here have mostly evolved from laboratory tests, which are generally accelerated tests (under current, voltage or temperature restrictions, higher than usual operating constraints). The damage reported is, however, representative of the damage which can be seen in certain applications. We will try to show the accessible electrical magnitudes, which enable us to detect, for diagnosis purposes, some of this damage. We will also show that in the current state of the power conditioning moduli, some of this damage is still very difficult to measure. Beforehand, we will present the main technologies of the components and power moduli in order to better understand the physical origin of the damage or even the reported failure modes in the following.

9.3.1. *Presentation of power electronic moduli in diagnosis*

9.3.1.1. *Packaging*

Power electronics components, for average and high power applications, use MOS power transistors (metal oxide semi-conductors), or IGBT (Insulated Gate Bipolar Transistor). They are generally presented as flat-packs, or in some cases for very high powers, as press-packed, so as to enable a better evacuation of the heat (Figure 9.17).

4 FPGA: *Field Programmable Gate Array*.

For the moduli, these power devices are composed of a stack of different materials. The first level is comprised of different dies, generally silicon based, which represent the active part of the component. The current power supply to these dies is generally ensured by aluminum bonding wires, with a diameter ranging from 100 to 500 µm. The dies are assembled (soldered) onto an insulating substrate. This substrate is formed by an insulating ceramic (generally in Al2O3 or AlN), metalized on both sides with copper, according to a DCB type process (direct copper bonded) for ensuring a good adhesion of the copper on the ceramic [SCH 03], Figure 9.18. The ceramic ensures the electric insulation and the evacuation of the heat flux released by the die. The DCB substrate is generally assembled (through soldering) on a metallic board, which is used as a mechanical support to fix the module on the cooling plate through a thermal interface (Figure 9.18).

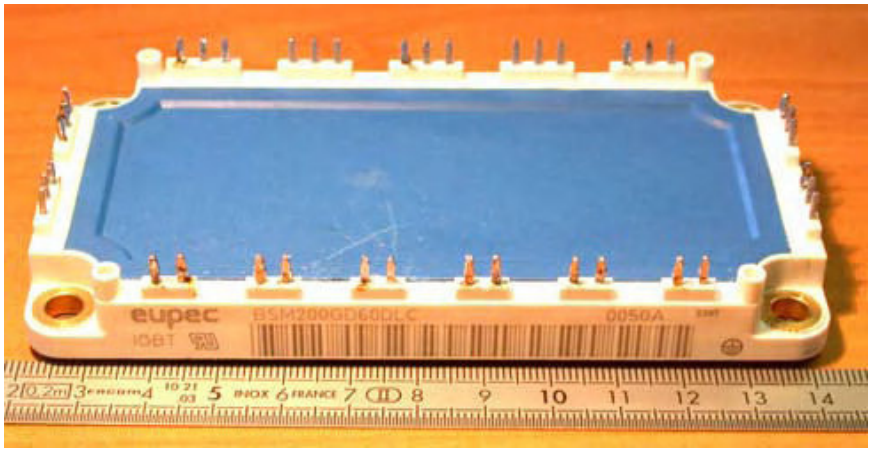

a)

b)

Figure 9.17. *a) IGBT module, average power voltage inverter (600V-200A); b) high powered IGBT module (3300V-1200A)*

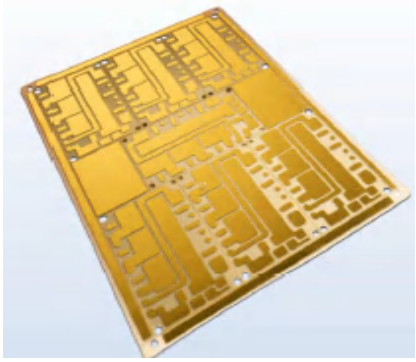

Figure 9.18. *Example of DCB substrate with copper metalization (CURAMIK)*

The baseplate is generally made of copper, even if composite baseplates in aluminum and silicon carbide (AlSiC) have been developed and combined with AlN ceramics to reduce thermal fatigue. In fact, AlSiC shows satisfactory thermal conductivity (but lower than for copper) and presents a thermal dilatation coefficient which is closer to aluminum nitride than copper. The module is properly screwed to the heatsink, depending on the clamping torque.

In these cast casings, the IGBT dies are soldered onto the DCB by using high temperature alloys. The complete assembly is then soldered onto the board at a lower temperature (Figure 9.19). These soldered joints can be used as mechanical, electric and thermal interfaces. In fact, they ensure the mechanical support of the different components, the electrical connection between the dies and the metalized substrate connected to the external power connections. Finally, they enable the thermal flux to conduct between the active elements and the baseplate.

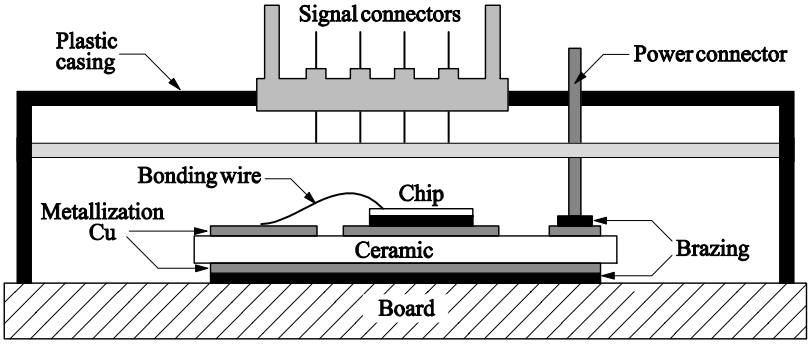

Figure 9.19. *Diagram showing the assembly of a power module*

Figure 9.20 shows a cross-section of a power module which enables us to assess the thicknesses of the layers of the different materials. The figure on the left represents an observation under an optical microscope of a micro section of the IGBT module, and on the right it shows a close up under the electronic microscope of a localized area under an IGBT die.

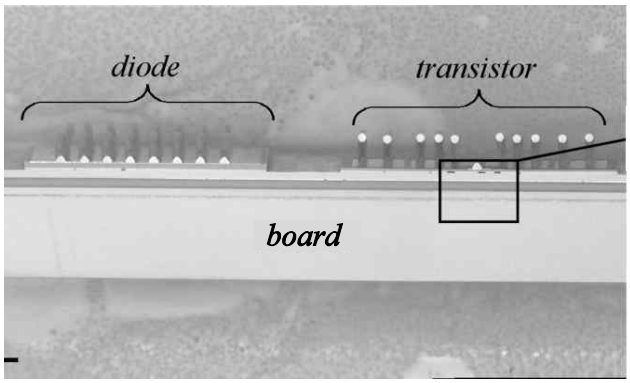

a)

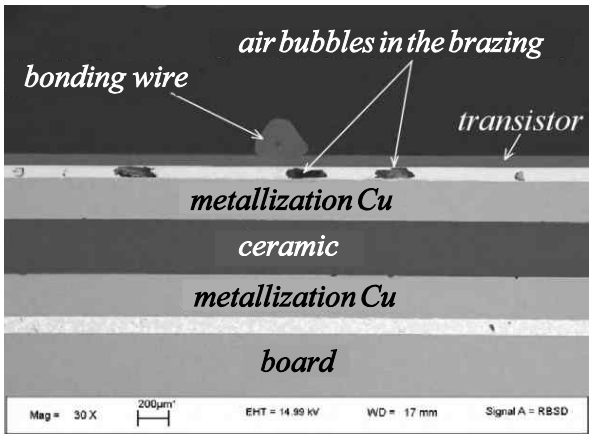

b)

Figure 9.20. *Observations under optical microscope (left) and electronic microscope (right) of a micro section on an IGBT module*

Figure 9.21 shows the die and more particularly the layer of metallization deposited on the die. This technique ensures that the different elementary cells making up the module are in parallel (more than 10^6 cells/cm²) to inhibit a parasitic transistor (for MOFSET) or a thyristor (for the IGBT) depending on the kind of die, and finally, to enable ultrasonic welding of the bonding wires. The following table shows the thickness of the different materials, which are involved in composing the module.

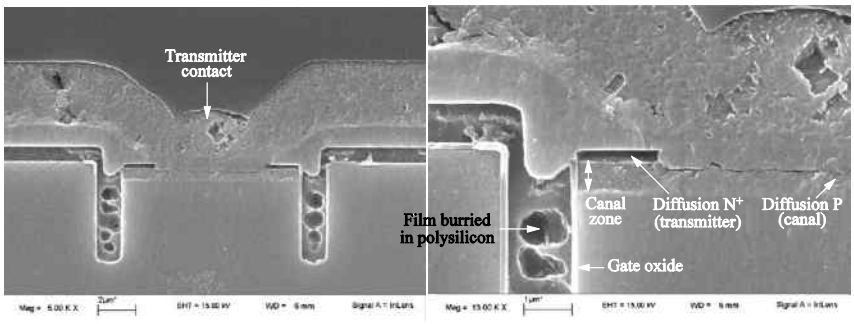

Figure 9.21. *IGBT die elementary cell*

Component	Material	Thickness (µm)
Transistor	Si	70
Front side metalization	Ti Ni	0.32 0.43
Diode	Si	210
Front size metalization	Cr Ni	0.14 0.78
Transistor and diode soldered	SnAg	80 (diode) 80 to 120 (transistor)
Ceramic	Al, O	375
Metalization on ceramic	Cu	280
DCB soldered /Board	PbSn	95
Board	Cu	2,900
Internal and external board coating	Ni	6

Table 9.7. *Nature and size of materials used to assemble an IGBT module, example of a 600V module*

We can also find moduli without a baseplate, where the DCB substrate (AlN or Si_3N_4) is deposited directly on the heatsink by using a thermal interface. This solution allows for better thermal performances and avoids using soldering between the baseplate and the DCB substrate, which is often a source of failure. But the lack of baseplate and the fragile nature of the ceramic stipulate that the condition of the cooler surface is excellent. For some of the high power IGBT devices, which do not have the board, the ceramic substrate is held due to pressure on the cooler, as is the case for moduli proposed by SEMIKRON (SKiiP) [SCH 03] where the electrical

contacts are pressed onto the substrate (Figure 9.22a), just like the ceramic on the sink. The lack of baseplate and thermal interfaces makes it possible to decrease the thermal resistance of the whole assembly. In the MiniSKiiP moduli (Figure 9.22b) made by the same company, this principle of pressure contacts is combined with pressure spring contact technology. These are loaded to establish all the electrical connections between the power module and the control board.

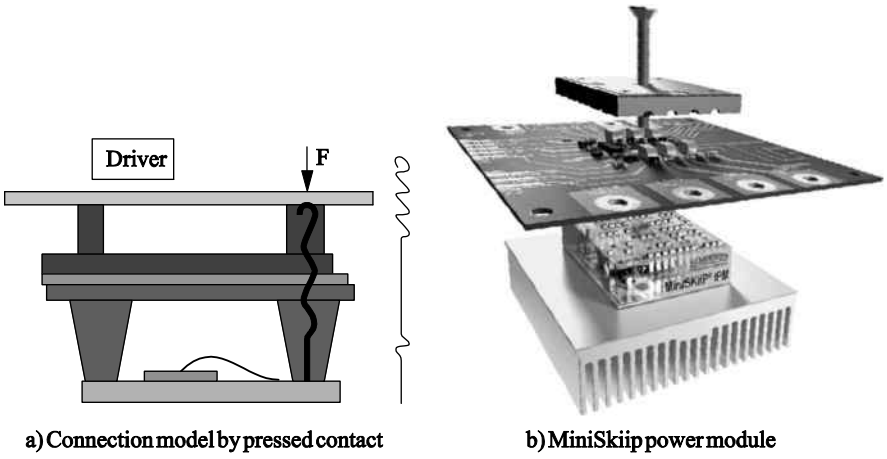

Figure 9.22. *Moduli with no Semikron® board*
a) model showing pressure-contact connection; b) MiniSKiiP power module

In some cases, and to optimize thermal flux evacuation, the baseplate (or the substrate for moduli with no board) is also the cooler [SCH 00, IVA 03]. This solution means that we can dispense with the baseplate/cooler thermal interface and increase the convective exchange between the fluid and the cooler walls.

Replacing bonding wires by soldering pins or balls in 3D technologies means that two insulating substrates and a 2-sided cooler can be positioned on top of each other. The dies are then cooled on both sides (Figure 9.24), so that the dissipation of heat can be managed more effectively.

Finally, the pressurized casing means that we can dispense with soldering and therefore report the failures that are usually found while assembling the moduli.

At present, these casings are reserved exclusively for very high power application components. The following figures show the materials used in these casings, and the manner in which the IGBT dies are placed into parallel connections.

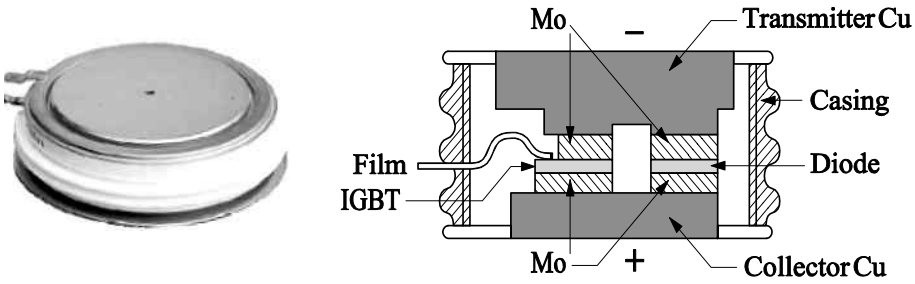

Figure 9.23. *Example of integrated coolers.*
a) Cooler integrated into the board [SCH 00];
b) cooler integrated into the DCB_Curamik [SCH 07]

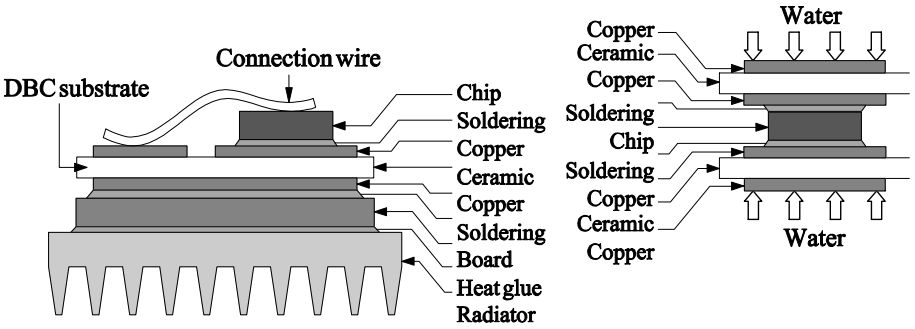

Figure 9.24. *3D assembly architecture enabling 2-sided die cooling [BUT 07]*

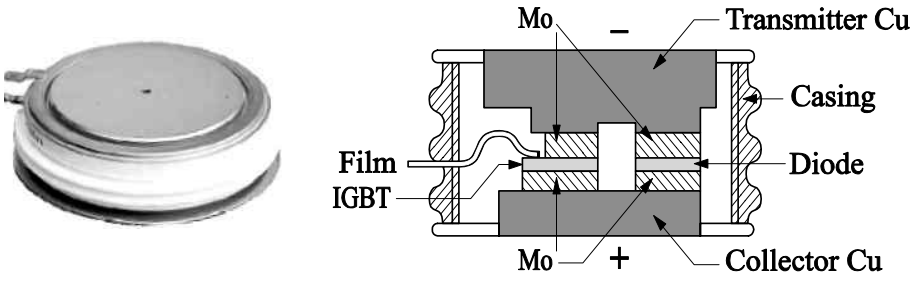

Figure 9.25. *Press-pack casing (source ABB)*

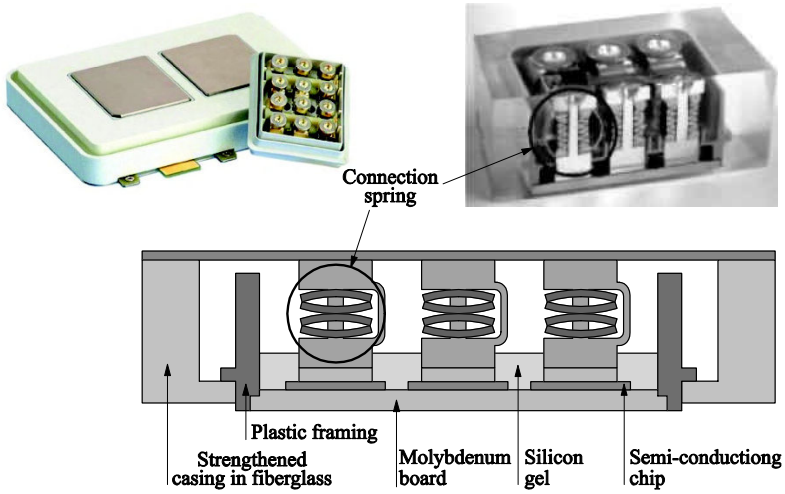

Figure 9.26. *Putting the dies into parallel connection (source: ABB)*

9.3.1.2. *Power dies*

The active elements in a power assembly are the dies (IGBT or MOSFET), which are made of a semi-conducting material (silicon), measuring a few hundreds of microns in thickness. To enable flow of high current, several dies are placed in parallel. Figure 9.27 shows an opened IGBT inverter module, of 600V-200A, showing the 6 IGBT dies and the 6 diode dies (smaller surface area).

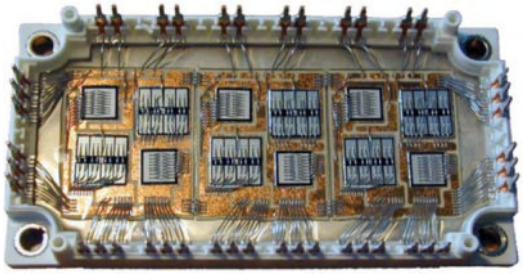

Figure 9.27. *Opened IGBT module 600V/200A, cast casing*

Faced with an ever increasing densification and operating temperature, as well as a reduced volume, the silicone has started reaching its thresholds, in terms of operating temperature. To resolve this, the trend is to develop high Gap semi-conducting materials (GaN and today, mainly SiC), so that it is possible to push back the operating limitations in the breakdown voltage/temperature reference frame. For

SiCs, the critical electrical field (7 times larger than for the Si) and the good level of heat conductivity will significantly reduce the size of the power devices.

However, the electronics industry, in general, and the power electronics industry, in particular, is still widely dominated by silicon. In fact, regarding the power components, there is currently no other semi-conducting material that can compete in terms of material quality, maturity of component production technology and production costs. Thus, to improve electrical and thermal performance, important progress has been made on the dies. We may note the generalization of trench grids (see Figure 9.21), which enables additional integration density and therefore a reduced die surface area. For IGBT moduli, Field Stop or Soft Punch Through technologies have made it possible to optimize losses in the on-state/losses in conduction, by minimizing the baseplate thickness and by controlling the excess charge levels injected around the baseplate in conduction regime. This also results in an increased integration density, as shown in the following figure. The reduced silicon volume results in larger integration and reduced costs.

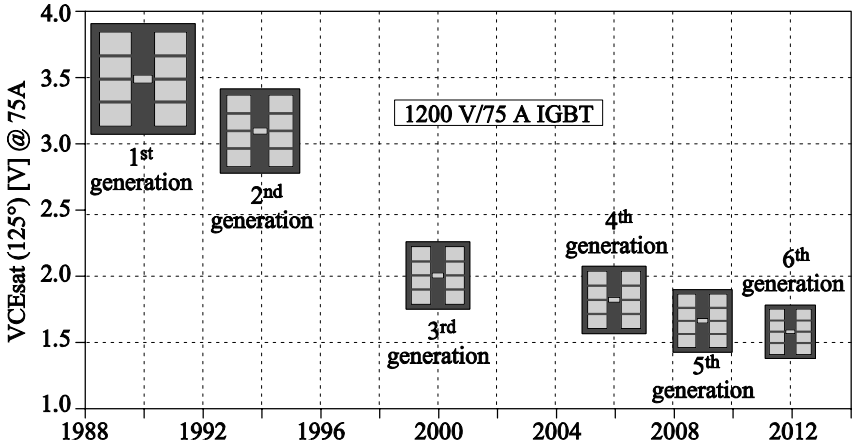

Figure 9.28. *Evolution of IGBT die sizes [BAY 08]*

The compensation for these gains in volume is the increased current density during the on-state, and therefore generally an increased power density, and consequently the die temperature.

9.3.1.3. *Conclusion*

Power moduli ensure an energy conversion function. They are built with single components that can be combined with a freewheel diode to realize a chopper, as an inverter arm, as a complete bridge or a three-phase inverter. They sometimes integrate the energy recovery chopper.

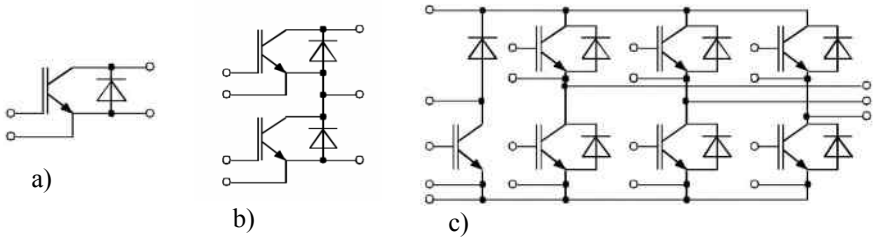

Figure 9.29. *Examples of converter structures integrated into power moduli, a) IGBT and freewheel diode, b) inverter arm, c) three-phase inverter and recovery chopper*

From a diagnosis point of view, power moduli present very few measurement possibilities. If we use the three-phase voltage inverters, as an example, the three arms are generally connected in parallel inside the module. The Kelvin source contacts used by the control drivers can also be used for a precise voltage measurement in the on-state, or even for measuring the resistance between the source contact and the source Kelvin contact (between pins 8 to 10 on the following figure). This resistance is representative of the bonding wires, the DCB copper track resistance, the power pin resistance and different contact resistances.

In general, we may also note the presence of a CTN resistance soldered onto the ceramic substrate, which gives the temperature of the area where it is positioned. In general, the temperature that can be estimated from this resistance, is the image of the module's baseplate temperature. Forthcoming results will prove that this temperature cannot be used to evaluate the aging characteristics of the module.

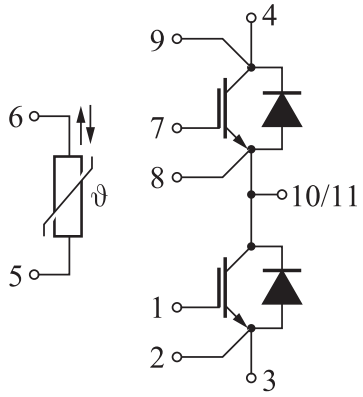

Figure 9.30. *Accessibility to the IGBT on an inverter arm*

9.3.2. *Causes and main types of degradation of power electronics moduli*

9.3.2.1. *Thermal fatigue strains*

The main causes for the degradations discussed in the following section are due to thermal fatigue strains on the converter moduli, particularly those stemming from heat cycles coming from profile missions in the transport domain. In fact, power converters used in transport systems are confronted with an important demand to reduce weight and size, and therefore tend toward highly integrated structures. These devices undergo a significant increase in the power density and often find themselves subjected to high thermal strains. The constraints both reside in the temperature levels in the surrounding environment which can be very high or very low, and in the cyclic temperature variations. The temperature levels reduce reliability, and temperature cycling is a factor, which aggravates degradation.

For example, the environment underneath a car hood imposes temperature cycles on the power devices, which vary between −40°C and 120°C. Another example is the closeness of the power electronics in an aircraft jet engine, where the environment temperatures may vary (in the worst case scenario) between −55°C and 200°C. These environmental temperature cycles are called "passive thermal cycles". In addition, the power dissipated in the active dies creates additional temperature variations of a lower amplitude (a few tens of degrees), but with a higher frequency. The latter type of thermal cycles are known as "active". Of course, the power components are subjected to both types of cycles, in a combined way. These cycles are illustrated in Figure 9.31, with the passive cycles in a continuous line and the active cycles in hatched lines.

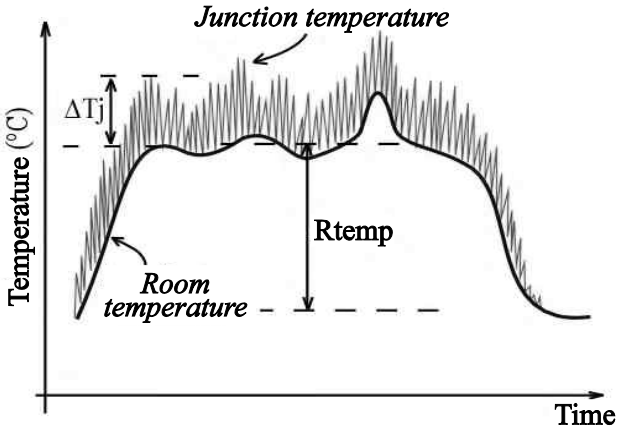

Figure 9.31. *"Active" and "passive" temperature cycles*

In terms of lifespan, the automobile domain requires devices that must satisfy demands of around 8,000 operating hours with around 400,000 power cycles. With regard to avionics, these requirements are in the order of 50,000 hours for equipment, which corresponds to 5,000 take off/landing phases for average flight durations of around 10 hours.

Although higher temperatures may be responsible for aging and malfunction in the dies, the causes for failure at high temperatures and under strong temperature variations mainly concern the assembly portion, where the main types of degradation are presented hereafter.

9.3.2.2. *Degradation in connection wires*

Problems relating to the resistance of the bonding wires, in relation to thermal cycles, have been widely studied and described in literature [CIA 02, LEF 03, HAM 99, RAM 00, PAS 02, OLD 04]. The most widely listed failure modes linked to the bonding wires are wire lift off (Figure 9.32a) and heel cracks (Figure 9.32b). The first mode is due to the difference in dilatation between the aluminum wire and the silicon substrate which, in the end, cracks the bonding foot on the interface when subjected to thermal cycles. The second mode is less frequent in the power components, and is due to thermal-mechanical cyclic strains. This type of degradation may be linked to bends in the wire itself, or to repetitive thermal effects due to too high current densities flowing in the connection wire, or finally an additional cause may be an unoptimized bonding process.

This type of damage may be detected by measuring the voltage drop across the components during on-state. However, the thermal resistance can increase due to cracks within the soldered joints that lead to a reduction in the cooling ability of the die. Therefore the measurements should be corrected to diagnose the fault.

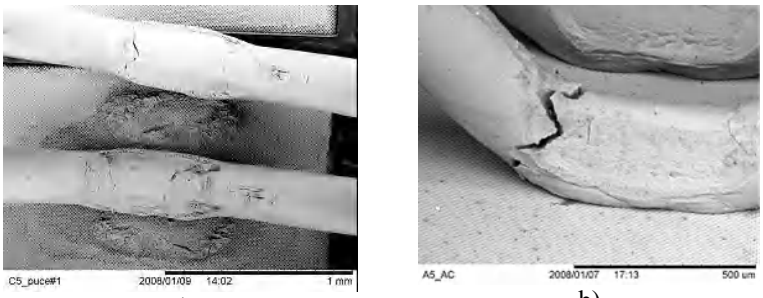

a) b)

Figure 9.32. *Different damages to bonding wires, a) wire lifting; b) heel crack*

9.3.2.3. *Metallization damage at the top side of the die*

Figure 9.33 shows SEM observations[5] of the condition of the transmitter metallization with several identical IGBT dies, under stressed active thermal cycles in different conditions. Figure 9.33a shows metallization before aging, where we can notice the elementary cell patterns, separated by around 15 µm, as well as the aluminum grains. The metallization in Figure 9.33b has undergone 250,000 cycles with variations in the junction temperature ΔT_j = 60°C at low room temperature (between 35°C and 95°C). In these conditions, despite the very high number of thermal cycles, the metallization remains visibly unaffected. As the metallization has undergone less number of cycles (100,000), Figure 9.33c shows visible damage for amplitudes of identical temperatures (ΔTj = 60°C), but on a much higher level (between 90°C and 150°C). Finally, Figure 9.33d shows a metallization which has barely undergone 47,000 thermal cycles, but is under far more severe conditions (ΔT_j = 80°C, between 90°C and 170°C). This lower number of cycles has nonetheless lead to high levels of damage in the metallization, which demonstrates a highly disturbed aspect with "crevices" on the grain joints, where the cell patterns are hardly visible. These results clearly show that this damage is greatly dependent on the ΔTj and also on the maximum temperature level reached (T_{jmax}), but it is still difficult to determine the most predominant factor for such a type of damage. However, it is likely that the thermal cycles are responsible for these degradations, and also that their effect depends on the maximum junction temperature. This is indicated in [CIA 02], which refers to a maximum junction temperature of 110°C, where these degradations would become significant.

Figure 9.34 [DET 04] shows a micro-section of an IGBT cell, where the metallization damage leads to "microcracks", which may result in the disconnection of the elementary cells. This intergranular loss of cohesion, where the aluminum grains are no longer jointed, has been observed by FIB[6] analyzes on samples that have been subjected to thermal cycles [KHO 07b].

One effect of these die metallization degradations is the increased resistance in this layer (Figure 9.35). This effect was demonstrated by specific "four wire" measurements, carried out on IGBT dies which were subjected to special thermal cycles (following repetitive short-circuits) [ARA 08]. However, these measurements have led to metallization degradations, which are entirely comparable to those shown in Figure 9.33. These regularly carried out measurements during the aging process show that after a period where no evolution in the resistance is reported, then a regular increase is observed.

5 SEM: scanning electron microscopy.
6 FIB: *Focused Ions Beam.*

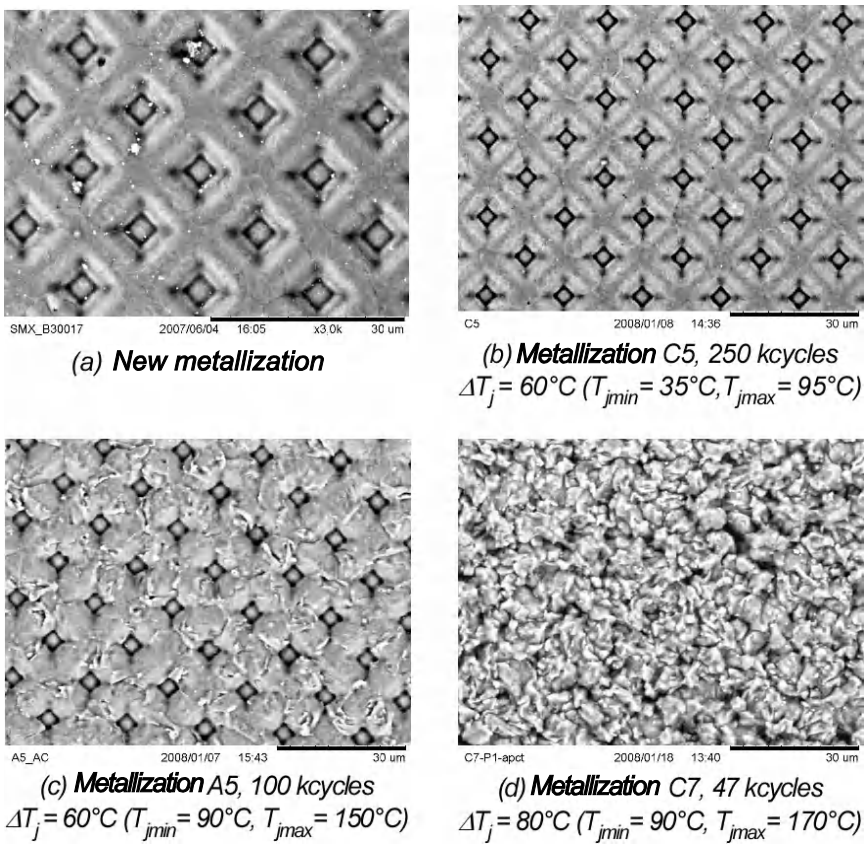

Figure 9.33. *SEM observations of IGBT die metallizations having undergone different thermal cycling conditions*

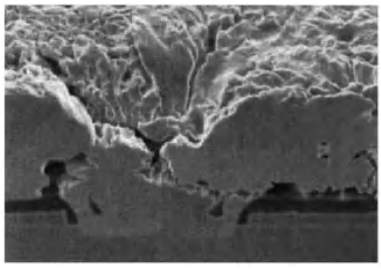

Figure 9.34. *Micro-section of a damaged metallization through thermal cycling on a cell [DET 04]*

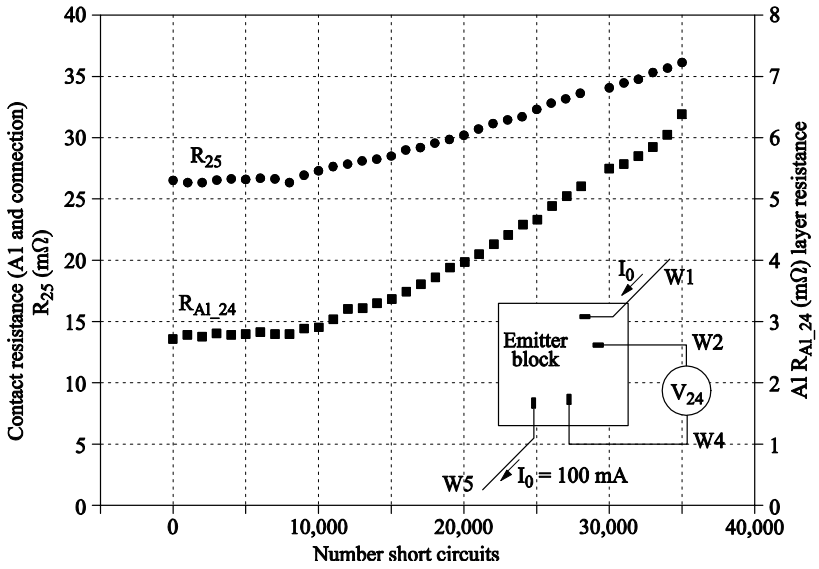

Figure 9.35. *Metallization degradation of an IGBT transmitter subjected to repetitive short-circuit cycles and successive increased layer resistance [ARA 08]*

Unfortunately, this damage is difficult to detect without specific measurement devices and will remain concealed by the damaged caused by bonding wires or the contacts between wires and the metallization.

9.3.2.4. *Soldering damage*

We may find two types of soldering in a power module: that connecting the active die to the metalized insulating substrate, and that between the substrate and the module baseplate (Figure 9.19). In principle, the second type has "softer" mechanical characteristics than the first type and, moreover, a larger surface area. These two reasons mean that the soldering on the baseplate is likely to break more easily than the soldering on the die due to thermal cycles, as we can see in Figure 9.36a.

However, in extreme temperature conditions, a less frequent degradation mode is "cavitation" (Figure 9.36b). In fact, the phenomenon is certainly more linked to the higher temperature attained, which is dangerously close to the melting temperature, than the temperature variation. Here, we by no means observe fractures, but rather a phenomenon of matter transportation (thermomigration) within the soldering, during thermal cycles that lead to cavity creation.

These degradations increase the thermal resistance in the electronic module assembly and thus make the heat transfer from hot sources (semi-conducting power

dies) to the cold source (cooler) less efficient. This leads to increased temperature levels in the assembly and, in particular, in the active die. These degradations can be detected by measuring the thermal resistance in the assembly.

9.3.2.5. *Insulating substrate degradation*

The experimental results from the passive thermal cycling have shown us that the thickness of the DCB (Direct copper bonding, see section 7.3.1.1) substrate metallization will affect the upper side of these substrates, with risks of conchoidal fracturing [DUP 06]. This is referred to as a "peeling" phenomenon on the metallizations, generally in copper, which are attached to the ceramic. However, these fractures occur in conditions of relatively severe temperature changes, and after a certain number of thermal cycles. Figure 9.37 shows this type of degradation for temperature cycles of 210°C, where the cycles vary between −30°C and 180°C in the AlN ceramics (635 µm) and Cu (300 µm). The number of failure cycles depends on the severity of the cycle and the DCB structure (nature and thickness of the ceramic, thickness of the copper metallization). The thickness of the copper metallizations affects the lifespan of the DCB substrate; the thin metallizations resist cycling better than the thick ones. Similar results were observed and published in [SCH 03, DAL 95, MIT 99, NAG 00].

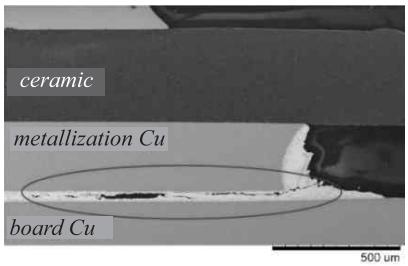

a)

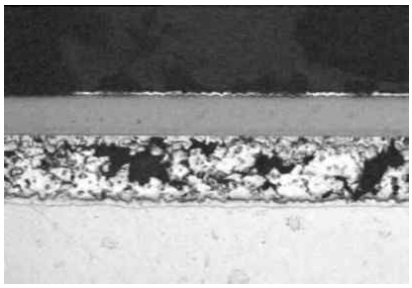

b)

Figure 9.36. *Soldering damage. a) fracture in the board soldering/ceramic substrate [BOU 08]; "cavitation" in the die soldering*

These fractures are due to strains in the ceramics, which grow unceasingly larger during the cycles. This is a consequence of the hardening effect of the copper films, and is induced by the different dilatation coefficients between both materials. During the thermal cycles, the strains in the ceramic increase, due to hardening of the copper, until its acceptable limit is reached.

Still, these degradations increase the thermal resistance of the whole assembly and could be detected by its measurement.

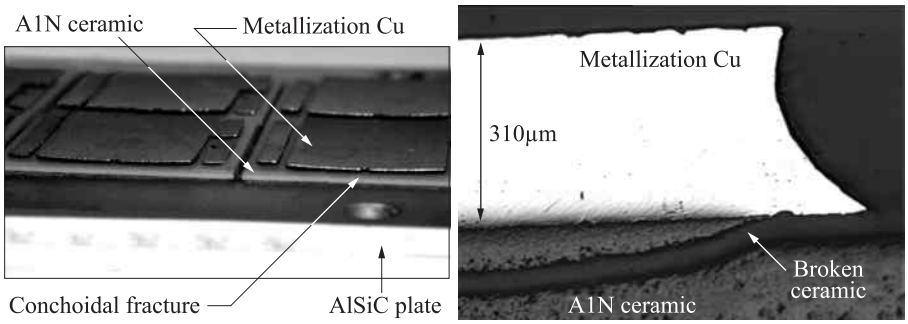

Figure 9.37. *Ceramic fracturing after 90 cycles a) general view; b) micro-section*

9.3.3. *Interconnection degradation effects on electrical characteristics and potential use for diagnosis*

9.3.3.1. *Degradation in connection wires*

The indicator that is usually used for detecting bonding wire damage is the direct voltage drop. The bonding wires are among the most fragile elements in the power moduli. It has been shown that moduli subjected to power injection cycles could present the beginnings of heel cracks without having a measureable effect on the direct voltage drop.

We must wait for considerable damage in the wires or the interface between the wire and the die metallization, so that this effect can be detected by measuring the voltage drop in the on-state. The following figure shows, in particular, the variations in the on-state voltage drop during the application of 250,000 power injection cycles corresponding to a rise in the junction temperature of 60°C. The damage reported on the dies after these 250,000 cycles is shown in Figure 9.33. We note an increase of only 3% on the on-state voltage drop at the end of testing.

Similar measurements were carried out on low voltage MOFSET moduli. The on-state voltage drop was continually recorded during the whole cycling test

duration, which made it possible to follow the on-state resistance of the different dies making up the module. The following figure shows the result for the three low level transistors in the integrated three-phase voltage inverter. We may notice two severe variation phases in the resistance on the transistor T4, which can be correlated with a "heel crack fracture" failure type.

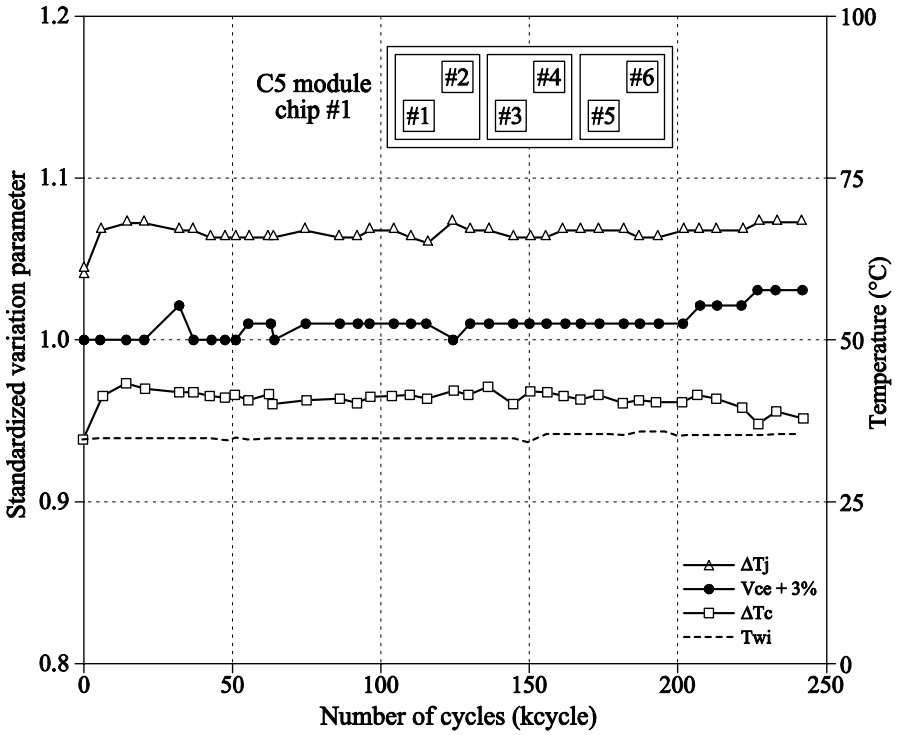

Figure 9.38. *Evolution of the direct voltage drop of die #1 of the C5 module after 250,000 cycles, Twin = 35°C, ΔTj = 60°C, Ic = 315A*

The fracturing of a few wires relates to a very advanced condition of aging in the component. The heightened resistance noticed here, after the wires have been raised to only 3%, is still very difficult to detect.

The active cycling tests, presented below, were also responsible for a significant level of aging in the layer of metallization deposited on the dies. The very low variations in the on-state resistance show that the aging effect of the metallization layer is very difficult to detect using an on-state resistance measurement.

9.3.3.2. *Oxide gate degradation*

Oxide gate degradation generally results in the occurrence of a local leakage current crossing the oxide layer, which results in creation of a short-circuit. The degradation could be due to charge traps in the oxide caused by the application of an electrical field to the oxide terminals, or by the injection of hot carriers in the oxide. This degradation mode was highlighted by MOS power transistors [MAN 00b].

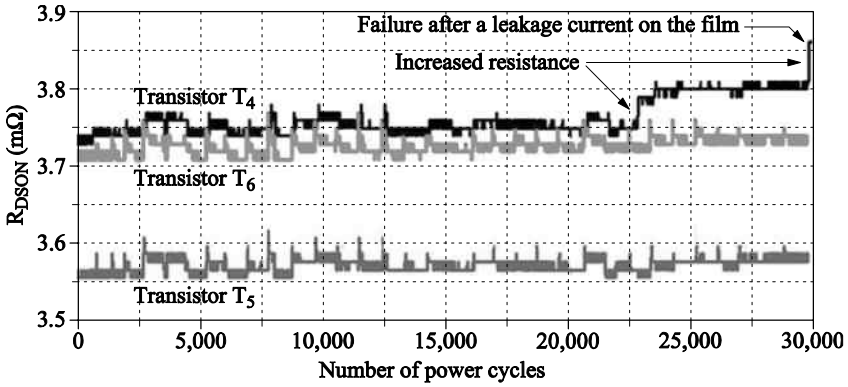

a) On-state resistance variation

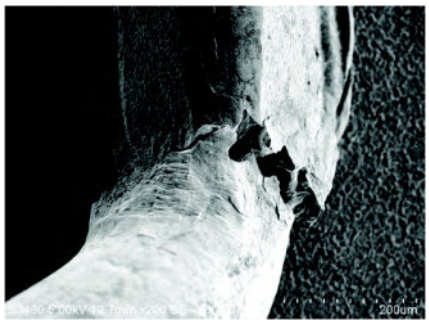

b) Bracked heel

Figure 9.39. *Power cycling in an MOFSET module (I = 150A, T_{CASE} = 90°C, T_{JMAX} = 170°C), variation of the on-state resistance; b) bonding heel cracks*

One of the ways for assessing the reliability of the oxide gate is to outline the current-voltage (I-V) characteristics and to carry out TDDB tests (Time Dependent Dielectric Breakdown) [MAN 00]. However, with these methods it is impossible to observe the oxide properties during the power cycling process, or during operation, which makes this failure mode the most critical, since it is difficult to detect. Thus, the gate breakdown is unpredictable and leads to instant failure in the module.

9.3.4. *Effects of interface degradation on thermal characteristics and potential use for diagnosis*

As stated in the previous section, the separation of soldering between the active die and the insulating ceramic, or even between the insulating ceramic and the board, results in an increase of the local interface contact resistance. This leads to a progressive increase in the thermal resistance between the dies and the board, and therefore a similarly gradual yet abnormal increase in the die temperatures, finally leading to the module's destruction. These degradations directly affect the thermal characteristics of the devices, and may consequently be detected by using techniques, which analyze the structures' thermal responses. The most frequently used techniques are based on transient thermal impedance analysis, which we will present in the following section.

9.3.4.1. *Fault or degradation detection in the die soldering*

The example described above is not caused by degradation as a result of thermal fatigue. They are more linked to manufacturing faults, but the resultant faults are indeed comparable. Figure 9.40 shows acoustic images of samples, which represent the active dies soldering, taken from [REN 01].

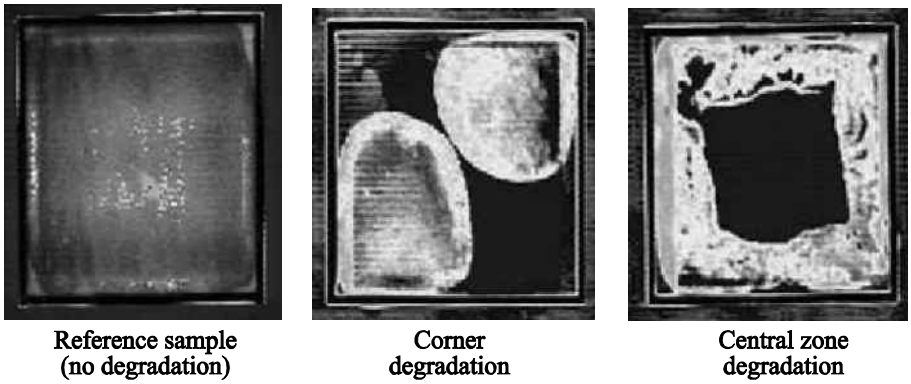

Figure 9.40. *Fault types in the soldering of active dies [REN 01]*

The technique used here appears in the function analysis, which is known as the structure function [PRO 67, SZE 88], and enables the entire thermal flux pathway to locate material transitions (interfaces), or detect changes in the materials' thermal properties. This function gives the cumulated thermal capacities C_{Σ} and the cumulated thermal resistances R_{Σ} of the system measured from the heat source (Figure 9.41). More precisely, the function studied here is that of the differential

structure function, where the ordinate axis is the parameter $K(R_\Sigma) = \frac{dC_\Sigma}{dR_\Sigma}$, with the abscissa axis remaining as R_Σ. Figure 9.42 gives the differential structure functions of the samples presented in Figure 9.41. We can observe that the first peaks, which represent the active dies, are localized to the same value of Rth, but the following peak presents a more or less large delay in Rth according to the effects of the fault. In the case of a soldered join in good condition, there is minimal distancing of value Rth from the peak, but a slight increase in the faults in the corners, and even more so for faults in the middle.

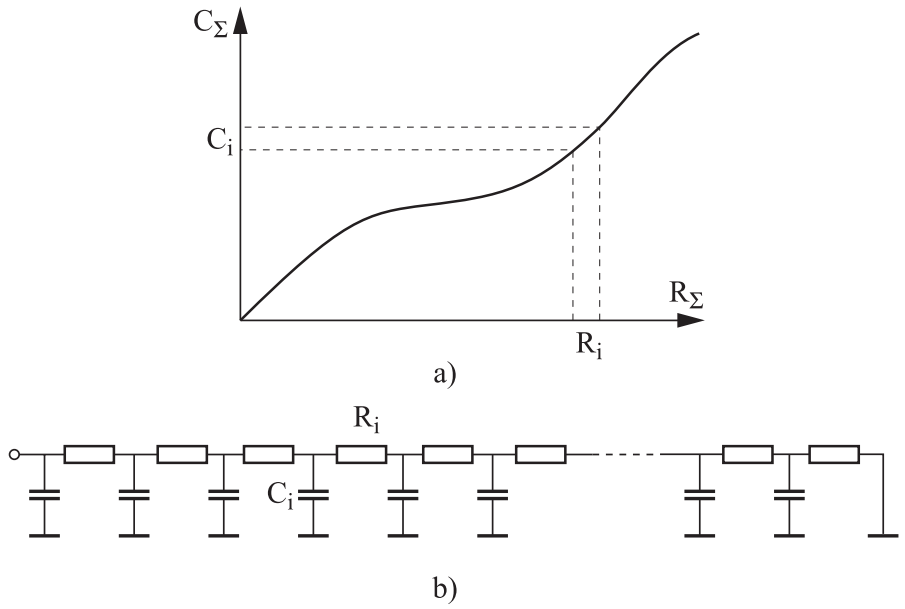

Figure 9.41. *The structure function and the equivalent corresponding thermal network [REN 01]*

9.3.4.2. *Fault or degradation detection in the board brazing*

Figure 9.43 shows the acoustic image of the interfaces between a board and the 6 ceramic substrates of a high power IGBT module, where this module is used for railway traction. The black sections relate to the undamaged areas of the brazing, with a correct local contact resistance. The light areas of the interface represent the areas damaged by delamination in the brazing with very high localized contact resistance values.

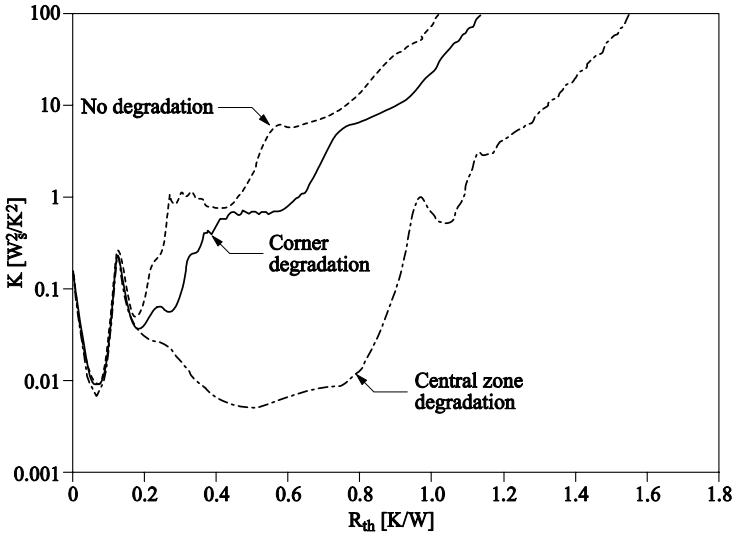

Figure 9.42. *Differential structure function of different cases of brazing faults in Figure 9.41 [REN 01]*

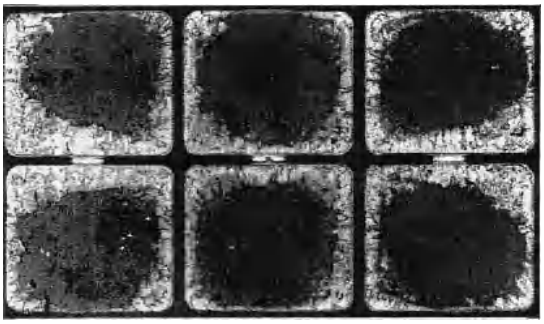

Figure 9.43. *Acoustic image of the ceramic/board interfaces after aging through thermal cycling (source: LTN INRETS)*

Such a degradation in the brazing between the ceramic substrate and the baseplate results in an increased thermal resistance between the junction (die) and the board, which is written as T_{THJC} of around 40% here. Evolution is sensitive, provided that the delaminated brazing significantly changes the power flux flowing from the dies toward the baseplate, and that the dies are not too far away from the edges of the DCB. Estimating the thermal resistance requires that we determine the dissipated losses in the established regime, the die temperature (average temperature for measurements using a heat sensitive parameter), and finally the baseplate

temperature, ideally underneath the die. We can note here that a precise estimation of the thermal resistance requires suitable methodology and instrumentation, which (for an application) can be extremely tricky to implement.

9.4. Conclusion

This chapter has covered the detection and diagnosis of faults in static converters from two angles: the first angle concerns the methods for diagnosing power module and the second (closer to the physical aspect of the component and module) describes principal failure mechanisms. This study has shown that the temperature of the environment, as well as the temperature variations due to the thermal cycles, are the main causes for failure. It has also shown that these failures can be correlated to parametric variations of the on-state resistance, the thermal resistance, or the transient thermal impedance. However, these variations are not only difficult to measure, but they are also – for on-state resistances, representing failures linked to connections – low in amplitude. For now, they cannot act as signatures that could be used for a robust diagnosis. This is a field of investigation for developing better knowledge of degradation mechanisms, developing adequate embedded sensors, and diagnosis methods based on highly correlated data with low variation.

Non-destructive thermal and/or electrical control could also be a potential area of research with:

– a section on modeling, dimensioning and integrating sensors into the component or module;

– a section on accurate thermal modeling of the component and integrating the modeling within system modeling;

– a section on the use of inversion techniques for characterization, or diagnostics studies, by using the thermal history.

The precise understanding of degradation mechanisms could also contribute to identifying laws of aging, as well as end-life criteria, which could enrich models for designing and dimensioning. Finally, these models and the thermal history of the component or module could be adjustment factors of the laws of control in normal mode or during operating modes in degraded mode.

9.5. Bibliography

[ARA 08] ARAB M., LEFEBVRE S., KHATIR Z., BONTEMPS S., "Experimental investigations on trench field stop IGBTs under repetitive short-circuit operations", *IEEE Power Electronics Specialists Conference*, Rhodes, Greece, June 2008.

[BAY 08] BAYRER R., "Higher Junction Temperature in Power Modules – a demand from hybrid cars, a potential for the next step increase in power density for various Variable Speed Drives", *PCIM'*08, 2008.

[BOU 08] BOUARROUDJ M., Etude de la fatigue thermo-mécanique de modules électroniques de puissance en ambiance de températures élevées pour des applications de traction de véhicules électriques et hybrides, PhD Thesis for ENS-Cachan, October 2008.

[BUH 94] BUHLER H., *Réglage par logique floue*, Presses Polytechniques et Universitaires Romandes, Lausanne, 1994.

[BUT 07] BUTTAY C., RASHID J. *et al*., "High performance cooling system for automotive inverters", *EPE 07*, Aalborg, 2007.

[CIA 02] CIAPPA M., "Selected failure mechanisms of modern power modules", *Microelectronics Reliability*, vol. 42, p. 653-667, 2002.

[DET 04] DETZEL T.H., GLAVANOVICS M., WEBER K., "Analysis of wire bond and metallization degradation mechanisms in DMOS power transistors stressed under thermal overload conditions", *Microelectronics Reliability*, vol. 44, p. 1485-1490, 2004.

[DAL 95] DALAL K.H. *et al*., "Design trade-offs and reliability of power circuit substrates with respect to varying geometrical parameters of direct copper bonded Al2O3 and BeO", *IEEE Industry Applications Conference Annual Meeting*, p. 923-929, October 1995.

[DEL 07] DELPHA C., DIALLO D., BENBOUZID M.E.H., MARCHAND C., "Pattern recognition for diagnosis of inverter fed induction machine drive: a step toward reliability", *2007 IET Colloquium Reliability in Electromagnetic Systems*, Paris, 2007.

[DEL 08] DELPHA C., DIALLO D., BENBOUZID M.E.H., MARCHAND C., "Application of classification methods in fault detection and diagnosis of inverter fed induction machine drive: a trend towards reliability", *European Physical Journal of Applied Physics*, no. 43, p. 245-251, 2008.

[DIA 05] DIALLO D., BENBOUZID M.E.H., HAMAD D., PIERRE X., "Fault detection and diagnosis in an induction machine drive: a pattern recognition approach based on Concordia stator mean current vector", *IEEE Transactions Energy Conversion*, vol. 20, no. 3, p. 512-519, September 2005.

[DUP 06] DUPONT L., KHATIR Z., LEFEBVRE S., BONTEMPS S., "Effects of metallization thickness of ceramic substrates on the reliability of power assemblies under high temperature cycling", *Microelectronics Reliability*, vol. 46, p. 1766-1771, 2006.

[HAM 99] HAMIDI A., BECK N., THOMAS K., HERR E., "Reliability and lifetime evaluation of different wire bonding technologies for high power IGBT modules", *Microelectronics Reliability*, vol. 39, p. 1153-1158, 1999.

[IVA 03] IVANOVA M., AVENAS Y., SCHAEFFER C., GILLOT C., BRICARD A., "Apport de la microthermie pour le refroidissement des systèmes", *Journées électrotechniques du club EEA*, Amiens, 12-13, March 2003.

[JAM 99] JAMBU M., *Méthodes de bases de l'analyse de données*, Eyrolles, Paris, 1999.

[KAU 87] KAUFMANN A., *Nouvelles logiques pour l'intelligence artificielle*, Hermès, Paris, 1987.

[KHO 07a] KHOMFOI S., TOLBERT L.M., "Diagnosis and reconfiguration for multilevel inverter drive using AI-based techniques", *IEEE Transactions Industrial Electronics*, vol. 54, no. 6, p. 2954-2968, December 2007.

[KHO 07b] KHONG B. *et al*., "Characterization and modeling of aging failures on power MOSFET devices", *Microelectronics Reliability*, vol. 47, p. 1745-1750, 2007.

[LEF 03] LEFRANC G. *et al*., "Aluminum bond-wire properties after 1 billion mechanical cycles", *Microelectronics Reliability*, vol. 43, p. 1833-1838, 2003.

[LU 09] LU B., SHARMA S.K., "A literature review of IGBT fault diagnostic and protection methods for power inverters", *IEEE Transactions Industry Applications*, vol. 45, no. 5, p. 1770-177, September-October 2009.

[MAN 00] MACA J.V., WONDRAK W. *et al*., "High temperature time dependent dielectric breakdown of power MOSFETs", *HITEC Session V*, 2000.

[MIL 95] MILITARY HANDBOOK 217F, Reliability prediction of electronic equipment, 28 February 1995.

[MIT 99] MITIC G., BEINERT R. *et al*., "Reliability of AlN Substrates and their Solder Joints in IGBT Power Modules", *Microelectronics Reliability*, vol. 39, p. 1159-1164, 1999.

[MOH 09] MOHAGHEGHI S., HARLEY R.G., HABETLER T.G., DIVAN D., "Condition monitoring of power electronic circuits using artificial neural networks", *IEEE Transactions Power Electronics*, vol. 24, no. 10, p. 2363-2367, October 2009.

[MOR 88] MORRISSON D.F., *Multivariate Statistical Methods*, p. 415, McGraw-Hill, Singapore, 1988.

[MUR 06] MURPHEY Y., MASRUR M.A., CHEN Z., ZHANG B., "Model-based fault diagnosis in electric drives using machine learning", *IEEE/ASME Transactions Mechatronics*, vol. 11, no. 3, p. 290-303, June 2006.

[NAG 00] NAGATOMO Y., NAGASE T., "The study of the power modules with high reliability for EV use", *17th EVS Conference*, Montreal, October 2000.

[NEJ 00] NEJJARI H., BENBOUZID M.E.H., "Monitoring and diagnosis of induction motors electrical faults using a current Park's vector pattern learning approach", *IEEE Transactions Industry Applications*, vol. 36, no. 3, p. 730-735, May-June 2000.

[OLD 04] OLDERVOLL F., STRISLAND F., "Wire-bond failure mechanisms in plastic encapsulated microcircuits and ceramic hybrids at high temperatures", *Microelectronics Reliability*, vol. 44, no. 6, p. 1009-1015, 2004.

[OND 09] ONDEL O., CLERC G., BOUTLEUX E., BLANCO E., "Fault detection and diagnosis in a set "inverter–induction machine" through multi-dimensional membership function and pattern recognition", *IEEE Transactions Energy Conversion*, vol. 24, no. 2, p. 431-441, June 2009.

[PAS 02] PASSAGRILLI C., GOBBATO L., TIZIANI R., "Reliability of Au/Al bonding in plastic packages for high temperature (200ºC) and high current applications", *Microelectronics Reliability*, vol. 42, no. 9-11, p. 1523-1528, 2002.

[PRO 67] PROTONOTARIOS E.N., WING O., "Theory of non-uniform RC lines", *IEEE Transactions on Circuit Theory*, vol. 14, no. 1, p. 2-12, 1967.

[RAM 00] RAMMINGER S., SELIGER N., WACHUTKA G., "Reliability model for AI wire bonds subjected to heel crack failures", *Microelectronics Reliability*, vol. 40, p. 1521-1525, 2000.

[REN 01] RENCZ M., SZEKELY V., "Determining partial thermal resistances in a heat flow path with the help of transient measurements", *Proceedings of the 7th THERMINIC Workshop*, Paris, p. 250-256, 24-27, September 2001.

[SAP 90] SAPORTA G., *Probabilités, analyse des données et statistique*, Technip, Paris, 1990.

[SCH 00] SCHULZ-HARDER J. *et al*., "Micro channel water cooled power modules", *PCIM'00*, Nuremberg, June 2000.

[SCH 03] SCHULZ-HARDER J., "Advantages and new development of direct bonded copper substrates", *Microelectronics Reliability*, vol. 43, p. 359-365, 2003.

[SCH 07] SCHULZ-HARDER J., MEYER A., "Hermetic packaging for power multidie modules", *EPE07*, 2007.

[SZE 88] SZEKELY V., VAN BIEN T., "Fine structure of heat flow path in semiconductor devices: a measurement and identification method", *Solid-State Electronics*, vol. 31, p. 1363-1368, 1988.

[THO 95] THORSEN O.V., DALVA M., "A survey of the reliability with an analysis of faults on variable frequency drives in the industry", *European Conference on Power Electronics and Applications*, Seville, p. 1033-1038, 1995.

[ZAD 65] ZADEH L.A., "Fuzzy sets", *Information and Control*, vol. 8, p. 338-353, 1965.

[ZID 03] ZIDANI F., DIALLO D., BENBOUZID M.E.H., NAIT SAID M.S., "Induction motor stator faults diagnosis by a current concordia pattern based fuzzy decision system", *IEEE Transactions Energy Conversion*, vol. 18, no. 4, p. 469-475, December 2003.

[ZID 08] ZIDANI F., DIALLO D., BENBOUZID M.E.H., NAIT SAID R., "A fuzzy-based approach for the diagnosis of fault modes in a voltage-fed PWM inverter induction motor drive", *IEEE Transactions Industrial Electronics*, vol. 55, no. 2, p. 586-596, February 2008.

List of Authors

Imène Ben AMEUR BAZINE
LAII
Poitiers
France
and
LSE
Tunis
Tunisia

Smail BACHIR
LAH
Poitiers
France

Sadok BAZINE
LAH
Poitiers
France
and
LSE
Tunis
Tunisia

Mohamed BENBOUZID
LBMS
Brest
France

Monia Ben Khader BOUZID
LSE
Tunis
Tunisia

Gérard CHAMPENOIS
LAII
Poitiers
France

Isabelle CHANTEUR
PSA
Vélizy-Villacoublay
France

Guy CLERC
Laboratoire AMPERE
Lyon
France

Mikaël CUGNET
INES-RDI
CEA Grenoble
France

Claude DELPHA
L2S
Paris
France

Demba DIALLO
LGEP
Paris
France

Mohamed EL KAMEL OUMAAMAR
Electro technical laboratory
Constantine
Algeria

Emmanuel FOULON
VALEO Systèmes thermiques
La Verrière
France

Sylvie GRUGEON
LRCS
Amiens
France

Khaled JELASSI
LSE
Tunis
Tunisia

Zoubir KHATIR
LTN
INRETS
Versailles
France

Stéphane LARUELLE
LRCS
Amiens
France

Stéphane LEFEBVRE
SATIE
CNAM Paris
France

Luc LORON
IREENA
Polytech'Nantes
France

Jean-Claude MARQUES
LAGEP
Lyon
France

Sandrine MOREAU
LAII
Poitiers
France

Najiba MRABET BELLAAJ
LSE
Tunis
Tunisia

Alain OUSTALOUP
IMS-LAPS
Bordeaux
France

Thierry POINOT
LAII
Poitiers
France

Hubert RAZIK
Laboratoire AMPERE
Lyon
France

Jocelyn SABATIER
IMS-LAPS
Bordeaux
France

Bernard SAHUT
PSA
Vélizy-Villacoublay
France

Emmanuel SCHAEFFER
IREENA
Polytech'Nantes
France

Jean-Marie TARASCON
LRCS
Amiens
France

Jean-Claude TRIGEASSOU
IMS-LAPS
Bordeaux
France

Index

C

D

E

F

H

I

J

K

L

M

R

S

T

V

W